JNC TY8400 2001-006

JNC-DOE Collaborative Program on Mass Transport : Characterization and Predictive Technologies

2000 — 2001 Annual Report

July, 2001

Ernest Orlando Lawrence Berkeley National Laboratory

〒３１９－１１８４　茨城県那珂郡東海村村松４番地４９
核燃料サイクル開発機構
技術展開部　技術協力課

JNC TY8400 2001-006
2 0 0 1 年 7 月

JNC-DOE Collaborative Program on Mass Transport : Characterization and Predictive Technologies
(JNC-DOE 共同研究「水理・物質移動：サイト特性調査及び予測技術」)

2000 – 2001 Annual Report
(共同研究報告書)

Principal Investigator : Chin –Fu Tsang[1] and Kenzi Karasaki[1]

要 旨

JNC/DOE 間の共同研究計画は、地層中への放射性廃棄物の処分において重要な役割を担っているプロセスを支配する基本的な物理及び化学特性についての理解を深めるとともに、不均質な地層中での核種移行や地層からの核種放出についての調査手法や予測手法を開発することを目的として策定されている。

共同研究計画にしたがって、2000 年度は以下の 6 つのタスクを実施した。

1. 水圧と地表面変位を用いた逆解析技術の開発
非定常の水圧変化とそれに起因する地表面変位の観測データを利用して逆解析を行ない、地層の透水係数分布を推定するアルゴリズムを開発した。この手法は、水圧変化に伴う、地表面変位の計測データを使用するのみであるので、解析に必要なデータを取得するために多くの試錐孔を使用する必要がなく経済的であり、また、地表面の変位と地下の空隙率の変化の関係を比較的容易に理解するのに適している。本手法をカリフォルニア州レイモンドサイトでの原位置試験に適用した結果、高透水性帯の存在が予測された。

2. ランダム媒体中の水理・物質移行に関する平均化方程式の開発
不十分なフィールドデータを外挿する際に、そこでのパラメータはランダム分布のような統計分布に従うことが予め仮定される。本研究では、ランダム媒体中の水理・物質移行に関する平均化方程式の一般形の導出方法を提案した。一般形の導出には、統計問題におけるグリーン関数の存在の仮定、グリーン関数の一般的性質、透水係数、空隙率、流速に関するランダム場におけ

[1] Earth Science Division, Ernest Orlando Lawrence Berkeley National Laboratory, University of California, Berkeley, California 94720, USA.

る基本情報を使用した。

3. レイモンドサイトにおけるサイト特性調査手法のまとめ
カリフォルニア州レイモンドサイトで実施された多くの地球物理学的及び水理学的調査の結果についてのまとめを行った。実験でキャリブレートされるモデルが自然条件のもとで汚染物質の輸送を適切に予測できるということは保証できない。一方、それらのモデルがどの程度コスト効果があるか、どの程度の詳細さが必要かについて調べるのは興味深い。また、システムの平均的挙動を評価するために数回の長期の大規模な試験を実施することは、数多くの小規模スケールの実施して総合的に評価するよりも良好な結果を得る。

4. 飽和・不飽和領域媒体中の水理・物質移行の動的チャンネリング
不均質性が強く、飽和・不飽和状態にある媒体中の水理・物質移行の動的チャンネリングについてレビューした。流れのチャンネリング現象は、透水係数分布と水圧分布に依存する。本研究では3次元領域における透水係数変化と空間的相関範囲の関数としてチャンネリングの出現を記述した。また、飽和・不飽和状態にある不均質媒体中のチャンネリング流れの影響について議論した。

5. マトリクス拡散を考慮した粒子追跡法の開発と注水・揚水トレーサ試験への適用
有限なマトリクスブロック中への拡散を考慮にいれて亀裂中のトレーサ移行を解析する粒子追跡法を開発した。この方法は、Yamashita and Kimura (1990) の手法を拡張したものである。この方法を、マトリクス拡散を有する不均質亀裂中の物質移動に関する多くの解析的及び準解析的解を用いて検証した。さらに、この方法を不均質亀裂中の注水・揚水トレーサ試験に適用し、破過曲線を算出した。

6. 亀裂交差部でのトレーサの混合
本研究では、亀裂交差部でのトレーサ混合特性と伝達確率に関する数値シミュレーションを実施した。ランダムウォーク、粒子追跡法を亀裂交差部におけるトレーサ移行解析に使用した。広範囲のペクレ数に対してシミュレーションの結果と既存の数値解及び解析解と比較した。

7. 諸外国における性能評価手法のレビュー
NIREX-95、SITE-94、TILA-99 のレビューを行ない、それぞれのレポートで採用している性能評価手法の調査結果及び課題についてまとめた。さらにこれらの議論を踏まえ、H-12 レポートに対する提言を行なった。

Contents

JNC-DOE Collaborative Program on Mass Transport :
Characterization and Predictive Technologies
2000-2001 Annual Report iv

A Coupled Inversion of Pressure and Surface Displacement
D.W.Vasco, Kenzi Karasaki and Kiyoshi Kishida 1

Exactly Averaged Equations for Flow and Transport in Random Media
Mark Shvidler and Kenzi Karasaki 53

Multidisciplinary Fractured Rock Characterization Study at Raymond Field Site, Raymond, California
Kenzi Karasaki, Barry Freifeld, Andrew Cohen, Ken Grossenbacher, Paul Cook and Don Vasco
..... 76

Dynamic Channeling of Flow and Transport in Saturated and Unsaturated Heterogeneous Media
Chin-Fu Tsang, Luis Moreno, Yvonne W. Tsang, and Jens Birkhölzer 112

A Particle-Tracking Method for Advective Transport in Fractures with Diffusion into Fracture Matrix Blocks with Application to Tracer Injection-Withdrawal Testing
Y.W. Tsang and C.F. Tsang 141

Tracer Mixing at Fracture Intersections
Guomin Li 167

PA Methodologies from a Combined Review of NIREX95, SITE-94 and TILA-99
Chin-Fu Tsang 196

2000-2001 Annual Report

JNC-DOE Collaborative Program on Mass Transport: Characterization and Predictive Technologies

Principal Investigators

Chin-Fu Tsang and Kenzi Karasaki

Earth Sciences Division
Ernest Orlando Lawrence Berkeley National Laboratory
One Cyclotron Road
Berkeley, CA 94720, USA
Fax: 1 510 486 5686

Background

This is the eighth year of a continuing collaborative program which started in April, 1993 under an Annex pursuant to the Agreement of November 20, 1986 between the Nuclear Power and Fuel Development Corporation (PNC), Japan and United States Department of Energy (DOE) on Cooperation in the Area of Radioactive Waste Management. The Annex was originally signed on March 26, 1993 to be effective for four years, and was subsequently renewed on September 15, 1997 for three additional years based on the renewed PNC-DOE Binational Agreement. The subject of research covered under this Annex is Mass Transport: Characterization and Predictive Technologies. In 1998, PNC was renamed Japan Nuclear Cycle Development Institute (JNC). The DOE Office overseeing this annex agreement is the Office of Environmental Management, Office of Sciences and Technology (EM-50). The work is performed at the Earth Sciences Division of the Ernest Orlando Lawrence Berkeley National Laboratory with funding support from JNC.

Objectives

The primary objective of this Collaborative Program is to (a) improve the understanding of the fundamental physics and chemistry that govern the processes which play a significant role in radio active waste isolation/disposal in geologic systems and (b) develop characterization and modeling methodologies for predicting release and transport of radio nuclides in heterogeneous geologic media. The Collaborative Program focuses on the definition and investigation of the processes of primary importance to the release and transport of radionuclides, and the development and application of theories and models to predict the phenomena accurately. Available laboratory and field experiments within and outside of the Collaborative Program provide the basic data to test the validity of the theories and the modeling approach itself.

2000-2001 Activities

The activities in this project year covered seven studies.

The first study develops a coupled inversion technique of pressure and surface displacements. One of our main focuses in this project has been the development of inversion techniques. Inversion techniques are a very powerful tool for analyzing interference tests conducted in a heterogeneous system. However, the solution to the inversion problem is inherently non-unique. Any independent observations that relate to the pressure tests can make the analysis more reliable. Last year we developed an efficient and robust algorithm for estimating the permeability distribution from pressure measurements. This year we have developed an inversion algorithm that uses transient pressure observations and surface displacement measurements, which provides an efficient technique for estimating subsurface permeability variations. The methodology has the advantage of utilizing surface observations, which are typically much less expensive than measurements requiring boreholes. Furthermore, unlike many other geophysical observables, the relationship between surface deformation and pore fluid volume changes is relatively well understood. Our treatment enables us to partition the estimation problem into a

sequence of three linear sub-problems. An application of the approach to a set of tilt and borehole pressure data from the Raymond field site in California illustrates its efficiency and utility. The observations are associated with a well test in which fluid is withdrawn from a shallow fracture zone. During the test thirteen tiltmeters recorded the movement of the ground surface. Simultaneously, nine transducers measured pressure changes in boreholes intersecting the fracture system. We are able to image a high permeability, north trending channel located within the fracture zone. The existence and orientation of this high permeability feature is substantiated by a semi-quantitative analysis of some 4,000 transient pressure curves.

The second study describes the development of exactly averaged equations for flow and transport in random media. Today's computers are becoming more and more powerful, enabling numerical simulations of groundwater flow with a huge number of grid cells. In some cases, a model is run with a million grid cells. This fact makes analytical solutions appear obsolete. However, analytical solutions are still useful in providing some insights to the physical processes of interest. In numerical simulations, all the grid cells still have to be assigned with appropriate parameters. Because it is impossible to test a million pieces of rocks, the properties are inferred from a limited number of tests. When extrapolating the scarce field data, it is common to assume that the parameters obey some statistical distribution such as the random distribution. We have developed exactly averaged equations for flow and transport in random media. Approximate solutions have been presented in the past. However, the properties of approximate averaging methods are not yet fully understood. For example, the convergence behavior and the accuracy of truncated perturbation series are not well known. Furthermore, the calculation of the high-order perturbations is very complicated. In this section a method of finding the general form of exactly averaged equations for flow and transport in random fields is presented. We used (1) an assumption of the existence of the Green's functions for appropriate stochastic problems, (2) some general properties of the Green's functions, and (3) the some basic information about the random fields of the conductivity, porosity and flow velocity.

We presented a general form of the exactly averaged non-local equations for the following cases. 1) Steady-state flow with sources in porous media with random

conductivity. 2) Transient flow with sources in compressible media with random conductivity and porosity. 3) Non-reactive solute transport in random porous media. The problem of uniqueness and the properties of the non-local averaged equations for the cases with some type of symmetry (isotropic, transversal isotropic, orthotropic) are discussed. We analyzed the hypothesis and the structure of the non-local equations in the general case of stochastically homogeneous fields.

The third is a summary of the characterization techniques that were used at the Raymond field site. We have summarized the results of a multitude of geophysical and hydrological characterization techniques that were tested at the Raymond field site in California. The rock type at the site is granite, which is one of the potential host rocks for the nuclear waste repository. Some characterization techniques were quite effective in delineating fractures.

Our experience thus far indicates that when conducting field experiments, particularly in a fractured rock, it is extremely important to make certain that what is being measured is actually what is intended to be measured. Wellbore conditions can alter conditions imposed at the surface, and an observation well can play a greater role than just as an access for measuring downhole conditions. One may end up measuring the "permeability" of boreholes rather than that of the rock or the wellbore hydrodynamic properties rather than the rock dispersivity.

Characterization of a fractured rock is extremely challenging. Even with the level of effort outlined in this study, we are not very confident that the model that is calibrated to the experiments thus far can adequately predict contaminant transport behavior under natural conditions. On the other hand, it is of interest to investigate how much effort is cost-effective and/or how much detail is necessary. This is dependent on the nature of the problem as well as the spatial and time scale of the problem. Sometimes it may be better to conduct few long-term/large-scale tests to let the system present its average behavior than to conduct many small scale tests and piece the results together to predict the behavior.

The fourth study investigates dynamic channeling of flow and transport in saturated and unsaturated heterogeneous media. Dynamic channeling of flow and transport in strongly heterogeneous, saturated and unsaturated media is reviewed. Focusing or channeling of flow is dependent on both the permeability distribution and the pressure field. In the case of unsaturated media, it is also dependent on the degree of saturation. The emergence of flow channeling as a function of permeability variability (as measured by its standard deviation) and the spatial correlation range in three-dimensional porous systems is described. We also discuss the effects of channelized flow on two problems of practical interest for saturated and unsaturated heterogeneous media.

The fifth study covers the development of a particle-tracking method for advective transport in fractures with diffusion into finite matrix block with application to tracer injection-withdrawal testing. A particle-tracking method has been developed to calculate tracer transport in fractures with diffusion into finite rock matrix blocks. The method is an extension of the work of Yamashita and Kimura (1990), which is only applicable to diffusion into an infinite matrix. The new method has been verified against a number of analytic or semi-analytic solutions for transport in a homogeneous fracture medium with matrix diffusion. The method is applied to the calculation of tracer breakthrough curves for a hypothetical tracer injection-withdrawal experiment in a heterogeneous fracture zone, with variable hydraulic properties and finite matrix blocks.

The sixth study investigates tracer mixing at fracture intersections. Discrete network models are one of the approaches used to simulate a dissolved contaminant, which is usually represented as a tracer in modeling studies, in fractured rocks. The discrete models include large numbers of individual fractures within the network structure, with flow and transport described on the scale of an individual fracture. Numerical simulations for the mixing characteristics and transfer probabilities of a tracer through a fracture intersection are performed for this study. A random-walk, particle-tracking model is applied to simulate tracer transport in fracture intersections by moving particles through space using individual advective and diffusive steps. The simulation results are compared with existing numerical and analytical solutions for a continuous intersection over a wide range of Peclet numbers. This study attempts to characterize the relative concentration at the outflow branches for a continuous

intersection with different flow fields. The simulation results demonstrate that the mixing characteristics at the fracture intersections are a function not only of the Peclet number but also of the flow field pattern.

Finally, the seventh study presents a discussion of the PA methodologies from a combined review of NIREX95, SITE-94 AND TILA-99 projects. The goal is to extract the best methodologies for conducting performance assessment of a nuclear waste repository and to discuss the lessons learned from these three efforts. In light of these discussions, some suggestions for JNC's H-12 Report are put forward.

2000-2001 Reports

A Coupled Inversion of Pressure and Surface Displacement
D. W. Vasco, Kenzi Karasaki, and Kiyoshi Kishida

Exactly Averaged Equations for Flow and Transport in Random Media
Mark Shvidler and Kenzi Karasaki

A Multidisciplinary Fractured Rock Characterization Study at Raymond Field Site, Raymond, California
Kenzi Karasaki, Barry Freifeld, Andrew Cohen, Ken Grossenbacher, Paul Cook and Don Vasco

Dynamic Channeling of Flow and Transport in Saturated and Unsaturated Heterogeneous Media
Chin-Fu Tsang, Luis Moreno, Yvonne W. Tsang, and Jens Birkholzer

A Particle-Tracking Method for Advective Transport in Fractures with Diffusion info Finite Matrix Blocks with Applications to Tracer Injection-Withdrawal Testing
Y.W. Tsang and C.F. Tsang

Tracer Mixing at Fracture Intersections
Guomin Li

PA Methodologies from a Combined Review of NIREX95, SITE-94 and TILA-99
Chin-Fu Tsang

A coupled inversion of pressure and surface displacement

D. W. Vasco, Kenzi Karasaki, and Kiyoshi Kishida
Berkeley Laboratory, University of California, Berkeley, California

Short title: INVERSION OF PRESSURE AND DISPLACEMENT

Abstract. A coupled inversion of transient pressure observations and surface displacement measurements provides an efficient technique for estimating subsurface permeability variations. The methodology has the advantage of utilizing surface observations, which are typically much less expensive than measurements requiring boreholes. Furthermore, unlike many other geophysical observables, the relationship between surface deformation and reservoir pore fluid volume changes is relatively well understood. Our treatment enables us to partition the estimation problem into a sequence of three linear sub-problems. An application of the approach to a set of tilt and borehole pressure data from the Raymond field site in California illustrates it's efficiency and utility. The observations are associated with a well test in which fluid is withdrawn from a shallow fracture zone. During the test thirteen tiltmeters recorded the movement of the ground surface. Simultaneously, nine transducers measured pressure changes in boreholes intersecting the fracture system. We are able to image a high permeability, north trending channel located within the fracture zone. The existence and orientation of this high permeability feature is substantiated by a semi-quantitative analysis of some 4,000 transient pressure curves.

Introduction

Surface deformation, typically in the form of subsidence, has long been associated with subsurface fluid flow. Early observations of subsidence are linked to the extraction of oil and gas [Geertsma, 1973; Chilingarian et al., 1995]. Such subsidence is particularly noticeable in fields adjacent to coastal areas, such as the Wilmington field in California [Colazas and Strehle, 1995]. Severe subsidence problems have also been associated with withdrawal of water from coastal aquifers, such as near Venice, Italy [Gambolati and Freeze, 1973; Gambolati et al., 1974; Lewis and Schrefler, 1978].

In general, any deformation of the Earth's surface has been viewed as deleterious, an undesirable side-effect of the extraction or injection of fluids. Correspondingly, much effort has been devoted to understanding and predicting the compaction and consolidation induced by fluid withdrawal [Geertsma, 1957; Booker and Small, 1974; Poland et al., 1975; Narasimhan et al., 1978; Safai and Pinder, 1980; Bear and Corapcioglu, 1981; Segall 1985; Smith and Booker, 1993; Bai and Abousleiman, 1997]. Fewer investigations have focused on the utility of surface displacement data in furthering our understanding of the dynamics of fluids in the subsurface. A notable exception is the use of surface displacement observations to infer the geometry of hydrofractures [Evans et al., 1982; Du et al., 1993; Castillo et al., 1997]. In addition, surface deformation associated with the intrusion of volcanic fluids has been used to infer properties of the intruding fluid body, such as its depth [Mogi, 1958; Savage and Clark, 1982; Savage and Cockerham 1984; Vasco et al., 1988; Wicks et al., 1998]. Recently, such techniques have been extended to the monitoring of fluid motion associated with shallow injection [Vasco et al., 1998] and petroleum production [Vasco et al., 2000a]

There are several reasons for using surface displacement information to monitor fluid flow. First, data gathered at the surface are generally less expensive than data acquired in boreholes. In fact, surface displacement data are often far less costly than are many types of geophysical observations, such as three-dimensional seismic data. In

recent years we have witnessed a revolution in technologies for measuring surface motion. Many of the advances have been space-based, with the advent of the Global Positioning System (GPS) and Interferometric Synthetic Aperture Radar (InSAR) [Bamler and Hartl, 1998]. In particular, InSAR promises to resolve surface displacements at a sub-centimeter level, on a scale of 30 meter by 30 meter pixels, over hundreds of square kilometers [Hoffmann et al., 2001]. This technology has already been used to image subsidence associated with geothermal production [Massonnet et al., 1997; Vasco et al., 2001], aquifer-system compaction [Galloway et al., 1998; Hoffmann et al., 2001], and mining [Carnec et al., 1996]. Furthermore, surface displacements are sensitive to temporal changes induced by fluid flow. In this sense, surface deformation is somewhat akin to transient pressure measurements. This is in contrast to seismic data, which are primarily influenced by static properties of the subsurface. Finally, the relationship between surface displacements and reservoir fluid mass changes is fairly well established, based upon Biots [1941] formulation. To be sure, there may be departures from ideal poroelasticity, and modifications of Biots theory have been noted [Burridge and Keller, 1981; Fowler and Noon, 1999]. However, on the whole, Biots [1941] formulation is the starting point for most investigations of the deformation over a poroelastic reservoir.

In this paper we extend the work of Vasco et al. [2000a] to consider the inversion of surface deformation and borehole pressure data. Our primary goal is the integration of surface displacement and borehole pressure data to infer subsurface permeability variations. To this end, we must consider the coupled problem of deformation in a poroelastic body. At this point it is perhaps appropriate to clarify the sense in which our approach is a 'coupled' formulation. As elaborated below, there are two sets of differential equations governing fluid flow and displacements in a porous medium, those of Biot [1941]. Specifically, there are three equations describing the displacements and an equation describing the evolution of the fluid pressure. Historically, we have seen the development of two main approaches for studying fluid flow in deformable porous

media. In one approach, the uncoupled or two-step treatment, the scalar equation governing fluid pressure is solved first. The resulting pressure field is then used as a source to drive the deformation of the porous medium. The alternative is to solve the both sets of equations simultaneously, the coupled approach. The relative merits of these two methodologies and the validity of the uncoupled approach are still topics of vigorous discussion [Gambolati, 1977; Lewis and Schrefler, 1978; Lewis et al., 1991; Gambolati, 1992; Lewis et al., 1992; Zimmerman, 2000; Gambolati et al., 2000]. In our analysis of surface displacement and borehole pressure data we consider both the differential equations for displacement and pressure. In this sense, our approach is a coupled treatment.

There is another type of coupling in which the flow properties, in particular permeability, is a function of pore pressure, stress, and temperature [Raghavan et al., 1972; Samaniego et al., 1977; Cook, 1987; Noorishad et al., 1992; Rutqvist et al., 1998; Wu and Pruess, 2000]. In this work we will not consider variations in permeability as a function of pressure. Including such an effect leads to a non-linear equation for pressure which may be quite difficult to solve. Furthermore, the exact variation of permeability with pressure is not well established and must be determined empirically. Finally, the dependence of permeability on pressure only appears to be significant in high-pressure injection tests [Rutqvist et al., 1998; Wu and Pruess, 2000]. Thus, for our application to low-pressure testing at the Raymond field site in California, this effect is likely to be small.

Methodology

In this section we present our approach for estimating subsurface permeability variations, based upon borehole pressure and surface displacement data.

Governing Equations

Mechanical properties and deformation. In our study of a deforming poroelastic medium we shall adopt the formulation of Rice and Cleary [1976]. The primary quantities of interest are the pore pressure, p, and the total stress, σ_{ij}, associated with a volume element of the medium. These two variables are related to the strain ϵ_{ij} and the pore fluid mass per unit volume $m = \rho_0 v$, where ρ_0 is the fluid density and v is the reference volume, by the equations [Rice and Cleary, 1976].

$$2\mu\epsilon_{ij} = \sigma_{ij} - \frac{\nu}{1+\nu}\sigma_{kk}\delta_{ij} + \frac{3(\nu_u - \nu)}{B(1+\nu)(1+\nu_u)}p\delta_{ij} \tag{1}$$

$$\Delta m = m - m_0 = \frac{3\rho_0(\nu_u - \nu)}{2\mu B(1+\nu)(1+\nu_u)}\left[\sigma_{kk} + \frac{3}{B}p\right] \tag{2}$$

which involve four elastic constants: μ (shear modulus), ν (Poisson ratio), B (Skemptons coefficient), and ν_u (undrained Poisson ratio). These material constraints are discussed in more detail by Rice and Cleary [1976].

We are interested in quasi-static deformation in which we may neglect inertial terms in the equation of equilibrium. In terms of the total stress the equilibrium equations are

$$\frac{\partial \sigma_{ij}}{\partial x_j} = 0 \tag{3}$$

[Rice and Cleary, 1976]. Because we shall be considering surface displacement, it is useful to rewrite the equilibrium equations (3) in terms of the displacements of the medium $u_i, i = 1, 2, 3$. By solving equations (1) and (2) for σ_{ij} in terms of ϵ_{ij} and Δm and noting that the strain is related to the displacements by [Lewis and Schrefler, 1987]

$$\epsilon_{ij} = \frac{1}{2}\left(\frac{\partial u_i}{\partial x_j} + \frac{\partial u_j}{\partial x_i}\right) \tag{4}$$

we may write the stresses in terms of displacements and the change in pore fluid mass per unit volume [Segall, 1985; Vasco et al., 2000a]

$$\sigma_{ij} = \mu\left(\frac{\partial u_i}{\partial x_j} + \frac{\partial u_j}{\partial x_i}\right) + \lambda_u \frac{\partial u_k}{\partial x_k}\delta_{ij} - \frac{BK_u}{\rho_0}\Delta m \delta_{ij}, \tag{5}$$

where we have defined the undrained Lame constant

$$\lambda_u = \frac{2\nu_u \mu}{1 - 2\nu_u} \tag{6}$$

and the undrained bulk modulus

$$K_u = \frac{2\mu(1+\nu_u)}{3(1-2\nu_u)}. \tag{7}$$

Substituting (5) into the equilibrium equations (3) we obtain a partial differential equation for the displacements

$$\frac{\partial}{\partial x_j}\left[\mu\left(\frac{\partial u_i}{\partial x_j} + \frac{\partial u_j}{\partial x_i}\right)\right] + \frac{\partial}{\partial x_j}\left[\lambda_u \frac{\partial u_k}{\partial x_k}\right]\delta_{ij} = f_i(\mathbf{x}) \tag{8}$$

where $f_i(\mathbf{x})$ denotes the augmented source term

$$f_i(\mathbf{x}) = \frac{\partial}{\partial x_j}\left[\frac{BK_u}{\rho_0}\Delta m\right]\delta_{ij}. \tag{9}$$

Hydrological properties and fluid flow. We begin with Darcy's law, the constitutive equation governing pore fluid diffusion [Bear, 1972]

$$\mathbf{v} = \rho_0 \frac{k}{\mu_f}\nabla p \tag{10}$$

where $\mathbf{v}$ denotes the fluid velocity, k is the permeability, and μ_f is the fluid viscosity. The conservation of the pore fluid mass is described by the equation [Rice and Cleary, 1976]

$$\nabla \cdot \mathbf{v} + \frac{\partial \Delta m}{\partial t} = \rho_0 q \tag{11}$$

where q is a source term. In equation (11) we have made use of the fact that the initial pore fluid mass per unit volume is constant. In what follows we shall assume that the movement of the solid phase is much smaller than the motion of the pore fluid. Substituting for $\mathbf{v}$ from (10), equation (11) becomes

$$\nabla \cdot \left(\rho_0 \frac{k}{\mu_f}\nabla p\right) + \frac{\partial \Delta m}{\partial t} = \rho_0 q \tag{12}$$

a relationship between the pressure and the time change of the pore fluid mass per unit volume. Note that for steady-state conditions, the time derivative vanishes and Δm does not appear explicitly in equation (12). This is in accordance with the observation that coupling only occurs under time transient conditions [Lewis and Schrefler, 1987].

Inversion of Displacement and Pressure Observations

Our primary goal is to combine observations of surface displacement and borehole pressure measurements in order to infer reservoir flow properties such as permeability. To accomplish this we have devised a three-step approach in which we first utilize the displacement and pressure data to estimate the change in fluid mass per unit volume, Δm, in the subsurface. For this step, equations (2) and (8) are the active constraints. We then map our estimate of Δm into subsurface pressure, as described below. Based upon the derived pressure variation we may then use equation (12) to infer variations in permeability. An important feature of our staged approach is that each step is linear. We now describe each step in more detail.

Estimation of pore fluid mass change and pressure. In this subsection we describe the first two steps of our procedure: estimating the changes in pore fluid mass per unit volume and mapping these estimates into pressure variations. Our estimate of $\Delta m(\mathbf{x}, t)$ shall be based upon observations of surface displacement and borehole pressure measurements. The surface displacements are related to changes in $\Delta m(\mathbf{x}, t)$ via equation (8). Because $\Delta m(\mathbf{x}, t)$ enters equation (8) on the right-hand-side, as a source term, the inverse problem is linear. The solution of the inverse problem for $\Delta m(\mathbf{x}, t)$, which follows from equation (8), has been discussed elsewhere [Vasco et al., 1998; Vasco et al., 2000a]. Therefore, we shall merely give the result, which is based upon the work of Segall [1985],

$$u_i(\mathbf{x}, t) = \frac{B}{\rho_0} \int_V g_i(\mathbf{x}, \mathbf{y}) \Delta m(\mathbf{y}, t) dV \tag{13}$$

where $g_i(\mathbf{x},\mathbf{y})$ is the Greens function solution of equation (8) [Stakgold, 1979] and $\mathbf{y}$ denotes the position in the volume V, the integration variable. That is $g_i(\mathbf{x},\mathbf{y})$ is the solution of (8) for a delta function source term, located at position $\mathbf{y}$. As noted by Vasco et al. [2000a], $g_i(\mathbf{x},\mathbf{y})$ may be derived analytically for simple models such as a homogeneous half-space. Alternatively, we may approximate $g_i(\mathbf{x},\mathbf{y})$ for arbitrary poro-elastic media by solving equation (8) using a numerical technique such as finite differences.

In order to find the constraint provided by pressure measurements, we solve equation (2) for $p(\mathbf{x},t)$

$$p(\mathbf{x},t) = \frac{B}{3}\left[\frac{2\mu B(1+\nu)(1+\nu_u)}{3\rho_0(\nu_u-\nu)}\Delta m - \sigma_{ii}\right]. \tag{14}$$

An expression for σ_{ij}, in terms of the displacements and Δm is found in equation (5). Utilizing the integral representation (13) for $u_i(\mathbf{x},t)$, we may write [Segall, 1985]

$$\sigma_{ij} = \frac{B}{\rho_0}\int_V G_{ij}(\mathbf{x},\mathbf{y})\Delta m(\mathbf{y},t)dV - \frac{BK_u}{\rho_0}\Delta m(\mathbf{x},t)\delta_{ij} \tag{15}$$

where

$$G_{ij} = \mu\left(\frac{\partial g_i}{\partial x_j} + \frac{\partial g_j}{\partial x_i}\right) + \lambda_u\frac{\partial g_k}{\partial x_k}\delta_{ij}. \tag{16}$$

Substituting the integral representation of σ_{ij} given above into equation (14) we arrive at an integral equation for $\Delta m(\mathbf{x},t)$ [Hackbusch, 1995]

$$p(\mathbf{x},t) = C_\nu\Delta m(\mathbf{x},t) - \frac{B^2}{3\rho_0}\int_V G_{ii}(\mathbf{x},\mathbf{y})\Delta m(\mathbf{y},t)dV \tag{17}$$

where

$$C_\nu = \frac{B^2}{\rho_0}\left[\mu\frac{2}{3}\frac{(1+\nu)(1+\nu_u)}{(\nu_u-\nu)} - 3K_u\right]. \tag{18}$$

Equations (13) and (17) are the constraints we require to infer the spatial variation of $\Delta m(\mathbf{x},t)$. It is important to note that both equations are linear in the unknown $\Delta m(\mathbf{y},t)$.

For a numerical implementation of the inverse problem we first discretize the functional (13) and the integral equation (17). This is accomplished by a basis function expansion of the spatially varying quantity $\Delta m(\mathbf{y}, t)$ and consideration of a particular time t. That is, we represent $\Delta m(\mathbf{y}, t)$ as a sum of M orthogonal basis functions

$$\Delta m(\mathbf{y}, t) = \sum_{l=1}^{M} \delta m_l(t) \Upsilon_l(\mathbf{y}) \tag{19}$$

where $\delta m_l(t)$ are the expansion coefficients and $\Upsilon_l(\mathbf{y})$ are the basis functions [Parker, 1994]. We shall use the rectangular constant basis functions and a cell or block based representation of $\Delta m(\mathbf{y}, t)$. For these functions, $\Upsilon_l(\mathbf{y})$ takes the value one in the lth cell and zero outside of the cell. Upon substituting our representation (19) into the functional (13) we arrive at

$$u_i(\mathbf{x}_j, t) = \sum_{l=1}^{M} \Gamma^l{}_i(\mathbf{x}_j) \delta m_l(t) dV \tag{20}$$

where

$$\Gamma^l{}_i(\mathbf{x}_j) = \frac{B}{\rho_0} \int_{V_l} g_i(\mathbf{x}_j, \mathbf{y}) dV. \tag{21}$$

Note that the integration in (21) is over the volume V_l of the lth cell or grid block of the model. Similarly, the integral equation (17) is approximated by

$$p(\mathbf{x}_k, t) = C_\nu \delta m_k(t) - \sum_{l=1}^{M} \Gamma^l{}_{ii}(\mathbf{x}_k) \delta m_l(t) dV \tag{22}$$

where $\delta m_k(t)$ denotes the change in pore fluid mass per unit volume in the cell in which $\mathbf{x}_k$ is located. The function $\Gamma^l{}_{ii}(\mathbf{x}_k)$ is defined as the integral

$$\Gamma^l{}_{ii}(\mathbf{x}_k) = \frac{B^2}{3\rho_0} \int_{V_l} G_{ii}(\mathbf{x}_k, \mathbf{y}) dV. \tag{23}$$

In order to reliably estimate the parameters $\delta m_k(t)$ for $k = 1, ..., M$ we typically gather a set of measurements of both surface deformation and borehole pressures. Let us denote the vector of surface deformation observations at time t by $\mathbf{u}(t)$, of length N_d say. The pressure observations similarly comprise the vector $\mathbf{p}(t)$ of length N_p. We may

then write our complete set of constraints on the vector of unknowns, $\delta\mathbf{m}(t)$, as a linear system. The matrix representation of the system of equations is

$$\begin{bmatrix} \mathbf{u}(t) \\ \mathbf{p}(t) \end{bmatrix} = \begin{bmatrix} \mathbf{U} \\ \mathbf{P} \end{bmatrix} \delta\mathbf{m}(t) \tag{24}$$

where the matrices $\mathbf{U}$ and $\mathbf{P}$ contain the coefficients from (20) and (22). The inverse problem entails solving the system (24) for the vector $\delta\mathbf{m}(t)$, given a set of observations and computed coefficients. There are some stability issues associated with solving the system (24) which we have not touched upon. For example, there is the issue of non-uniqueness which can be quite severe in three-dimensional situations. We shall discuss the mechanics of estimating $\delta\mathbf{m}(t)$ in more detail in our numerical illustration.

Given estimates of $\delta m_k(t)$, the computation of pressure in each grid block is a straight-forward evaluation of the right hand side of (17). For a discrete grid of cells we consider the summation given by (22). That is, we cycle through each cell in our grid, evaluating (22)

$$p(\mathbf{x}_k, t) = C_\nu \delta m_k(t) - \sum_{l=1}^{M} \Gamma^l_{ii}(\mathbf{x}_k)\delta m_l(t) \tag{25}$$

for $\mathbf{x}_k$ located at the center of each grid block. This is equivalent to solving the forward problem and is a stable procedure. Note that the staged inversion described here is not a simultaneous inversion. Thus, it is possible to produce volume changes which map into implausible pressure variations. In our numerical illustration we describe regularization schemes which penalize such unrealistic solutions.

Estimation of permeability. Given estimates of subsurface pressure variations we may now solve for flow properties such as permeability. For this task we return to equation (12), describing the conservation of pore fluid mass. Note that if $p(\mathbf{x}, t)$ and $\Delta m(\mathbf{x}, t)$ are known, estimation of $k(\mathbf{x})$ reduces to the solution of a linear system of equations. To see this, consider the integral formulation of the inverse problem derived in the Appendix. In particular, equation (A9) relates $p(\mathbf{x}, t)$, $q(t)$, and $\Delta m(\mathbf{x}, t)$ to the

permeability variation from a specified background model, $\delta k(\mathbf{x})$.

$$\delta p(\mathbf{x},t) = -\int_V \nabla G_f(\mathbf{x},\mathbf{y},t)\cdot\nabla p(\mathbf{y},t)\delta k(\mathbf{y})dV \tag{26}$$

where $\delta p(\mathbf{x},t)$ is given by equation (A8) in the Appendix. We should emphasize that the deviation, $\delta k(\mathbf{x})$, may be arbitrarily large. Given estimates of $p(\mathbf{x},t)$ and $\Delta m(\mathbf{x},t)$, equation (26) reduces to a linear equation in $\delta k(\mathbf{x})$. For such equations we may apply techniques from linear inverse theory [Parker, 1994] in order to find the permeability.

We may discretize equation (26) using a basis expansion much like (19)

$$\delta k(\mathbf{y}) = \sum_{l=1}^{M} \delta k_l \Upsilon_l(\mathbf{y}). \tag{27}$$

The quantity δk_l is an expansion coefficient which we may interpret as the average permeability in the l-th block. Again, the basis functions $\Upsilon_l(\mathbf{y})$ are rectangular constant functions associated with a cell-based representation. The discrete form of (26) is

$$\delta p(\mathbf{x}_k,t) = \sum_{l=1}^{M} K^l(\mathbf{x}_k,t)\delta k_l \tag{28}$$

where

$$K^l(\mathbf{x}_k,t) = \int_{V_l} \nabla G_f(\mathbf{x}_k,\mathbf{y},t)\cdot\nabla p(\mathbf{y},t)dV. \tag{29}$$

As noted above, given an estimate of the pressure field $p(\mathbf{y},t)$, equation (28) becomes a linear equation for the grid block permeabilities, δk_l

Applications

Numerical Illustration

In order to highlight the essential elements of our approach, we consider a set of simulated surface tilt and borehole pressure values. The tilts and pressures are based upon a reservoir simulation of fluid production from a heterogeneous layer, extending from 200 to 210 meters in depth. The permeability variations within this layer are shown in Figure 1. The permeability varies by several orders of magnitude, from under 0.3

mDarcies to over 350 mDarcies. The overall well configuration is that of a five-spot, with a central rate-constrained producer and four adjacent pressure-constrained injectors. The heterogeneous poroelastic layer is embedded within an elastic half-space. The top and bottom of the layer comprise no-flow boundaries while the edges are constant pressure boundaries. The steady-state pressure changes, obtained from a streamline simulator [Datta-Gupta and King, 1995], are mapped directly into changes in pore fluid mass per unit volume, $\Delta m(\mathbf{x}, t)$. This is accomplished by solving equation (17), or its discrete counterpart (25), for $\Delta m(\mathbf{x}, t)$, given $p(\mathbf{x}, t)$ and the material properties of the poroelastic layer and the elastic half-space. Alternatively, we could adopt an uncoupled formulation and neglect the stress-induced pressure component, σ_{kk}, in equation (14).

The surface deformation is found by evaluating the integral (13) using a half-space Green's function $g_i(\mathbf{x}, \mathbf{y})$ and the distribution of pore fluid mass change per unit volume, $\Delta m(\mathbf{x}, t)$. In this illustration, and in our application, we shall work with surface tilt. Surface tilt is the change in vertical displacement with respect to a change in position, the horizontal gradient of the vertical displacement (u_3). As such, it is a vector with two components: $\partial u_3/\partial x$ and $\partial u_3/\partial y$. For infinitesimal strain we may think of tilt as the angular change of the surface normal vector induced by the deformation of the surface. The half-space Greens function for surface tilt, obtained by straight-forward differentiation, is given in Vasco et al. [2000a]. For our numerical illustration we consider a six by six grid of tiltmeters on the surface. Though this may seem like an extensive set of instruments, it must be remembered that tiltmeter experiments frequently involve 20 to 30 instruments. Furthermore, with the advent of new technologies such as Interferometric Synthetic Aperture Radar (InSAR), there is the potential to obtain extremely dense sampling [Galloway et al., 1998].

Estimation of pore fluid mass change and pressure. Given the 72 surface tilts (two components per station) and the 5 steady-state pressures (1 producer and 4 injectors), we seek estimates of pressure variation within the confined layer. We

represent the variation within the layer by a 21 by 21 grid of cells. Each cell is characterized by a constant permeability which may be distinct from the values in other blocks. Also, the pressure is variable from block to block in the grid. Initially, we estimate for the pore fluid mass per unit volume vector $\delta\mathbf{m}(t)$ by solving the linear system (24). However, because we have more unknowns (441) than constraints (77) any solution of equation (24) is likely to be unstable with respect to errors in the data and numerical noise in our computations. That is, features of the inverse model are likely to change significantly if the data are perturbed only slightly.

Perhaps the most commonly applied technique for stabilizing the inverse problem is to introduce some form of regularization [Tarantola, 1987; Parker, 1994]. Mathematically, such regularization takes the form of additional functions penalizing aspects of the model. For example, if we have confidence in some prior model of pore fluid mass change per unit volume in the reservoir $\delta\mathbf{m}^0(t)$, we might attempt to find a solution which honors the data and does not deviate significantly from this initial model. For a more compact formulation, let us define the data vector

$$\mathbf{d} = \begin{pmatrix} \mathbf{u} \\ \mathbf{p} \end{pmatrix} \tag{30}$$

and the coefficient matrix

$$\mathbf{M} = \begin{pmatrix} \mathbf{U} \\ \mathbf{P} \end{pmatrix}. \tag{31}$$

The most frequently invoked misfit measure is the sum of the squares of the residuals [Gill et al., 1981]

$$S_d = \sum_{i=1}^{N} \left(d_i - \sum_{l=1}^{M} M_{il}\delta m_l \right)^2 \tag{32}$$

where $N = N_d + N_p$ is the total number of observations and M is the total number of model parameters (grid blocks). We wish to minimize the misfit S_d subject to the requirement that our model remain close to the prior values $\delta\mathbf{m}^0(t)$. A quantitative

measure of deviation from $\delta \mathbf{m}^0$ is given by the quadratic form

$$S_n = \sum_{l=1}^{M} \left(\delta m^0{}_l - \delta m_l \right)^2 \tag{33}.$$

Another model attribute used to regularize the inverse problem is model roughness. The underlying idea is that our data are not sensitive to small scale spatial variations in model properties. Therefore, we can only hope to stably recover the larger scale features of our model. To this end, we introduce a penalty term which minimizes the 'roughness' of our model, as measured by

$$S_r = \sum_{k=1}^{M} \left(\sum_{l=1}^{M} L_{kl} \delta m_l \right)^2 \tag{34}$$

where L_{kl} is a roughening operator (matrix) which approximates a spatial differencing operator [Menke, 1984].

As noted above, our inversion consists of a sequence of linear problems and is not a simultaneous inversion. Therefore, we might produce pressure fields which are implausible. For example, a volume change model could result in a solution in which pressure increases away from an injection well. We may implement regularization terms to penalize such unrealistic solutions. A simple type of regularization penalizes volume changes which are more distant from pumping wells. Assuming relatively homogeneous mechanical properties, we expect the largest volume changes to be found close to an injection or producing well. Thus, we can include a penalty term which increases with radial distance from the pumping well.

$$S_p = \sum_{l=1}^{M} \left| \mathbf{x}_p - \mathbf{x}_l \right|^2 \delta m_l \tag{35}$$

where $\mathbf{x}_p$ is the location of the pumping well and $\mathbf{x}_l$ is the position of the center of the lth block. Another approach is to include explicit positivity constraints on the gradient of the volume change distribution. For example, we could include positivity constraints on the radial component of the pressure gradient as measured from the pumping well. In a

deformable medium it is possible to produce interesting effects, not seen in undeforming aquifers. For example, it is possible to obtain local pressure increases even when fluid is being withdrawn from a confined aquifer. We observe this in Figure 12, where a negative drawdown is predicted to the east and west of the pumping well. The negative drawdown is calculated even though only volume decreases are observed (Figure 5). We also observe this phenomena in our actual data (Figure 6) for wells SE-4 and SW-4.

Summing up the respective contributions from (32), (33), (34), and (35) we have a penalized misfit function

$$S = S_d + W_n S_n + W_r S_r + W_p S_p \tag{36}$$

where W_n, W_r, and W_p are scaling coefficients which control the relative importance of honoring the prior model, obtaining a smooth model, and maintaining the largest volume changes nearest the pumping well, with respect to fitting the data. There are a number of strategies for chosing W_n, W_r, and W_p which range from trial and error to the systematic construction of trade-off curves [Parker, 1994]. We seek a solution which minimizes the penalized misfit S. Because the individual terms in (36) are linear or quadratic forms, the necessary conditions for a minimum constitute a system of linear equations [Gill et al., 1981; Parker, 1994]. If we include explicit positivity constraints on the volume change gradient we must resort to a constrained least squares solver [Gill et al., 1981]. Note that, because of the regularization, we now have more constraints than unknowns and the solution of the augmented linear system is stable with respect to numerical noise and data perturbations. We use the iterative linear system solver LSQR [Paige and Saunders, 1982] to obtain our estimates of $\delta\mathbf{m}$. The distribution of pore fluid mass per unit volume is then mapped into grid block pressures using equation (25). The resulting pressure estimates are shown in Figure 2, along with the steady-state pressure distribution calculated using the streamline simulator [Datta-Gupta and King, 1995]. There is overall agreement, with a large pressure decrease to the northwest of the

producing well. There are difference in detail between the synthetic and estimated grid block pressures. These differences are most likely due to the imposed regularization, the norm and roughness penalties.

Estimation of permeability. The next step is to infer the lateral variation in permeability within the layer, based upon our estimate of the pressure distribution (Figure 2). The computational task is to solve equation (28) for the block permeabilities δk_l. Our Green's function, $G_f(\mathrm{y}, t)$, is that of a confined layer [Carslaw and Jaeger, 1959] with a uniform permeability. The calculated pressure is with respect to the uniform layer, the boundary conditions, and the flow rates of the producing and injecting wells. The exact expression is given by equation (A8). Note that in equation (28) we have the same number of data $\delta p(\mathrm{x}_k, t)$ as unknowns. If we consider the transient situation in which we have pressure estimates for several times, as in the Raymond field case, the problem becomes formally over-determined. Even though the problem is not formally under-determined we shall still impose some degree of regularization. This will reduce the amplification of errors in the data and in our matrix of coefficients. For example, $K^l(\mathrm{x}_k, t)$ depends on our pressure estimates, as is evident from equation (29). Given that our pressure estimates are the result of an inversion, and that our knowledge of the material constants is imperfect, the resulting coefficients are likely to contain errors. In order to regularize the inverse problem we include a norm penalty (33), a roughness penalty (34), and a penalty which favors volume change near the pumping well (35). Thus, our penalized misfit function is of the form (36).

Our estimate of permeability variation within the layer is shown in Figure 3. There is overall agreement between the patterns in Figures 1 and 3. In both models we find northeasterly trending high and low permeability features, forming short, almost linear segments. For example, a low permeability trend intersects the producing well in the center. Also, we recover the overall higher permeability in the southeastern quadrant of the fracture zone. There are differences in the detailed distribution of the anomalies.

Thus, we are able to recover the overall permeability variation but we the fine scale details.

The Raymond Field Site

Characterizing flow and transport in fractures can be a daunting task. Disentangling the complex geometry and interaction of various intersecting fracture sets is often extremely difficult, given a limited set of surface and borehole observations. Furthermore, the available geophysical and hydrological data may be sensitive to different and very specific aspects of the fractures themselves, making data integration problematic. However, fractured rocks constitute a major component of the subsurface and it is important to extend our ability to characterize them. In order to gain experience in utilizing multiple data sets for characterizing flow and transport within fractured rocks, a dedicated field site was established near the town of Raymond, California. At this site many high quality hydrological and geophysical data sets were acquired and analyzed. An overview of the many data sets gathered at the Raymond field site may be found in Karasaki et al. [2000]. In this section we shall focus on a set of surface tilt and borehole pressure measurements collected during a production test in August of 1995.

Site description. The field site itself consists of nine boreholes drilled to approximately 90 meters depth in the granodiorite of the Sierra Nevada foothills [Karasaki et al., 2000]. The configuration of the boreholes is that of an inverted V with the apex oriented in a northerly direction (Figure 4). Based upon an extensive set of geophysical, borehole, and hydrological data it was determined that a few fractures or fracture zones contribute to the flow into the boreholes [Cohen, 1993]. The conceptual model which has emerged contains two dipping fracture zones or sets of fractures: one centered at about 25 to 30 meters and another at a depth of approximately 60 meters. The top of the uppermost fracture zone, determined by its borehole intersections, is indicated by the contours in Figure 4.

Tiltmeter and pressure monitoring of pump tests. In August of 1995 a series of pressure tests were conducted at the Raymond site. During these tests the ground surface was monitored by an array of 15 tiltmeters. This was part of an effort to better understand the response in the nine boreholes during pressure testing [Karasaki et al., 2000]. In particular, distant boreholes experienced an inverted pressure response in which pressure would increase during fluid withdrawal. Subsequently, these tilt data have proved valuable in provided a qualitative image of flow within the uppermost fracture zone [Vasco et al., 1998]. The details of the instrument placement and data reduction may be found in Vasco et al. [1998]. Here we shall consider the 13 tiltmeters which provided usable data during a two hour production test, conducted on August 15th (Figure 4). In that test water was pumped from borehole 00 (the apex of the inverted V) at a rate of 0.4 l/s. The quality of the data may be judged by an examination of the tilt series in Figure 5. The vertical lines in this figure designate the beginning and the end of pumping. The surface tilts were measured every minute for the duration of the test. The level of noise and bias in these data is characterized by the deviation of the pre-injection tilts from zero. For the most part, the pre-event surface tilts are extremely close to zero, the primary exception is tiltmeter 14.

The tilt data form one of our basic data sets, the other is composed of pressure observations from seven of the boreholes. The borehole pressures were sampled every 5 seconds during the test. In this section we shall work with hydraulic head or drawdown rather than pressure (Figure 6). A notable feature of Figure 6 is the significant response in boreholes SE1 and SE3 relative to the more westerly boreholes of the SW series. Also observe the slightly inverted early responses in the more remote boreholes (SE4 and SW4). The characteristics of this pumping test, the strong response in the SE boreholes and the inverted responses in SE4 and SW4, are extremely robust. In particular, these features are reproduced in all such tests, involving both pumping out of and injection into borehole 00.

Inversion of tiltmeter and pressure observations. For our analysis of drawdown and tiltmeter data we shall consider the first seven minutes of the test. In working with the early part of the test we minimize the possible inelastic response of the fracture zone. Also, at later times the changes in pore fluid mass within the fracture zone extend beyond the boundaries of our tiltmeter array, making it difficult to define the extent of the deforming region. Our representation of the upper fracture zone consists of a dipping layer (Figure 4). The geometry of the layer is determined both by borehole intersections and geophysical observations [Karasaki et al., 2000]. The fracture zone is decomposed into a 15 by 15 grid of cells for a total of 225 unknowns. Rather than solving for pore fluid mass changes, we estimate fractional volume changes within each grid block. This involves a simple scaling by the fluid density which is well known and constant.

Initially, we conduct two distinct inversions of the tilt and pressure observations. Our data correspond to measurements taken five minutes after pumping began. In the first inversion only the tilt data are used to infer volume changes within the fracture zone. The result, shown in Figure 7a, indicates significant volume change extending south from the pumping well 00. There are well defined volume changes to the west of the pumping well, extending beyond boreholes SW1 and SW2. An inversion based only upon head observations produces a very different distribution of volume change within the fracture zone (Figure 7b). In Figure 7b the largest volume decrease is found in the cell containing the pumping well. There is little volume decrease in that part of the fracture zone intersecting the SW boreholes, in agreement with the head observations (Figure 6). In summary, by themselves, the tilt and head data suggest very different models of fracture zone volume decrease. The question remains: Is it possible to find a volume change model which will satisfy both data sets simultaneously?

Before describing the results of our coupled tilt and head inversion, we shall address the issue of estimating poroelastic parameters for the fracture zone and the surrounding

granodiorite. As indicated by equations (1) and (2), there are four important material properties associated with our formulation: the shear modulus (μ), Poisson's ratio (ν), the undrained Poisson's ratio (ν_u), and Skemptons coefficient (B). It is evident from equations (13), (16), (17), and (18) that the values of these parameters will influence our mapping of surface tilt and head variations into subsurface volume change. Unfortunately, obtaining estimates of all of these parameters is very difficult, even in a laboratory setting. Furthermore, if we could obtain such estimates, say from experiments on cores, it is not clear just how these laboratory values would scale-up to the larger-scale properties which are effective in our field experiment. There is also the issue of lateral variations in the poroelastic properties over the fracture zone itself. It is likely that the mechanical properties of the fracture zone vary over the field site. However, the magnitude and nature of this variation is unknown at present. One possible remedy is to solve for the mechanical properties as a function of position over the fracture zone. That is, a simultaneous inversion for both volume change and mechanical properties. However, this would render the inverse problem non-linear and introduce a significant degree of non-uniqueness. At this stage of our investigation we felt that it is better to obtain rough or average estimates of the parameters and then determine if we could find a volume change model which is compatible with both the surface deformation and head measurements. If this is not possible we are compelled to consider a more detailed distribution of poroelastic properties. This is the approach followed in this paper. Because Poisson'r ratio varies in a fairly narrow range of 0.0 to 0.5 we chose to fix both Poisson's ratio and the undrained Poisson's ratio. The Poisson's ratio is associated with the surrounding granodiorite, for which a value of 0.25 is thought to be appropriate. Our estimate of undrained Poisson's ratio, 0.30, comes from rock physics experiments.

In order to estimate values of Skemptons coefficient (B) and the shear modulus (μ) we conducted a series of coupled inversions. In each inversion we varied both B

and μ, constructing a grid displaying the logarithm of the error as a function of these two parameters (Figure 8). Note that by plotting the logarithm of the error, we are emphasizing the small variations in misfit. Still, an examination of Figure 8 reveals that the combined misfit is relatively insensitive to variations in the shear modulus. It is only when μ drops below about 300 MPa that the misfit begins to increase significantly. Similarly, the misfit does not vary much when B is greater that 0.5. Thus, there is a large region, the right-most portion of the contour plot (Figure 8) for μ greater than about 100 MPa, over which the misfit is fairly constant. The lowest contour line bounds an area with B between 0.7 and 1.0 and with μ between 300 and 600 MPa. We should note that this range in shear modulus agrees with an earlier study conducted by Infraseismic Diagnostic Monitoring, the company conducting the tilt survey. In that study, $\mu = 552$ MPa and $B = 1.0$ are found to produce a reasonable match to the tilt data, given the pressure changes observed within the fracture zone. Based upon Figure 8, we take the average poroelastic constants for the fracture zone to be $B = 0.9$ and $\mu = 400$ MPa. These estimates will be used in all subsequent coupled inversions.

We note that it is possible to estimate Skempton's coefficient B using the borehole head data. Specifically, we can use the head variation induced by atmospheric loading and Earth tides to infer B [Roeloffs et al., 1989; Rojstaczer and Agnew, 1989; Rojstaczer and Riley, 1990]. The static-confined response of a well to air pressure changes p_b is related to the undrained Poisson's ratio (ν_u) and the B value by

$$B = \frac{2}{3(1+\nu_u)}\left[1 - \frac{w\rho g}{p_b}\right] \tag{37}$$

where w is the change in water level [Rojstaczer and Agnes, 1990].

Our coupled inversion of tilt and head follows from solving the necessary equations for a minimum of the penalized misfit (36). We included penalty terms for model norm, model roughness, and distance weighting in order to ensure that the largest volume changes are near the pumping well. As noted above, these equations are linear and

may be solved using a standard solver such as LSQR [Paige and Saunders, 1982]. The resulting model of volume decrease within the fracture zone is shown in Figure 9. The coupled model contains features common to both the tilt and head inversions (Figures 7a and 7b). For example, the largest volume decrease is found in the grid block containing the pumping well. Also, the volume decrease is asymmetric, elongated to the south of borehole 00. Finally, the volume decrease is generally greater for wells to the east (the SE series) than for those to the west. We can now consider how well our volume change model matches both the tilt and head observations. In Figure 10 the observed tilt and head data are plotted against values predicted by the volume change model of Figure 9. For the most part, the predictions of the volume change model agree quite well with the observations. There is a tilt value of about -1 micro-radian which is under-predicted, but this corresponds to the noisy tiltmeter 14 (Figure 5) and is likely to be an outlier. Thus, we can find a volume change model compatible with both sets of observations.

The high quality of the tilt and head data enables us to construct estimates of the volume changes within the fracture zone as a function of time. Specifically, we can image fractional volume changes on a minute by minute basis, the sampling interval of our tiltmeters (Figure 11). In general, the volume decrease within the fracture zone is greatest around the pumping well. Over time, the volume decrease propagates rapidly to the south, reaching the edge of the tiltmeter array in about five minutes. We are unable to resolve fracture zone changes much beyond the extent of our tiltmeter array. There is an interesting transition in the pattern of volume change within the fracture zone. For approximately the first three minutes the volume decrease appears to extend to the south-southeast, just to the east of the boreholes in the SE series. However, sometime around four minutes there is a shift to the west. Thereafter, the southern extension of volume change is found within the array of wells, between the SE and SW boreholes (Figure 11).

Based upon equation (22) and our chosen poroelastic parameters we can map

our volume change model into a pressure distribution within the fracture zone. For illustrative purposes we shall consider the mapping of volume changes after five minutes of pumping (Figure 12a). Because we are working with hydraulic head and drawdown we present the result in terms of meters head drawdown. An interesting aspect of this figure are the regions of negative drawdown. Well SW4 lies within a region of somewhat negative drawdown, in agreement with the observed inverted response (Figure 6). For well SE4 the response after four minutes of pumping is nearly zero, slightly different from the negative response seen in Figure 6.

With estimates of head variations in hand we now consider the determination of fracture zone permeability itself. Computationally, we must solve equation (28), using the fracture zone pressure variations to compute the coefficients (29) as well as in calculating the right-hand-side (A8). In computing Q according to equation (A2) we require the time derivative of the pore fluid mass per unit volume. This is approximated by differencing the estimates in Figure 11. That is, in computing $\partial m/\partial t$ five minutes into the test we difference the volume change at six minutes and four minutes and divide by 120 seconds. The result is then scaled by density to estimate pore fluid mass change with time. We also estimate the spatial gradient of the pressure field by differencing. The Green's function is associated with the background model, a confined layer. In equation (28) there are an equal number of equations and parameters. Even so, we incorporate norm and roughness regularization in the inversion. The result, shown in Figure 12b, contains a narrow high permeability channel situated just to the west of the SE series of wells. Higher permeabilities are also found to the northwest of the pumping well 00.

Following the procedure described above, we can use the six estimates of volume decrease in the fracture zone (Figure 11) to calculate fracture zone permeability. In addition, we computed, but do not show, the fracture zone volume decrease corresponding to seven minutes of pumping. Thus, we can use the volume changes at

five times (2, 3, 4, 5, and 6 minutes) to estimate permeability in the fracture zone. Now the inverse problem is formally over-determined, as we have five times as many equations as unknowns. The resulting inversion is shown in Figure 13. Overall, the image is very similar to the result in Figure 12b. Again, we find a high permeability channel extending southward from well SE1. Also, present is the higher permeability region to the northwest of the pumping well.

One advantage associated with working at the Raymond site is the extensive set of experimental results at our disposal. We may use these results to examine the validity of our permeability estimates (Figure 13). In particular, we compare our results with a semi-quantitative analysis of some 4000 cross-well interference tests by Cook [1995]. These tests involved approximately 15 injection events per well, in all nine wells. Pressure was simultaneously monitored in 31 intervals within the adjacent boreholes. Because of the large number of interference tests, a formal inversion of the pressure observations was not feasible. Rather, a binary inversion algorithm was devised in which the pressure data was reduced to a binary set, in which 1 indicates a response to injection and 0 represents little or no response. This method was subsequently generalized to account for variations in response amplitude. The details of this analysis are given by Cook [1995]. All potential connections between the various borehole intervals are shown in Figure 14a, projected onto a horizontal plane. Figure 14b portrays those intervals which display mutual responses to injection. The significant connections are between intervals of the easternmost SE wells. A three-dimensional depiction indicates that, for the most part, the responding intervals lie within the depth range of the fracture zone [Karasaki et al., 2000]. These results are in excellent agreement with our estimated zone of higher permeability [Figure 13] which trends along the line formed by the SE boreholes.

Conclusions

Hydrologic characterization is often hampered by a relative paucity of observations. In particular, measurements are often limited to a select number of boreholes in which a few tests are conducted. The addition of geophysical data may help in this regard, but it is often difficult to relate such observations directly to flow properties. Surface deformation observations have the advantage of being gathered remotely, even from satellites. Furthermore, the equations relating reservoir pore fluid mass changes and surface displacements are well known for a poroelastic medium. Thus, surface displacements can provide an important adjunct to hydrologic data, such as transient pressure measurements. In this paper we have shown how to integrate surface tilt and transient pressure data to infer permeability variations in the subsurface. An important feature of this approach is that the inverse problem is partitioned into a series of three linear sub-problems. Each sub-problem may be solved quite efficiently, requiring just a few minutes of computation. In our application to tilt and borehole pressure data from the Raymond field site we are able to image a high permeability channel within a shallow fracture zone. As noted above, our results agree with the analysis of an extensive set of crosswell transient pressure tests [Cook, 1995; Karasaki et al., 2000].

This investigation constitutes our first attempt at combining displacement and dynamic reservoir data. As such, there are several directions in which this work could be generalized. First, it is desirable to have better estimates of the mechanical properties of the poroelastic medium. One possibility is to gather additional data from the boreholes, using borehole extensometers. Combining this with the pressure data we could then estimate the large-scale variations in material properties. We could also use the variation of the water level in each well in response to atmospheric loading and Earth tides to infer the large-scale distribution of B [Roeloffs et al., 1989; Rojstaczer and Agnew,1989; Rojstaczer and Riley, 1990]. Alternatively, we could formulate the inverse problem in terms of quantities which are not as sensitive to mechanical properties. We could

also utilize the arrival time of the peak slope of the pressure, a kinematic quantity, as described in Vasco et al. [2000b]. This quantity depends of the hydraulic diffusivity of the medium and not on the particular pressure amplitude. This requires sufficient sampling of the surface deformation in time and an adequate distribution of instruments. It may also be possible to combine early time data with steady state observations to estimate both flow and mechanical properties. This would require solving a non-linear inverse problem in an iterative fashion. For the simultaneous inversion we may take advantage of the fact that pressure should change monotonically from a pumping or injection well in the direction of flow. We could also integrate other types of data such as tracer observations. For example, once the flow field has reached steady-state a tracer may be injected. Then, the pressure and displacement data can be used to infer the pressure field associated with the tracer migration. A second area we need to explore in more depth is that of regularization and resolution. The problems we treated in this work were largely two-dimensional. For more complex three-dimensional situations the degree of non-uniqueness could be quite severe. The role of regularization will be even more important. Thus, more work is needed in devising and testing possible penalty terms for the coupled tilt and pressure inversion. Particular attention needs to be paid to maintaining physically plausible volume and pressure variations. Furthermore, model assessment is critical in three-dimensional situations. In such cases we need to compute model parameter resolution in order to quantify the degree in which our estimates are large-scale averages of volume changes [Parker, 1994]. In the future we want to examine the mapping of errors in the pressure and tilt data into errors in the permeability estimates. Given the structure of our sequential linear inversion, this should be straight-forward.

Appendix

In this Appendix we derive an integral formulation of the inverse problem for flow. We begin with the conservation equation (12) written as

$$\nabla \cdot (k(\mathbf{x})\nabla p) = \frac{\mu_f}{\rho_0} Q \tag{A1}$$

where Q is the augmented source term

$$Q = \rho_0 q - \frac{\partial \Delta m}{\partial t}. \tag{A2}$$

We shall write the permeability as a sum of a background distribution $k^0(\mathbf{x})$ plus some, possibly large, deviation from the background $\delta k(\mathbf{x})$

$$k(\mathbf{x}) = k^0(\mathbf{x}) + \delta k(\mathbf{x}). \tag{A3}$$

Because we are free to adopt any background model we shall assume that $k^0(\mathbf{x})$ is such that we can compute a Green's function for the structure. That is, we may solve the equation

$$\nabla \cdot \left(k^0(\mathbf{x})\nabla G_f(\mathbf{x},\mathbf{y},t)\right) = \delta(t)\delta(\mathbf{x}-\mathbf{y}) \tag{A4}$$

and derive an analytical expression for $G_f(\mathbf{x},\mathbf{y},t)$ [Stakgold, 1979]. Substituting equation (A3) into (A1) we find

$$\nabla \cdot \left(k^0(\mathbf{x})\nabla p\right) + \nabla \cdot (\delta k(\mathbf{x})\nabla p) = \frac{\mu_f}{\rho_0} Q. \tag{A5}$$

Thus, we have the equation

$$\nabla \cdot \left(k^0(\mathbf{x})\nabla p\right) = \frac{\mu_f}{\rho_0} Q - \nabla \cdot (\delta k(\mathbf{x})\nabla p) \tag{A6}$$

which is the pressure equation for the background medium $k^0(\mathbf{x})$ with an augmented source term. We can use the Green's function solution to write

$$p(\mathbf{x},t) = \frac{\mu_f}{\rho_0} \int_V G_f(\mathbf{x},\mathbf{y},t) Q(\mathbf{y},t) dV$$

$$-\int_V G_f(\mathbf{x},\mathbf{y},t)\nabla\left(\delta k(\mathbf{y})\nabla p(\mathbf{y},t)\right)dV. \qquad (A7)$$

For brevity we define the term

$$\delta p(\mathbf{x},t) = p(\mathbf{x},t) - \frac{\mu_f}{\rho_0}\int_V G_f(\mathbf{x},\mathbf{y},t)Q(\mathbf{y},t)dV. \qquad (A8)$$

If we assume that we either know the permeability at the boundary of our model or that the boundary is so far away that is does not influence our pressure computation, we can take $\delta k(\mathbf{x})$ equal to zero on the boundary. We may then transfer the gradient term onto the Green's function in equation (A7) and we have

$$\delta p(\mathbf{x},t) = -\int_V \nabla G_f(\mathbf{x},\mathbf{y},t)\cdot\nabla p(\mathbf{y},t)\delta k(\mathbf{y})dV. \qquad (A9)$$

Thus, we have derived an integral expression connecting the pressure distribution and the permeability. Note that, because the pressure depends on the permeability distribution, both $p(\mathbf{y},t)$ and $\delta k(\mathbf{y})$ are unknown and the inverse problem is non-linear. If we are able to specify $p(\mathbf{y},t)$ a priori, the inverse problem for $k(\mathbf{y})$ reduces to a linear equation.

Acknowledgments. We would like to thank Paul Cook of LBNL for providing his analysis of the numerous transient tests conducted at the Raymond Field Site. Support was provided by JAPEX (Japan Petroleum Exploration Co.) and JNC (Japan Nuclear Cycle Development Corp). All computations were carried out at the Center for Computational Seismology.

References

Bai, M., and Y. Abousleiman, Thermoporoelastic coupling with application to consolidation, *Int. J. Num. Anal. Meth. Geomech.*, **21**, 121-132, 1997.

Bamler, R., and P. Hartl, Synthetic aperture radar interferometry, *Inverse Problems*, **14**, 1-54, 1998.

Bear, J., *Dynamics of Fluids in Porous Media*, Dover Publications, 1972.

Bear, J., and M. Y. Corapcioglu, Mathematical model for regional land subsidence due to pumping 2. Integrated aquifer subsidence equations for vertical and horizontal displacements, *Water Resour. Res.*, **17**, 947-958, 1981.

Biot, M. A., General theory of three-dimensional consolidation, *J. Appl. Phys.*, **12**, 155-164, 1941.

Booker, J. R., and J. C. Small, A method of computing the consolidation behaviour of layered soils using direct numerical inversion of Laplace transforms, *Int. J. Num. Anal. Meth. Geomech.*, **11**, 363-380, 1974.

Burridge, R., and J. Keller, Poroelasticity equations derived from microstructure, *J. Acoust. Soc. Am.*, **28**, 1140-1146, 1998.

Carnec, C., D. Massonnet, and C. King, Two examples of the use of SAR interferometry on displacement fields of small spatial extent, *Geophys. Res. Letts.*, **23**, 3579-3582, 1996.

Carslaw, H. S., and J. C. Jaeger, *Conduction of Heat in Solids*, Oxford University Press, Oxford, 1959.

Castillo, W., S. Hunter, P. Harben, C. Wright, R. Conant, and E. Davis, Deep hydraulic fracture imaging: Recent advances in tiltmeter technologies, *Int. J. Rock Mech. and Min. Sci.*, **34**, 3-4, 1997.

Cohen, A., *Hydrologic Characterization of Fractured Granitic Rock Aquifer, Raymond California*, M. S. thesis, University of California, Berkeley, 1993.

Chilingarian, G. V., E. C. Donaldson, and T. Yen, *Subsidence Due to Fluid Withdrawal*, Elsevier Science Publ., Amsterdam, 1995.

Colazas, X. C., and R. W. Strehle, Subsidence in the Wilmington oil field, Long Beach,

California, USA, in *Subsidence Due to Fluid Withdrawal*, edited by G. V. Chilingarian, E. C. Donaldson, and T. Yen, Elsevier Science Publ., Amsterdam, 1995.

Cook, N. G. W., Coupled processes in geomechanics, in *Coupled Processes Associated with Nuclear Waste Repositories*, edited by C.-F. Tsang, Academic Press, Orlando, FL, 1987.

Cook, P. J., *Analysis of Interwell Hydraulic Connectivity in Fractured Granite*, M. S. thesis, University of California, Berkeley, 1995.

Datta-Gupta, A., and M. J. King, A semianalytic approach to tracer flow modeling in heterogeneous permeable media, *Adv. Water Resour.*, **18**, 9-24, 1995.

Du, Y., A. Aydin, and L. Murdoch, Incremental growth of a shallow hydraulic fracture at a waste remediation site, Oakbrook, Illinois, from inversion of elevation changes, *Int. J. Rock Mech. and Min. Sci.*, **30**, 1273-1279, 1993.

Evans, K. F., G. R. Holzhausen, M. D. Wood, The geometry of a large-scale nitrogen gas hydraulic fracture formed in Devonian shale: An example of fracture mapping using tiltmeters, *SPE J.*, **22**, 755-763, 1982.

Fowler, A. C., and C. G. Noon, Mathematical models of compaction, consolidation, and regional groundwater flow, *Geophys. J. Int.*, **136**, 251-260, 1999.

Galloway, D. L., K. W. Hudnut, S. E. Ingebritsen, S. P. Phillips, G. Peltzer, F. Rogez, and P. A. Rosen, Detection of aquifer system compaction and land subsidence using interferometric synthetic aperture radar, Antelope Valley, Mojave Desert, California, *Water Resour. Res.*, **34**, 2573-2585, 1998.

Gambolati, G., Deviations from Theis solution in aquifers undergoing three-dimensional consolidation, *Water Resour. Res.*, **13**, 62-68, 1977.

Gambolati, G., Comment on 'Coupling versus uncoupling in soil consolidation', *Int. J. Num. Anal. Meth. Geomech.*, **16**, 833-835, 1992.

Gambolati, G., and R. A. Freeze, Mathematical simulation of the subsidence of Venice, 1, Theory, *Water Resour. Res.*, **9**, 721-733, 1973.

Gambolati, G., P. Gatto, and R. A. Freeze, Mathematical simulation of the subsidence of Venice, 2, Results, *Water Resour. Res.*, **10**, 563-577, 1974.

Gambolati, G., P. Teatini, D. Bau, and M. Ferronato, Importance of poroelastic coupling in dynamically active aquifers of the Po river basin, Italy, *Water Resour. Res.*, **36**, 2443-2459, 2000.

Geertsma, J., The effect of fluid pressure decline on volumetric changes of porous rocks, *Trans. AIME*, 331-340, 1957.

Geertsma, J., Land subsidence above compacting oil and gas reservoirs, *J. Petro. Tech.*, **25**, 734-744, 1973.

Gill, P. E., W. Murray, and M. H. Wright, *Practical Optimization*, Academic Press, 1981.

Hackbusch, W., *Integral Equations*, Birkhauser, Basel, 1995.

Hoffmann, J., H. A. Zebker, D. L. Galloway, and F. Amelung, Seasonal subsidence and rebound in Las Vegas Valley, Nevada, observed by synthetic aperture radar interferometry, *Water Resour. Res.*, **37**, 1551-1566, 2001.

Karasaki, K., B. Freifeld, A. Cohen, K. Grossenbacher, P. Cook, and D. Vasco, A multidisciplinary fractured rock characterization study at Raymond field site, Raymond CA, *J. of Hydrology*, **236**, 17-34, 2000.

Lewis, R. W., and B. Schrefler, A fully coupled consolidation model of the subsidence of Venice, *Water Resour. Res.*, **14**, 223-230, 1978.

Lewis, R. W., and B. Schrefler, *The Finite Element Method in the Deformation and Consolidation of Porous Media*, Wiley, New York, 1987.

Lewis, R. W., B. A. Schrefler, and L. Simoni, Coupling versus uncoupling in soil consolidation, *Int. J. Num. Anal. Meth. Geomech.*, **15**, 533-548, 1991.

Lewis, R. W., B. A. Schrefler, and L. Simoni, Author's reply, 'Coupling versus uncoupling in soil consolidation', *Int. J. Num. Anal. Meth. Geomech.*, **16**, 835-837, 1992.

Massonnet, D., T. Holzer, and H. Vadon, Land subsidence caused by East Mesa geothermal field, California, observed using SAR interferometry, *Geophys. Res. Letts.*, **24**, 901-904, 1997.

Menke, W., *Geophysical Data Analysis: Discrete Inverse Theory*, Academic Press, San Diego, 1984.

Mogi, K., Relations between the eruptions of various volcanoes and the deformations of the

ground surfaces around them, *Bull. Earthquake Res. Inst.*, **36**, 99-134, 1958.

Narasimhan, T. N., P. A. Witherspoon, and A. L. Edwards, Numerical model for saturated-unsaturated flow in deformable porous media 2. The algorithm, *Water Resour. Res.*, **14**, 255-261, 1978.

Noorishad, J., C.-F. Tsang, and P. A. Witherspoon, Theoretical and field studies of coupled behaviour of fracture rocks, 1, Development and verification of a numerical simulator, *Int. J. Rock Mech. and Min. Sci.*, **29**, 401-409, 1992.

Paige, C. C., and M. A. Saunders, LSQR: An algorithm for sparse linear equations and sparse linear systems, *ACM Trans. Math. Software*, **8**, 195-209, 1982.

Parker, R. L., *Geophysical Inverse Theory*, Princeton University Press, 1994.

Poland, J. F., B. E. Lofgren, R. L. Ireland, and R. G. Pugh, Land subsidence in the San Joaquin Valley, California as of 1972, *U. S. Geological Survey Professional Paper*, **437-H**, 78 p, 1975.

Raghavan, R., D. T. Scorer, and F. G. Miller, An investigation by numerical methods of the effect of pressure-dependent rock and fluid properties, *SPE J.*, 267-276, 1972.

Rice, J. R., and M. P. Cleary, Some basic stress diffusion solutions for fluid-saturated elastic porous media with compressible components, *Reviews of Geophys. and Space Phys.*, **14**, 227-241, 1976.

Roeloffs, E. A., S. S. Burford, F. S. Riley, and A. W. Records, Hydrologic effects on water level changes associated with episodic fault creep near Parkfield, California, *J. Geophys. Res.*, **94**, 12387-12402, 1989.

Rojstaczer, S., and D. C. Agnew, The influence of formation material properties on the response of water levels in wells to Earth tides and atmospheric loading, *J. Geophys. Res.*, **94**, 12403-12411, 1989.

Rojstaczer, S., and F. S. Riley, Response of the water level in a well to Earth tides and atmospheric loading under unconfined conditions, *Water Resour. Res.*, **26**, 1803-1817, 1990.

Rutqvist, J., J. Noorishad, and C.-F. Tsang, Determination of fracture storativity in hard rocks using high-pressure injection testing, *Water Resour. Res.*, **34**, 2551-2560, 1998.

Safai, N. M., and G. Pinder, Vertical and horizontal land deformation due to fluid withdrawal, *Int. J. Num. Anal. Meth. Geomech.*, **4**, 131-142, 1980.

Samaniego, V. F., W. E. Brigham, and F. G. Miller, An investigation of transient flow of reservoir fluids considering pressure-dependent rock and fluid properties, *SPE J.*, 140-149, 1977.

Savage, J. C., and M. M. Clark, Magmatic resurgence in Long Valley Caldera, California: Possible cause of the 1980 Mammoth Lakes earthquakes, *Science*, **217**, 531-533, 1982.

Savage, J. C., and R. S. Cockerham, Earthquake swarm in Long Valley Caldera, California, January 1983: Evidence for dike inflation, *J. Geophys. Res.*, **89**, 8315-8324, 1984.

Segall, P., Stress and subsidence resulting from subsurface fluid withdrawal in the epicentral region of the 1983 Coalinga earthquake, *J. Geophys. Res.*, **90**, 6801-6816, 1985.

Smith, D. W., and J. R. Booker, Green's functions for a fully coupled thermoporoelastic material, *Int. J. Num. Anal. Meth. Geomech.*, **17**, 139-163, 1993.

Stakgold, I., *Greens Functions and Boundary Value Problems*, John Wiley and Sons, New York, 1979.

Tarantola, A., *Inverse Problem Theory*, Elsvier, New York, 1987.

Vasco, D. W., L. R. Johnson, and N. E. Goldstein, Using surface displacement and strain observations to determine deformation at depth, with an application to Long Valley Caldera, California, *J. of Geophys. Res.*, **93**, 3232-3242, 1988.

Vasco, D. W., K. Karasaki, and L. Myer, Monitoring of fluid injection and soil consolidation using surface tilt measurements, *J. of Geotech. and Geoenv. Eng.*, **124**, 29-37, 1998.

Vasco, D. W., K. Karasaki, and C. Doughty, Using surface deformation to image reservoir dynamics, *Geophysics*, **65**, 132-147, 2000a.

Vasco, D. W., H. Keers, and K. Karasaki, Estimation of reservoir properties using transient pressure data: An asymptotic approach, *Water Resour. Res.*, **36**, 3447-3465, 2000b.

Vasco, D. W., C. Wicks, Jr., K. Karasaki, and O. Marques, Geodetic imaging: Reservoir monitoring using satellite interferometry, *Geophys. J. Int.*, (in press), 2001.

Wicks, C., Jr., W. Thatcher, and D. Dzurisin, Migration of fluids beneath Yellowstone Caldera inferred from satellite radar interferometry, *Science*, **282**, 458-462, 1998.

Wu, Y., and K. Pruess, Integral solutions for transient fluid flow through a porous medium with pressure-dependent permeability, *Int. J. Rock Mech. and Min. Sci.*, **37**, 51-61, 2000.

Zimmerman, R. W., Coupling in poroelasticity and thermoelasticity, *Int. J. Rock Mech. and Min. Sci.*, **37**, 79-87, 2000.

D. W. Vasco, Earth Sciences Division/Building 90, Berkeley Laboratory, 1 Cyclotron Road, Berkeley, CA 94720.

Kenzi Karasaki, Earth Sciences Division/Building 90, Berkeley Laboratory, 1 Cyclotron Road, Berkeley, CA 94720.

Kiyoshi Kishida, Earth Sciences Division/Building 90, Berkeley Laboratory, 1 Cyclotron Road, Berkeley, CA 94720.

Received _____

Figure 1. Spatial variation in permeability use to generate the synthetic head and tilt values. The injection well is indicated by a star. The four pumping wells are denoted by open circles.

Figure 2. (Left) Steady-state pressure change in the subsurface calculated by a streamline reservoir simulator, based upon the permeability distribution in Figure 1. (Right) Pressure change estimated by the inversion of surface tilts and borehole pressure values.

Figure 3. Inferred permeability variation, based upon the estimated pressure variation in Figure 2.

Figure 4. Depth to the top of the uppermost fracture zone at the Raymond field site. The depth distribution was obtained by fitting a plane to the intersection of the fracture zone and the boreholes. The nine boreholes at the field site are indicated by stars. The tiltmeter locations are represented by open circles.

Figure 5. Reduced tilt data associated with the August 15th production test. The pumping interval is bounded by the vertical lines.

Figure 6. Drawdown recorded during the August 15th production test. The observations are from packed-off intervals within seven wells of the borehole array.

Figure 7. (Left) Fracture zone pore fluid volume decrease, as determined by an inversion of tilt data only. (Right) Fracture zone pore volume decrease estimated solely from borehole head measurements.

Figure 8. Contour plot of misfit to the tilt and pressure data, as a function of Skemptons coefficient (B) and shear modulus (μ).

Figure 9. Coupled inversion of head and surface tilt data for fracture zone pore volume changes.

Figure 10. (Left) Observed versus calculated tilt values for the coupled inversion. The calculated tilts are associated with the volume change model in Figure 9. (Right) Observed and calculated head change for the seven boreholes where observations were gathered (00, SE1, SE3, SE4, SW1, SW3, SW4).

Figure 11. Fracture zone pore volume decreases for six time intervals.

Figure 12. (Left) Estimated distribution of drawdown in the fracture zone, obtained by mapping the pore volume decrease into head. (Right) Fracture zone permeability variations from a uniform background. The estimates are based upon the head distribution in the left panel. The scale depicts the relative variation in permeability, $\delta K/K_0$, where K_0 is the background permeability. Note that this is equivalent to variations in $\delta \ln K$.

Figure 13. Fracture zone permeability obtained from an inversion of five time intervals (2, 3, 4, 5, and 6 minutes). As in Figure 12b, the scale depicts the relative variation in permeability, $\delta K/K_0$.

Figure 14. (A) Straight line connections between intervals within the nine boreholes at the Raymond site. The straight lines connect pumping and observing intervals associated with some 135 injection tests. (B) Lines connecting those intervals which displayed significant mutual pressure response to injection. The boreholes are indicated by filled circles, borehole deviations are responsible for the paths traced by the circles.

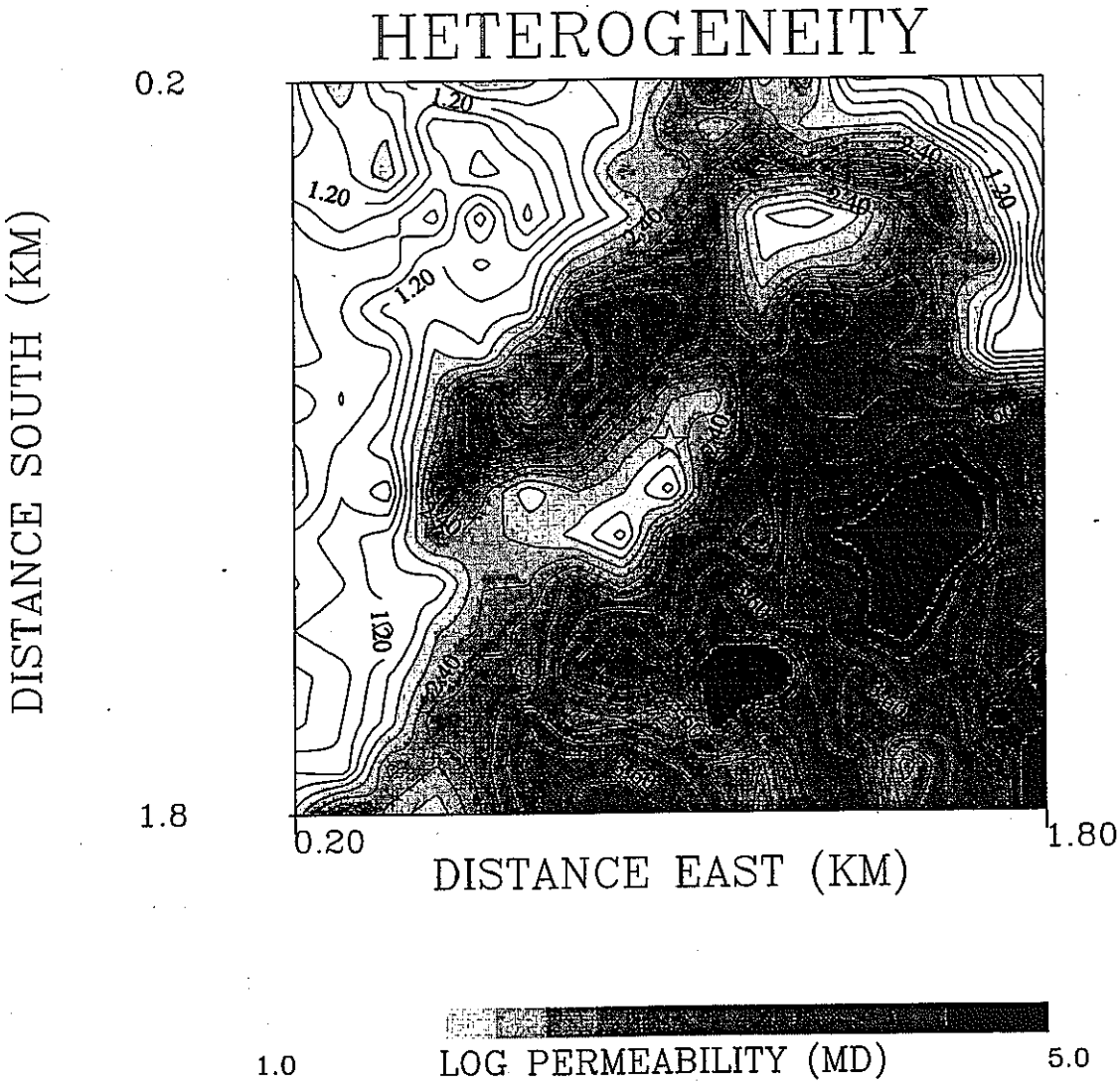
HETEROGENEITY
0.2
1.8
DISTANCE SOUTH (KM)
0.20
1.80
DISTANCE EAST (KM)
1.0
LOG PERMEABILITY (MD)
5.0
CONTOUR FROM -0.30000 TO 5.4000 CONTOUR INTERVAL OF 0.30000 PT(3,3)= 1.9799

Figure 1

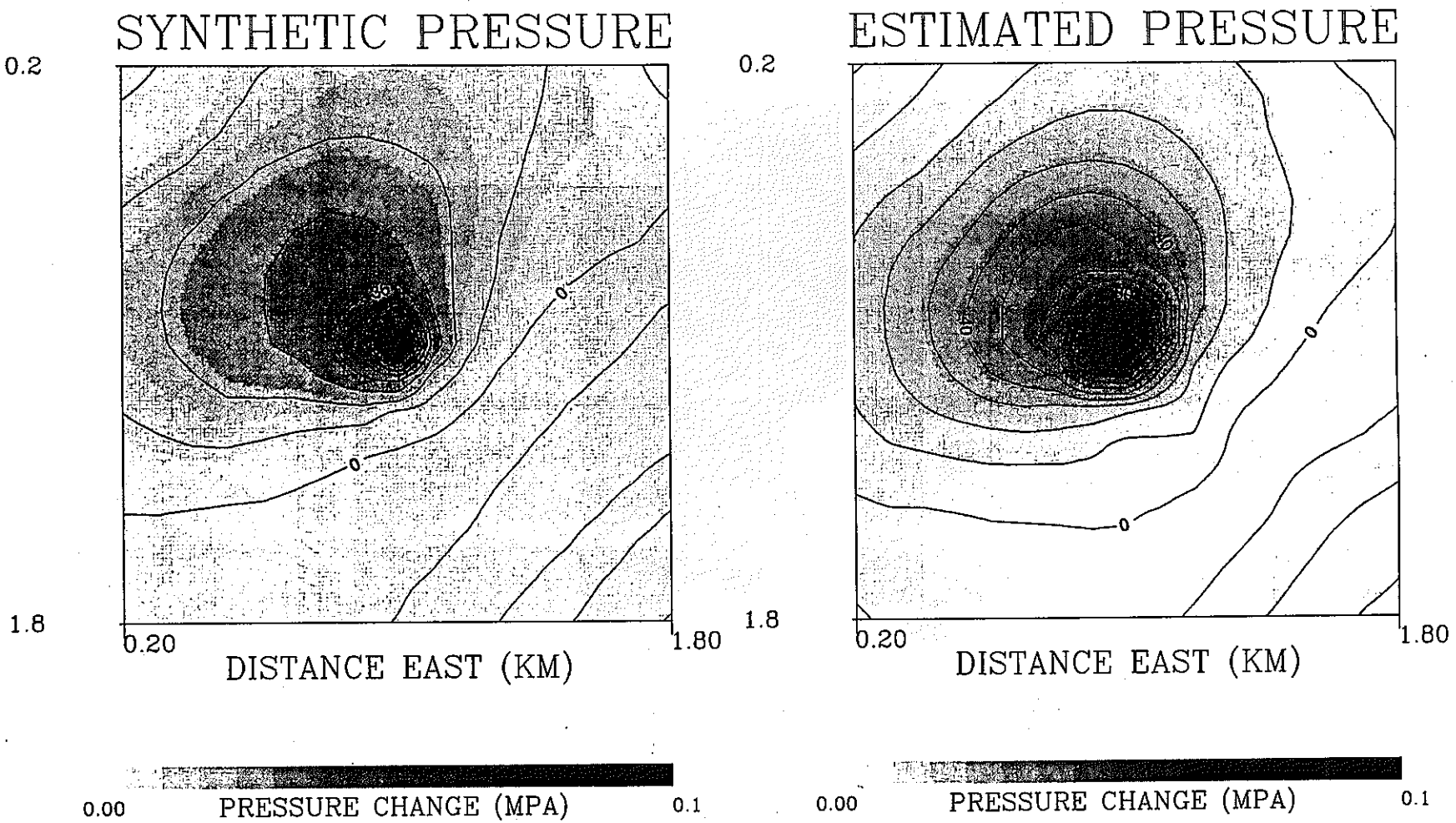

Figure 2

CONTOUR FROM -0.36000E-01 TO 0.10800 CONTOUR INTERVAL OF 0.90000E-02 PT(3,3)= -0.76199E-02 LABELS SCALED BY 1000.0CONTOUR FROM -0.30000E-01 TO 0.13000 CONTOUR INTERVAL OF 0.10000E-01 PT(3,3)= -0.10137E-01 LABELS SCALED BY 1000

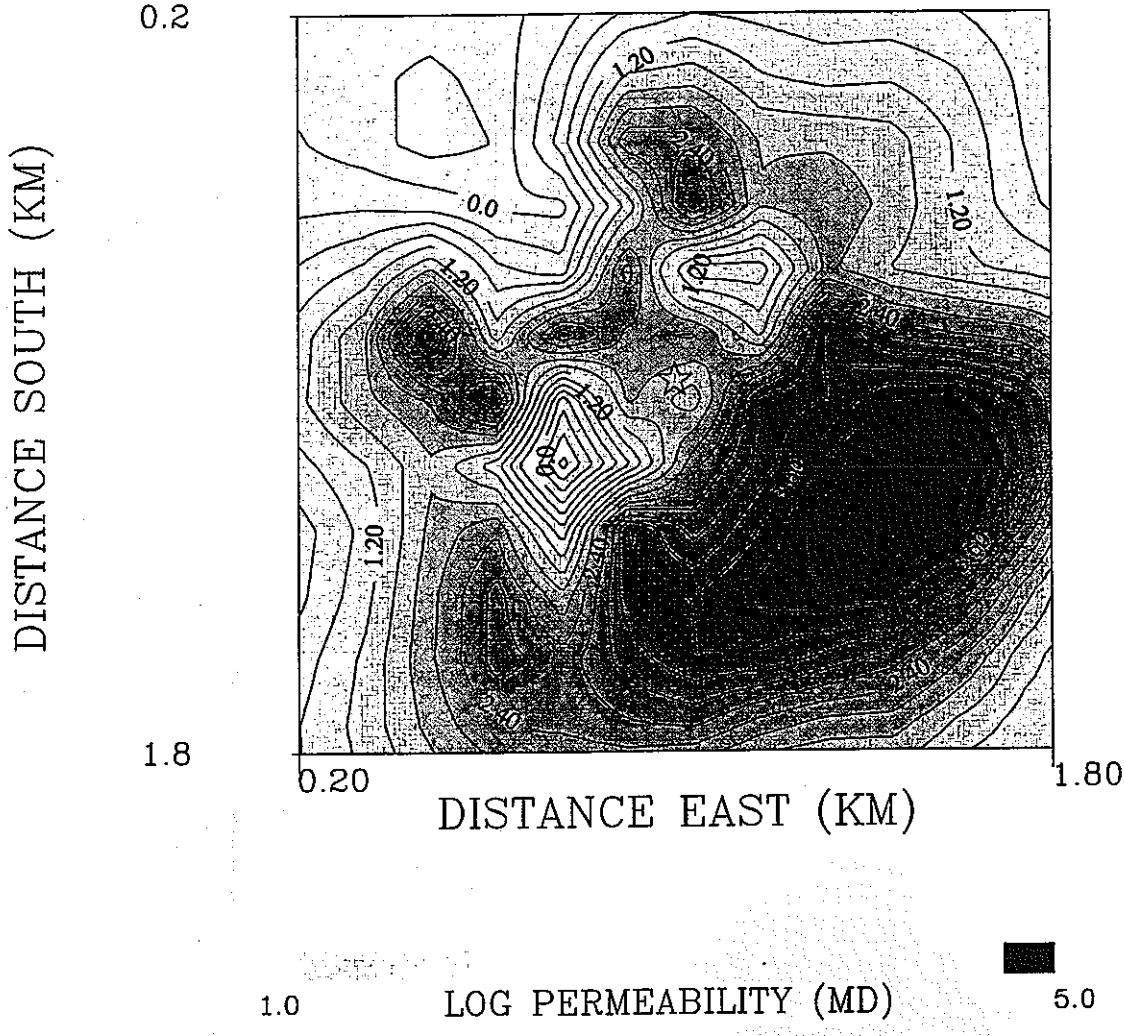
0.2
1.8
DISTANCE SOUTH (KM)
0.20
1.80
DISTANCE EAST (KM)
1.0
LOG PERMEABILITY (MD)
5.0
0.0
1.20
2.40
CONTOUR FROM -0.90000 TO 4.8000 CONTOUR INTERVAL OF 0.30000 PT(3,3)= 0.94894

Figure 3

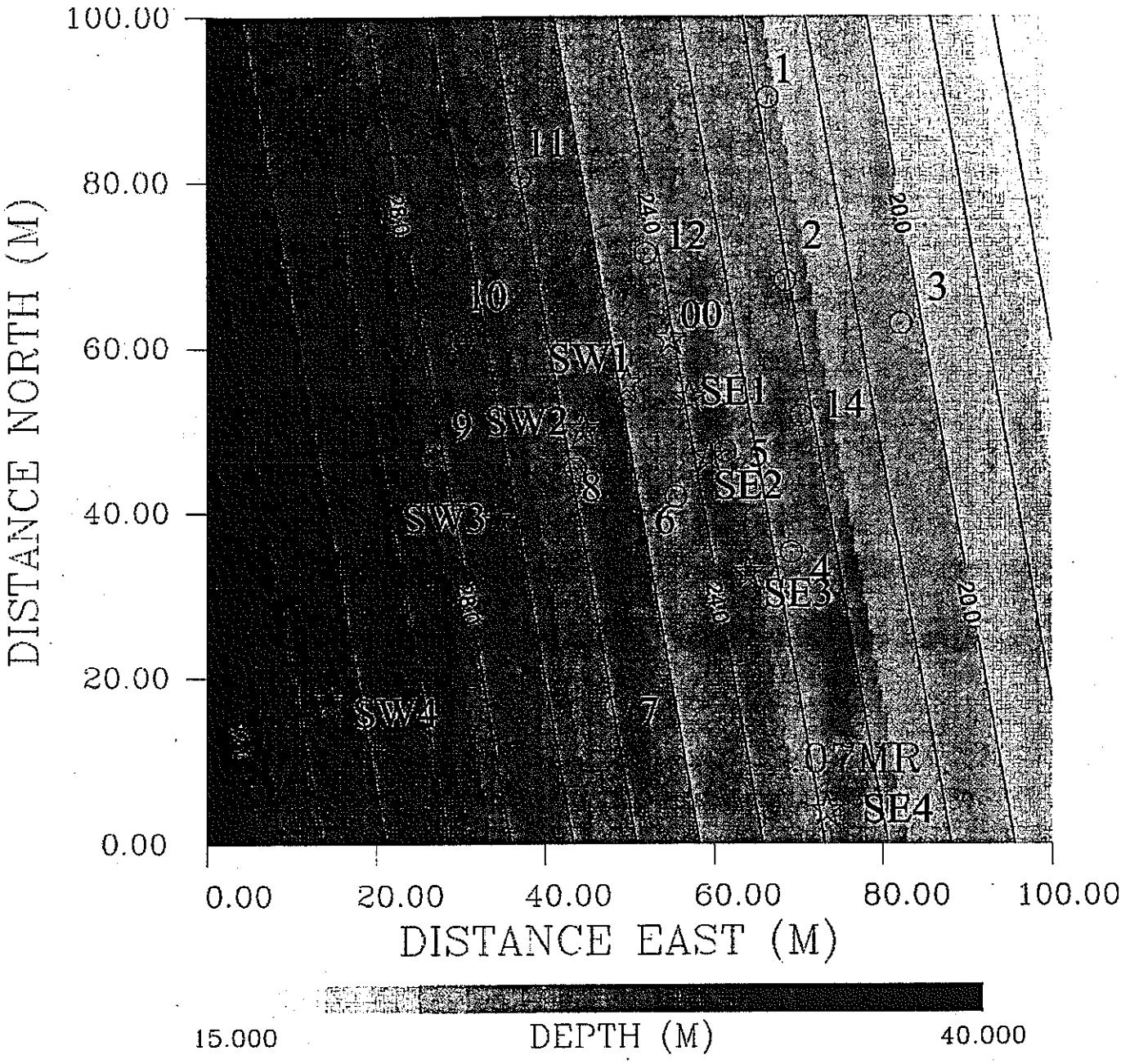
100.00
80.00
60.00
40.00
20.00
0.00
DISTANCE NORTH (M)
0.00
20.00
40.00
60.00
80.00
100.00
DISTANCE EAST (M)
1
11
12
2
3
10
00
SW1
SE1
14
9
SW2
5
8
SE2
SW3
6
4
SE3
7
07MR
SE4
SW4
15.000
DEPTH (M)
40.000

Figure 4

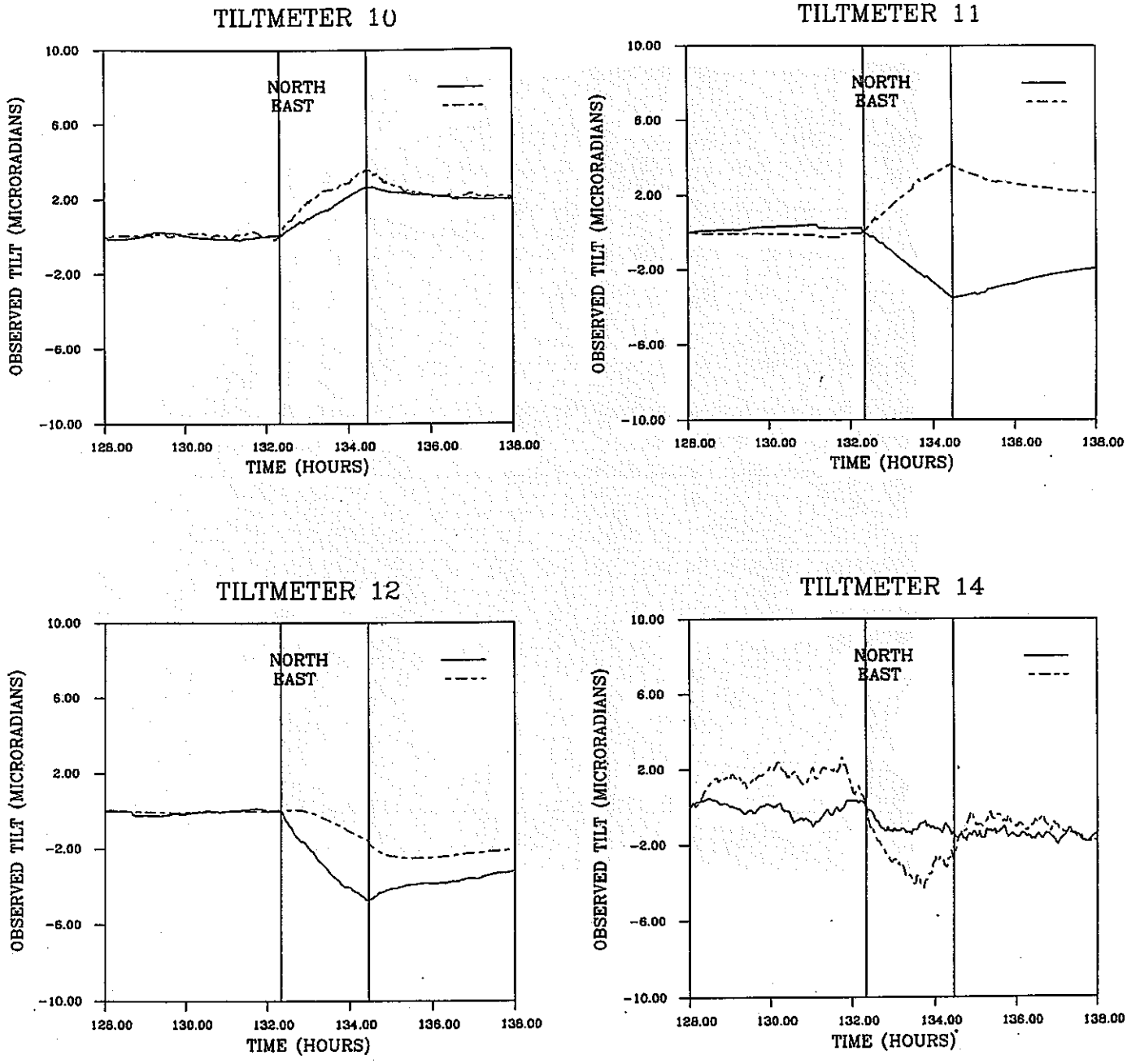
TILTMETER 10
TILTMETER 11
TILTMETER 12
TILTMETER 14
NORTH
EAST
OBSERVED TILT (MICRORADIANS)
TIME (HOURS)
10.00
6.00
2.00
-2.00
-6.00
-10.00
128.00
130.00
132.00
134.00
136.00
138.00

Figure 5(a)

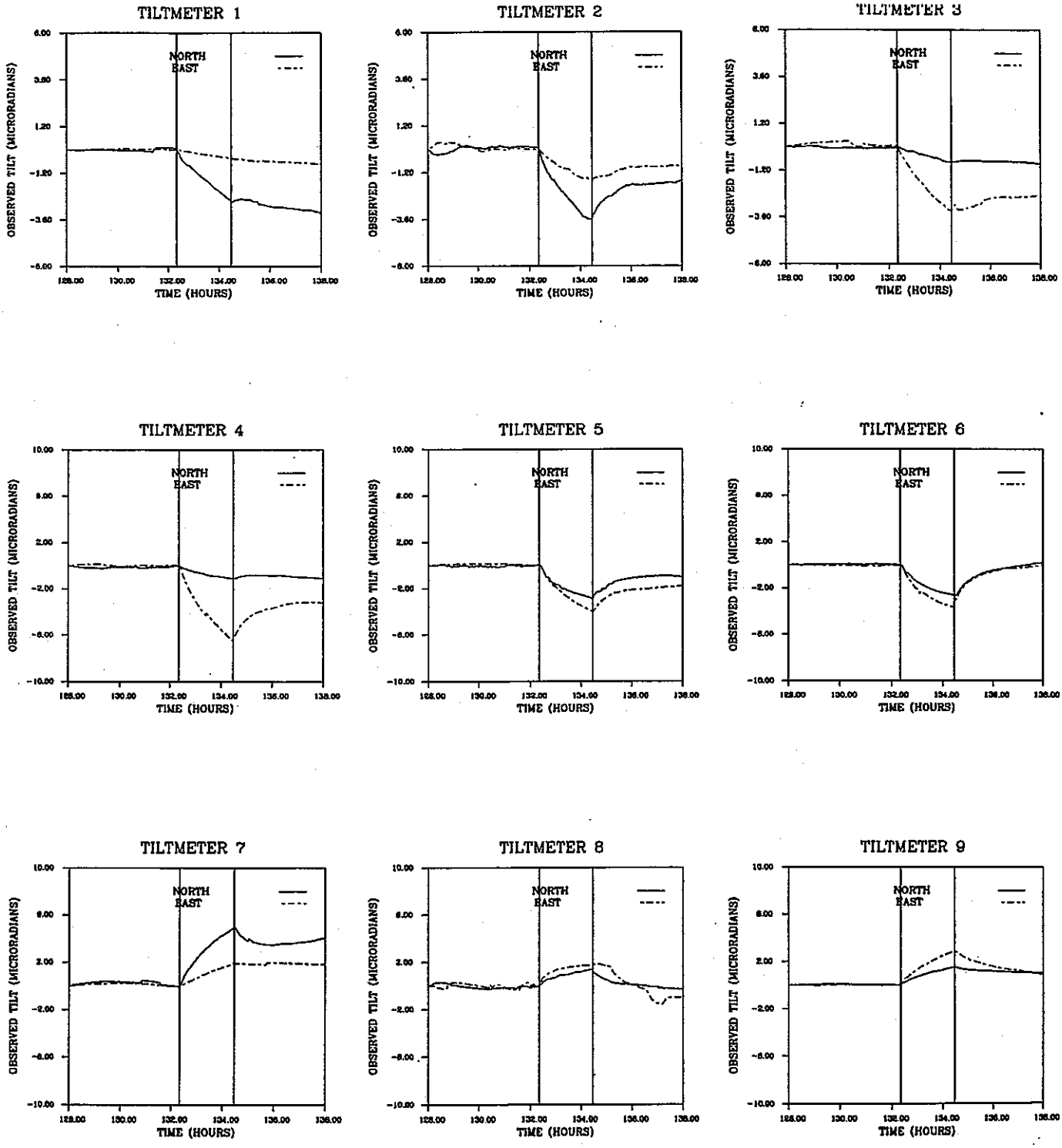
TILTMETER 1
TILTMETER 2
TILTMETER 3
TILTMETER 4
TILTMETER 5
TILTMETER 6
TILTMETER 7
TILTMETER 8
TILTMETER 9
NORTH
EAST
OBSERVED TILT (MICRORADIANS)
TIME (HOURS)

Figure 5(b)

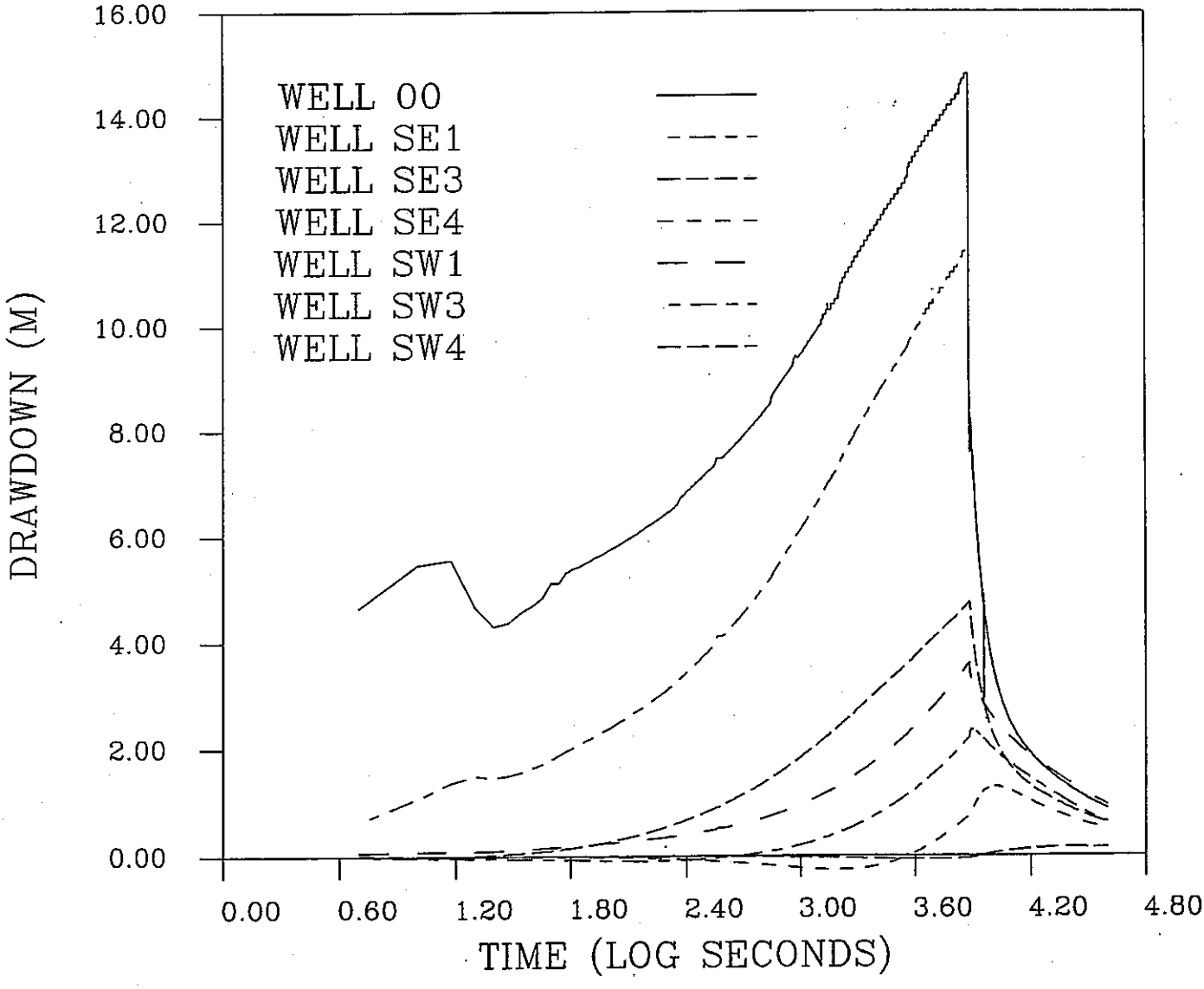
16.00
14.00
12.00
10.00
8.00
6.00
4.00
2.00
0.00
DRAWDOWN (M)
WELL 00
WELL SE1
WELL SE3
WELL SE4
WELL SW1
WELL SW3
WELL SW4
0.00
0.60
1.20
1.80
2.40
3.00
3.60
4.20
4.80
TIME (LOG SECONDS)

Figure 6

5 Minutes

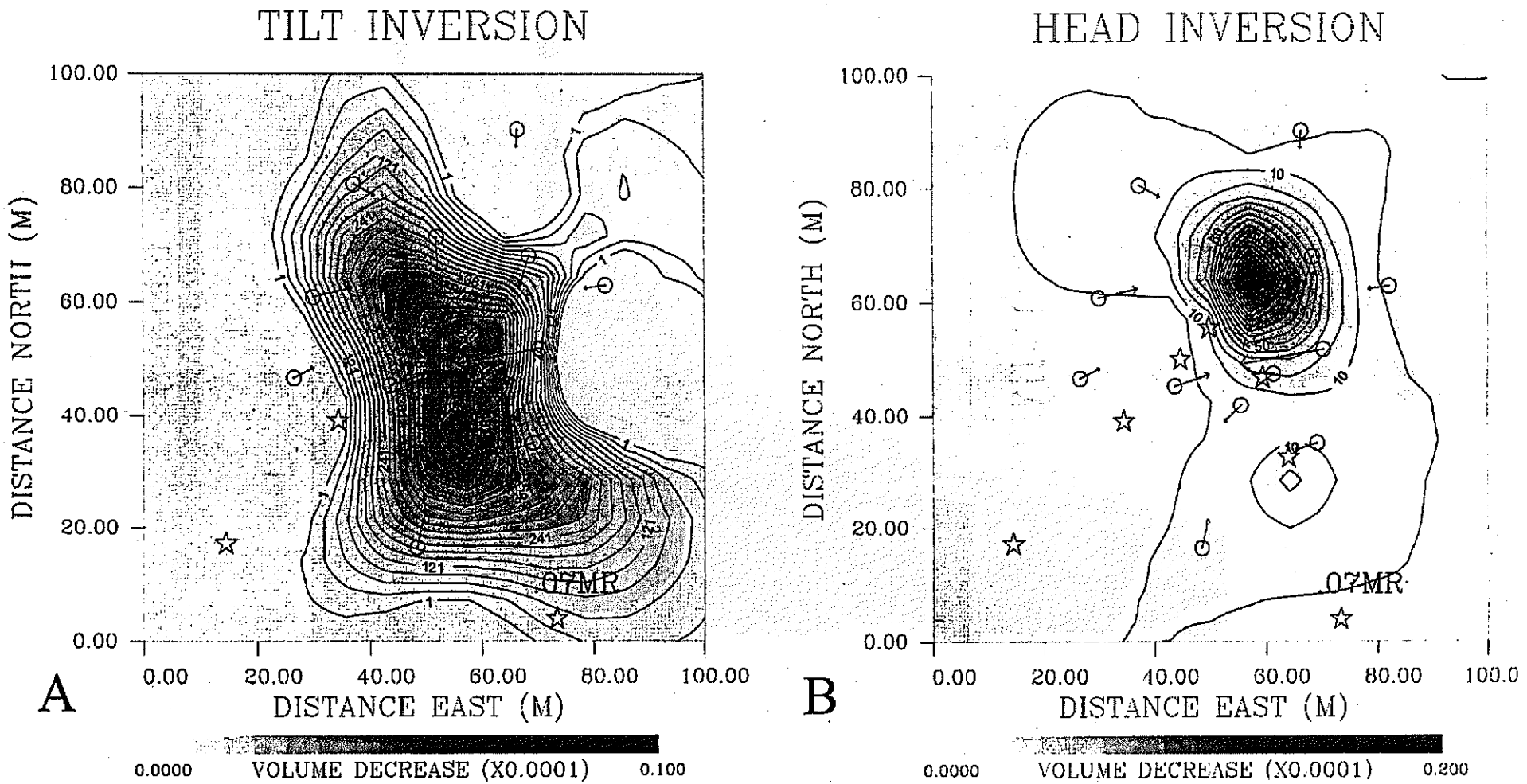

Figure 7

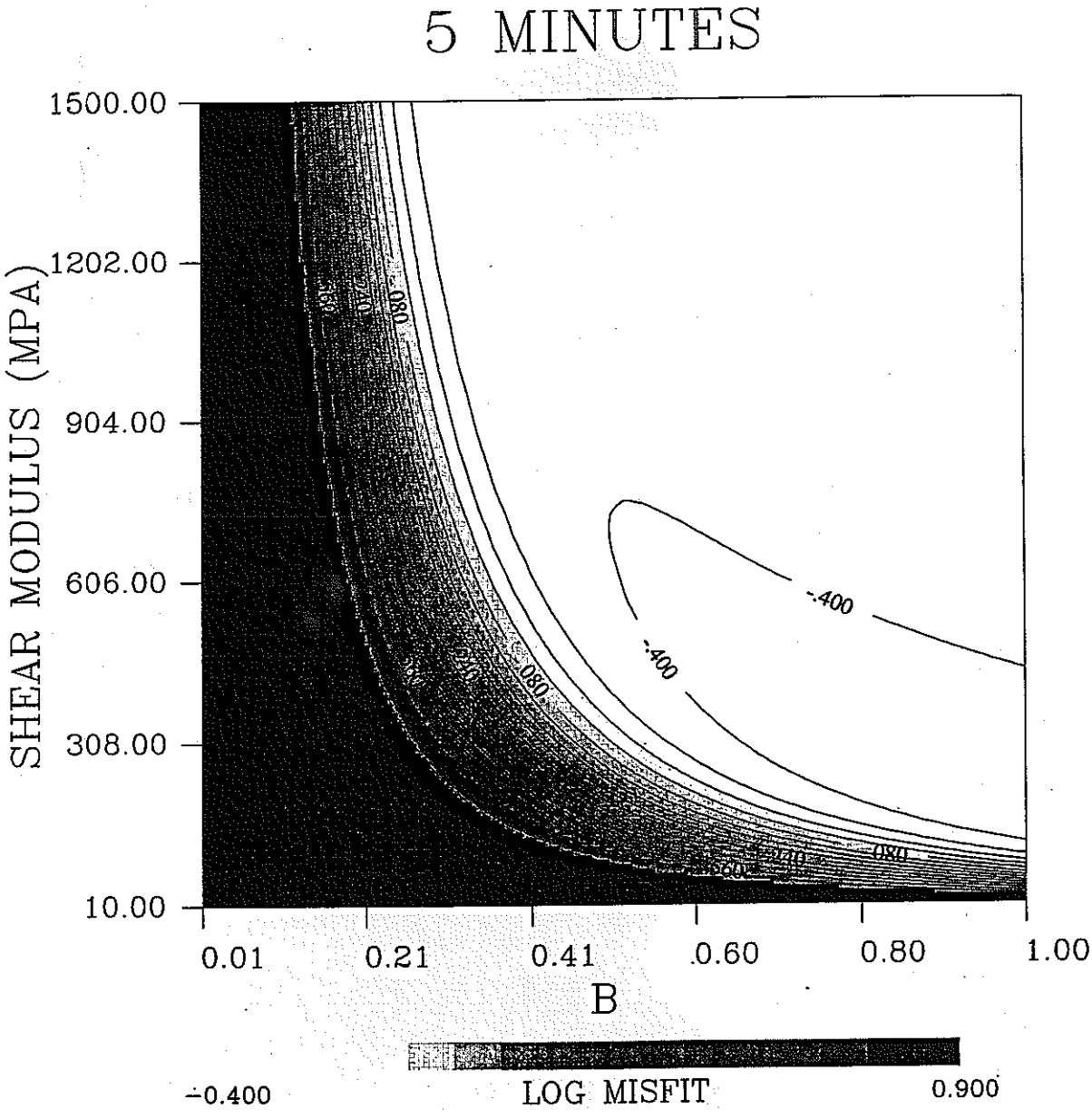
5 MINUTES
1500.00
1202.00
904.00
606.00
308.00
10.00
SHEAR MODULUS (MPA)
0.01
0.21
0.41
.0.60
0.80
1.00
B
-0.400
LOG MISFIT
0.900

Figure 8

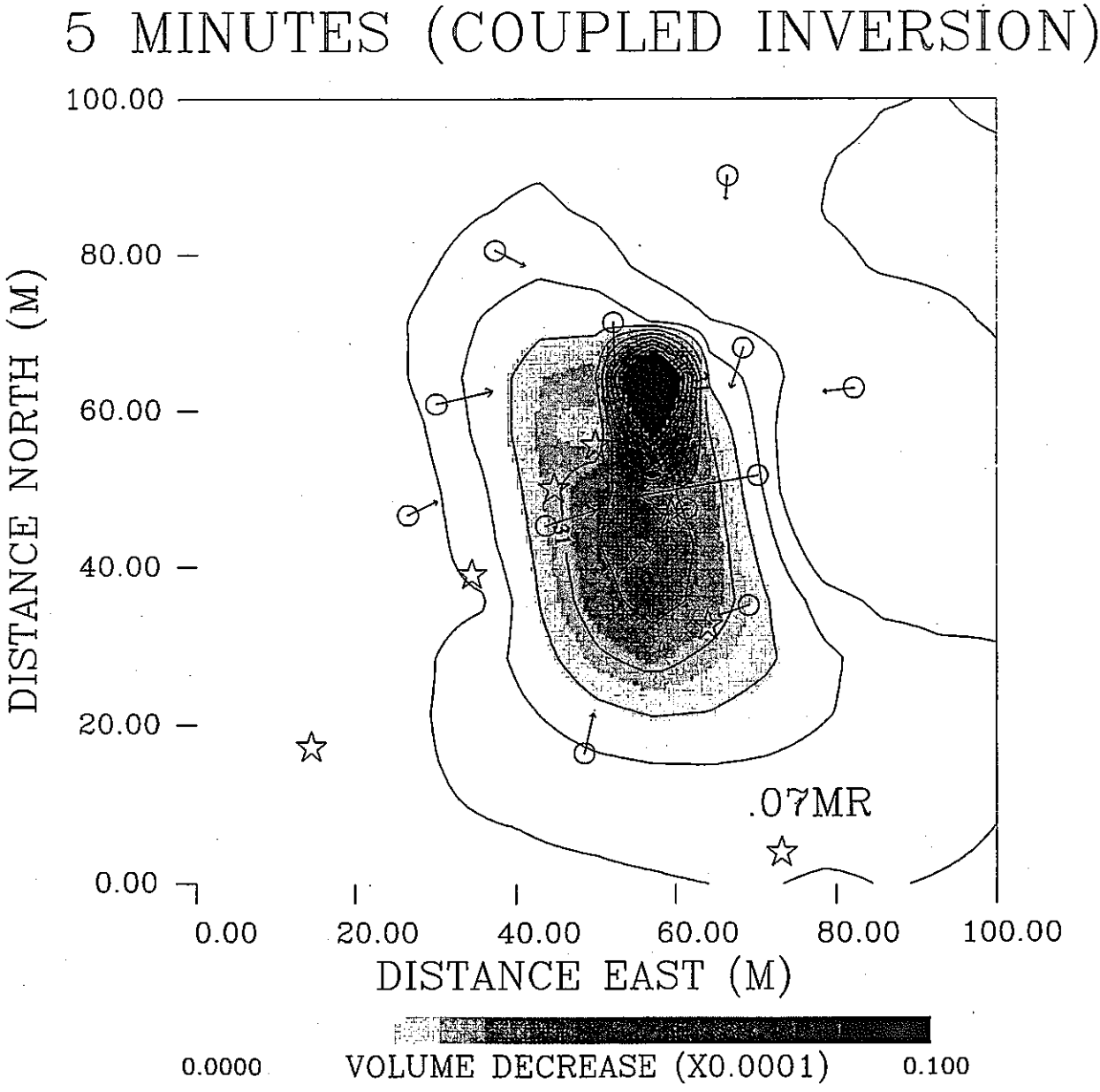
5 MINUTES (COUPLED INVERSION)
100.00
80.00
60.00
40.00
20.00
0.00
DISTANCE NORTH (M)
0.00
20.00
40.00
60.00
80.00
100.00
DISTANCE EAST (M)
.07MR
0.0000
VOLUME DECREASE (X0.0001)
0.100

Figure 9

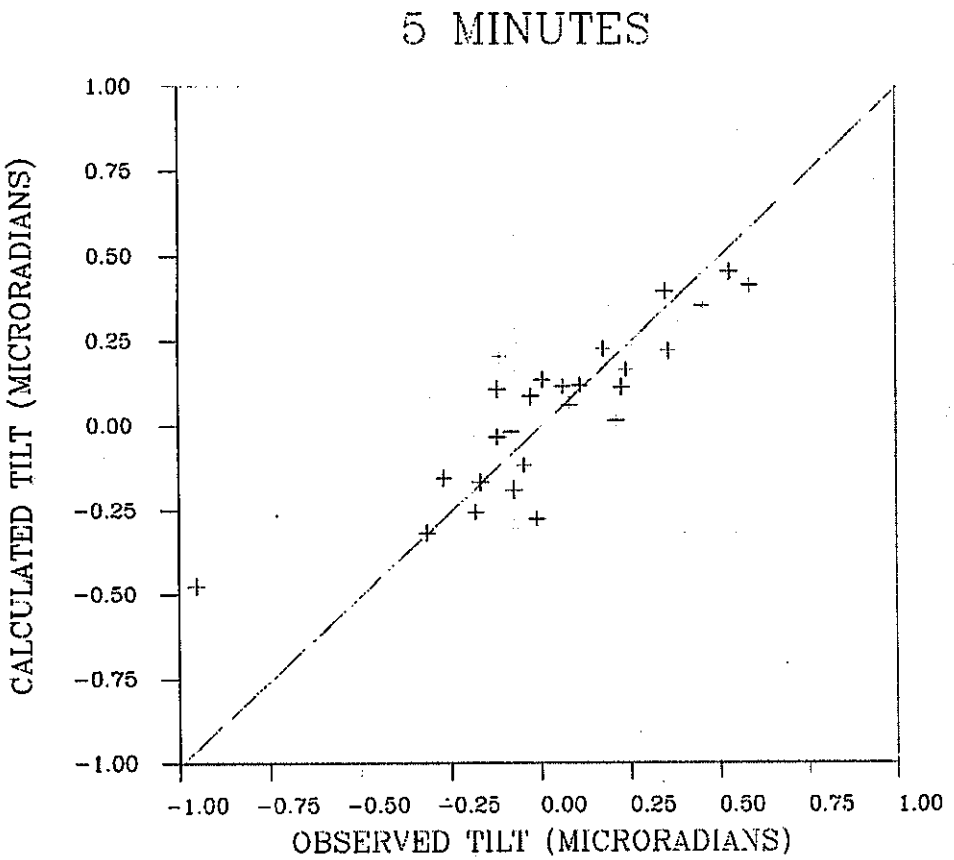
5 MINUTES
CALCULATED TILT (MICRORADIANS)
1.00
0.75
0.50
0.25
0.00
-0.25
-0.50
-0.75
-1.00
-1.00 -0.75 -0.50 -0.25 0.00 0.25 0.50 0.75 1.00
OBSERVED TILT (MICRORADIANS)

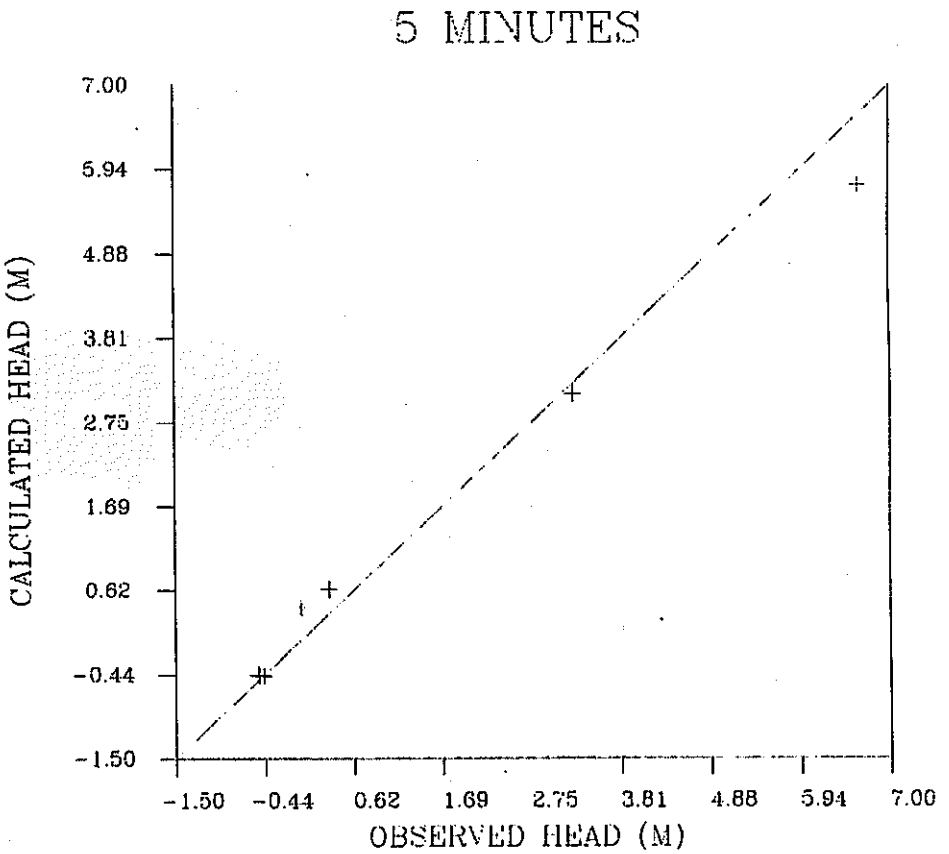
5 MINUTES
CALCULATED HEAD (M)
7.00
5.94
4.88
3.81
2.75
1.69
0.62
-0.44
-1.50
-1.50 -0.44 0.62 1.69 2.75 3.81 4.88 5.94 7.00
OBSERVED HEAD (M)

Figure 10

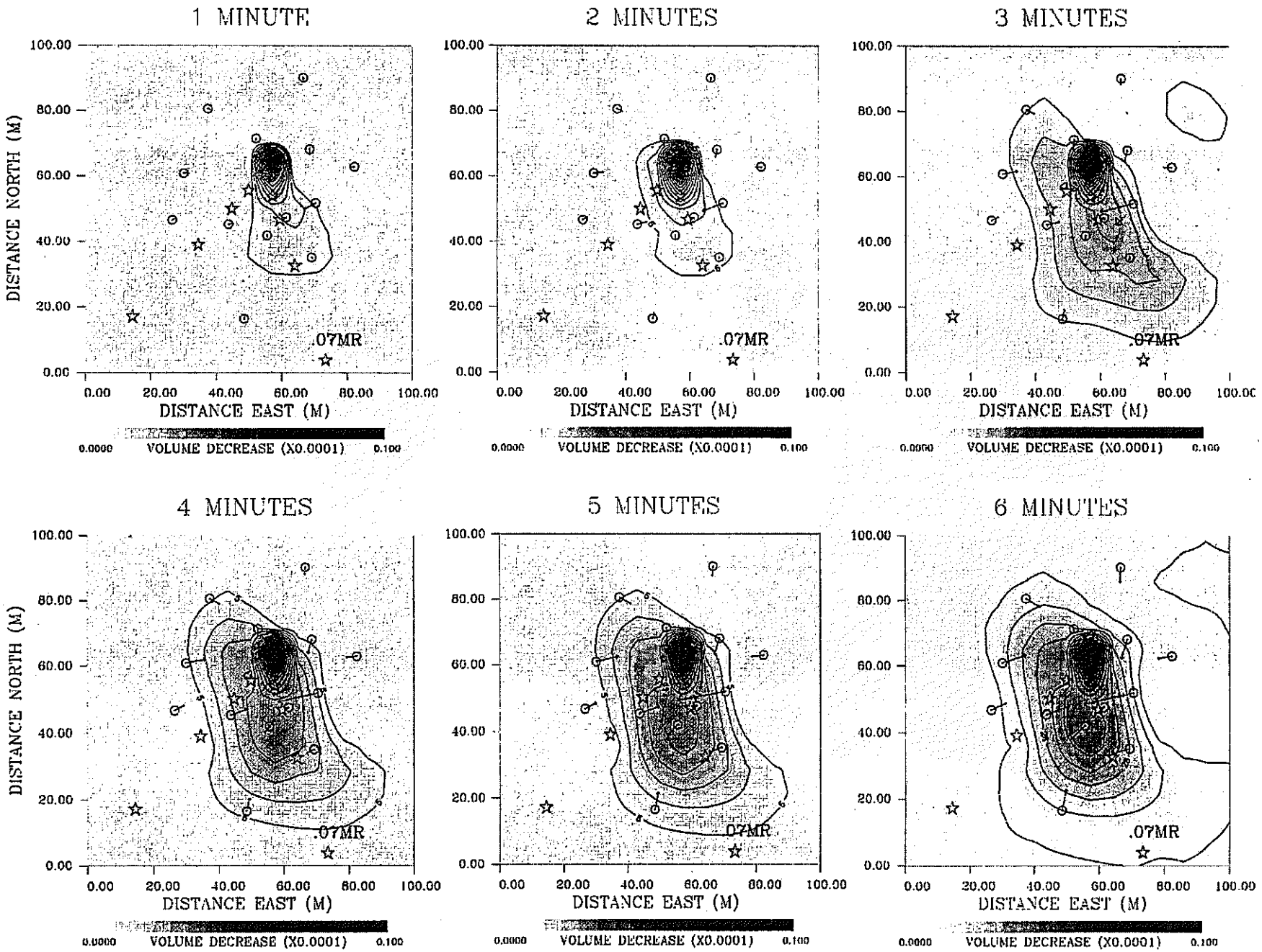
1 MINUTE
2 MINUTES
3 MINUTES
4 MINUTES
5 MINUTES
6 MINUTES
DISTANCE NORTH (M)
DISTANCE EAST (M)
VOLUME DECREASE (X0.0001)
.07MR
0.00
20.00
40.00
60.00
80.00
100.00
0.0000
0.100

Figure 11

5 Minutes

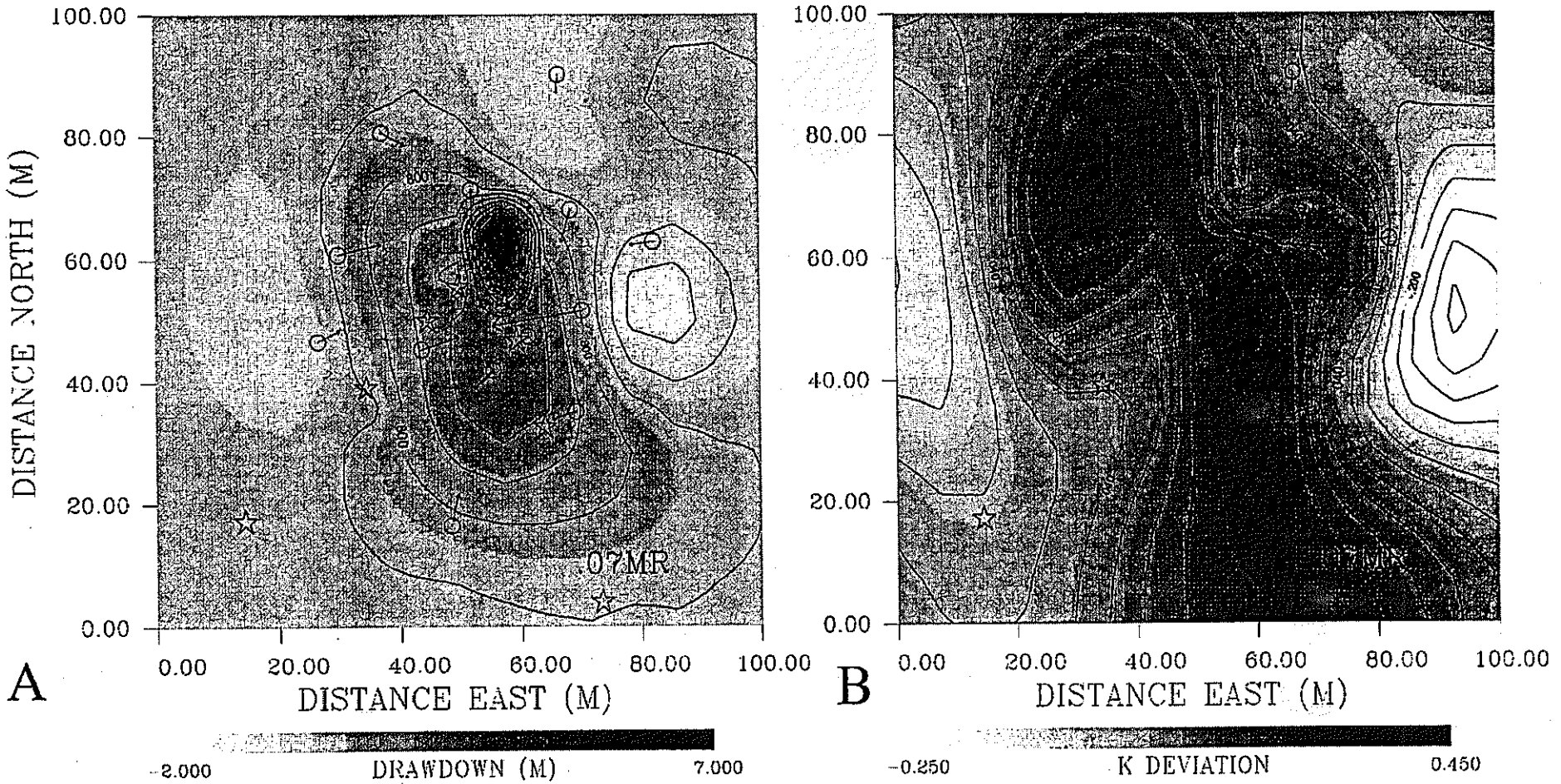

Figure 12

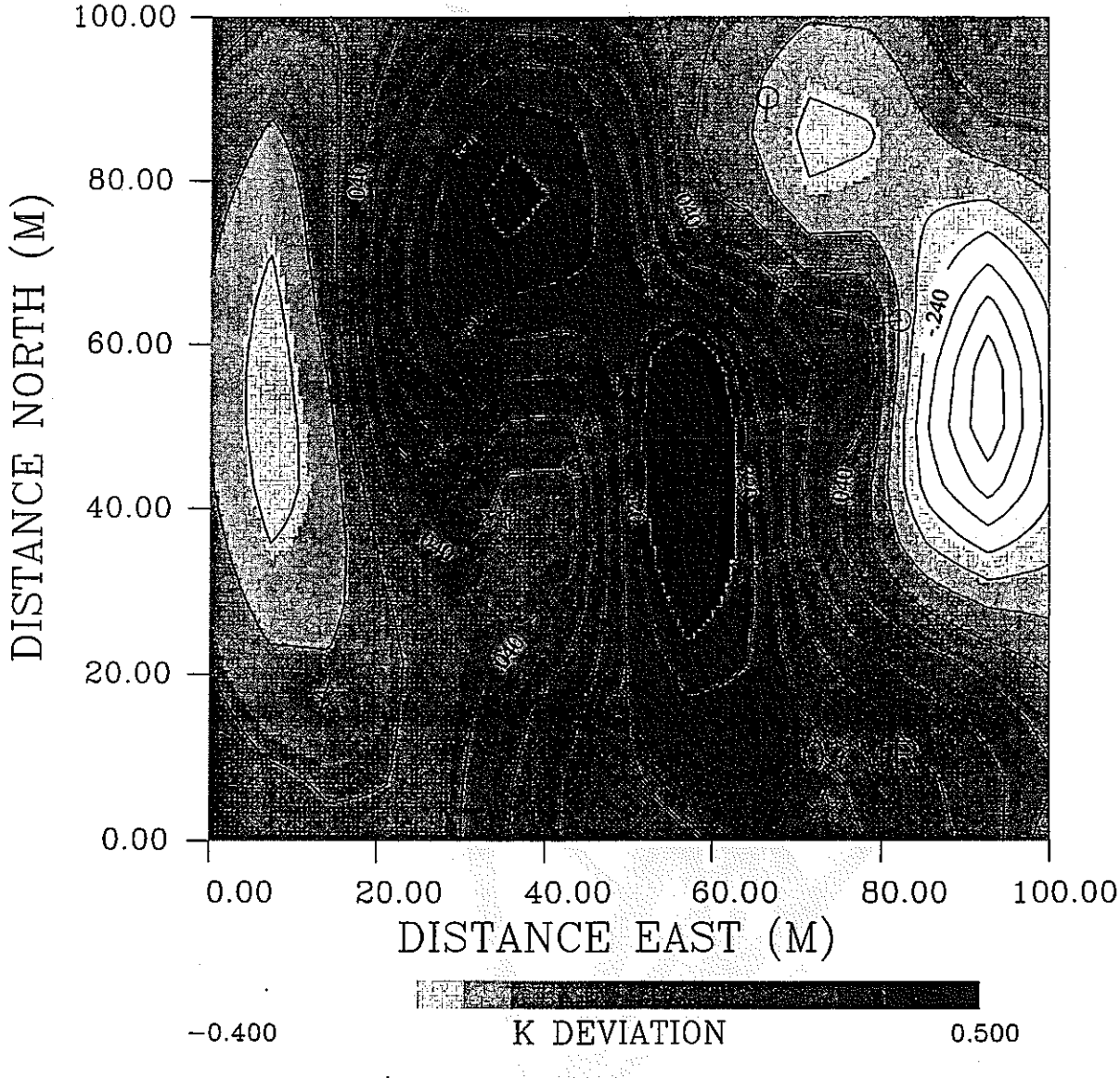
100.00
80.00
60.00
40.00
20.00
0.00
DISTANCE NORTH (M)
0.00
20.00
40.00
60.00
80.00
100.00
DISTANCE EAST (M)
-0.400
K DEVIATION
0.500

Figure 13

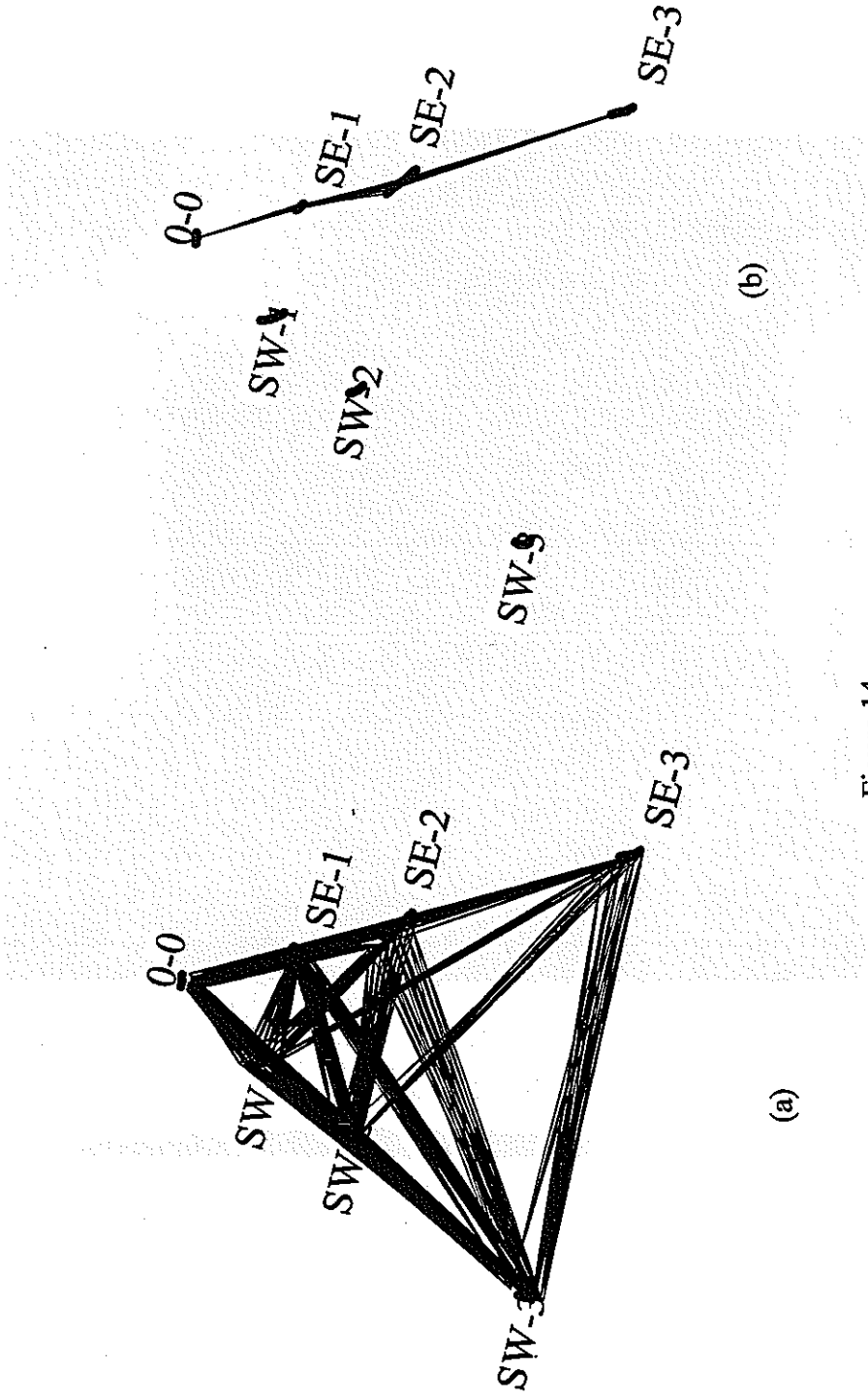

Figure 14

Exactly averaged equations for flow and transport in random media

Mark Shvidler and Kenzi Karasaki

Earth Sciences Division, Lawrence Berkeley National Laboratory, 1 Cyclotron Rd, MS 90-1116, Berkeley, CA 94720;

Abstract

It is well known that exact averaging of the equations of flow and transport in random porous media can be realized only for a small number of special, occasionally exotic, fields. On the other hand, the properties of approximate averaging methods are not yet fully understood. For example, the convergence behavior and the accuracy of truncated perturbation series. Furthermore, the calculation of the high-order perturbations is very complicated. These problems for a long time have stimulated attempts to find the answer for the question: Are there in existence some exact general and sufficiently universal forms of averaged equations? If the answer is positive, there arises the problem of the construction of these equations and analyzing them. There exist many publications related to these problems and oriented on different applications: hydrodynamics, flow and transport in porous media, theory of elasticity, acoustic and electromagnetic waves in random fields, etc. We present a method of finding the general form of exactly averaged equations for flow and transport in random fields by using (1) an assumption of the existence of Green's functions for appropriate stochastic problems, (2) some general properties of the Green's functions, and (3) the some basic information about the random fields of the conductivity, porosity and flow velocity. We present a general form of the exactly averaged non-local equations for the following cases. 1.Steady-state flow with sources in porous media with random conductivity. 2. Transient flow with sources in compressible media with random conductivity and porosity .3. Non-reactive solute transport in random porous media. We discuss the problem of uniqueness and the properties of the non-local averaged equations, for the cases with some types

of symmetry (isotropic, transversal isotropic, orthotropic) and we analyze the hypothesis of the structure non-local equations in general case of stochastically homogeneous fields.

1. INTRODUCTION

Recently the methods of analysis for the flow and transport in random media are finding ever-widening applications in science and technology of various physical processes. It is possible to select an investigation strategy from the following three approaches.

(1) Exact analytical approach: It is well known that exact analytical averaging of the equations of flow and transport in random porous media can be realized only for a small number of special, occasionally exotic, fields.

(2) Numerical approach: Numerically solve appropriate equations for representative sets of realizations of random fields. This approach is so-called the Monte Carlo technique. The information obtained in this way makes it possible to find the highest moments together with computing the local and mean fields of pressure, velocity, etc. However, the exceptionally large volume of calculation and the difficulty for generalizing the results and finding relations between the known and unknown functionals restrict the significance of this approach.

(3) Use of a perturbation technique: Every so often one can use the series expansion of small parameters, which specifies the deviation of some fields from their mean values. This approach usually utilizes analytical techniques. Although it is possible to find many results, it should be pointed out that it involves significant difficulties. Even in problems of comparatively simple structures one can usually find only the first terms of expansions, because the analytical difficulties grow very quickly with the numbers of terms. Moreover, the convergence of the expansions is not very well studied, especially when the deviation is not very small. One approach utilizes the distinctive space scales

for fast oscillating fields as a small parameter. This approach, so-called "homogenization", was largely developed for investigation of processes with periodical structures. Many rigorous results were obtained that justify the method, although the computation of the results is highly laborious. For random structures, which is the focus of the present paper, some results have been obtained but the constructive theory is still absent.

Generally speaking, direct averaging and defining the functionals and the relations between them are exceptionally complicated. However, the fundamental information contained in the local equations and their structure has not been sufficiently utilized. Later we will show that investigation in this direction leads to, for example, finding the forms for relations between averages fields. We show that this is possible in some cases without actually solving appropriate equations but by presupposing only the existence of the solutions and using their general properties.

The following question has for a long time stimulated attempts to find the answer: Are there in existence some exact general and sufficiently universal forms of averaged equations for transport of mass, moment, energy, etc? If the answer is positive, then there arises a quest to construct the equations and to analyze them.

Many publications can be found related to this subject that discuss different applications. They include hydrodynamics, flow and transport in porous media, theory of elasticity, acoustic and electromagnetic waves in random fields (ex.: Batchelor,1953; Monin and Yaglom, 1965, 1967; Tatarsky, 1967; Saffman, 1971; Klyatskin, 1975 ,1980; Shermergor , 1979; Shvidler, 1985;Dagan, 1989; Bakhvalov and Panasenko, 1989; Zhikov et all, 1993; Neuman and Orr , 1993; Indelman and Abramovich, 1994; Indelman, 1996; Teodorovich, 1997; Shvidler and Karasaki, 1999).

We present a method of finding the general form of exactly averaged equations by using (1) an assumption of the existence of random Green's functions for appropriate stochastic problems, (2) some general properties of the Green's functions, and (3) the information about the random fields of the conductivity, porosity and flow velocity. We present a general form of the exactly averaged non-local equations for the following cases: 1. Steady-state flow with sources in porous media with random conductivity, 2. Transient flow with sources in compressible media with random conductivity and porosity, 3. Non-reactive solute transport in random porous media. In this paper we discuss the properties of the non-local averaged equations. The case 1is presented in detail and for other cases we present only the basic results.

We discuss the problem of uniqueness and the properties of the non-local averaged equations for the cases with some type of symmetry (isotropic, transversally isotropic and orthotropic). We also present and analyze the hypothesis used to develop the non-local equations in a general case of stochastically homogeneous fields.

2. STEADY-STATE FLOW WITH SOURCES

We consider the steady flow with sources in a heterogeneous porous unbounded domain. The condition of continuity is given by the equation:

$$\frac{\partial\, v_l(x)}{\partial\, x_l} = f(x) \tag{1}$$

Here $x=(x_1,x_2,x_3)$ is a 3-dimensional vector with components $x_l\,(l=1,2,3)$, the function $f(x)$ is the density of sources and we assume that it is locally integrable function, $v(x)$ is the Darcy's velocity vector.

The local Darcy's equation we present in conservative form as condition for momentum.

$$\sigma^{-1}(x)v(x)+\nabla u(x)=0 \tag{2}$$

Here $\sigma(x)=\{\sigma_{lm}(x)\}$ is the second rank conductivity tensor symmetric by subscripts. We assume that it is positive definite, local tensor, that is for any x and vector ξ, the elliptic condition is satisfied.

$$\xi_m \sigma_{lm}(x)\xi_l \geq \vartheta|\xi|^2, \quad (\vartheta>0) \tag{3}$$

For the pressure or head $u(x)$ we assume the condition

$$u(x)=0 \text{ for } |x|\to\infty \tag{4}$$

3. STOCHASTIC FORMULATION

We assume that the tensor $\sigma(x)$ is a stochastically homogeneous random field. That is, for any vector x and an arbitrary vector h, the all finite-dimensional probability distributions for random field $\sigma(x+h)$ doesn't depend on the arbitrary vector h. Let $f(x)$ be a non-random sources density function. We introduce the random Green's function $g(x,y)$ for the problem described (1), (2) and (4), so that $g(x,y)$ satisfies the following equations:

$$\frac{\partial}{\partial x_m}\left[\sigma_{lm}(x)\frac{\partial g(x,y)}{\partial x_l}\right]=-\delta(x-y) \tag{5}$$

$$g(x,y)=0 \text{ for } |x|\to\infty \tag{6}$$

In the general case we can now write the solution for the problem (1), (2) and (4):

$$u(x)=\int g(x,y)\, f(y)\, dy^3 \tag{7}$$

where $dy^3 = dy_1\, dy_2\, dy_3$ and the integration is over the all unbounded 3-D space.

We introduce the averaged fields over the ensemble of realization of the random function $\sigma(x)$:

$$U(x)=\langle u(x)\rangle, V(x)=\langle v(x)\rangle, G(x,y)=\langle g(x,y)\rangle \tag{8}$$

As long as $\sigma(x)$ is a stochastically homogeneous field, the mean Green's function is invariant over translation in space, and therefore. depends on the difference x-y. Hence we have:

$$U(x)=\int G(x-y)f(y)d\,y^3 \tag{9}$$

Averaging the equation (2) we have

$$V_i(x)=\int \Gamma_i(x-y)f(y)dy^3 \tag{10}$$

where

$$\Gamma_i(x-y)=-\left\langle \sigma_{ij}(x)\ \frac{\partial\ g(x,y)}{\partial\ x_j}\right\rangle \tag{11}$$

We shall call the vector $\Gamma(x-y)$ the mean Green's velocity. By substituting (10) into equation (1) we find the relation of compatibility for components $\Gamma_i(x-y)$:

$$\frac{\partial\ \Gamma_i(x-y)}{\partial\ x_i}=\delta(x-y) \tag{12}$$

Therefore, the mean pressure $U(x)$ and the mean velocity $V_i(x)$ are convolution integrals for source density $f(x)$ and the mean Green's function $G(x-y)$ and the vector-function $\Gamma(x-y)$, respectively.

The equations (9) , (10) and the averaged equation of (1):

$$\frac{\partial V_l(x)}{\partial x_l} = f(x) \tag{13}$$

make up the closed system of equations for averaged fields $U(x)$ and $V(x)$. This system contains the kernels, $G(x-y)$ and $\Gamma(x-y)$, that are non-random functional from the random conductivity field $\sigma(x)$ and the random Green's function $g(x,y)$. Of course, the explicit definition of the functionals G and Γ is very difficult to obtain in the general case(for any random field $\sigma(x)$). For now the existence of these functionals in itself is significant. There is a possibility to determine some of their features that help find a general form of the averaged equations of which the equations (9), (10) and (13) are a part of. Later we will find them in different forms.

3. FOURIER ANALYSIS

We consider the Fourier transform T_F and inverse Fourier transform T_F^{-1} for analyzing the equations with convolutions in all space.

$$T_F\left[\varphi(x)\right] = \overline{\varphi}(k) = \int \exp\left[-2\pi j(x\cdot k)\right]\varphi(x)\,dx^3 \tag{14}$$

$$T_F^{-1}\left(\overline{\varphi}(k)\right) = \varphi(x) = \int \exp\left[2\pi j(k\cdot x)\right]\overline{\varphi}(k)\,dk^3 \tag{15}$$

where $j = \sqrt{-1}$.

Applying T_F to equations (9), (10), (12) and (13) we have the linear algebraic equations in *k*-space:

$$\overline{U}(k) = \overline{G}(k)\,\overline{f}(k) \tag{16}$$

$$\overline{V}_l(k) = \overline{\Gamma}_l(k)\;\overline{f}(k) \tag{17}$$

$$2\pi jk_l\bar{\Gamma}_l(k)=1 \tag{18}$$

$$2\pi jk_l\bar{V}_l(k)=\bar{f}(k) \tag{19}$$

After eliminating $\bar{f}(k)$ from equations (16) and (17) we find the equation that bind the scalar field $\bar{U}(k)$ and the vector field $\bar{V}(k)$:

$$\bar{V}_l(k)=\bar{\Pi}_l(k)\ \ \bar{U}(k) \tag{20}$$

where

$$\bar{\Pi}_l(k)=\bar{\Gamma}_l(k)\bar{G}^{-1}(k) \tag{21}$$

From (18) and (21) we obtain the condition of compatibility the components vector $\bar{\Pi}(k)$:

$$2\pi ik_l\bar{\Pi}_l(k)=\bar{G}^{-1}(k) \tag{22}$$

The scalar function $G(x-y)=G(y-x)$ and the vector-function $\Gamma(x-y)=-\Gamma(y-x)$ and their Fourier transformations $\bar{G}(k)$ and $\bar{\Gamma}(k)$ are real- even and imaginary- odd functions of k respectively.

The equations (20) and (16) are a closed system with respect to functions $\bar{U}(k)$ and $\bar{V}_l(k)$. By applying the T_F^{-1} transform to (20), we can write the convolution equation:

$$V_l(x)=-\int\Pi_l(x-y)U(y)dy^3 \tag{23}$$

Thus the equation (23) connect $V(x)$, the mean velocity at point x, and the distribution of $U(y)$ in all space with the help of the vector-operator $\Pi(x-y)$:

$$\Pi_l(x)=\int\Gamma_l(x-y)Q(y)dy^3 \tag{24}$$

here

$$Q(x)=\mathrm{T}_F^{-1}\left[\bar{G}^{-1}(k)\right] \tag{25}$$

is an even real function. It is obvious that $\Pi_l(x)$ is an odd real function. Obviously, the kernel-vector $\Pi(x-y)$ is a non-random mapping for the random field $\sigma(x)$ and does not depend on the source density, $f(x)$. If the vector field of the mean velocity $V(x)$ and the scalar field $U(x)$ describe one averaged flow process in one unbounded stochastic homogeneous system, the kernel-vector $\Pi(x-y)$ is the unique operator that realizes (describes) in x-space the linear relation between them in the form of (23). In k-space it becomes the vector-function $\bar{\Pi}(k)$. Note that in the singular case of non-random conductivity $\sigma_{lm}(x)=\sigma\delta_{lm}$, where $\sigma=const$, the kernel-vectors $\Pi_l(x-y)$ and $\bar{\Pi}_l(k)$ are:

$$\bar{G}(k)=\left(4\sigma\pi^2k^2\right)^{-1},\ \bar{\Gamma}_l(k)=-\sigma jk_l/2\pi k^2,\ \text{and}\ \bar{\Pi}_l(k)=-2\sigma\pi jk_l, \tag{26}$$

$$\Pi_l(x-y)=-\sigma\frac{\partial\delta(x-y)}{\partial x_l} \tag{27}$$

It easy to see that the exact averaged equation (20) is reversible. If we know the field $\bar{U}(k)$, from (20) we can directly define the field $\bar{V}(k)$ and vice versa. From (20) for any l, if we know the field $\bar{V}_l(k)$, we can write $\bar{U}(k)=\bar{V}_l(k)/\bar{\Pi}_l(k)$.

4. GLOBAL SYMMETRY

We continue the analysis of the averaged equations and assume that the random field $\sigma(x)$ satisfies some symmetry conditions that are related to the structural properties of the field as a whole. We shall call this type of symmetry global.

ISOTROPY: Let the random conductivity tensor $\sigma(x)$ be an isotropic field. In this case the imaginary vector $\overline{\Pi}(k)$ in any orthogonal coordinate system is proportional to vector $2\pi jk$. It is invariant for any rotation and reflection on coordinate planes $k_l = 0$ and depends on $|k|$ only. We can write

$$\overline{\Pi}_l^{(i)}(k) = -\overline{\Pi}_{*l}^{(i)}(|k|)2\pi jk_l \tag{28}$$

where $\Pi_{*l}^{(i)}(|k|)$ is scalar and positive even function, such that $\overline{\Pi}_{*1}^{(i)} = \overline{\Pi}_{*2}^{(i)} = \overline{\Pi}_{*3}^{(i)} = \overline{\Pi}_{*}^{(i)}$.

Then

$$\overline{V}_l(k) = -\mathrm{B}_{lm}^{(i)}(k)2\pi jk_m\overline{U}(k) \tag{29}$$

$$\overline{\mathrm{B}}_{lm}^{(i)}(k) = \Pi_{*}^{(i)}(|k|)\delta_{lm} \tag{30}$$

and therefore in x-space we have the relations:

$$V_l(x) = -\int \mathrm{B}_{lm}^{(i)}(|x-y|)\frac{\partial U(y)}{\partial y_m}dy^3 \tag{31}$$

$$V_l(x) = -\int \Pi_{*}^{(i)}(|x-y|)\frac{\partial U(y)}{\partial y_l}dy^3 \tag{32}$$

ORTHOTROPY: If the field $\sigma(x)$ is orthotropic then there exists an orthogonal coordinate system such all the stochastic multipoint moments of the random field are invariant to the reflection in the planes $k_l = 0$. In this case the components $\overline{\Pi}_l(k)$ can be written as

$$\overline{\Pi}_l^{(o)}(k) = -\overline{\Pi}_{*l}^{(o)}(k)2\pi jk_l \tag{33}$$

where summation over l is not implied. $\overline{\Pi}^{(o)}_{*l}(k)$ are positive and even functions of k that depends on $|k_1|,|k_2|,|k_3|$. In orthotropic system the averaged equations are in the forms:

$$\overline{V}_l(k) = -\overline{\Pi}^{(o)}_{*l}(k) 2\pi j k_l \overline{U}(k) \tag{34}$$

(no summation over l!)

$$\overline{V}_l(k) = -\overline{\mathrm{B}}^{(o)}_{ml}(k) 2\pi j k_m \overline{U}(k) \tag{35}$$

The components tensor $\overline{\mathrm{B}}^{(o)}$ takes the form:

$$\overline{\mathrm{B}}^{(o)}_{ml} = \delta_{ml} \overline{\Pi}^{(o)}_{*m}(k) \tag{36}$$

which means that the tensor $\overline{\mathrm{B}}^{(o)}$ is diagonal. Evidently the equations (34) and (35) are reversible and the averaged conservative equation has the form:

$$-2\pi k_l \overline{U}(k) = \overline{R}^{(o)}_{ml} \overline{V}_m(k) \tag{37}$$

where $\overline{R}^{(o)} = \left[\overline{\mathrm{B}}^{(o)}\right]^{-1}$ is the diagonal tensor of resistance.

TRANSVERSAL ISOTROPY: In the case of transversal isotropy, it is invariant relative to the rotation around one axes of coordinate system, for example, k_3 , and reflection on any plates $k_l = 0$, we have $\overline{\Pi}^{(t)}_{*1} = \overline{\Pi}^{(t)}_{*2} \neq \overline{\Pi}^{(t)}_{*3}$, where scalar functions $\overline{\Pi}^{(t)}_{*l}(k)$ depend on invariant corresponding rotation and reflections. In this case of symmetry,

$$\overline{\Pi}^{(t)}_{l}(k) = -\overline{\Pi}^{(t)}_{*l}(k) 2\pi j k_l \tag{38}$$

(no summation over l!), where the function $\overline{\Pi}^{(t)}_{*l}(k)$ is positive and even on k, that depends on $\left(k_1^2 + k_2^2\right)^{1/2}, |k_1|, |k_2|, |k_3|$. In the transversal isotropic system the averaged equations are:

$$\overline{V}_l(k) = -\overline{\Pi}^{(l)}_{*l} 2\pi j k_l \overline{U}(k) \tag{39}$$

$$\overline{V}_l(k) = -\overline{\mathrm{B}}^{(l)}_{ml}(k) 2\pi j k_m \overline{U}(k) \tag{40}$$

where the components of the tensor $\overline{\mathrm{B}}^{(l)}$ are:

$$\overline{\mathrm{B}}^{(l)}_{ml}(k) = \delta_{ml} \overline{\Pi}^{(l)}_{*m}(k) \tag{41}$$

It easy see that tensor $\overline{\mathrm{B}}^{(l)}$ is diagonal and $\overline{\mathrm{B}}^{(l)}_{11}(k) = \overline{\mathrm{B}}^{(l)}_{22}(k) \neq \overline{\mathrm{B}}^{(l)}_{33}(k)$. The averaged equation (40) is reversable.

In summary, for any orthogonal coordinate systems in the case of isotropy the averaged equation is reversible and the tensor $\overline{\mathrm{B}}^{(i)}(k)$ is spherical. In the case of transversal isotropy if the orthogonal coordinate system is oriented so that one of the axes, for example, k_3 coincides with the axis of rotation, and the other two are oriented arbitrarily, the averaged equation is reversable, the tensor $\overline{\mathrm{B}}^{(t)}(k)$ is diagonal, and $\overline{\mathrm{B}}^{(t)}_{11}(k) = \overline{\mathrm{B}}^{(t)}_{22}(k) \neq \overline{\mathrm{B}}^{(t)}_{33}(k)$. Finally, in the case of orthotropy, if the axes of the orthogonal coordinate system are the orthotropy axes, the averaged equation, too, is reversible and the tensor $\overline{\mathrm{B}}^{(o)}(k)$ is diagonal. However, it is well to bear in mind that in each of the studied cases of symmetry, the components of the tensors $\overline{\mathrm{B}}^{(\alpha)}(k)$, where $\alpha = i,t,o$, remain invariant related to the superscript α. Therefore, in all three basic cases of symmetry $(\alpha = i,t,o)$ for a suitable orientation of the coordinate axes the averaged equation is

$$\overline{V}^{(\alpha)}_l(k) = -\overline{\mathrm{B}}^{(\alpha)}_{ml}(k) 2\pi j k_m \overline{U}(k) \tag{42}$$

$$\overline{\mathrm{B}}^{(\alpha)}_{ml}(k) = \delta_{ml} \overline{\Pi}^{(\alpha)}_{m}(k) \tag{43}$$

(no summations assumed in (43) over subscript m!)

Because $\overline{\Pi}_l(k)$ are imaginary and odd functions of vector k, the diagonal components of tensor $\mathrm{B}^{(\alpha)}(k)$ are even and real functions. Now we write the component $\overline{\mathrm{B}}_{ll}^{(\alpha)}(k)$ in the following form:

$$\overline{\mathrm{B}}_{ll}^{(\alpha)}(k)=\overline{\mathrm{B}}_{ll}^{(\alpha)}(0)\overline{F}_{ll}^{(\alpha)}(z) \tag{44}$$

Here $\overline{F}_{ll}^{(\alpha)}(z_1,z_2,z_3)$ is a dimensionless function of the dimensionless variables $z_l=\Delta_l k_l$, where Δ_l are linear scales of the random field $\sigma(x)$, for example, the correlation scales. It is evident that $\overline{F}_{ll}^{(\alpha)}(0)=1$. Expanding the function $\overline{F}_{ll}^{(\alpha)}(z)$ in a Taylor series we can write:

$$\overline{\mathrm{B}}_{ll}^{(\alpha)}(k)=\overline{\mathrm{B}}_{ll}^{(\alpha)}(0)\sum_{n=n_1+n_2+n_3=0}^{\infty}\frac{1}{n!}\frac{\partial\overline{F}_{ll}^{(\alpha)}(0)}{\partial z_1^{n_1}\partial z_2^{n_2}\partial z_3^{n_3}}k_1^{n_1}k_2^{n_2}k_3^{n_3}\Delta_1^{n_1}\Delta_2^{n_2}\Delta_3^{n_3} \tag{45}$$

Substituting (45) into (42) and taking into account that all the odd derivatives of $\overline{F}_{ll}^{(\alpha)}(z)$ at z=0 are zero, we can write the expansions for the mean velocity $V_l^{(\alpha)}(x)$ in x-space:

$$V_l^{(\alpha)}(x)=-\overline{\mathrm{B}}_{ll}^{(\alpha)}(0)\sum_{n=n_1+n_2+n_3=0}^{\infty}\frac{(-1)^n\Delta_1^{2n_1}\Delta_2^{2n_2}\Delta_3^{2n_3}}{(2n)!(2\pi)^{2n}}\frac{\partial^{2n}\overline{F}_{ll}^{(\alpha)}(0)}{\partial z_1^{2n_1}\partial z_2^{2n_2}\partial z_3^{2n_3}}\frac{\partial^{2n+1}U(x)}{\partial x_l\partial x_1^{2n_1}\partial x_2^{2n_2}\partial x_3^{2n_3}} \tag{46}$$

$$V_l^{(\alpha)}(x)=-\overline{\mathrm{B}}_{ll}^{(\alpha)}(0)\sum_{n=n_1+n_2+n_3=0}^{\infty}\frac{\Delta_1^{2n_1}\Delta_2^{2n_2}\Delta_3^{2n_3}\mathrm{I}_{ll,n}^{(\alpha)}(n_1,n_2,n_3)}{(2n)!}\frac{\partial^{2n+1}U(x)}{\partial x_l\partial x_1^{2n_1}\partial x_2^{2n_2}\partial x_3^{2n_3}} \tag{47}$$

where the power moment $\mathrm{I}_{ll,n}^{(\alpha)}(n_1,n_2,n_3)=\int z_1^{2n_1}z_2^{2n_2}z_3^{2n_3}F_{ll}^{(\alpha)}(z)\,dz^3$ and $\mathrm{I}_{ll,0}^{(\alpha)}(0,0,0)=1$. The important question is: What is the behavior of the expansions (46) or (47) in the limiting case when $\Delta_l\to 0$ that correspond to the theory of homogenization and the concept of effective conductivity (see Bakhvalov and Panasenko, 1984; *Zhikov et all*, 1993)? We should note that in the first terms of both expansions (n=0) the coefficients of the derivatives do not contain Δ_l

explicitly. By setting some restrictions to the source density $f(x)$, the behavior the oldest derivatives of $U(x)$ can be sufficiently limited. All the other terms of these expansions tend to zero for $\Delta_l \to 0$. In this case we have the averaged equation:

$$V_l^{(\alpha)}(x) = -\overline{B}_{ll}^{(\alpha)}(0)\frac{\partial U(x)}{\partial x_l} \tag{48}$$

where $\overline{B}_{ll}^{(\alpha)}(0)$ are the diagonal components of the effective conductivity tensor. Notice that according to the theory of homogenization the tensor of the effective conductivity exists and is constant in all Euclidian space R^3. This is true if, for any limited domain $Q \in R^3$, the source density function $f(x)$ belongs to Sobolev`s functional space $H^{-1}(Q)$, or for example belongs to the square integrable functional space $L^2(Q)$, that is embedded in $H^{-1}(Q)$ space. Furthermore, if in any orthogonal coordinate system the tensor of the local random conductivity is symmetric and positive definite, the tensor of the effective conductivity is also symmetric and positive definite, so-called elliptic, (*Zhikov at all,* 1993). The principal part of the expansions (46) and (47) corresponds with the theory of homogenization limit and can be used for computing the effective conductivity. In the cases of symmetry: isotropic $(\alpha = i)$, transversal isotropy $(\alpha = t)$ and orthotropy $(\alpha = o)$, the averaged equation has the form:

$$V^{(\alpha)}(x) = -B_*^{(\alpha)}\nabla U(x) \tag{49}$$

where the diagonal tensor of the effective conductivity is $B_{ml*}^{(\alpha)} = \delta_{ml}\overline{B}_{ll}^{(\alpha)}(0)$ or

$$B_*^{(\alpha)} = \begin{pmatrix} \overline{B}_{11}^{(\alpha)}(0) & 0 & 0 \\ 0 & \overline{B}_{22}^{(\alpha)}(0) & 0 \\ 0 & 0 & \overline{B}_{33}^{(\alpha)}(0) \end{pmatrix} \tag{50}$$

Obviously the principal axes for the both tensors $\overline{\mathrm{B}}^{(\alpha)}(k)$ and $\mathrm{B}_*^{(\alpha)}$ are identical to the coordinate axes.

Up to this point we have studied the fields with some symmetry in special orthogonal coordinate systems. If the orthogonal coordinate axes x_l' and k_l' are oriented arbitrarily and β_{lm} is the cosine of the angle between the axes x_l' and x_m, the effective conductivity tensor in the new coordinate system is $\mathrm{B}_*'^{(\alpha)} = \beta\,\mathrm{B}_*^{(\alpha)}\beta^{-1}$. This tensor is symmetric and positive definite (elliptic). The averaged equation in the arbitrary coordinate system x_l' has the form $V'^{(\alpha)}(x') = -\mathrm{B}_*'^{(\alpha)}\nabla U(x')$. But what if the diagonal tensor $\mathrm{B}_*^{(\alpha)}$ is unknown? Or to put it more precisely, what if we know that there exists some symmetry but the orientation of the principal axes is not known nor the parameter α? In this case we study again the vector $\overline{\Pi}_l(k')$ and its Taylor expansion around $k'=0$:

$$\overline{\Pi}_l(k') = \sum_{n=n_1+n_2+n_3=0}^{\infty} \frac{1}{n!}\frac{\partial \overline{\Pi}_l^n(0)}{\partial k_1'^{n_1}\partial k_2'^{n_2}\partial k_3'^{n_3}} k_1'^{n_1}k_2'^{n_2}k_3'^{n_3} \tag{51}$$

The component $\overline{\Pi}_l(k')$ is an odd function of $\tilde{k}$ and therefore at point $k'=0$ all even derivatives are zero. Thus

$$\overline{\Pi}_l(k') = \sum_{2n-1=n_1+n_2+n_3=1}^{\infty} \frac{1}{(2n-1)!}\frac{\partial^{2n-1}\overline{\Pi}_l(0)}{\partial k_1'^{n_1}\partial k_2'^{n_2}\partial k_3'^{n_3}} k_1'^{n_1}k_2'^{n_2}k_3'^{n_3} \tag{52}$$

The linear on variable k' part of this expansion is:

$$\overline{\Pi}_l^{(1)}(k') = \frac{\partial \overline{\Pi}_l(0)}{\partial k_m'} k_m' \tag{53}$$

We can write the linear approximation on k' for $\overline{V}_l(k')$:

$$\bar{V}_l^1(k') = -\left[-\frac{1}{2\pi j}\frac{\partial \bar{\Pi}_l(0)}{\partial k'_m}\right] 2\pi j k'_m \bar{U}(k) \tag{54}$$

By imposing some restrictions on the density $f(x)$ as discussed earlier, the oldest terms of the expansions of $\bar{V}_l(k')$ vanish in the homogenization limit. In this case we have the averaged equation:

$$V_l(x) = -\mathrm{B}'_{ml*}\frac{\partial U(x')}{\partial x'_m} \tag{55}$$

and from (54) we find the symmetric and positive definite real tensor of effective conductivity:

$$\mathrm{B}'_{ml*} = -\frac{1}{2\pi j}\frac{\partial \bar{\Pi}_l(0)}{\partial k'_m} \tag{56}$$

Thus, if we know the components $\bar{\Pi}_l(k')$, we can find the effective conductivity tensor and by using the standard method we can find its real eigenvalues and the orthogonal eigenvectors. Transition to a new eigen orthogonal system that is associated with the eigenvectors and transformation of the tensor B'_{ml*} to the new coordinates lead to a diagonal tensor B_{ml*} whose components are the eigenvalues tensor B'_{ml*}. As we mentioned earlier in the new eigen coordinate system the tensor $\bar{\mathrm{B}}_{ml}(k)$ is diagonal with the following components:

$$\bar{\mathrm{B}}_{ll}(k) = -\bar{\Pi}_l(k)/2\pi j k_l \tag{57}$$

5. ALTERNATIVE APPROACH

Majority of the past works related to the present subject used a different approach. From the outset they want to find the relation between the averaged flow velocity field and the gradient of mean pressure(head). To examine the validity of this approach we return to equation (20) again.

To recast it to the form like the *Darcy's* Law we introduce some tensor $\overline{K}_{lm}(k)$ that satisfies the equation:

$$\overline{\Pi}_l(k) = -\overline{K}_{ml}(k) 2\pi j k_m \tag{58}$$

and inserting (58) into (22), the condition of compatibility components vector $\overline{\Pi}(k)$, we obtain:

$$4\pi^2 \overline{G}(k) k_l \overline{K}_{ml}(k) k_m = 1 \tag{59}$$

It should be noted that this relation is not proven that the tensor $\overline{K}_{ml}(k)$ is elliptic, although it doesn't contradict that, because the factors –components k_l and k_m in (59)– are non-arbitrary.

The definition of $\overline{\mathrm{B}}_{ml}(k)$ with the system (58) for any k leads to three algebraic equations with nine unknown components. In x-space this problem amounts to three differential equations with nine unknown function-components. The both systems are non-closed and in general have unlimited sets of solutions. On the other hand, in the cases of global symmetry as shown above, the number of unknown functions reduce to three or less and it is possible to find a unique solution, the diagonal tensor $\overline{\mathrm{B}}_*(k)$. Even if there is no reason to believe that the types of the global symmetry discussed above exist, the fact remains that if the stochastically homogeneous field of the local random conductivity tensor $\sigma_{ml}(x)$ is symmetric and elliptic, the tensor of the effective conductivity $\overline{\mathrm{B}}_{ml}(0)$ is symmetric and elliptic as well. In this general case the eigen orthogonal coordinate system exists in which the tensor $\overline{\mathrm{B}}(0)$ is diagonal.

Now we will formulate **the hypothesis that for stochastically homogeneous fields in the eigen coordinate system for any *k*, the tensor $\overline{\mathrm{B}}(k)$ is also diagonal.** Note that in this case we have from (58):

$$\hat{\bar{B}}_{ll}(k) = -\bar{\Pi}_l(k)/2\pi j k_l, \hat{\bar{B}}_{ml}(k) = 0 \; if \; m \neq l \tag{60}$$

This solution is exact and unique with the formulated constraints.

Note that if we use any orthogonal coordinate system k_l'' that is different from the eigen system, and write:

$$\bar{B}_{ll}(k'') = -\bar{\Pi}_l(k'')/2\pi j k_l'', \bar{B}_{lm}(k'') = 0 \; if \; l \neq m \tag{61}$$

which is also a solution of system (58), we find that the limit of $\bar{B}_{ll}(k'')$ does not exist when $k'' \to 0$. In fact, inserting the linear part of expansion $\bar{\Pi}_l(k'')$ in the form of (53) into (61), we have:

$$\bar{B}_{ll}(k'') = \frac{1}{2\pi j}\frac{\partial \bar{\Pi}_l(k'')}{\partial k_m''}\frac{k_m''}{k_l''} \tag{62}$$

Here, the summation over m is implied! Because $\frac{\partial \bar{\Pi}_l(k'')}{\partial k_m''} \neq 0$ for $l \neq m$ and because the k_l'' coordinate system is not eigen, as $k'' \to 0$ the $\lim \bar{B}_{ll}(k'')$ does not exist.

6. NON-STEADY TRANSIENT FLOW WITH SOURCES

Let us consider the stochastic system of equations in a three-dimensional unbounded domain:

$$\frac{\partial m(x,t)}{\partial t} + \frac{\partial v_l(x,t)}{\partial x_l} = f(x,t) \tag{63}$$

$$m(x,t) = \alpha(x)u(x,t) \tag{64}$$

$$v_l(x,t) = -\sigma_{lj}(x)\frac{\partial u(x,t)}{\partial x_j} \tag{65}$$

$$u(x,t_0)=0 \tag{66}$$

Here $\alpha(x)$ and $\sigma(x)$ are statistically homogeneous random fields of the storage capacity and conductivity, respectively, and $u(x,t)$ is the pressure. We introduce the random Green's function $g(x,t,y,\tau)$, that is the solution to the system (63)-(66) for $f(x,t)=\delta(x-y)\delta(t-\tau)$. Let us introduce:

$$G(x-y,t-\tau)=\langle g(x,t,y,\tau)\rangle \tag{67}$$

$$N(x-y,t-\tau)=\langle \alpha(x)g(x,t,y,\tau)\rangle \tag{68}$$

$$\Gamma_l(x-y,t-\tau)=-\left\langle \sigma_{lj}(x)\frac{\partial\ g(x,t,y,\tau)}{\partial\ x_j}\right\rangle \tag{69}$$

We consider T_{FL} and T_{FL}^{-1}- the direct and inverse Fourier-Laplace transforms and use the following designations:

$$\bar{G}(k,\mu)=T_{FL}G,\quad \bar{N}(k,\mu)=T_{FL}N,\quad \bar{\Gamma}_l(k,\mu)=T_{FL}\Gamma_l \tag{70}$$

and introduce the following scalar function and vector:

$$\bar{S}(k,\mu)=\bar{N}(k,\mu)\bar{G}^{-1}(k,\mu),\quad \bar{\Pi}_l(k,\mu)=\bar{\Gamma}_l(k,\mu)\bar{G}^{-1}(k,\mu) \tag{71}$$

It easy to show that $\mu\bar{N}(k,\mu)+2\pi ik_l\bar{\Pi}_l(k,\mu)=\bar{G}^{-1}(k,\mu)$. Thus, the averaged system is

$$\frac{\partial M(x,t)}{\partial t}+\frac{\partial V_l(x,t)}{\partial x_l}=f(x,t) \tag{72}$$

$$M(x,t)=\int_{t_0}^{t}\int S(x-y,t-\tau)U(y,\tau)dy^3d\tau \tag{73}$$

$$V_l(x,t) = -\int_{t_0}^{t}\int \Pi_l(x-y,\, t-\tau)U(y,\tau)\,dy^3\,d\tau \tag{74}$$

$$U(x,t_0) = 0 \tag{75}$$

here

$U(x,t) = \langle u(x,t)\rangle$, $V_l(x,t) = \langle v_l(x,t)\rangle$, $M(x,t) = \langle m(x,t)\rangle$, $S(x,t) = T_{FL}^{-1}\,\overline{S}(k,\mu)$, and $\Pi(x,t) = T_{FL}^{-1}\overline{\Pi}(k,\mu)$.

7. NON-REACTIVE SOLUTE TRANSPORT

We consider the stochastic system of equations in a three dimensional unbounded domain:

$$\frac{\partial\, a(x,t)}{\partial t} + \frac{\partial\, q_l(x,t)}{\partial x_l} = f(x,t) \tag{76}$$

$$a(x,t) = \theta(x)c(x,t) \tag{77}$$

$$q_l(x,t) = v_l(x,t)c(x,t) - D_{lj}\frac{\partial c(x,t)}{\partial x_j} \tag{78}$$

$$c(x,t_0) = 0 \tag{79}$$

$$G_c(x-y,t-\tau) = \langle g_c\rangle,\ B(x-y,t-\tau) = \langle \theta(x)g_c\rangle,\ P_l(x-y,t-\tau) = \langle v_l(x)g_c\rangle \tag{80}$$

$$\overline{G}_c(k,\mu) = T_{FL}G_c,\ \overline{B}(k,\mu) = T_{FL}B,\ \overline{P}_l(k,\mu) = T_{FL}P_l,\ \overline{R}(k,\mu) = \overline{B}\overline{G}^{-1},\ \overline{W}_l(k,\mu) = \overline{P}_l\overline{G}^{-1}$$

It easy to show that $\mu\overline{R} + 2\pi i k_l \overline{W}_l = \overline{G}^{-1}$ Thus, the averaged system is:

$$\frac{\partial\ A(x,t)}{\partial\ t} + \frac{\partial\ Q_l(x,t)}{\partial x_l} = f(x,t) \tag{81}$$

$$A(x,t)=\int_{t_0}^{t}\int R(x-y,t-\tau)\;\; C(y,\tau)\;\; dy^3 d\tau \tag{82}$$

$$Q_l(x,t)=\int_{t_0}^{t}\int W_l(x-y,t-\tau)C(y,\tau)dy^3 d\tau \;\; -D_{lj}\frac{\partial\;\; C(x,t)}{\partial x_j} \tag{83}$$

$$C(x,t_0)=0 \tag{84}$$

Here

$$C(x,t)=\langle c(x,t)\rangle, Q_l(x,t)=\langle q_l(x,t)\rangle, R(x,t)=T_{FL}^{-1}\overline{R}(k,\mu), W_l(x,t)=T_{FL}^{-1}\overline{W}_l(k,\mu) \tag{85}$$

8. SUMMARY

We have described a general form of the exactly averaged equations of flow and transport in a stochastically homogeneous unbounded field with sources. We examined the correctness of the averaged descriptions for given fields and the generalized law for non-local models. A variant of the generalization for a given field with a unique kernel-vector and a kernel-tensor was presented. We discussed the problem of uniqueness and the properties of the non-local averaged equations for three types of global symmetry: namely, isotropic, transversal isotropic, and orthotropic. We have formulated a hypothesis of the structure for non-local equations in the general case of stochastically homogeneous fields.

ACKNOWLEDGEMENTS

The authors would like to thank Dr. Dmitri Silin for his constructive comments. This work was supported by JNC (Japan Nuclear Cycle Development Institute). This work was conducted under the US Department of Energy Contract No. DE-AC03-76SF00098.

REFERENCES

Bakhvalov, N.S., and G.P.Panasenko, Osrednenie Processov v Periodicheskich Sredach: Mathematicheskie Zadachi Mekhaniki Kompozitsionnykh Materialov, (In Russian)M., Nauka, 1984, English: Homogenization: Averaging Processes in Periodic Media; Mathematical Problems in the Mechanics of Composite Material, Kluwer Academic, Dordrecht: Boston, MA, 1989.

Dagan, G., Flow and Transport in Porous Formations, Springer-Verlag, 1989.

Indelman, P., and B.Abramovich. Nonlocal properties of nonuniform averaged flows in heterogeneous media, Water Resour.Res.,3385-3393, 1994.

Indelman, P., Averaging of unsteady flows in heterogeneous media of stationary conductivity, J. Fluid Mech.,**310**, 39-60, 1996.

Klyatskin, V.I., Statistical Description of Dynamical System With Random Parameters (In Russian), Nauka, 1975.

Klyatskin, V.I., Stochastic Equations and Wave in Random Heterogeneity Media.(In Russian), Nauka, 1980.

Monin, A.S. and A.M. Yaglom, Statisticheskaia Gidromekhanika: Mekhanika Turbulentnosti, (In Russian), M. Nauka, 1965-1967, 2v. English: Statistical Fluid Mecanics; Mechanics of Turbulence, Cambridge, MA, MIT Press, (1971-1975) 2v.

Neuman, S.P., and S.Orr, Prediction of steady state flow in nonuniform geologic media by conditional moments: Exact nonlocal formalism, effective conductivities, and weak approximation, Water Resour.Res., 341-364, 1993.

Saffman, P.G., On the boundary conditions at the surface of a porous medium, Stud.. Appl.Math., 93-101, 1971.

Shermergor, T.D., Theory of Elasticity in Micro-heterogeneous Media (In Russian), Nauka, 1979.

Shvidler, M.I., Statistical Hydrodynamics of Porous Media .(In Russian), Nedra,1985.

Shvidler, M. and K.Karasaki., Investigation of the Exactly Averaged Equations of Flow and Transport in Random Porous Media, In Transactions, 1999 AGU Fall Meeting, San Francisco, 1999.

Tatarsky, V.I., Wave Propagation in Turbulence Atmosphere (In Russian), Nauka, 1967.

Teodorovich, E.V., Calculation of the effective permeability of randomly inhomogeneous medium, JETP, **85**(1), July 1997.

Zhikov, V.V., S.M.Kozlov, O.A.Oleinik, Homogenization of Differential Operators.(In Russian).Nauka, 1993, English: Homogenization of Differential Operetors and Integral Functionals, Springer-Verlag, Berlin, 1994.

A Multidisciplinary Fractured Rock Characterization Study at Raymond Field Site, Raymond, California

Kenzi Karasaki*, Barry Freifeld*, Andrew Cohen*, Ken Grossenbacher**, Paul Cook* and Don Vasco*.

*Lawrence Berkeley National Laboratory
1 Cyclotron Rd. MS 90-1116, Berkeley, CA 94720
fax: +1-510-486-6759

**Financial Engines
1804 Embarcadero Rd., Palo Alto, California 94303

ABSTRACT

A dedicated field site was developed and a suite of experiments were conducted in the Sierra Nevada foothills, near the town of Raymond, California to develop and test a multi-disciplinary approach to the characterization of groundwater flow and transport in fractured rocks. A wealth of geologic, hydrologic and geophysical data was collected at the site using a variety of unique tools. A cluster of nine approximately 90m deep boreholes were drilled at the site in a V-shaped pattern with an angle of 60 degrees. The boreholes are spaced 7.5, 15, 30, and 60 meters from the central borehole. Various geophysical and hydrologic tests were conducted in and between these boreholes. Integration of cross-hole radar and seismic tomography, borehole flow surveys and images from a new digital borehole scanner indicated that groundwater flow is mainly confined to a few sub-horizontal fracture zones. A unique suite of hydraulic tests were conducted, in which three to four intervals in each of the nine boreholes were isolated using pneumatic packers. Some 130 injection tests were conducted, and more than 4,100 cross-hole transient pressure measurements were obtained. A computer algorithm was developed to analyze such massive interference data systematically. As a result of the analysis, an image of the fracture connections emerged, which is consistent with the geophysical data. High precision tiltmeters were effective in remotely characterizing the preferential flow path. Several radial convergent tracer tests were conducted by injecting a mixture of several conservative tracers and one sorbing tracer:

deuterium, fluorescein, lithium bromide and polystyrene micro-spheres. Some differences between the breakthrough curves are observed, which may be due to possible differences among so-called "conservative" tracers. Some characterization tools were found to be more effective than others in locating flowing fractures. However, no single tool was almighty. Characterization of fractured rock is extremely challenging and requires a stepwise and well-thought approach, which is basically a good old scientific approach. Prediction of transport based on the characterization results is even more challenging and one should always bare in mind that it is virtually impossible to uniquely characterize a fractured rock.

Key Words: fracture, tiltmeter, tracer, transport, tomography

INTRODUCTION

Many countries including the United States are considering geologic repository for disposing of high-level nuclear wastes. Most such repositories would be built in fractured rocks. Many ground-water contaminated sites are also fractured, where non-aqueous phase liquids (NAPLs) are often trapped in fractures and slowly release contaminants into groundwater. To assess the performance of a repository or to design a remediation plan for such contaminated sites, one must first understand the flow and transport system. However, characterization and prediction of flow and transport in a fractured rock mass is extremely difficult. The main reason for this is because the geometry of the flow path in a fractured rock mass is often very complex and heterogeneous, and therefore, very difficult to define. Field testing can be problematic for various reasons. The geometry of the fractures intersecting boreholes greatly influences test parameters and interpretation results (Karasaki, 1986, Cady et. al, 1993, Shapiro and Hsieh, 1993). In a network of fractures, there are typically no definable upper and lower flow boundaries and only a fraction of the interval length in a borehole is open to flow. Moreover, the representative

elementary volume (REV) may be much larger than the scale of the test, particularly for tracer tests (Endo, 1984). Assumptions regarding the flow geometry often have to be made a priori due to the lack of information. The analysis of the test results in light of necessary assumptions is difficult and non-unique, and often leads to model parameters estimates yielding large uncertainty in predictions of flow and transport. To improve field testing techniques and analysis methods for characterizing flow and transport properties of fractured rocks, a dedicated field site was established near the town of Raymond, California. A variety of unique geophysical and hydrological tests were conducted at the site. In the present paper, we give an overview of the various studies conducted. For more detailed discussion of each study readers are referred to the corresponding publication cited in the paper. Similar fracture characterization site in granitic rock has been established at Mirror Lake in New Hampshire (Goode et al., 1993; Shapiro and Hseih, 1993; http://toxics.usgs.gov/toxics/sites/mirror_page.shtml).

RAYMOND FIELD SITE

The Raymond Field Site is located in the Sierra Nevada foothills, approximately 3.2 kilometers east of Raymond, California and 100 kilometers north of the city of Fresno (Figure 1). The site lies within the Knowles Granodiorite, which is light-gray, equi-granular and non-foliated (Bateman, 1992). It is widely used as a building material in California (Bateman and Sawka, 1981). The site is located on the land owned by the Coldspring Granite Company, which operates a quarry in the nearby area.

A cluster of nine boreholes were drilled and driller's logs indicate that relatively unweathered granite is located beneath less than 8 m of soil and regolith. The boreholes are laid out in a reverse V-shaped pattern with increasing spacing between boreholes (Figure 2). Spacings of 7.5, 15, 30, and 60 meters from the central borehole were chosen to allow the study of directional and scale effects on the flow and transport parameters. The angle between the southwest and southeast leg is approximately 60

degrees. Two of the boreholes, SW-2 and SE-2, are reamed to 25 cm in diameter with the remaining boreholes being 15 cm. The boreholes are cased to approximately 10 meters and vary in depth between 75 and 100 meters. The water level is normally between 2 and 3 meters below the surface.

GEOLOGICAL INVESTIGATION

Detailed geologic and fracture mapping of exposed outcrops in the vicinity of the Raymond Field Site was constructed using the curved scan-line technique (Grossenbacher, et al., 1997). The geologic map of the vicinity of Raymond Field Site is shown in Figure 3. Zawislanski (1994) mapped fractures in the vicinity of the site with a particular focus on the distribution of pegmatite dikes. Mabee and Hartcastle (1997) attempted to correlate surface lineaments to subsurface hydrology. Quantitative analysis of fracture intervals at 10 surface outcrops and in 9 boreholes was conducted. Correlation study between grain size and macroscopic and microscopic fracture intervals and porosity was performed and it was found that there is a significant correlation between the two. Such surface fracture studies were necessary to augment the borehole fracture data that are biased against vertical fractures (Martel, 1999).

An abandoned quarry approximately 1 kilometer west of the site provides a vertical exposure of the granite for fracture mapping and fracture coring. The quarry face was mapped extensively to supplement the fracture information at the well site. Surface profiles of large fracture surfaces were also collected at the quarry. Some profiles extend over 4 meters, which is probably among the largest fracture surface profile ever taken. A method to digitize such data for statistical analysis was developed (Grossenbacher, et al. 1996). Tectono-fractographic technique (Bahat, 1991; Bahat et al, 1995 and 1999) was then used to study the fracturing processes. The data are useful for modeling flow in fractures using actual data obtained at a much larger scale than a typical core. An innovative method of collecting fracture samples was developed to study in-situ aperture and tortuosity of fractures. In this method a resin

is injected into the fracture opening and after hardening of the resin, a core is drilled out with an intact fracture. The core is then cut diagonally to expose a fracture cross section and then made into a thin section. A photographic image can then be used to study alteration near the fracture, as well as digitized for waveform analysis of the fracture profile (Figure 4).

GEOPHYSICAL SURVEYS AND IMAGING

Geophysical logs included natural gamma, resistivity, acoustic televiewer (ATV), caliper, and borehole deviation (Paillet, 1994). Benito (1994) correlated fractures observed by an ATV with those observed at outcrops. Cohen et al. (1996) evaluated various borehole characterization tools conducted at the site. Conventional television camera logs using fish-eye lens were run in all the nine holes. In addition, high-resolution digital borehole color scanner (BSS) surveys were conducted (Thapa, 1996). In contrast to the conventional borehole television survey, the BSS produces an unfolded image of the borehole wall at an extremely high resolution of up to 0.1mm pixel. The image is stored in a digital format as well as on a VHS tape in an analog format. The digital image can be later processed to produce color hardcopies. Due to the digital nature of the image, various computer aided image analyses can be performed. Such analyses include an automatic fracture detection (Thapa, 1997) and fracture friction angle calculations (Thapa, 1994).

Two different types of intra-borehole flow surveys were also conducted in most boreholes. One was performed by using a heat-pulse flow meter (Paillet, 1994; Paillet et al., 1996). The other survey was conducted by first replacing the borehole fluid with de-ionized water and, subsequently, repeatedly running a conductivity probe down the borehole to monitor changes in the fluid conductivity under a pumping condition (Tsang et. al, 1990; Paillet and Pedler, 1996). Figure 5 shows a comparison of conventional geophysical logs and the fluid logging results from SW-1 borehole. Also shown is an image

from the digital borehole scanner. The advantage of the optical scanner is that one can differentiate open fractures from filled or closed fractures. The heat pulse flow survey was useful in quantifying the inflow and outflow rate distribution (Paillet, 1998), while the fluid logging was particularly useful in pin-pointing inflow locations, i.e., the flowing fractures (Cohen, 1996). The latter was found to be even more effective when combined with the images obtained from the digital borehole scanner as shown in Figure 5 (Thapa and Karasaki, 1996).

High resolution cross-hole seismic tomography surveys were conducted between ten pairs of boreholes. Results from the surveys conducted between the five boreholes closest to 0-0, (0-0, SE-1, SW-1, SE-2, and SW-2) were analyzed by simultaneously inverting the travel times and amplitudes (Vasco et al., 1996). Vasco et. al showed that there are two zones where both velocities and amplitudes are strongly attenuated: at a depth of 30 m and 60 m. The 30 m depth coincides with the location of an anomaly identified by a ground penetrating cross-hole radar survey (Korkealaakso et al, 1993). The radar tomography survey was conducted between SW-1 and SW-3 between the depths of 15 and 45 m. The results from the cross-hole radar tomography and the cross-hole seismic tomography are shown in Figure 6. Three borehole logs, resistivity, ATV, and caliper from SW1 and SW3 are superimposed on both ends for comparison. Both tomography results indicate that there is a major feature at a depth of approximately 30 m, although the two tomographies indicate different dip angle for the imaged feature. It should be noted that these surveys respond to different physical properties, i.e., the seismic method responds to a rock stiffness contrast, and the radar responds to the electromagnetic properties of the rock. The seismic tomography and the fluid logging indicate that there is another feature at a depth of approximately 60m, for which radar tomography is not available. The information obtained by the geophysical surveys was used to determine the types of hydraulic tests and the locations for setting

packers. It is shown in the following sections that the feature detected by the geophysical methods is indeed hydrologically significant.

HYDROLOGIC DATA ACQUISITION SYSTEM

During hydrological field testing many parameters are both monitored and controlled simultaneously. At the Raymond Field Site, pressures are monitored in up to 29 different packed-off intervals while we simultaneously monitor flow rates and analyze water chemistry. To simplify the task of data acquisition and analysis, a new data gathering system was built around a PC. One PC controls an automated sampling table, opening and closing valves, and also logs pressure and chemical concentration data from all the measurement locations throughout the site. The ability to observe and manipulate the data collection in real-time was given a high priority in the development of the system. Unlike conventional data loggers, this allows interactive testing, so that any equipment problems can be quickly addressed. Also, controlled parameters such as flow rates can be adjusted while a test is underway. This is especially useful if monitored parameters start to fluctuate out of an allowable range.

Pneumatic packers are used to isolate zones in each borehole. In the 25 cm boreholes, SW-2 and SE-2, sliding head packers manufactured by TAM Corporation are employed, while in the remaining 15 cm boreholes, fixed-head packers made by Roctest are used. The packers have feed-throughs so that both fluids and electrical signals can be passed to the surface. In total, there are six TAM packers and sixteen Roctest (fixed ends) packers creating the 29 intervals being monitored for pressure.

A schematic of the new data acquisition system is shown in Figure 7. Data collection from up to forty different transducers can be accomplished at a rate of 1 Hz. Analysis of fluorescent tracers is accomplished using a flow-through cell in a fluorometer and ionic tracer concentration is determined using ion specific electrodes. The output from these chemical concentration measuring devices are

available in real-time on the computer. A computer-controlled sampling table with the capacity of 144 bottles, was built so that samples can be taken back to the lab for further analysis. In several months of field use, the fully automated data collection system has proven to be highly reliable, even for extended multi-week tests.

HYDRAULIC TESTS

Various kinds of hydraulic tests have been conducted. These include single well pump tests, falling head slug tests, pressure injection tests and several interference tests with various packer and pumping well configurations. Prematurely terminated slug tests (PTST) (Karasaki, 1990(a); Karasaki, 1990(b)) were also conducted in selected boreholes. In a PTST or systematic drillstem test, a slug test is shut in or terminated before it completes and subsequent pressure recovery is monitored. Some pump tests were conducted without packers to investigate the effect of short-circuiting by boreholes (Cohen, 1993). In other pump tests the upper fracture zone in each borehole was isolated with packers. A minimum of two packers were used in each borehole with a total of 22 packers in 9 boreholes. A total of 29 transducers were used to instrument each packed-off zone.

In one pump test, well 0-0 was pumped at a constant rate of 11 liters/min. Figure 8 shows the transient pressure data from selected intervals during the pumping. It is interesting to note that the intervals in wells 0-0, SE-1, SE-2, SW-1, and SW-2 display what looks like a unit-slope at early time whereas wells SE-4 and SW-4 have different transient characteristics from those of the other wells. It was postulated that the first four wells are intersecting a region with high permeability and low storage and that SW-4 and SE-4 lie outside of this region. The results from these tests indicate that flow is mainly confined in the two sub-horizontal fracture zones and that there is a high degree of heterogeneity within the zones. The finding that the sub-horizontal fractures are hydrologically active is not entirely

surprising. The drawdown data as well as the tiltmeter surveys discussed later indeed indicate that there are preferential pathways within the fracture zone, which means that the fracture is partially closed and partially open. It is possible that there are vertical fractures that are hydrologically significant and were not detected by the vertical boreholes. It does seem that it is the vertical fractures that hydrologically connect the two fracture zones.

Another observation is that the larger the time or the distance from the pumping well, the closer the pressure responses are in the upper and lower zone in a same well. This indicates that the features in the upper and lower zone identified by the geophysical logs are hydraulically connected with each other. Furthermore, a significant degree of heterogeneity within and among the wells was observed. Drawdowns in the SE boreholes are generally higher than in SW wells indicating preferred high permeability in the south-east direction. Results from the tiltmeter surveys discussed in the later section also indicates a preferential flow in the direction of SE boreholes. Some log-log time drawdown curves exhibit non-Theis characteristics that may be caused by non-uniform and discontinuous fracture connection. Some of the data, however, may have been affected by the very existence of the boreholes, i.e., the storage capacity and "conductivity" of boreholes are comparable or greater than those of the rock. Therefore, observation wells may act like reservoirs and/or short circuit otherwise unconnected fractures.

SYSTEMATIC INJECTION TESTS AND FRACTURE CONNECTIVITY ANALYSIS

Systematic injection tests were conducted in all nine wells. A straddle packer string with an interval length of 6 m was used to isolate and inject water into the packed-off interval. A pneumatically controlled downhole-valve was used to start and stop the injection. The pressure in the water tank was controlled and maintained at a constant pressure using compressed air. Neither the flow rate nor the downhole pressure was actively controlled; they spontaneously adjusted themselves accordingly to the

transmissivity of the injection interval. In general it is easier to analyze the resulting transient data if either the downhole pressure or flow rate is held constant. The advantages of the present method are the simplicity of the set-up and the ease of test execution. A typical duration of an injection test was, on the average, ten minutes. After each test, the packer string was lowered by approximately 6 m. Depth intervals sealed by the packers during a particular injection test were kept unobstructed during the next, so that the entire length of the well was tested. There were approximately 15 injection tests per well in all nine wells. While these injection tests were being conducted, the pressures in the remaining 31 intervals were simultaneously monitored. As a result, a total of some 4000 interference pressure transients were recorded. Figure 2 shows an unfolded view of the well field and a typical packer configuration during the tests. An analysis of the injection data provides an estimate of the near-wellbore transmissivity distribution along each well, while the interference data provide information about inter-well connectivity (Karasaki et al, 1994b).

To construct a hydrologic model using such a large number of interference data, an heuristic approach such as type curve matching would be impossible. With 9 wells there are 36 well pairs. With 15 injections per well there are 225 possible connections between each pair, which suggests that if the site geology were to consist of permeable porous rocks there would be 8,100 connections to sort through. Some systematic approach is the only practical alternative. Full wave form inversion using the entire transient data (Mauldon et al., 1993; Nakao et al., 1999), however, would also be impractical, because as many as 135 forward simulations would have to be made for each iteration. A prohibitively large amount of computer space and time would be required to reach a reasonable answer.

To keep the computer time and size practical, and to still take advantage of such a large amount of cross-hole information, the binary inversion method was developed (Cook, 1996). In this method each

set of interference transient pressure data was reduced down to a binary set: 1 (yes) if an observation zone responds to an injection, and 0 (no) otherwise. This method was later extended to incorporate the magnitude of pressure responses (Cook, 1996). In analyzing connections between wells, only the existence of a response has been investigated as a first step (binary inversion). The next step is to take into account the magnitudes of responses coupled with flow rates for injected intervals. These measures will have to be normalized not only to distances between wells but to heights between zones since some of the wells are so close together. By visualizing connectivity with various cut-off values, one can focus on features at different scales.

Each well had only three to four packed-off zones for observation, which doesn't lead to very high resolution when looking for possible connections. However, if the injected intervals (as many as twenty per well) are taken into account for pairs of wells, the resolution can be increased substantially. If (1) a given injection with a measurable flow creates a response in a packed-off zone in another well, and (2) this second well has an interval with flow somewhere in this zone when *it* is later injected, and (3) this later injection in turn registers a response in the original well in a zone containing the original injection, then a note is made that these two injected intervals are hydraulically connected (Figure 9). Since the injected intervals are roughly 20 ft in length, the method affords a twenty foot resolution per connection.

A computer algorithm that performs the logic described above and also keeps track of all the overlapping packer locations was developed. A further refinement to sorting for connections between pairs of wells was made to sort for shared connections in various combinations of wells. A routine that examines connections for N wells at a time works much like the two-well routine but searches for reciprocal responses in all N wells. For example, in a combination of 3 wells, a given injection interval

would have to have responses in the other two wells. In addition, these two wells would have to be connected to each other at those same response points. As the number of wells N is increased, the number of criterion tests for a possible connection increases proportionally to N(N-1).

The twenty foot resolution and reciprocal connection criteria afforded by the injection test can be significantly enhanced by incorporating other data such as fluid logging. Fluid logging appears to pin-point the location of flowing fractures in wells within inches. Instead of using the center of an interval for connectivity analysis, we subsequently used the exact location of the flowing features and thus enhanced the resolution significantly (Cook, 1996). By doing so, we assumed that most of the flow occurs through fractures, which would be a reasonable assumption for fractured granite. In addition, we quantified the degree of connection by evaluating the magnitude of response normalized by the distance and the source strength.

Figure 10a shows a perspective view of all the possible connections between intervals in the seven nearest wells. Wells SW-4 and SE-4 are excluded from the plot for clarity. Each line represents a possible connection between length intervals tested by an injection. Note the extreme density of lines indicative of the large number of cross-hole tests conducted. Figure 10(b) shows the result from the inversion analysis. If the rock is a porous medium, we expect all the lines to remain after the analysis. However, as can be seen from the figure, the result is an image of two horizontal features, one at a depth of approximately 30m and another at approximately 60m. As noted in the previous section, these features correspond to those identified by the geophysical surveys. Another interesting result is the lack of connection between the features.

It should be noted that actual fracture connections or pressure propagation pathways are probably not straight lines. The lines in the figure merely indicate that there is a connection (in some manner)

between two given length intervals. However, if there is a dominant feature such as a fracture zone in the present case, the lines would form a plane, effectively imaging the zone itself.

TILTMETER SURVEY

During the pressure tests, an interesting phenomenon was observed. While water was being pumped or injected in one well, opposite pressure responses were observed in some intervals in the wells in distance. For example, the pressure in the bottom interval of SE-4 increased initially while 0-0 was being pumped, and conversely, the pressure declined during the injection at 0-0. The phenomena was completely reversible and repeatable. The possibility of electrical noise was ruled out. Cook (1996) postulated that this is due to the mechanical opening and closing of the fracture. To investigate such hydro-mechanical properties of the fracture zone, we monitored the surface deformation during pumping and injection using extremely high precision tiltmeters. Tiltmeter surveys are commonly used to monitor hydrofracturing processes. Recently, they are beginning to be used to map reservoir flow geometry.

When fluid is produced from or injected into a reservoir, it causes volume changes in the reservoir, which in turn induce displacements on the ground surface. If the reservoir is horizontal and homogeneous, the induced displacements will be distributed concentrically around the production/injection borehole. In the case of the surface tilts, tilt vectors will be radially convergent to or divergent from the borehole. If a preferential flow path such as a fault zone exists in the reservoir, the distribution of the volume change and subsequent surface displacements will be skewed. An inversion algorithm can be used to estimate the distribution of the volume changes in the reservoir. The larger the volume change is at a particular location, the more fluid is likely to have moved in or out of the location. The distribution of volume change is tightly coupled with that of the reservoir flow properties: permeability and compressibility.

Nine high resolution tiltmeters were placed in shallow holes and two were directly placed on the ground surface. A total of three surveys were conducted. In the first two tests, well 0-0 was pumped at two different flow rates, and in the third test, water was injected in well 0-0. All three surveys showed consistent results. As expected, tilt vectors were not concentric. The tilt amplitudes were larger in the SE direction. Vasco et. al (1998) inverted the tilts and the subsurface structure was revealed (Figure 11). The results of the inversion show the distributions of the volume changes in the fracture zone at different times during the pumping. The region of large volume change extends toward SE direction, indicating a preferential flow in the direction, which is consistent with the cross-hole hydraulic test results discussed earlier.

RADIAL CONVERGENT TRACER TEST

In a radial convergent tracer test, a well is pumped for an extended period of time prior to the test to establish a radially convergent flow field. Subsequently tracers are released from a injection well, or in some cases from multiple injection wells (Hodgkinson and Lever, 1983, Moench, 1995). We conducted a series of radial convergent tracer tests using several pairs of wells with varying distance and direction. Wells used are SW-3, SE-1, and SE-3 with 0-0 being used as the pumping well. Adjustments and improvements were made on each new test based on the experience gained in the preceding tests. We made adjustments in the types and amount of tracers, the tracer delivery system, and tracer analysis methods. Tracers used include: fluorescein, deuterium, fluoride, potassium bromide, and lithium bromide. In some tests, polyurethane micro-spheres were also used as tracers (Karasaki et al, 1994a; Freifeld et al, 1995). All the tracers except for lithium are regarded as conservative tracers. It advisable to conduct batch tests to check the "conservativeness" of the tracers with the host rock and the injection plumbing.

Care was taken to minimize the volume in the injection interval and to mix the tracers well in the interval. We eventually chose to use a weak dipole system to enhance tracer delivery by re-injecting back 10 per cent of the pumping rate. The rate was arbitrarily chosen and it is desirable to test at different rates as well. We also devised a separate plumbing system to re-circulate the fluid for better mixing in the injection zone. The flow field was still predominantly radially convergent.

In Figure 12 the breakthrough curves from the test between SE-3 to 0-0 are shown. These wells are 30m apart. We chose the upper fracture zone to inject tracers. As in the most other tests, well 0-0 was first pumped at a constant rate of 7.5 liters/min for several days prior to the tracer injection to establish a quasi-steady flow field. 0.75 liters/minute of pumped fluid was injected back into the injection zone. Tracer injection was done in three different stages. First, a tracer mixture of deuterium (1kg) and fluorescein (1g) was injected, two hours later they were followed by lithium bromide (200g in 2 liters) and four hours later by micro-spheres (0.36μ diameter, 4.18×10^{13} spheres in 1 liter). Lithium bromide was separated from other tracers because due to its higher density, bromide may cause the tracer mixture plume to sink to the bottom of the injection zone. The micro-spheres were separated because they were dyed with fluorescent dye, which might affect the fluorescein readings. The pumping continued for about one week, during which the pressure in all 29 zones and the flow rate at the discharge line were continuously monitored and recorded. Sample water was taken from the discharge line every ten minutes using the automated sampling table for immediate fluorescein count and later ionic analysis in the laboratory. The first tracer arrival occurred at about 10 hours after the injection. Samples were collected up to 450 hrs after the injecting. Peak arrivals were roughly 30-40 hours after the injection.

The breakthrough curves of fluorescein, bromide, deuterium and lithium in Figure 12 are the mass concentration normalized to the injected mass. The unit is dimensionless mass concentration in

parts per billion. When compared to the tracer test results in the SW direction, the tracer arrived almost twice as fast in the SE direction. Although further analysis is needed, we obtained a twice as large apparent dispersivity as the test between SE-1 to 0-0, whose separation is 7.5 m. As can be seen from p figure three curves do not lie on top of each other, although these three tracers are presumably "conservative". It is surprising that fluorescein showed the lowest concentration. In another tracer test from SE-1 to 0-0, fluorescein had the highest concentration among the conservative tracers. It is not very clear why this is the case. Care was taken when making standards to avoid possible calibration errors. Fluorescein has been reported elsewhere to react with certain minerals in the rock, the rate of the reaction being PH dependent (Feunstein and Sellick, 1963; Deaner, 1973; Smart and Laidlaw, 1977). It is also known to degrade in sunlight (photodecomposition) and, conversely some organic growth in the discharge line or elsewhere gives apparent increase in the fluorescein concentration. Other possible scenarios for the difference in ionic tracers are that there may be differences in the degree of reaction (or non-reaction) among the tracers and/or these chemicals may have different mixing characteristics. After the tracers were injected, some tracer may have sunken in the injection zone, which is roughly ten times the volume of the injected fluid. It is also possible that the deuterium has diffused into the matrix more than bromide did. For microsphere results, readers are referred to Becker (1999).

SUMMARY AND DISCUSSION

A dedicated field testing site for fracture flow and transport produced a wealth of data. Results of intra-borehole flow surveys and cross-hole radar and seismic tomography surveys correlated very well with each other and identified a major feature at a depth of 30m. It was found that by conducting a large number of short cross-hole injection tests and analyzing the connectivity, one can begin to image the hydrologic structure of a fractured rock mass. The feature identified by the connectivity analysis coincided with the one identified by geophysical methods.

A priori information obtained by geophysical surveys and geologic observations can be useful in designing subsequent hydrologic investigations. Correlations exist between surface features (such as pegmatite dikes, variations in grain size and contacts between different rock units) and subsurface features (such as highly conductive fractures or fracture zones). The packer configurations and locations can be set to pack off the features observed in the borehole geophysical survey. This was indeed the case at the Raymond Field Site. We began our hydrologic tests with uneven and irregular packer locations. As we conducted more tests, we learned more about the flow system. We then fine-tuned the packer configurations to tighten the packed off zone or moved the zone entirely. This was fine for the purpose of conducting each specific test. However, the fact that packer geometry was different for different tests made it very difficult to compare the results between the tests. This is because the boreholes themselves are perhaps the most hydrologically conductive features, and depending on the packer locations, the flow paths may be different each time.

Our experience thus far indicates that when conducting field experiments, particularly in a fractured rock, it is extremely important to make certain that what is being measured is actually what is intended to be measured. Wellbore conditions can alter conditions imposed at the surface, and an observation well can play a greater role than just as an access for measuring downhole conditions. One may end up measuring the "permeability" of boreholes rather than that of the rock or the wellbore hydrodynamic properties rather than the rock dispersivity.

Characterization of fractured rock is extremely challenging. Even with the level of effort outlined in this paper, we are not very confident that the model that is calibrated to the experiments thus far can adequately predict contaminant transport behavior under natural conditions. On the other hand, it is of interest to investigate how much effort is cost-effective and/or how much detail is necessary. This is

dependent on the nature of the problem as well as the spatial and time scale of the problem. Sometimes it may be better to conduct few long-term/large-scale tests to let the system present its average behavior than to conduct many small scale tests and piece the results together to predict the behavior.

ACKNOWLEDGMENTS

This work was partially supported under U.S. Department of Energy Contract No. DEAC03-76SF00098 for the Director, Office of Civilian Radioactive Waste Management, Office of External Relations, and was administered by the Nevada Operations Office, U.S. Department of Energy. The presented work was conducted in collaboration with U.S. Geological Survey, Denver. The deuterium was supplied and analyzed by Mark Conrad of Lawrence Berkeley Laboratory. Bruce Robinson and Matt Becker of Los Alamos National Laboratory supplied the micro-spheres and conducted analysis of the micro-spheres. Authors would like to thank them and many others who participated in the project in various capacities. Authors would also like to thank Boris Faybishenko and Chin-Fu Tsang for reviewing this paper.

REFERENCES

1. Bahat, D, Tectonofractography, Springer-Verlag, New York, 1991.

2. Bahat, D., K. Grossenbacher, and K. Karasaki, "Investigation of Exfoliation Joints in Sandstone and Granite by Tectonographic Techniques" LBL Report No. 36973, 1995.

3. Bahat, D., K.Grossenbacher, and K. Karasaki, Mechanism of exfoliation joint formation in granitic rocks, Yosemite National Park, Journal of Structural Geology, 21(1), 85-96, 1999.

4. Bateman, P.C., Plutonism in the central part of the Sierra Nevada Batholith, California, Professional Paper No. 1483, U.S. Geological Survey, 1992.

5. Bateman, P.C. and W.N. Sawka, "Raymond Quadrangle, Madera and Mariposa Counties, California - Analytic Data," Professional Paper No. 1214, U.S. Geological Survey, 1981.

6. Benito, P.H., Measurement of hydrogeologic fracture parameters at surface outcrops as a possible method for identifying high-yield fractures in a bedrock aquifer, Raymond, California. Honors thesis, Dept. Geology, Amherst College, Amherst MA, 1994.

7. Becker, M.W., P.W. Reimus , and P. Vilks, Transport and attenuation of carboxylate-modified latex microspheres in fractured rock laboratory and field tracer tests, Ground Water, 37(3), 387-395, 1999.

8. Cady, C., S. Silliman, and E. Shaffern, Variation in Aperture Estimate Ratios From Hydraulic and Tracer Tests in a Single Fracture, Water Resour. Res., 29(9), 2975-2982, 1993.

9. Cohen, A.J.B., Hydrogeologic Characterization of a Fractured Granitic Rock Aquifer, Raymond, California, M.S. Thesis, University of California, Berkeley, LBL-34838, 1993.

10. Cohen, A.J.B., K. Karasaki, S. Benson, G. Bodvarsson, B. Freifeld, P. Benito, P. Cook, J. Clyde, K. Grossenbacher, J. Peterson, R. Solbau, B. Thapa, D. Vasco, P. Zawislanski, Hydrogeologic Characterization of Fractured Rock Formations: A Guide for Groundwater Remediators, EPA Project Summary, EPA/600/S-96/001, May 1996.

11. Cook, P., Analysis of Interwell Hydraulic Connectivity in Fractured Granite, M.S. Thesis, University of California, Berkeley, 1996.

12. Deaner, D.G., Effect of Chlorine on Fluorescent Dyes, J. of Water Poll. Control Fed., 45(3), 507-514, 1973.

13. Endo, H.K., J.C.S. Long, C.R. Wilson, and P.A. Witherspoon, A model for investigating mechanical transport in fracture networks, Water Resour. Res., 20(10), 1390-1400, 1984.

14. Feunstein, D.L., Sellick, R.E., Fluorescent Tracers for Dispersion Measurements, J. San. Eng. Div., ASCE:89:SA4, 1-21, 1963.

15. Freifeld, B., K. Karasaki, R. Solbau, and A.J.B. Cohen, "Reactive Transport Studies at the Raymond Field Site," in Proceedings, 6th International High Level Radioactive Waste Management Conference, Las Vegas, 1995.

16. Goode, D.J., P.A Hsieh,. A.M. Shapiro, W.W. Wood, and T.F. Kraemer, Concentration history during pumping from a leaky aquifer with stratified initial concentration, in Shen, H.W., Su, S.T., and Wen, F., eds., Proceedings of the 1993 National Conference on Hydraulic Engineering, San Francisco, Calif., July 25-30, American Society of Civil Engineers, 29-35, 1993.

17. Grossenbacher, K., D. Bahat, and K. Karasaki, "TRIANGULATOR: excel spreadsheets for converting relative bearings to XYZ coordinates, with applications to scaling photographs and orienting surfaces," Computers and Geosciences, 22(10), 1053-1059, 1996.

18. Grossenbacher, K., K. Karasaki, and D. Bahat, "Curved Scanline Theory," Mathematical Geology, 29(5), 629-651, 1997.

19. Hodgkinson, D.P. and D. A. Lever, Interpretation of a field experiment on the transport of sorbed and non-sorbed tracers through a fracture in crystalline rock, Radioact. Waste Manage. Nucl. Fuel. Cycle, 4(2), 129-158, 1983.

20. Karasaki, K., Well Test Analysis in Fractured Media, Ph.D. Thesis, University of California, Lawrence Berkeley Laboratory Annual Report LBL-22090, 1986.

21. Karasaki, K., Prematurely Terminated Slug Tests, Lawrence Berkeley Laboratory Report LBL-27528, 1990.

22. Karasaki, K., Analysis of Well Test Data from Selected Intervals in Leuggern Deep Borehole-Verification and Application of PTST Method, LBL Report, LBL-27914, 1990(a).

23. Karasaki, K., A Systematized Drillstem Test, Water Resour. Res., 26(12), 2913-2919, 1990(b).

24. Karasaki, K., B. Freifeld, and C. Davison, LBL-34707, also in the Proceedings of 5th International High Level Radioactive Waste Management Conference, Las Vegas, 1994.

25. Karasaki, K., B. Freifeld, P. Cook, and A. Cohen, Hydrologic Imaging of Fractured Rock, in Proceedings of XVIII International Symposium on the Scientific Basis for Nuclear Waste Management, Kyoto, Japan, 1994.

26. Korkealaakso, J., O. Okko, and P. ja Hassinen, Borehole radar measurements at the Raymond test site. Rock Mechanics Symposium. Papers of the Engineering - Geological Survey of Finland, Espoo. 12p., 1993.

27. Mabee, S.B., and K.C. Hardcastle, "Analyzing outcrop-scale fracture features to supplement investigations of bedrock aquifers", Hydrogeology Journal, 5(4), 21-36, 1997.

28. Martel, S., Analysis of fracture orientation data from boreholes, Environ. & Engineer. Geoscience, 5(2), 213-233, 1999.

29. Mauldon, A. D., K. Karasaki, S.J. Martel, J.C.S. Long, M. Landsfeld, A. Mensch, and S. Vomvorus, An Inversion Technique for Developing Models for Fluid Flow in Fracture Systems Using Simulated Annealing, Water Resour. Res, 29, 3775-3789, 1993.

30. Moench, A., Convergent radial dispersion in a double-porosity aquifer with fracture skin: Analytical solution and application to a field experiment in fractured rock, Water Resour. Res., 31(8), 1823-1835, 1995.

31. Nakao, S., J. Najita, and K. Karasaki, Sensitivity Study on Hydraulic Well Testing Inversion Using Simulated Annealing, Groundwater, 37(5), 736-747,1999.

32. Paillet, F.L., personal communication, 1994.

33. Paillet, F.L., R.E. Crowder, and A.E. Hess, High-resolution flowmeter logging applications with the heat-pulse flowmeter: Journal of Environmental Engineering Geophysics, 1(1), 1-11, 1996.

34. Paillet, F.L., and W.H. Pedler, Integrated borehole logging methods for wellhead protection applications, Engineering Geology, 42, 155-165, 1996.

35. Paillet, F.L., Flow modeling and permeability estimation using borehole flow logs in heterogeneous fractured formations, 34(5), 997-1010, 1998.

36. Shapiro, A., and P. Hsieh, A new method of performing controlled injection of traced fluid in fractured crystalline rock, U.S. Geological Survey Toxic Substances Hydrology Program Technical Meeting, Colorado Springs, Co., September 20-24, 1993.

37. Smart, P.L. and I.M.S. Laidlaw, An evaluation of some fluorescent dyes for water tracing, Water Resour. Res., 13(1), 15-33, 1977.

38. Thapa, B., Analysis of In-Situ Rock Joint Strength Using Digital Borehole Scanner Images, Ph.D. Thesis, University of California, Berkeley, 1994.

39. Thapa, B. and K. Karasaki, Observations of Joint persistence and connectivity across boreholes, in Proc. 2nd North American Rock Mechanics Symp., Montreal, Quebec, Publisher: Balkema, 1996.

40. Thapa, B., P. Hughett, and K. Karasaki, Semi-Automatic Analysis of Rock Fracture Orientations from Borehole Wall Images, Geophysics, 62(1), 129-137, 1997.

41. Tsang, C. F., P. Hufschmied, F. Hale, Determination of fracture inflow parameters with a borehole fluid conductivity logging method, Water Resour. Res., 26(4), 561-578, 1990.

42. Vasco, D. W., J.E. Peterson, and E.L. Majer, A simultaneous inversion of seismic traveltimes and amplitudes for velocity and attenuation, Geophysics, 61, 1738-1757, 1996.

43. Vasco, D.W., Karasaki, K., and Myer, L., Inversion of surface tilt caused by fluid migration, 124(1), Jour. of Geotechnical and Geoenvironmental Engineering, 29-37, 1998.

44. Zawislanski, P., Surface Fracture Distribution at Raymond Field Site, Raymond, California, Lawrence Berkeley National Laboratory Report, LBNL-42675, 1994.

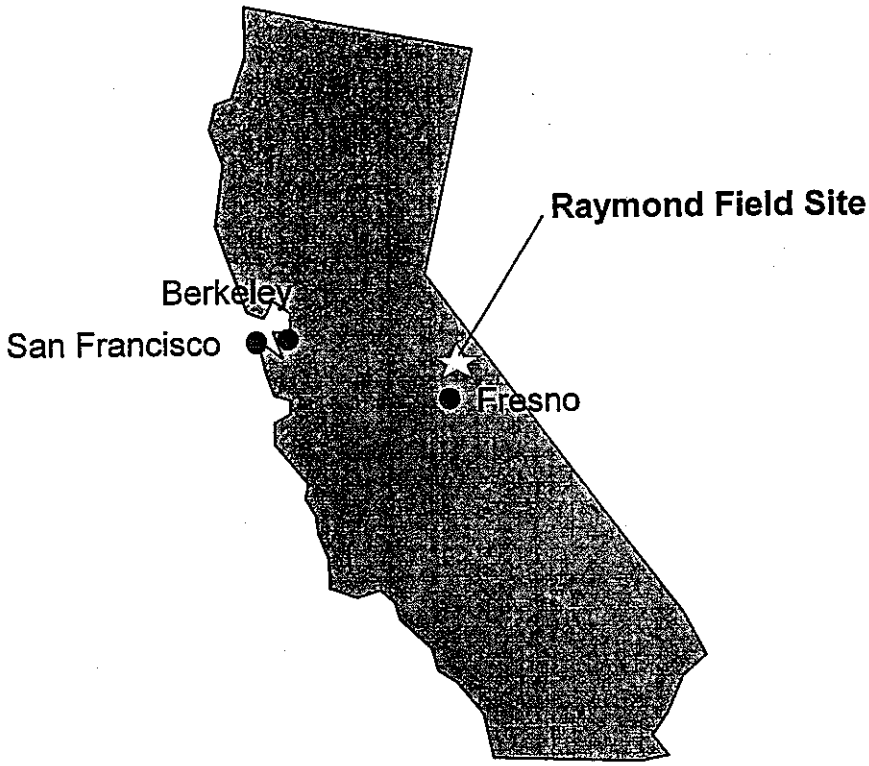

Figure 1. Location of the Raymond Field Site near Fresno, California.

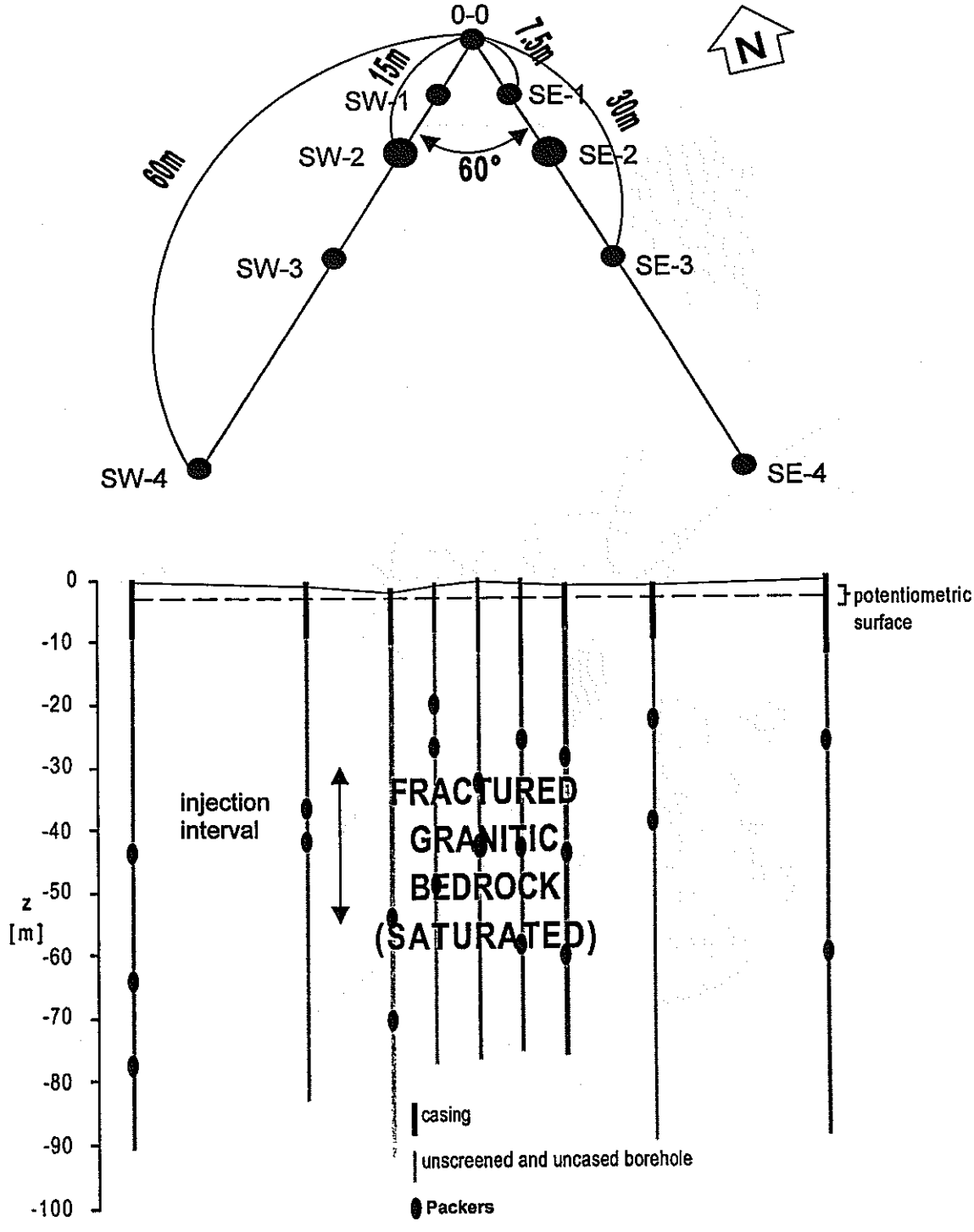

Figure 2. Well configuration at the Raymond Field Site. Large bullets and small bullets indicate 25cm and 15cm diameter wells, respectively. Unfolded view of the wells show typical packer locations during the systematic injection tests. Note that the length of the injection interval is much shorter than the packed- off zones in non-injection wells.

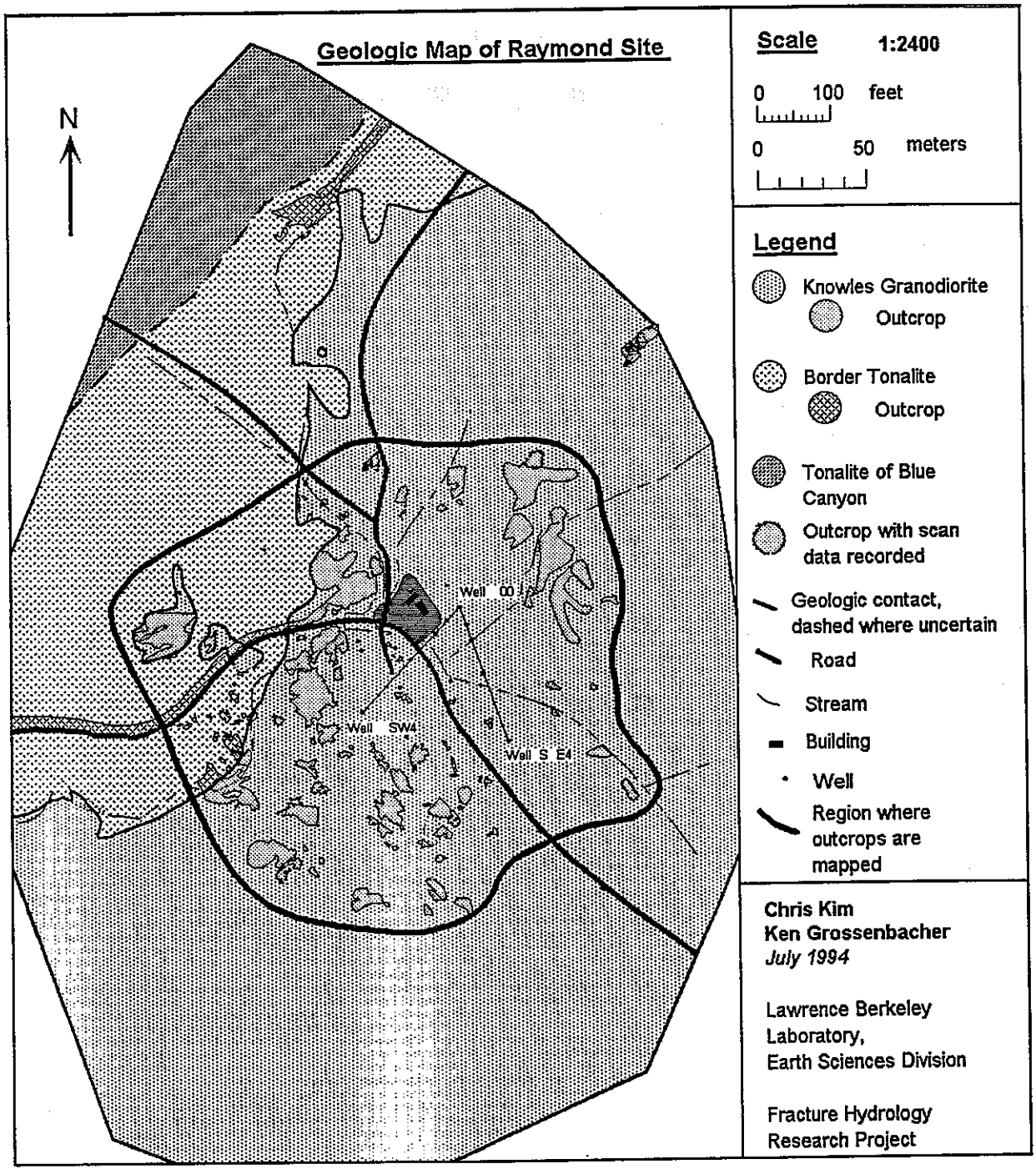

Figure 3. Geologic map of the vicinity of the Raymond Field Site.

Figure 4. The thin section of an open fracture captured by the resin injection technique.

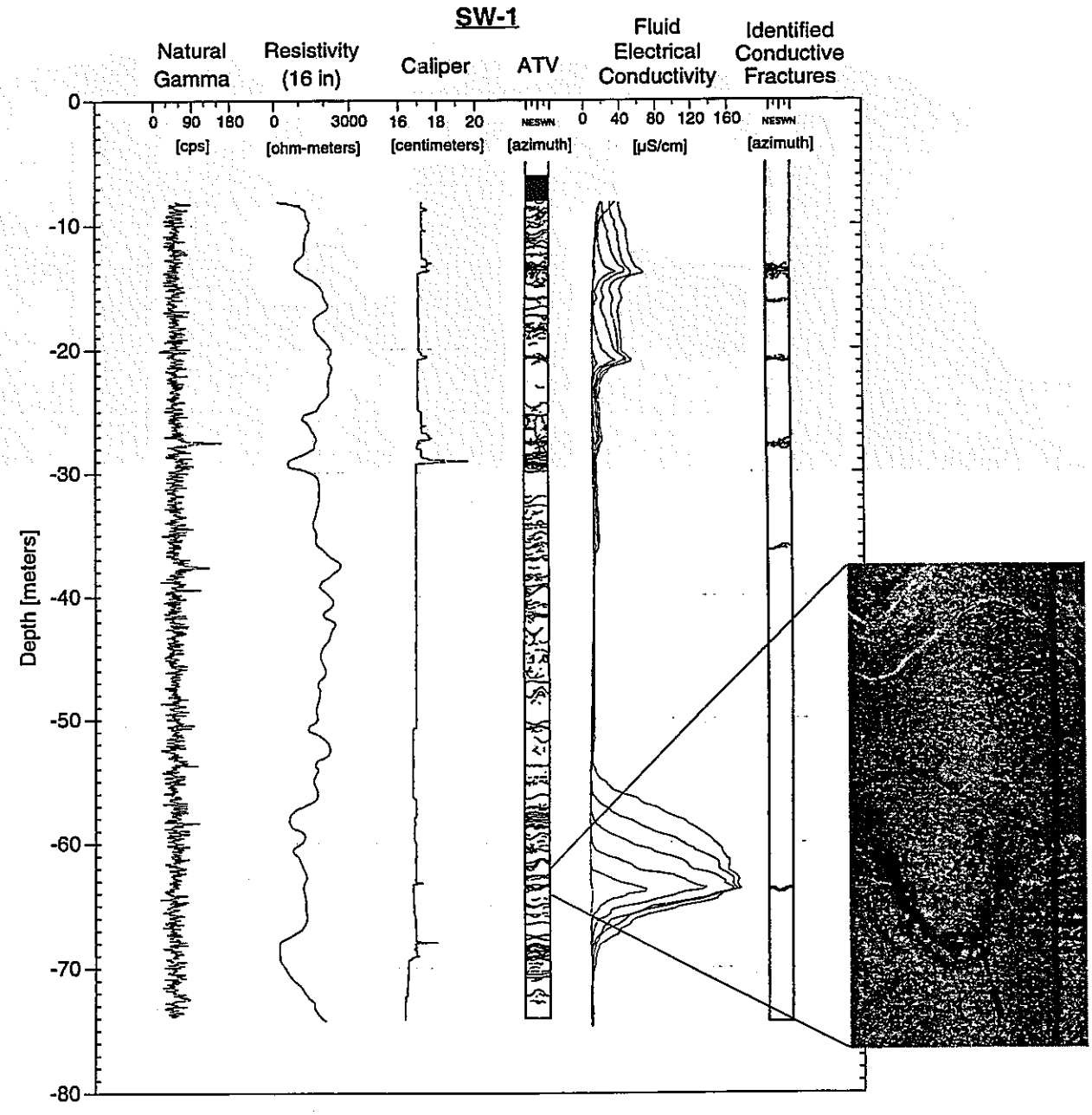

Figure 5 Comparison of conventional geophysical logs and fluid logging results from SW-1. Note that although the ATV log indicates numerous fractures there are only few flowing fractures. High conductivity anomalies indicate the locations of inflow, i.e., flowing fractures. Also shown is a 1m section image from an optical digital scanner. An open fracture is clearly visible and quartz veins appear as such.

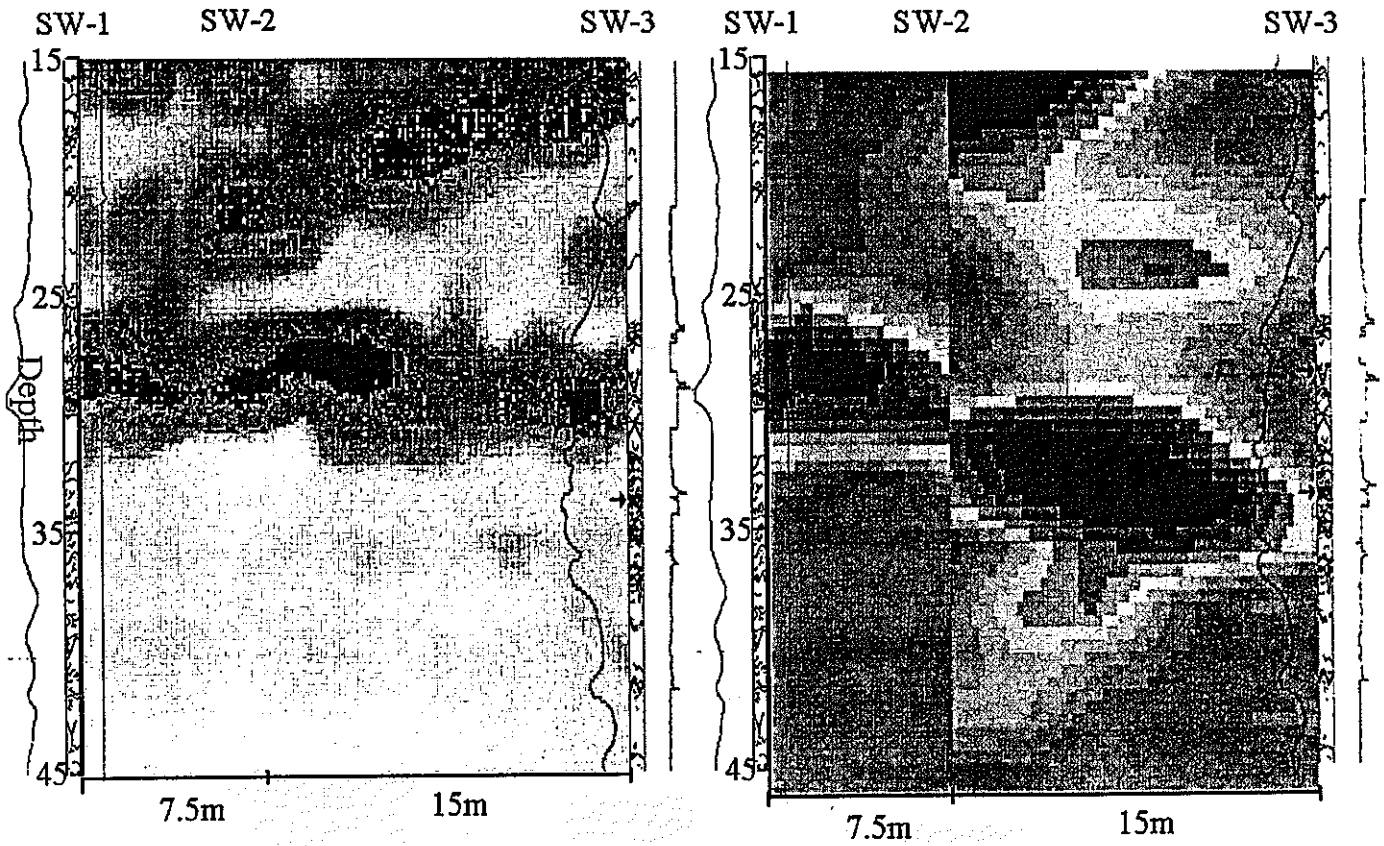

Figure 6 Radar (left) and seismic (right) tomography results are shown with resistivity, ATV, and caliper logs. Darker pixels indicate low velocity, and therefore, possible permeable fracture zones. The radar survey was conducted between SW-1 and SW-3, whereas the seismic survey was conducted from SW-2 to SW-1 and Sw-2 to SW-3. The depth for the two surveys were offset by 1 m.

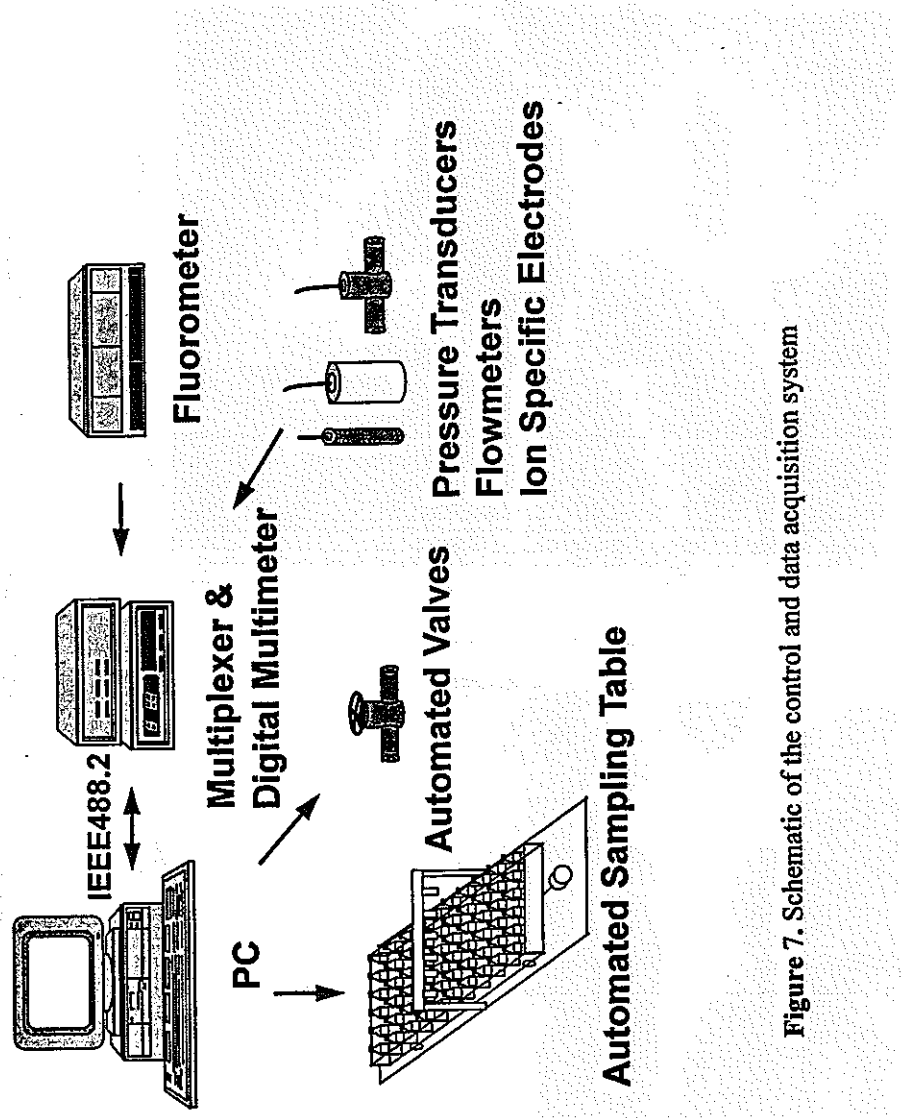

Figure 7. Schematic of the control and data acquisition system

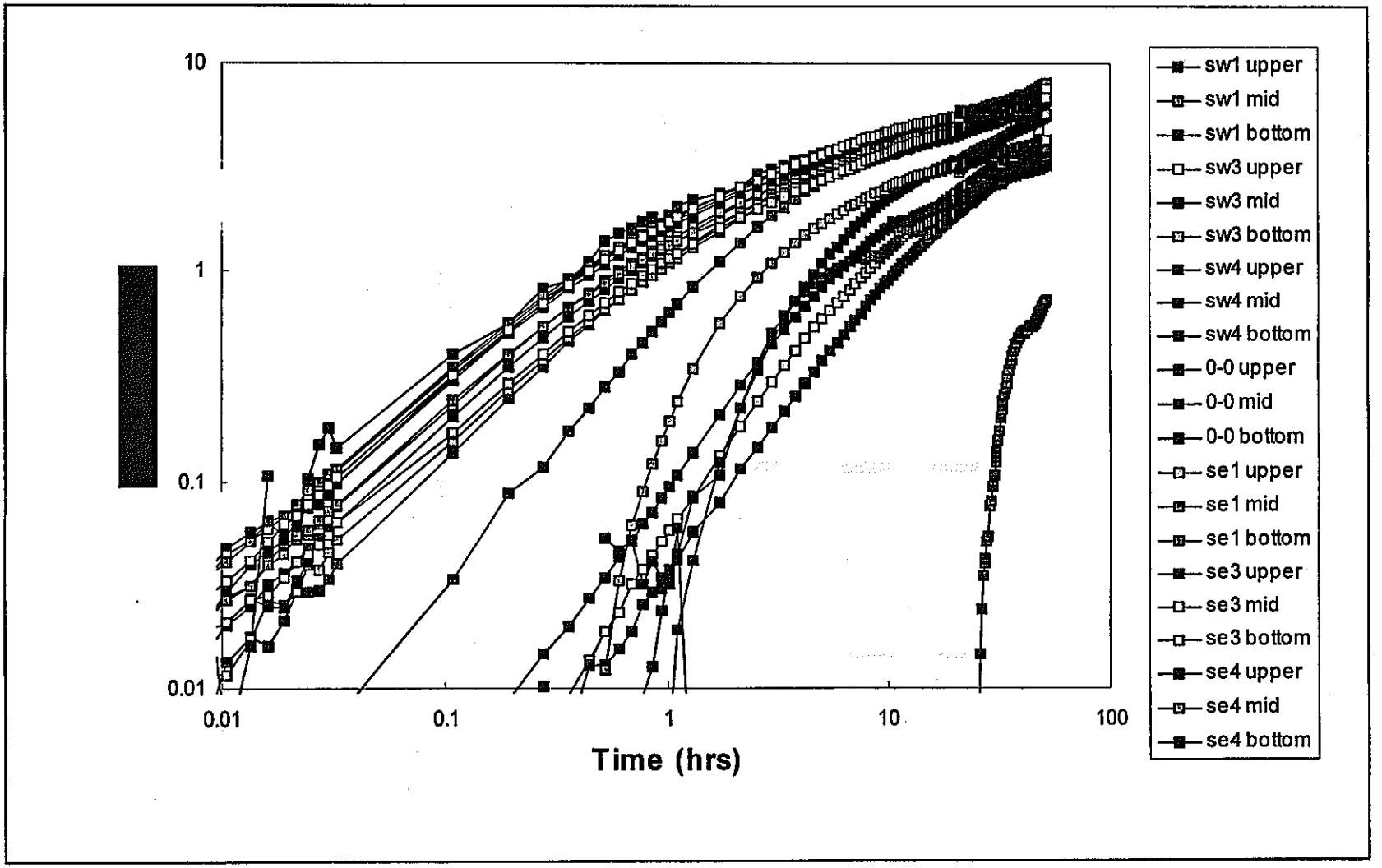

Figure 8 Transient pressure from selected intervals during a radial convergent tracer tests. Note that the data are only part of what were recorded simultaneously.

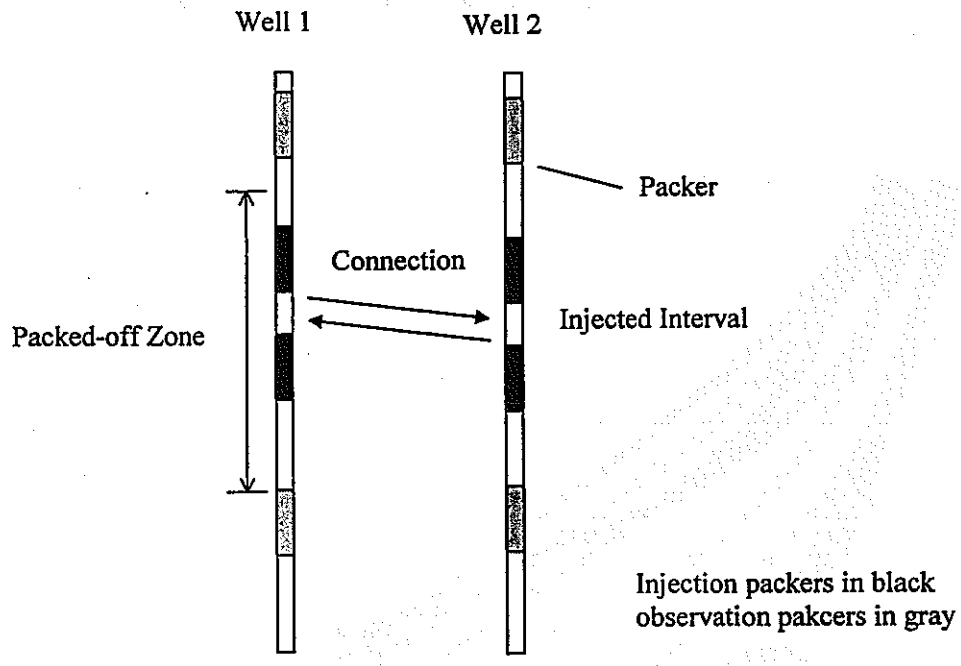

Figure 9 Schematic of how connectivity is determined. For a hydrologic connection to exist between the length intervals straddled by packers shown in black, the packed-off zone in Well 1 should have a pressure response when the injection string is in Well 2, and vice versa.

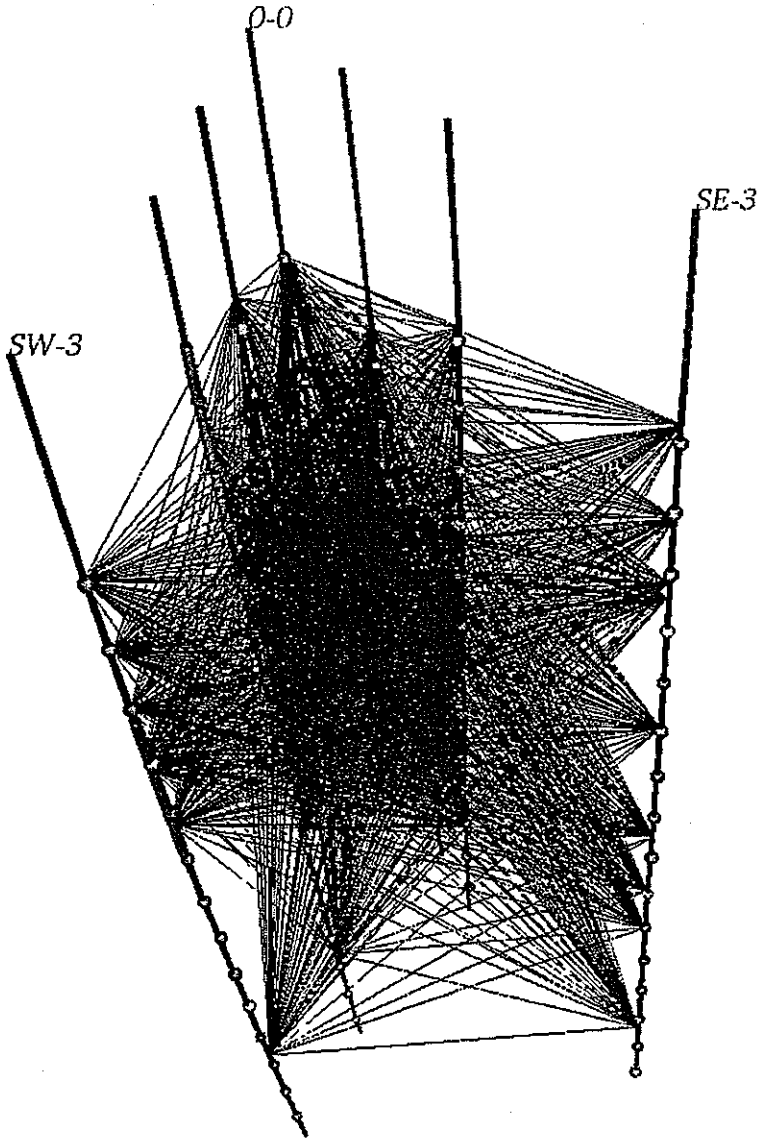

Figure 10(a). A perspective view of all the possible connections between intervals in the seven nearest wells.

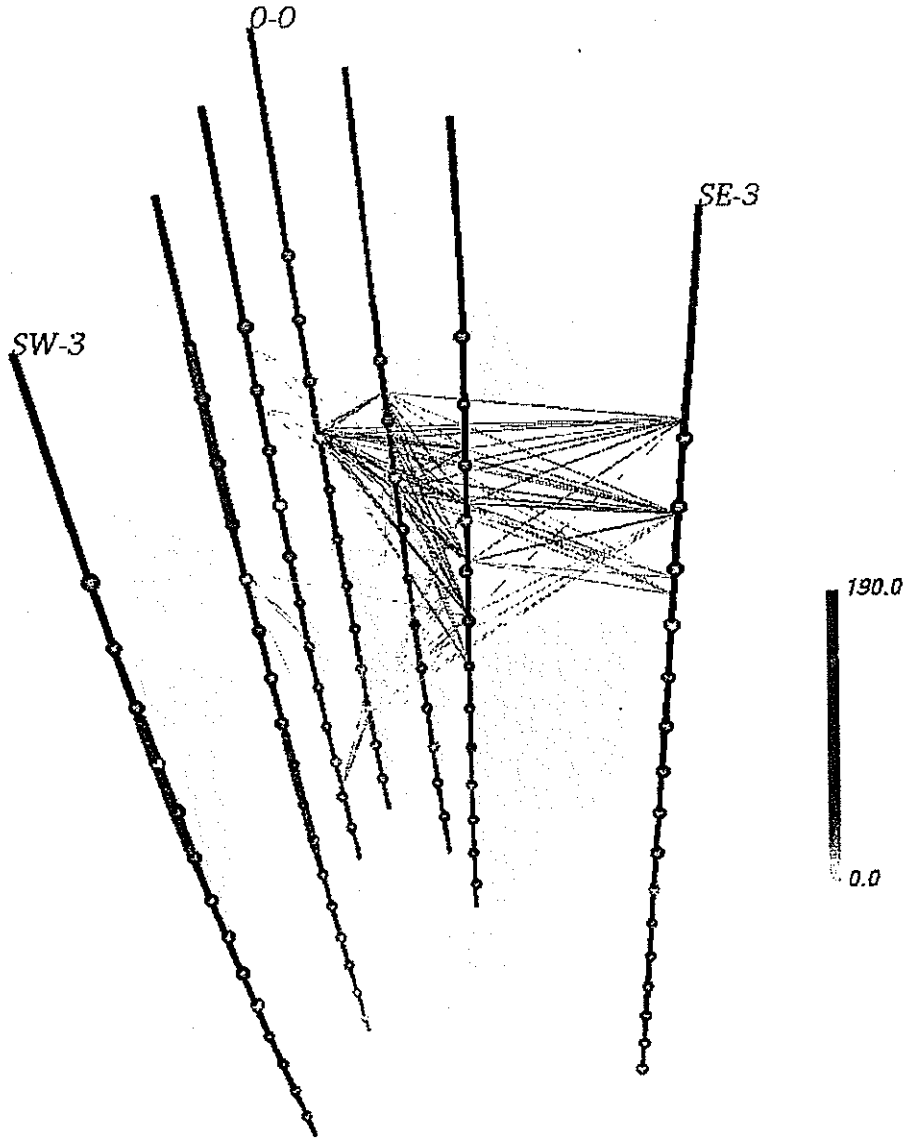

Figure 10(b). The result from the binary inversion analysis. Note that the connections are sparse and are concentrated in the two semi-horizontal planes. Also note that there are more connections in the SE direction. The color indicates the strength of response normalized by the flow rate and distance.

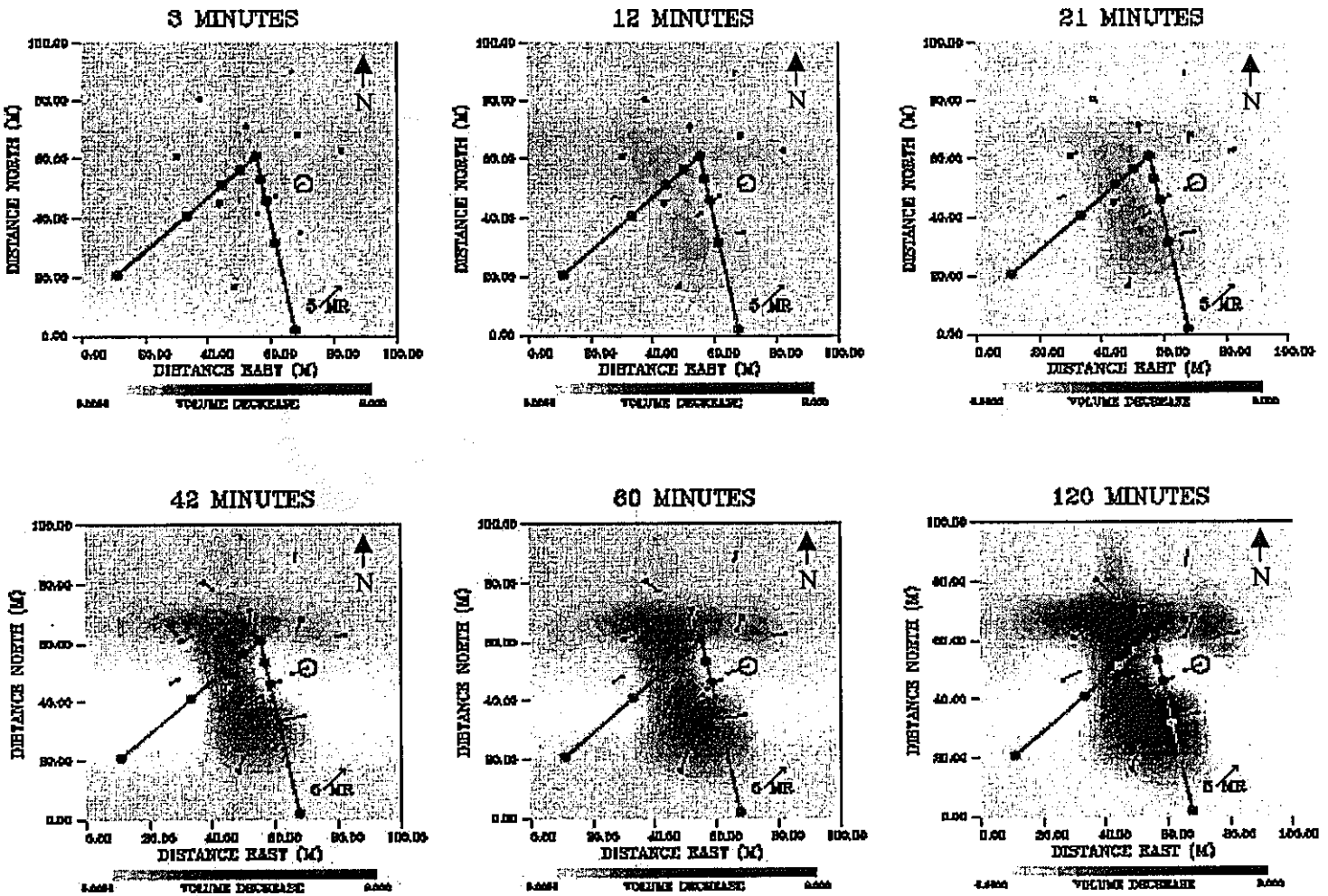

Figure 11 Inverted volume change distributions in the fracture zone at six different times during the pumping. The darker color indicates larger volume change. The observed tilt vectors and the well configuration are also shown. In all tiltmter surveys Well 0-0 (at the apex of the V) was pumped/injected.

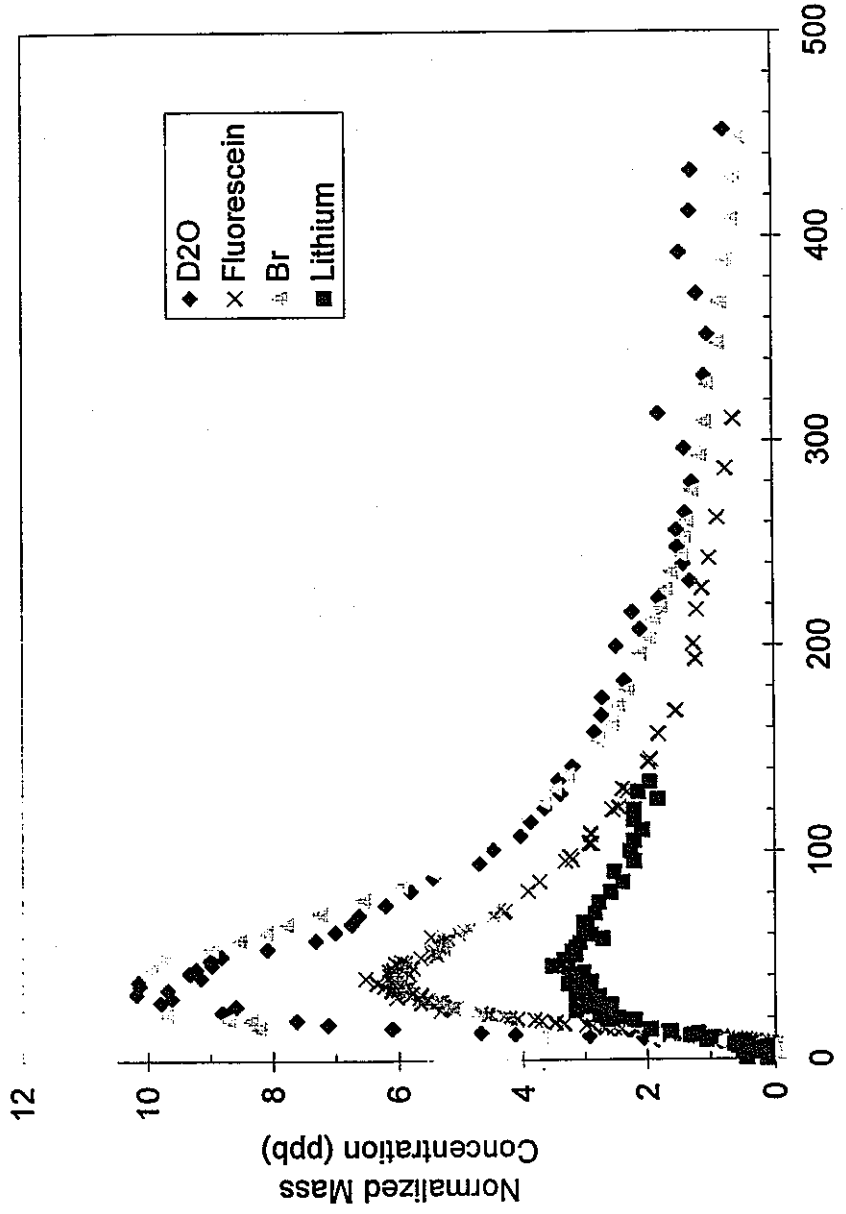

Figure 12 Tracer breakthrough curves from the weak dipole radial convergent test from well SE-3 to well 0-0. Note that deuterium, bromide and fluorescein are "conservative" tracers.

Dynamic Channeling of Flow and Transport in Saturated and Unsaturated Heterogeneous Media

Chin-Fu Tsang,[1] Luis Moreno,[2] Yvonne W. Tsang,[1] and Jens Birkhölzer[1]

[1]Earth Sciences Division
Ernest Orlando Lawrence Berkeley National Laboratory
University of California
Berkeley, California 94720

[2]Department of Chemical Engineering
Royal Institute of Technology
10044 Stockholm, Sweden

January 2000

The preparation of this report was supported by the Department of Energy, Office of Energy Research, Office of Basic Energy Sciences (DOE/ER-BES) Engineering and Geosciences Division, under Contract Number DE-AC03-76SF00098.

ABSTRACT

Dynamic channeling of flow and transport in strongly heterogeneous, saturated and unsaturated media is reviewed. Focusing or channeling of flow is dependent on both the permeability distribution and the pressure field. In the case of unsaturated media, it is also dependent on the degree of saturation. The emergence of flow channeling as a function of permeability variability (as measured by its standard deviation) and the spatial correlation range in three-dimensional porous systems is described. We also discuss the effects of channelized flow on two problems of practical interest for saturated and unsaturated heterogeneous media.

1. INTRODUCTION

Geologic formations consist of large scale heterogeneities, such as layering, regional zones, major faults and connected fractures, as well as smaller scale heterogeneities within each formation or region. We often assume that small scale heterogeneities can be smoothed, with its effects represented by a perturbation to the behavior of a homogeneous constant-property system. One well-known example is the problem of solute transport in a geologic formation. The solute velocity (advection) is calculated by assuming that the permeability of the medium is constant and the effect of heterogeneity caused by the presence of spatially varying permeability values is represented by a dispersion term which accounts for velocities greater and smaller than a mean velocity. This process is represented using the advective-dispersive equation, whose solution describes a solute plume migrating through a geologic formation with its boundaries smeared out due to the dispersion term. The tracer breakthrough curve (which is the solute or tracer concentration at an observation well or boundary, downstream from the source of the solute or tracer) displays a spread in time about the median tracer arrival time. The median arrival time can be calculated by assuming the medium to be homogeneous with constant properties.

The relationship between solute dispersion and the heterogeneity of the medium, characterized, for example, by the standard deviation around the geometric mean of permeability values, and the spatial correlation range, has been studied by many authors (Gelhar and Axness, 1983; Gelhar, 1986; Dagan, 1984, 1986, 1990; Neuman et al., 1987; Neuman and Zhang, 1990; Zhang and Neuman, 1990; Vomvoris and Gelhar, 1991; Graham and McLaughlin, 1990, 1991; Rubin, 1990, 1991a, 1991b; Tompson and Gelhar, 1990; Desbarats, 1990; Rajaram and Gelhar, 1991; Chin and Wang, 1992; Rubin and Dagan, 1992). In most of these studies, small variations in the hydraulic conductivities are assumed, and the applicability of results obtained is limited to moderately heterogeneous porous media. By moderately heterogeneous media, we mean that the standard deviation of log permeability $\log_{10}(k)$ is less than 1, or the standard deviation σ of natural log permeability, ln k, is less than approximately 2.

The interest in strongly heterogeneous system was stimulated by the study of flow in single fractures as represented by a two-dimensional (2-D) porous medium, whose permeability k at

every point is proportional to the square of the local fracture aperture. Tsang, Moreno, and coworkers (Tsang et al., 1988; Moreno et al., 1988, 1990; Moreno and Tsang, 1991) found that flow in strongly heterogeneous systems becomes channelized; i.e., it seeks out paths of least resistance, with a small percentage of the flow region carrying the main portion of the flow. Further, the velocity of this channelized flow can be as large as an order of magnitude more than the average flow rate expected if the medium were uniform (Tsang and Tsang, 1987, 1989). Later, the study was extended to three-dimensional (3-D) strongly heterogeneous systems (Moreno and Tsang, 1994). This kind of flow channeling may be termed "dynamic channeling", because it depends on both the permeability distribution and the pressure field applied to the system. Subsequently, it was found that such channeling effects also occur for water flow in 2D unsaturated media (Birkhölzer and Tsang, 1997). In this last case, the strength of the channeling effect and the locations of preferred flow paths are also dependent on the degree of saturation. In the present paper, flow in 3D unsaturated system is shown to exhibit similar results.

Flow channeling effects have been seen in many field experiments in fractured rocks. A review of these experiments was given by Tsang and Neretnieks (1998). The channeling model has been applied to analyze data from some of these experiments (see, for example, Tsang et al., 1991). For porous media, channelized flow has been noted in soils (Ghodrati and Jury, 1990; Booltink and Bouma, 1991; Roth et al., 1991; Flury et al., 1994; Buchter et al., 1995). The present paper gives an overview of flow channeling effects, and it is hoped that it will serve to stimulate further field studies from the view of the flow channeling phenomenon. In the next section, the basic approach to the calculation of flow channeling is described. Then the emergence of the channeling effect as a function of permeability standard deviation and spatial correlation length is presented. Following this, flow channeling effect for 3D unsaturated systems is discussed, and it is shown to be also a function of the average saturation level of the medium. Finally, the occurrence of channeling effects in two problems of practical interest for saturated and unsaturated heterogeneous media are described and their implications discussed.

2. BASIC APPROACH TO CALCULATE FLOW CHANNELING EFFECTS

We use a numerical approach to investigate the flow-channeling phenomenon because the strong heterogeneity precludes simple theoretical methods, which often use a perturbation approach applicable to cases with small standard deviations. A porous medium block is divided into cubic cells or grid elements of dimensions L_X, L_y, L_Z, where the three lengths are equal. These grid elements are assigned different permeability values according to a probability distribution. In our studies, we assume that the permeability values are lognormally distributed and correlated in space. An exponential covariance function is used, from which the permeability field can be generated using subroutines in a geostatistical software library (e.g. the SISIM module of GSLIB package by Deutsch and Journel, 1998). For each realization generated, the log permeability values in each grid element can be scaled about the mean, to obtain realizations with the same spatial correlation structure, but different standard deviations in permeability values (Tsang and Tsang, 1989). Thus, the probability distribution for lognormal permeability (k), with geometric mean k_o, may be written as,

$$f(k)dk = \frac{1}{(2\pi)^{1/2}\sigma k}\exp\frac{-(\ln k - \ln k_o)^2}{2\sigma^2}dk$$

$$= \frac{1}{(2\pi)^{1/2}\sigma}\exp\frac{-(\ln k - \ln k_o)^2}{2\sigma^2}d(\ln k).$$

If we replace $(\ln k - \ln k_o)$ by $\gamma(\ln k - \ln k_o)$ in this equation, we obtain again a lognormal distribution but with

$$\sigma \rightarrow \sigma/\gamma$$

where γ is a multiplicative factor to scale the standard deviation (σ) of the heterogeneous field. By choosing a range of γ values, we keep the same spatial structure but make the standard deviation vary over a wide range, from 0.5 to 6.0 in natural log. A standard deviation of 6.0 implies a very large variation in permeability over the porous medium block, so that 95% of the values are in an interval that covers about six orders of magnitude. We also use a range of values

for the spatial correlation length parameter in an exponential variagram model, from 0.025 to 0.2 times the transport distance. Note that for the exponential variagram, the effective correlation range is three times the spatial correlation length parameter.

Although the results presented in the paper are obtained using the particular geostatistical specifications as described above, similar results are also obtained with multiple realizations and alternative approaches, such as a non-parametric permeability distribution and spherical spatial correlation structures. Thus we believe that the conclusions presented in this paper on channeling as a function of permeability variance and spatial correlation length are independent of such specifics.

The flow calculations are based on steady-state flow conditions and followed the procedure used by Moreno et al. (1988), which was extended to three dimensions (Moreno and Tsang, 1994). In all the calculations, a pressure difference is assumed on two opposite faces of the rectangular porous-medium block with the remaining four sides closed to flow, and the porosity of the block is assumed to be constant. Then once the steady-state flow is calculated by, for example, a finite-difference method, the flow velocity at every point can be computed. Solute transport through the porous medium is simulated by a particle-tracking technique. Four thousand particles or more are introduced with the fluid at the high-pressure side of the porous block. The number of particles introduced in each inlet grid cell is proportional to the flow through that cell. They are randomly distributed on the inlet surface of the cell, and each particle is then followed through the porous medium. The particle tracking is carried out by calculating the velocity v of the particle in its actual location and then moving the particle a small distance $v\Delta t$. The time step Δt is set to be small enough to obtain consistent results. In most cases, Δt was set such that the travel distance is equal to 0.05 of the cell size. Using an even smaller time step increases the calculation time, but the accuracy of the results is only slightly improved.

Velocity is calculated using a three-dimensional linear interpolation scheme among the velocity vectors located at interfaces between the cell where the particle is located and all the adjacent cells. These velocity vectors are calculated from the pressure field computed earlier. No local dispersion within each path is considered in these calculations, but it may be included in a straightforward way (Tompson and Gelhar, 1990).

The particles are collected at the outlet surface, and the travel time for each particle is recorded. From this travel time distribution, we may determine the mean travel time and the variance of the travel times.

3. EMERGENCE OF FLOW CHANNELING WITH DEGREE OF HETEROGENEITY

Using the method described in the last section, we obtain results for both 2-D and 3-D flow in a heterogeneous medium. In Figures 1a–c, we show typical results for the 2-D case. In this case, a pressure difference is maintained between the upper and lower boundaries, while the side boundaries are closed to the flow. The flow domain is discretized into 200 × 200 grid cells and the spatial correlation length is chosen to be 0.05 of its linear dimension. Let us define λ and λ' as the ratios of, respectively, the spatial correlation length parameter and the effective correlation range to the flow dimension. Since the effective range is three times the correlation length parameter in exponential variogram, $\lambda = 0.05$ and $\lambda' = 0.15$ in these figures. The lines show the tracks of the fastest 90% of the particles. For a small standard deviation of natural log permeability, $\sigma = 0.5$, flow is essentially vertical. The travel time contrast is small among all the flow paths (see further discussions in Section 5 and Figure 8 below). However, as σ increases, this contrast greatly increases and flow is channelized (Figures 1b and 1c) with exit flow at the lower boundary concentrated at fewer and fewer locations.

Figures 1b and 1c may be compared with the experimental measurements by Bourke (1987) on a single fracture, which can be represented as a 2-D flow system with point permeability proportional to the square of the local fracture aperture. In his experiment, Bourke and his coworkers selected a fracture in the Cornish granite in England and drilled five boreholes in its plane with a length of about 2.5 m. Because the fracture plane undulates to a small extent, the five holes did not lie entirely in the fracture. Water was pressurized in one hole, and the holes on its two sides were divided into 7-cm intervals by the use of packers for measuring the flow rate into each of the different intervals. The process was repeated by pressurizing the five boreholes one at a time. Results showed that many of the packed intervals in the five boreholes did not receive inflows from the pressurized neighboring borehole. Figure 2 shows a sketch of the

connected flow pathways inferred from these measurements by Bourke (1987). As we can see, the flow areas occupy only about 20% of the fracture surface. This is mainly a result of the fracture apertures, and the corresponding permeability, not being uniform. Rather, the aperture varies over the fracture plane, and the pressurized water takes the easiest pathway from one drill hole to the other, resulting in channelized flow paths as shown.

Figures 3a–c show the results for 3-D, where the block is discretized into 40×40×40 grid cells and $\lambda' = 0.075$. Here again, for small σ, flow is vertical (Fig. 3a) with little contrast in travel time between fast and slow flows. As σ is increased to 2.0 and 6.0, flow becomes highly channelized, with exit flow on the lower boundary concentrated at a few discrete locations: ($x \sim 22$, $y \sim 15$), ($x \sim 5$, $y \sim 10$), ($x \sim 15$, $y \sim 15$) and ($x \sim 5$, $y \sim 35$).

Flow channeling also depends on the spatial correlation range as a fraction λ' of the flow distance. If λ' is small, though channeling does occur, the channels are closely spaced, and there are many of them over the flow domain, its effect is "averaged out." However, for λ' larger than ~0.3, it is found that flow channeling is important and is not very sensitive to the exact λ' value. Some typical results are shown in Figures 4a–c for the same σ value of 2.0, but λ' of 0.015, 0.15, 0.3 respectively.

Note that these flow channels are not the same as, but are in addition to, the discrete and connected high-permeability paths that may be present and visually discernable in the permeability spatial distribution. These channels occur because flow seeks out paths of least resistance in the heterogeneous medium under the applied pressure gradient. Thus, different flow channeling patterns are obtained as the pressure gradient changes in direction. We may call this "dynamic channeling" to emphasize the fact that these fast flow paths are a function of both the permeability distribution and the pressure field.

4. FLOW CHANNELING IN UNSATURATED POROUS MEDIA

Flow channeling effects as shown above for saturated porous media are expected to also occur for unsaturated systems, as has been shown by Birkhölzer and Tsang (1997), Roth (1995), and Roth and Hammel (1996) for 2-D systems. In this section, we shall show the results for 3-D

unsaturated media. To calculate liquid flow in the unsaturated case, we consider percolation under gravity. An effective permeability can be defined as the product of the intrinsic (or saturated) permeability k and the relative permeability k_r. The pressure is the sum of a capillary pressure P_{cap} and the reference pressure.

Both the capillary pressure and relative permeability depend on the saturation, and characteristic functions are used to describe these relations. In our study, we use the well-known van Genuchten-Mualem capillary pressure and relative permeability model [van Genuchten, 1980; Mualem, 1978], given as

$$P_{cap}(S_e) = -\frac{1}{\alpha}\left\{(S_e)^{-n/(n-1)} - 1\right\}^{1/n}$$

$$k_r(S_e) = (S_e)^{0.5}\left\{1-\left(1-(S_e)^{n/(n-1)}\right)^{1-1/n}\right\}^2$$

with the effective saturation defined as

$$S_e = (S - S_r)/(1 - S_r) .$$

Here S_r is the residual saturation, α is a scaling factor for the capillary-pressure function, and n characterizes the distribution of pore sizes within each grid element ($1 < n < \infty$).

In a heterogeneous porous medium, the characteristic functions of capillary pressure and relative permeability are not spatially constant. Areas of high permeability are expected to drain faster, on account of the large pore sizes and less capillary strength. Likewise, areas of low permeability are expected to maintain larger water saturations, on account of smaller pore sizes and stronger capillary suction. Consequently, areas with different permeabilities in our model region have to be assigned different capillary pressure functions. This is done by using spatially varying scaling factors α for the capillary pressure function. Leverett (1941) proposed a model to calculate the scaling factor α at a given location with permeability k as follows:

$$\alpha = \overline{\alpha}\left(k/\overline{k}\right)^{0.5}$$

where $\bar{k}$ and $\bar{\alpha}$ are reference values for the permeability and scaling factor, respectively. A number of investigators have shown that the above relationship holds for a variety of different soils (e.g., Davies, 1991; Wang, 1992).

In our study, we used the TOUGH2 code (Pruess, 1991), and the reference values for the scaling law are given as 10^{-12} m^2 = 1 μm^2 for the permeability $\bar{k}$ (equal to the geometric mean) and 10^{-4} Pa^{-1} for the scaling factor $\bar{\alpha}$. For the sake of simplicity, we assume that the spatial variability of pore sizes does not change from cell to cell within the model area. Then, the pore-size distribution coefficient n is not modified, allowing the relative permeability function to be the same over the whole model area. Sensitivity studies made (Birkholzer et al., 1999) have shown that the results are not sensitive to the exact value of n. We choose a pore size distribution coefficient of n = 2 and a residual saturation of S_r = 0.2. Note that for an unsaturated medium, the effective permeability is the product of intrinsic (or saturated) permeability and the relative permeability, so that the effective permeability values may have a wide spread even though the saturated permeability may have less variability, because of the saturation-dependent relative permeability function. It is the variation in effective permeability that gives rise to the channeling phenomenon.

Again, using the SISIM module of the GSLIB Geostatistical library (Deutsch and Journel, 1998), a 3-D heterogeneous field is generated on a $40 \times 40 \times 40$ grid to model a $10 \times 10 \times 10$ m^3 block. The four side boundaries are assumed to be closed to flow, and percolation inflow is imposed on the upper boundary at rates 1, 10^{-1}, 10^{-2}, 10^{-3}, and 10^{-5} times the flow rate Q_S, where Q_S is a large inflow rate which would result in fully saturated block at steady state (Birkhölzer and Tsang, 1997).

Figures 5a–c show the heterogeneous field and the saturation distributions for percolation rates 10^{-5} Q_S (low infiltration case, U1) and 10^{-2} Q_S (moderately high infiltration case, U3) cases, respectively. For this set of calculations, the mean intrinsic permeability is 1 μm^2, λ = 0.05, and σ = 4 in natural log (which is the same as σ = 1.737 in log to the base 10). Note that high saturation (and hence high liquid flow) locations are found near low-permeability (and hence high capillary) areas for the low-inflow case U1 with a low overall saturation. However, at higher inflow, it is not as clear that the anti-correlation holds. Further, we know that if the

medium is fully saturated, most liquid flow will be by way of high permeability areas, which is complementary to the U1 case.

Flow lines for the cases are calculated using the particle tracking technique described above. Figures 6a–c show these flow lines respectively for low inflow case U1; intermediate inflow case U3; and large inflow case S, in which the flow rate is Q_S. In case S, the 3-D block becomes fully saturated and corresponds to the situation described in Section 3. For results shown in Figure 6, the intrinsic permeability distributions in all the cases are identical. Note that strong flow-channeling is seen in the saturated case S and also in the low-inflow, low-saturation case U1, but is less important in the intermediate mean saturation case. The occurrence of an intermediate mean-saturation case where channeling is minimal was pointed out by Roth and Hammel (1996) and by Birkhölzer and Tsang (1997), and further discussion is presented in these references. Tracer breakthrough curves for the unsaturated heterogeneous systems as a function of saturation are also presented in Birkholzer and Tsang (1997).

As to be expected, the flow channels in case S and case U1 do not coincide, but rather they are complementary, i.e., the flow channels in case S are found exactly where channels do not occur in case U1. This result is further illustrated in Figure 7, which shows the permeability probability distribution sampled by the flow lines in the heterogeneous medium under different conditions. The broken line shows the intrinsic permeability probability distribution over the block. For the saturated case, Case S, lowest figure, the flow mainly samples the large permeability values, while for the "dryer" Case U1, the flow samples the low permeability values where the capillary effects are stronger. For the intermediate saturation case, the flow samples the middle-range values of permeability. In all cases, the range or standard deviation of permeability values sampled is less than that of the intrinsic permeability.

The results presented in this section demonstrate that the dynamic channeling effect for the unsaturated heterogeneous system depends not only on the permeability distribution and the pressure field, but also on the degree of saturation.

5. IMPLICATION OF FLOW CHANNELING ON TRACER BREAKTHROUGH CURVES FOR SATURATED MEDIA

In this and the next section, we discuss two practical problems for saturated and unsaturated media where flow channeling can play an important role. The first example is tracer transport in saturated porous media.

Let us consider the flow fields presented in Section 3 and Figures 3a-c. Let solute be deposited at the upper inflow boundary at time t = 0 and let it be followed by particle or tracer tracking. The particles representing the solute are then collected as a function of time at the lower exit boundary, integrated over the lower boundary area. Summing the arrivals of the particles builds up the tracer breakthrough curves, which describe the arrival of the solute resulting from a unit release at the upper boundary.

Figures 8a-b show breakthrough curves for different standard deviations in the permeability distribution and for two different ratios of the effective correlation range to travel distance. For the large correlation range ($\lambda' = 0.30$; Figure 8b), the breakthrough curves for small heterogeneity show a clear peak at t=1, which is the time of arrival if the porous medium has uniform permeability. When heterogeneity increases, the peak is wider and moves in the direction of shorter travel time, with a longer tail towards large travel times. If the heterogeneity becomes extremely large ($\sigma = 4$ or 6), the curves show a narrow peak again, but at very short travel times, and a long tail. When a very short correlation range was used ($\lambda' = 0.075$ case, Figure 8a), a clear peak at t=1 is obtained for porous media with small heterogeneity. As σ is made larger, the peak of the breakthrough curves is wider, but no clear peak is observed for the very large heterogeneity values. In the case (not shown in Figure 8) where a very large ratio of correlation range to travel length is used ($\lambda' > 0.6$), a clear peak at a very short travel time is displayed for extremely large heterogeneity values, but no single peak dominates when the standard deviation is decreased to 0.5 or smaller.

The solution of the conventional advective-dispersive equation describes well the situation shown in Figure 8a or Figure 8b for very small σ values up to approximately $\sigma = 1.0$ (see curves labeled $\sigma = 0.5$ and $\sigma = 1.0$). The velocities peak around the mean flow velocity with arrival time

t=1 and are symmetric on either side of the mean flow velocity. The spread of velocities about the mean increases with σ. However, as σ becomes much larger, with σ > 1.0, flow begins to be focused in a few channels (see Figures 3b-c), and the breakthrough curves show a much earlier peak, quite distinct from the t=1 peak, and a long tail. The early peak arrives at possibly one-tenth the time of travel in a constant-permeability medium (see σ = 6.0 case in Figure 8b). Such a phenomenon is believed to be seen in a number of field experiments (see, for example, the review by Tsang and Neretnieks, 1998). In particular, the field experiment described by Hadermann and Heer (1996) clearly show such results for a 2-D case.

These results have important practical significance. First, because of flow channeling, the peak arrival of a contaminant plume could be as much as an order of magnitude sooner than expected. This is an important concern for evaluating the potential migration of a contaminant plume, and its possibility needs to be accounted for in safety assessment. Second, because of the emergence of flow channeling at strong heterogeneity, the use of the conventional advective-dispersive equation to analyze this class of tracer breakthrough curves is very much in question.

6. IMPLICATION OF FLOW CHANNELING ON SEEPAGE INTO AN UNDERGROUND CAVITY IN UNSATURATED MEDIUM

Philip et al. (1989) presented the general theory of water exclusion from, or entry to, subterranean openings in a homogeneous uniform medium from steady, downward flow; and developed an analytical solution of the exclusion problem for cylindrical cavities. The solution is based on the assumption of an infinite flow region and spatially uniform downward flow far away from the cavity. If no water enters into the cavity, the gravity-driven downward flux must be diverted around the obstacle. From Darcy's law, this diversion requires a saturation increase at the crown of the opening to provide a pressure gradient driving water sideways and downwards. Thus an upstream retarded region develops, which culminates in an upstream stagnation point at the crown where zero velocity and maximum pressure is found. As water is diverted sideways and around the cavity, it forms a "roof drip lobe", with higher saturation and thus higher relative permeability and flow velocity. The stagnation point at the crown is the most likely location for water to reach full saturation, S = 1, at which condition the capillary barrier

presented by the drift becomes zero and water begins to seep into the open cavity. Philip et al. (1989) give an approximate expression for seepage to occur. Consider the case where the radius of the opening r = 5.0 m, k for the uniform medium = 10^{-13} m^2, $\alpha = 9.78 \times 10^{-4}$ 1/Pa, n = 2.7, and S_r = 0.01(Birkholzer et al. 1999). This happens to be the set of parameters appropriate to the Yucca Mountain site in Nevada where a large research program is underway to evaluate its suitability as a host site for a potential nuclear waste repository. We then find from Philip's theory that the percolation influx from the top of the domain must be larger than 1200 mm/yr before sufficient saturation is built up at the crown of the opening for seepage to occur.

However, if heterogeneity is present, the findings are substantially different. Birkhölzer et al. (1999) examined the case where $\sigma = 2.1$ in natural log and the spatial correlation length is 2 m, using three realizations of the generated heterogeneous field. A series of percolation influx rates were used from 10 to 1000 mm/yr. To show the flow pattern, we present in Figure 9 the saturation contours in three horizontal slices and three vertical slices of the 3-D block for 1000 mm/yr percolation flux. This figure clearly indicates the disturbance of the saturation distribution because of the presence of the drift. Thus, in the horizontal plane just above the drift, liquid accumulates at the crown as the vertical gravity-driven flow is being diverted around it, while in the horizontal plane below the drift, a low-saturation shadow develops. In addition to this flow-perturbation effect, the saturation contours also reflect the heterogeneity of the model area, showing several locations where "channelized" flow accumulates to high saturation values dependent on local permeability contrasts. At locations where the channelized flow reaches the cavity walls, the flow accumulates and the saturation increases toward unity, at which time water begins to seep into the cavity at these locations. For the particular example here, we find that seepage occurs when the percolation influx is about 25 mm/yr, about 50 times less than the result (>1200 mm/yr) for a homogeneous medium in the absence of flow channeling.

7. SUMMARY AND REMARKS

Dynamic channeling of flow and transport in strongly heterogeneous porous media gives rise to fast and localized flow paths, which are dependent on both the permeability distribution and the pressure field, and, for the case of unsaturated media, also on the degree of saturation. These

fast flow-paths occur in addition to the usual fast flow associated with the presence of connected high-permeablity zones, like faults or a series of connected fractures which can usually be traced visually in a fracture map. In this paper, we use a simple model to study the emergence of dynamic channelizing as a function of permeability variation and spatial correlation range, σ and λ'. Further, for an unsaturated medium, flow channeling is also shown to be dependent on the mean saturation of the medium, with the channeling effect strongest at low and full saturations, and a minimum effect at an intermediate mean-saturation value.

Dynamic channeling is a new area for study, requiring further investigation with respect to practical problems in the field. In this paper, two such problems are discussed as examples, (1) solute migration breakthrough curves and (2) potential seepage into an opening in unsaturated rocks. Studies of other problems that may be also affected by flow channeling are underway.

The study of flow channeling requires a stochastic approach because it is often difficult to have detailed deterministic data on spatial permeability distribution. The results obtained in such a study will also be stochastic. Thus, we have to consider multiple realizations, probabilities, and expectation. How to apply such results to practical problems of contaminant migration and safety assessment is still an open question.

ACKNOWLEDGMENTS.

Reviews and comments by Christine Doughty, Todd Rasmussen, Jonny Rutqvist and Vince Tidwell are very much appreciated. We thank Tom Nicholson for his encouragement of the preparation of this paper. We would also like to acknowledge that, as far as we are aware, the term 'dynamic channeling" was coined by Shlomo Neuman. This work was jointly supported by the Japan Nuclear Cycle Development Institute (JNC) under a Binational JNC/DOE Collaborative Agreement Annex with DOE Office of Environmental Management, Office of Science and Technology, and by the Director, Office of Science, Office of Basic Energy Sciences, of the U.S. Department of Energy (DOE) under Contract No. DE-AC03-76SF00098.

REFERENCES

Birkhölzer, J. and C.F. Tsang (1997). Solute Channeling in Unsaturated Heterogeneous Porous Media, *Water Resour. Res.* 33(10), 2221–2238, June, 1997.

Birkhölzer, J., G. Li, C.F. Tsang, and Y. Tsang (1999). Modeling Studies and Analysis of Seepage into Drifts at Yucca Mountain. *Journal of Contaminant Hydrology* 38(1–3), 349–384.

Booltink, H.W.G. and J. Bouma (1991). Physical and morphological characterization of bypass flow in a well-structured clay soil, *Soil Sci. Soc. Am. J.*, 55, 1249–1254.

Bourke, P.J. (1987). Channeling of Flow Through Fractures in Rock, *Proceedings of GEOVAL-1987 International Symposium*, pp. 167-178. Swedish Nuclear Power Inspectorate (SKI), Stockholm, Sweden, April 7–9.

Buchter, B., C. Hinz, M. Flury, and H. Flühler (1995). Heterogeneous flow and solute transport in an unsaturated stony soil monolith, *Soil Sci. Soc. Am. J.*, 59, 14–21.

Chin, D.A. and T. Wang (1992). An Investigation of the Validity of First-Order Stochastic Dispersion Theories in Isotropic Porous Media, *Water Resourc. Res.* 28(6), 1531–1542.

Dagan, G. (1984). Solute Transport in Heterogeneous Porous Formations, *J. Fluid Mech.* 145, 141–177.

Dagan, G. (1986). Statistical Theory of Groundwater Flow and Transport: Pore to Laboratory, Laboratory to Formation, and Formation to Regional Scale, *Water Resourc. Res.* 22(9), 120S–134S.

Dagan, G. (1990). Transport in Heterogeneous Porous Formations: Spatial Moments, Ergodicity, and Effective Dispersion, *Water Resourc. Res.* 26(6), 1281–1290.

Davies, P.B. (1991). Evaluation of the Role of Threshold Pressure in Controlling Flow of Waste-Generated Gas into Bedded Salt at the Waste Isolation Plant, Sandia National Laboratories report SAND90-3246, Albuquerque, NM.

Desbarats, A.J. (1990). Macrodispersion in Sand-Shale Sequences, *Water Resourc. Res.* 26(1), 153–163.

Deutsch, C.V., and A.G. Journel (1998). GSLIB, Geostatistical Software Library and User's Guide, Oxford University Press, 2nd ed., New York.

Flury, M., H. Flühler, W.A. Jury, and J. Leuenberger (1994). Susceptibility of soils to preferential flow of water: A field study, *Water Resour. Res.*, 30, 1945–1954, 1994.

Gelhar, L.W. (1986). Stochastic Subsurface Hydrology. From Theory to Applications, *Water Resour. Res.* 22(9), 135S–145S.

Gelhar, L.W. and C.L. Axness (1983). Three-Dimensional Stochastic Analysis of Macrodispersion in Aquifers, *Water Resourc. Res.* 19(1), 161–180.

Ghodrati, M. and W.A. Jury (1990). A field study using dyes to characterize preferential flow of water, *Soil Sci. Soc. Am. J.*, 54, 1558–1563.

Graham, W., D.B. McLaughlin (1990). Stochastic Analysis of Nonstationary Subsurface Solute Transport. 1. Unconditional Moments, *Water Resourc. Res.* 25(2), 215–232.

Graham, W., D.B. McLaughlin (1991). A Stochastic Model of Solute Transport in Groundwater: Applications to the Borden, Ontario, tracer test, *Water Resourc. Res.* 27(6), 1345–1359.

Hadermann, J. and W. Heer (1996). The Grimsel (Switzerland) Migration Experiment—Integrating Field Experiments, Laboratory Investigations and Modelling, *Journal of Contaminant Hydrology* 21(1–4), 87–100.

Leverett, M.C. (1941). Capillary behavior in porous solids, *AIME Trans.*, Vol. 142.

Moreno, L. and C.-F. Tsang (1991). Multiple-Peak Response to Tracer Injection Tests in Single Fractures: A Numerical Study, *Water Resour. Res.* 27(8), 2143–2150.

Moreno, L. and C.-F. Tsang (1994). Flow Channeling in Strongly Heterogeneous Porous Media: A Numerical Study, *Water Resources Research* 30(5), p. 1421–1430.

Moreno, L., C.F. Tsang, Y.W. Tsang, and I. Neretnieks (1990). Some Anomalous Features of Flow and Solute Transport Arising from Fracture Aperture Variability, *Water Resourc. Res.* 26(10), 2377–2391.

Moreno, L., Y.W. Tsang, C.-F. Tsang, F.V. Hale, and I. Neretnieks (1988). Flow and Tracer Transport in a Single Fracture: A Stochastic Model and Its Relation to Some Field Observations, *Water Resour. Res.* 24(12), 2033–2048.

Mualem, Y. (1978). A New Model for Predicting the Hydraulic Conductivity of Unsaturated Porous Media, *Water Resourc. Res.* 12, 513–522.

Neuman, S.P., and Y-K. Zhang (1990). A Quasi-Linear Theory of Non-Fickian and Fickian Subsurface Dispersion. 1. Theoretical Analysis With Application to Isotropic Media, *Water Resourc. Res.* 26(5), 887–902.

Neuman, S.P., C.L. Winter, and C.M. Newman (1987). Stochastic Theory of Field-Scale Dispersion in Anisotropic Porous Media, *Water Resourc. Res.* 23(3), 453–466.

Philip, J.R., J.H. Knight, and R.T. Waechter (1989). Unsaturated Seepage and Subterranean Holes: Conspectus, and Exclusion Problem for Circular Cylindrical Cavities. *Water Resources Research* 25(1), 16–28.

Pruess, K. (1991). TOUGH2 - A General-Purpose Numerical Simulator for Multiphase Fluid and Heat Flow, Lawrence Berkeley Laboratory report LBL-29400, Berkeley, CA.

Rajaram, H. and L.W. Gelhar (1991). Three-Dimensional Spatial Moments Analysis of the Borden Tracer Tests, *Water Resourc. Res.* 27(6), 1239–1251.

Roth, K. (1995). Steady state flow in an unsaturated, two-dimensional, macroscopically homogeneous Miller-similar medium, *Water Resour. Res.*, 31, 2127–2140.

Roth, K. and K. Hammel (1996). Transport of conservative chemical through an unsaturated two-dimensional Miller-similar medium with steady state flow, *Water Resourc. Res.* 32(6), 1653–1663, June 1996.

Roth, K., W.A. Jury, H. Flühler, and W. Attinger (1991). Transport of chloride through an unsaturated field soil, *Water Resour. Res.*, 27, 2533–2541.

Rubin, Y. (1990). Stochastic Modeling of Macrodispersion in Heterogeneous Porous Media, *Water Resourc. Res.* 26(1), 133–141.

Rubin, Y. (1991a). Prediction of Tracer Plume Migration in Disordered Porous Media by the Method of Conditional Probabilities, *Water Resourc. Res.* 27(6), 1291–1308.

Rubin, Y. (1991b). Transport in Heterogeneous Porous Media: Prediction and Uncertainty, *Water Resourc. Res.* 27(7), 1723–1738.

Rubin, Y. and G. Dagan (1992). Conditional Estimation of Solute Travel Time In Heterogeneous Formations: Impact of Transmissivity Measurements, *Water Resourc. Res.* 28(4), 1033–1040.

Tompson, A.F.B. and L.W. Gelhar (1990). Numerical Simulation of Solute Transport in Three-Dimensional, Randomly Heterogeneous Porous Media, *Water Resourc. Res.* 26(10), 2541–2562.

Tsang, C.F. and I. Neretnieks (1998). Flow Channeling in Heterogeneous Fractured Rocks. Reviews of Geophysics, Vol. 36, No. 2, pp. 275–298, May, 1998.

Tsang, C.F., Y.W. Tsang, and F.V. Hale (1991). Tracer Transport in Fractures: Analysis of Field Data Based on a Variable-Aperture Channel Model, *Water Resour. Res.* 27(12), 3095–3106.

Tsang, Y.W. and C.F. Tsang (1987). Channel Model of Flow Through Fractured Media, *Water Resour. Res.* 23(3), 467–479.

Tsang, Y.W. and C.F. Tsang (1989). Flow Channeling in a Single Fracture as a Two-Dimensional Strongly Heterogeneous Permeable Medium, *Water Resourc. Res.* 25(9), 2076–2080.

Tsang, Y.W., C.F. Tsang, I. Neretnieks, and L. Moreno (1988). Flow and Tracer Transport in Fractured Media: A Variable Aperture Channel Model and Its Properties, *Water Resour. Res.* 24(12), 2049–2060.

van Genuchten, M.T. (1980). A Closed-Form Equation for Predicting the Hydraulic Conductivity of Unsaturated Soil, *Soil Sci. Soc. Am. J.*, 892–898.

Vomvoris, E.G., L.W. Gelhar (1991). Stochastic Analysis of the Concentration Variability in a Three-Dimensional Heterogeneous Aquifer, *Water Resourc. Res.* 26(10), 2591–2602.

Wang, J.S.Y. (1992). Variations of Hydrological Parameters of Tuff and Soil, Proceedings of the Third Annual International High-Level Radioactive Waste Management Conference at Las Vegas, NV, 727–731.

Zhang, Y-K. and S.P. Neuman (1990). A Quasi-Linear Theory of Non-Fickian and Fickian Subsurface Dispersion. Application to Anisotropic Media and the Borden Site, *Water Resourc. Res.* 26(5), 887–902.

FIGURE CAPTIONS

Figure 1 a-c. Emergence of flow channeling, under a pressure step applied from the top to the bottom boundary, as a function of σ for a 2D heterogeneous medium. Tracer flow paths are shown for $\lambda' = 0.15$ and $\sigma = 0.5$, 2.0, and 6.0 in figures a, b, and c respectively. Numbers on the x and y axes indicate the number of grid elements so that the flow domain is 200 x 200 and the effective spatial correlation range is $200\lambda'$.

Figure 2. Flow channeling observed in the plane of a single fracture. The five boreholes are drilled in the fracture plane, which is, however, not entirely flat; thus some parts of boreholes are outside the fracture plane. Flow channels are found by cross-hole pressure-flow tests between isolated intervals (7-cm long) in the five boreholes. They are indicated as A, B, C, and D. (Taken from Bourke, 1987).

Figure 3 a-c. Emergence of flow channeling, under a pressure step applied from the top to the bottom boundary, as a function of σ for a 3D heterogeneous medium. Tracer flow paths are shown for $\lambda' = 0.075$ and $\sigma = 0.5$, 2.0, and 6.0 in figures a, b, and c respectively. Numbers on the x and y axes indicate the number of grid elements so that the flow domain is 40 x 40 x 40 and the effective spatial correlation range is $40\lambda'$.

Figure 4 a-c. Emergence of flow channeling, under a pressure step applied from the top to the bottom boundary, as a function of λ' for a 2D heterogeneous medium. Tracer flow paths are shown for $\sigma = 2.0$ and $\lambda' = 0.015$, 0.15, and 0.3 in figures a, b, and c respectively. Numbers on the x and y axes indicate the number of grid elements so that the flow domain is 200 x 200 and the effective spatial correlation range is $200\lambda'$.

Figure 5 a–c. (a) Spatial distribution of intrinsic permeability in $\log_{10}$ (k/k_{mean}). (b) Spatial distribution of water saturation for a low infiltration case (low mean saturation). (c) Spatial distribution of water saturation for a higher infiltration case (moderate mean saturation).

Figure 6. Flow paths are shown for a low infiltration, low mean saturation (a); intermediate infiltration and mean saturation (b); and large infiltration and fully saturated case (c). Note that flow channeling is strong for (a) and (c), but not so pronounced in (b).

Figure 7. Frequency distribution of intrinsic permeability for the flow channels (solid lines) and the entire flow domain (dotted line), for three cases of low, intermediate and full saturations, cases U1, U3 and S, respectively.

Figure 8 a–b. Breakthrough curves for different standard deviation σ values and for a ratio of correlation length to travel length λ' of .075 and 0.3 in figures a and b respectively. The x-axis gives the arrival time normalized to (i.e. in units of) the expected time if the medium were of constant permeability. The y-axis gives the concentration as a fraction of the input pulse concentration.

Figure 9. Saturation profiles in a 3D heterogeneous block with a drift, under percolation flux of 1000 mm/yr on the top boundary.

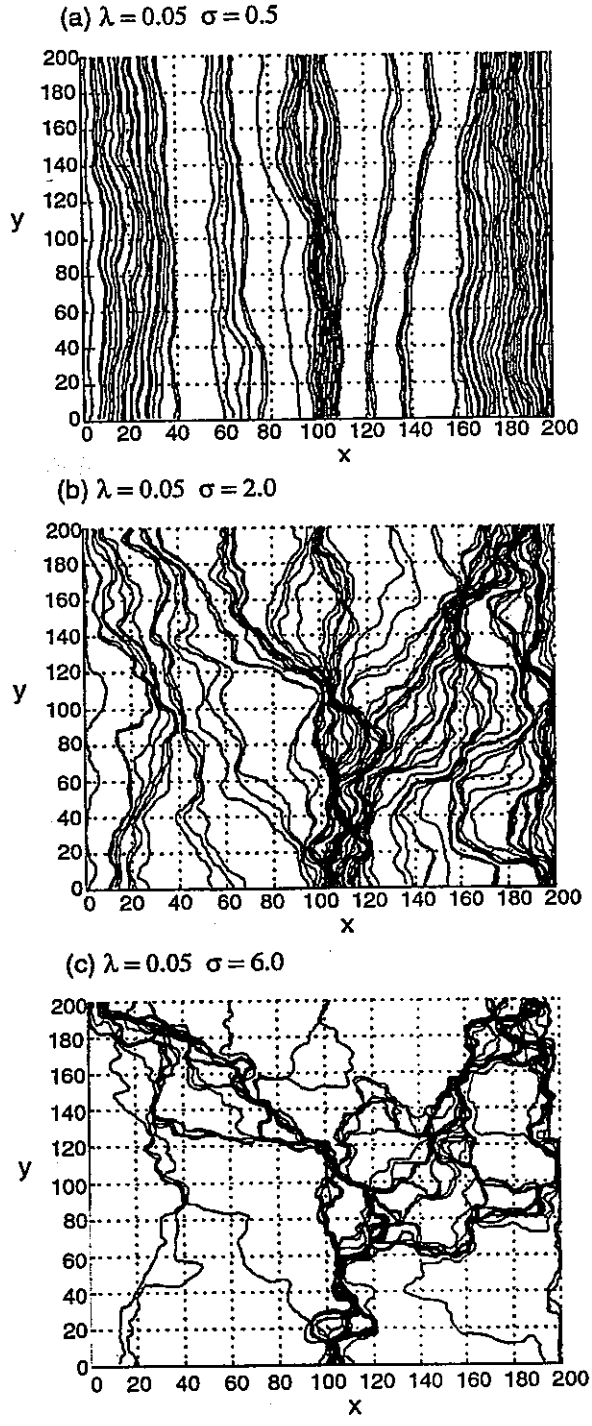

Figure 1 a-c. Emergence of flow channeling, under a pressure step applied from the top to the bottom boundary, as a function of σ for a 2D heterogeneous medium. Tracer flow paths are shown for $\lambda' = 0.15$ and $\sigma = 0.5$, 2.0, and 6.0 in figures a, b, and c respectively. Numbers on the x and y axes indicate the number of grid elements so that the flow domain is 200 x 200 and the effective spatial correlation range is $200\lambda'$.

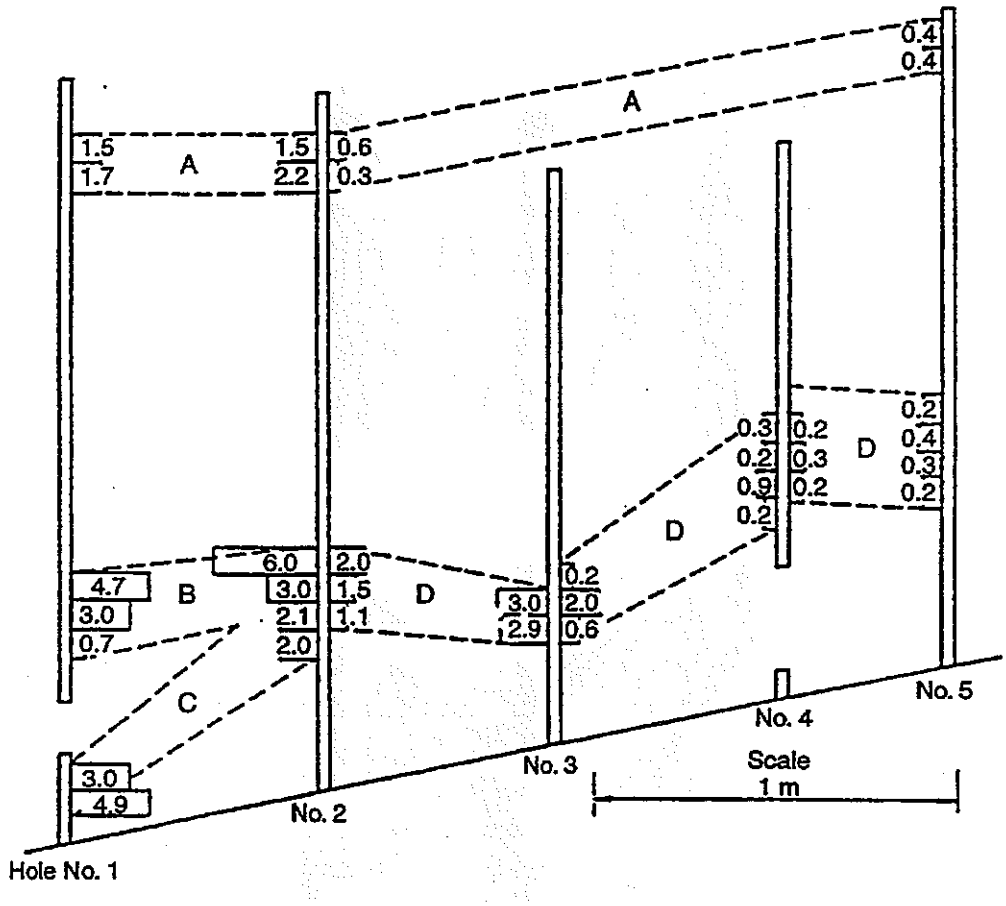

Figure 2. Flow channeling observed in the plane of a single fracture. The five boreholes are drilled in the fracture plane, which is, however, not entirely flat; thus some parts of boreholes are outside the fracture plane. Flow channels are found by cross-hole pressure-flow tests between isolated intervals (7-cm long) in the five boreholes. They are indicated as A, B, C, and D. (Taken from Bourke, 1987).

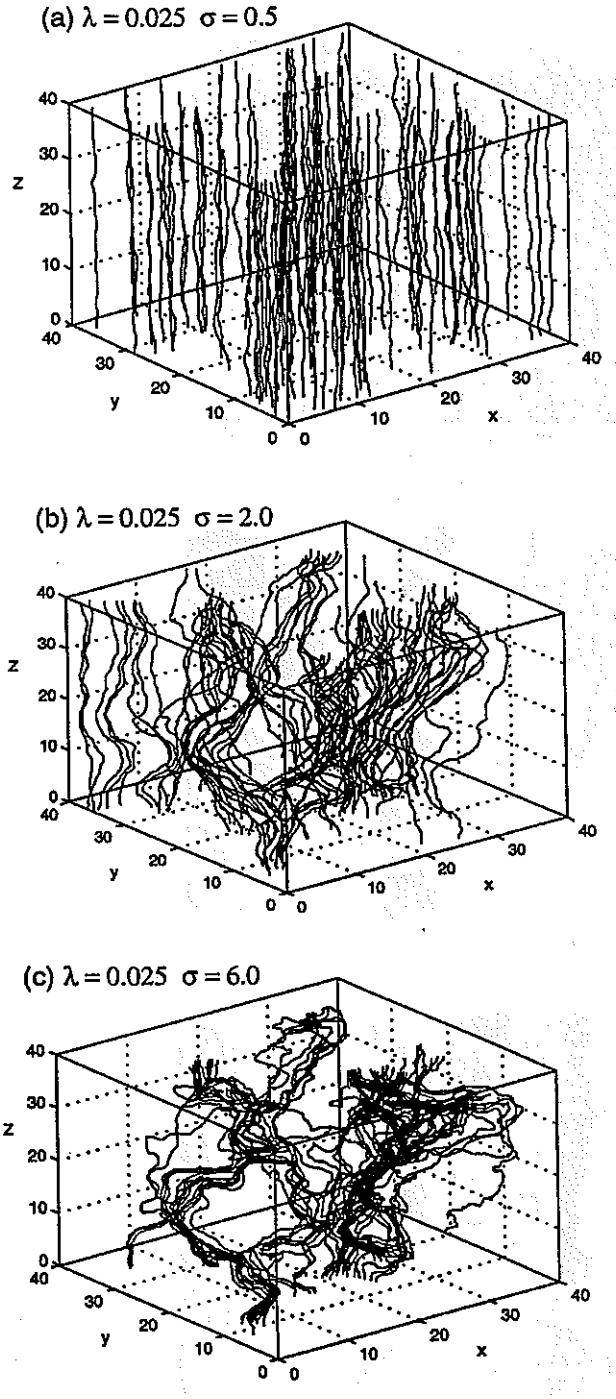

Figure 3 a-c. Emergence of flow channeling, under a pressure step applied from the top to the bottom boundary, as a function of σ for a 3D heterogeneous medium. Tracer flow paths are shown for $\lambda' = 0.075$ and $\sigma = 0.5$, 2.0, and 6.0 in figures a, b, and c respectively. Numbers on the x and y axes indicate the number of grid elements so that the flow domain is 40 x 40 x 40 and the effective spatial correlation range is $40\lambda'$.

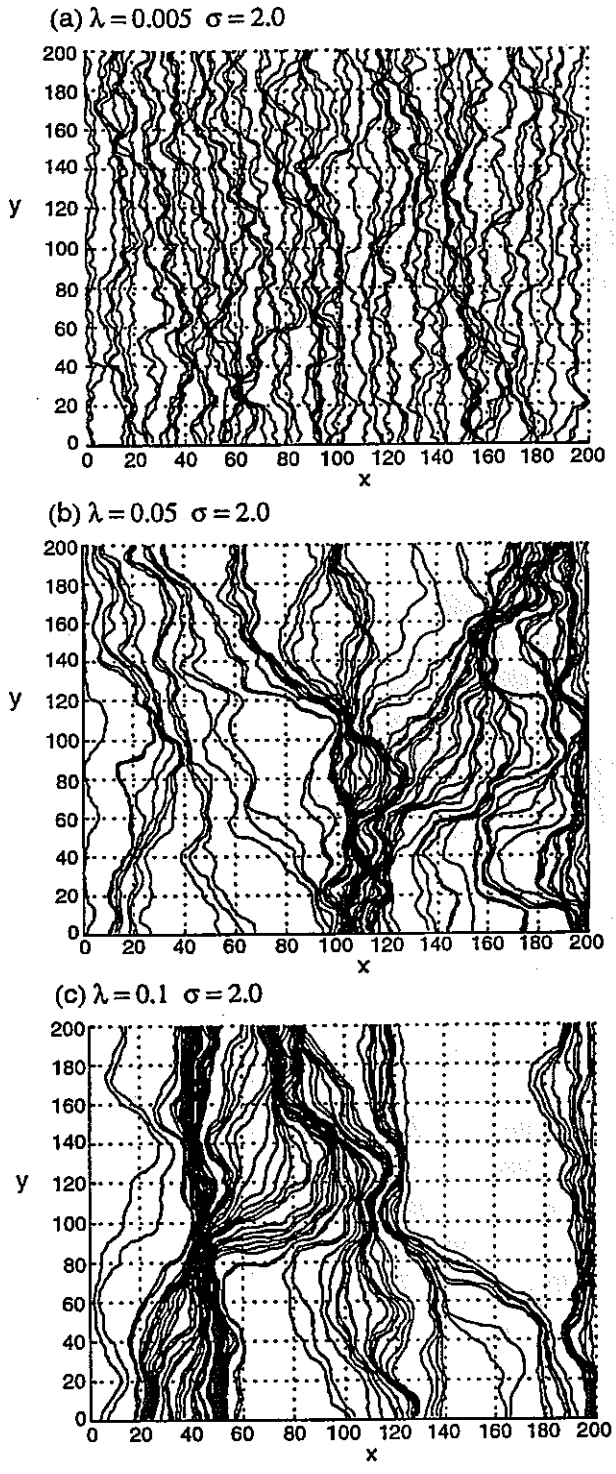

Figure 4 a-c. Emergence of flow channeling, under a pressure step applied from the top to the bottom boundary, as a function of λ' for a 2D heterogeneous medium. Tracer flow paths are shown for $\sigma = 2.0$ and $\lambda' = 0.015$, 0.15, and 0.3 in figures a, b, and c respectively. Numbers on the x and y axes indicate the number of grid elements so that the flow domain is 200 x 200 and the effective spatial correlation range is $200\lambda'$.

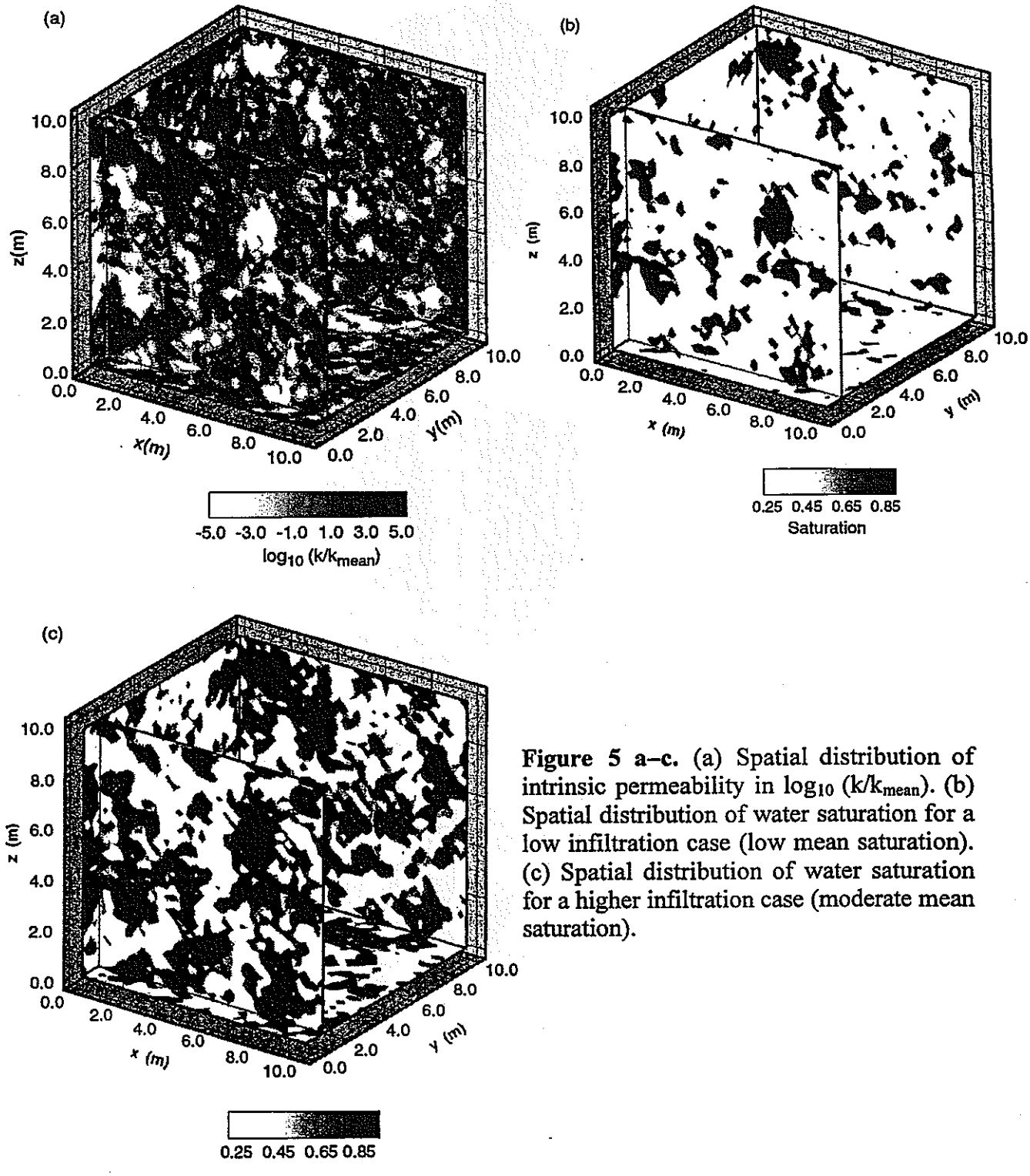

Figure 5 a–c. (a) Spatial distribution of intrinsic permeability in $\log_{10}$ (k/k_{mean}). (b) Spatial distribution of water saturation for a low infiltration case (low mean saturation). (c) Spatial distribution of water saturation for a higher infiltration case (moderate mean saturation).

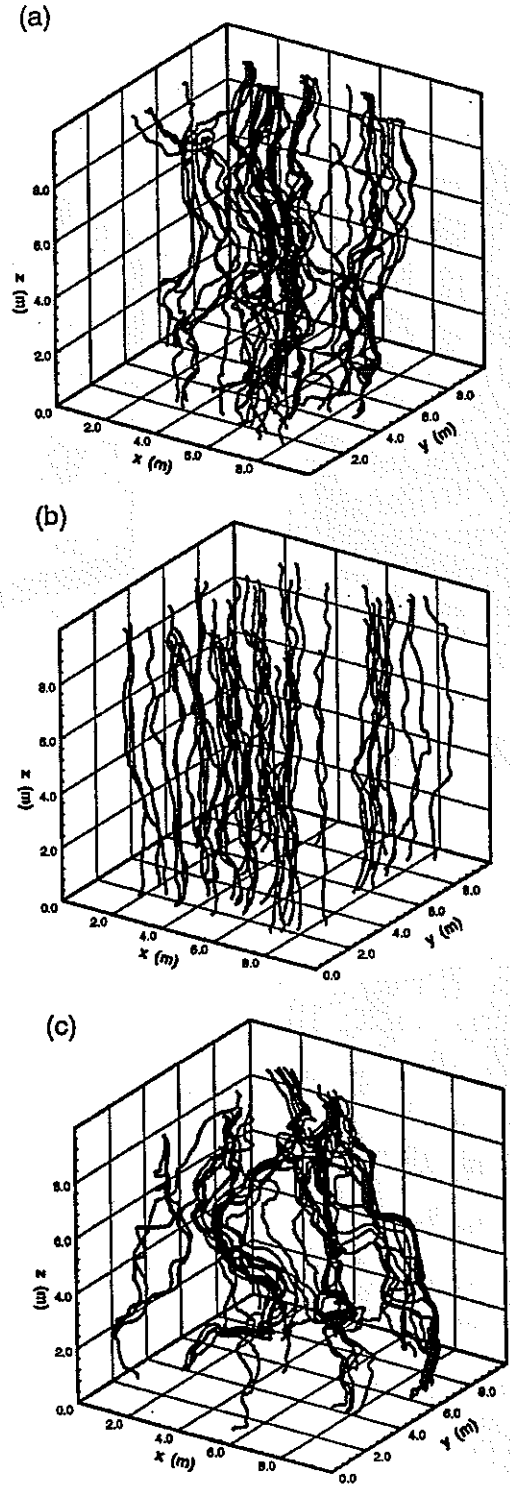

Figure 6. Flow paths are shown for a low infiltration, low mean saturation (a); intermediate infiltration and mean saturation (b); and large infiltration and fully saturated case (c). Note that flow channeling is strong for (a) and (c), but not so pronounced in (b).

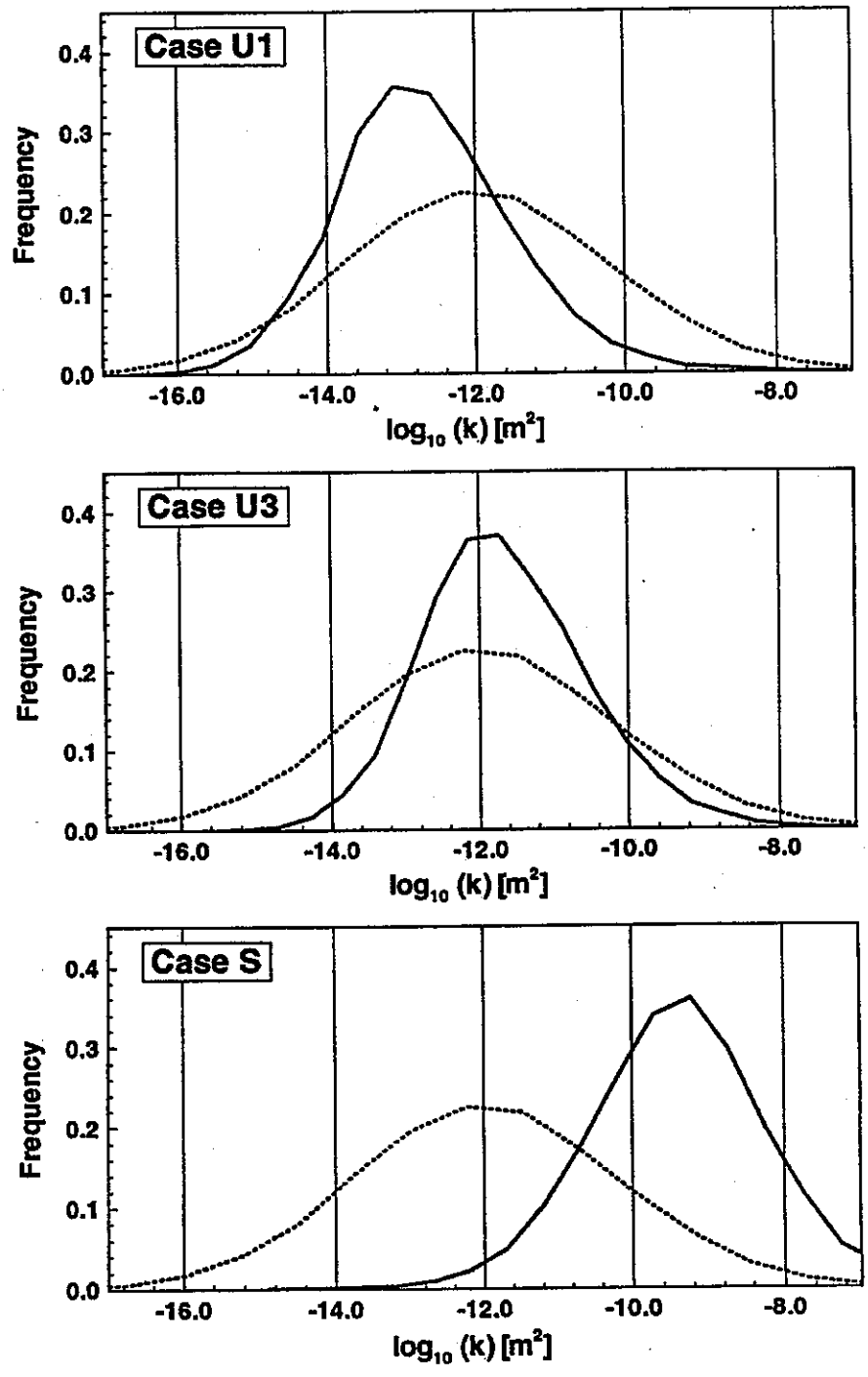

Figure 7. Frequency distribution of intrinsic permeability for the flow channels (solid lines) and the entire flow domain (dotted line), for three cases of low, intermediate and full saturations, cases U1, U3 and S, respectively.

a)

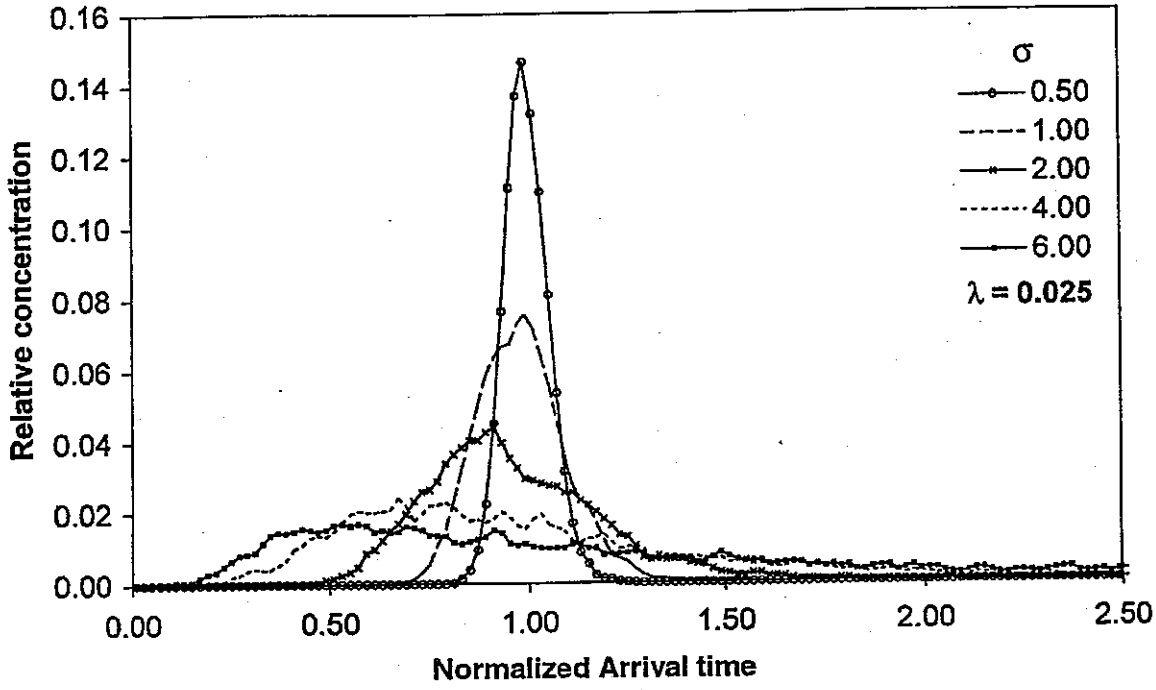

b)

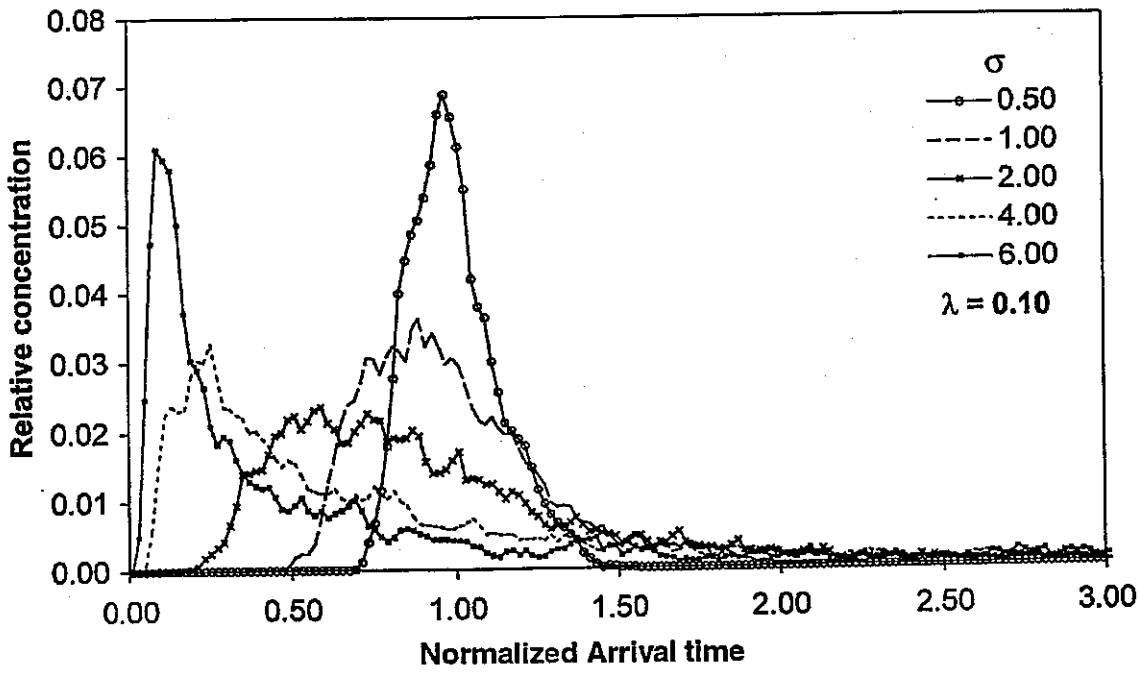

Figure 8 a–b. Breakthrough curves for different standard deviation σ values and for a ratio of correlation length to travel length λ′ of .075 and 0.3 in figures a and b respectively. The x-axis gives the arrival time normalized to (i.e. in units of) the expected time if the medium were of constant permeability. The y-axis gives the concentration as a fraction of the input pulse concentration.

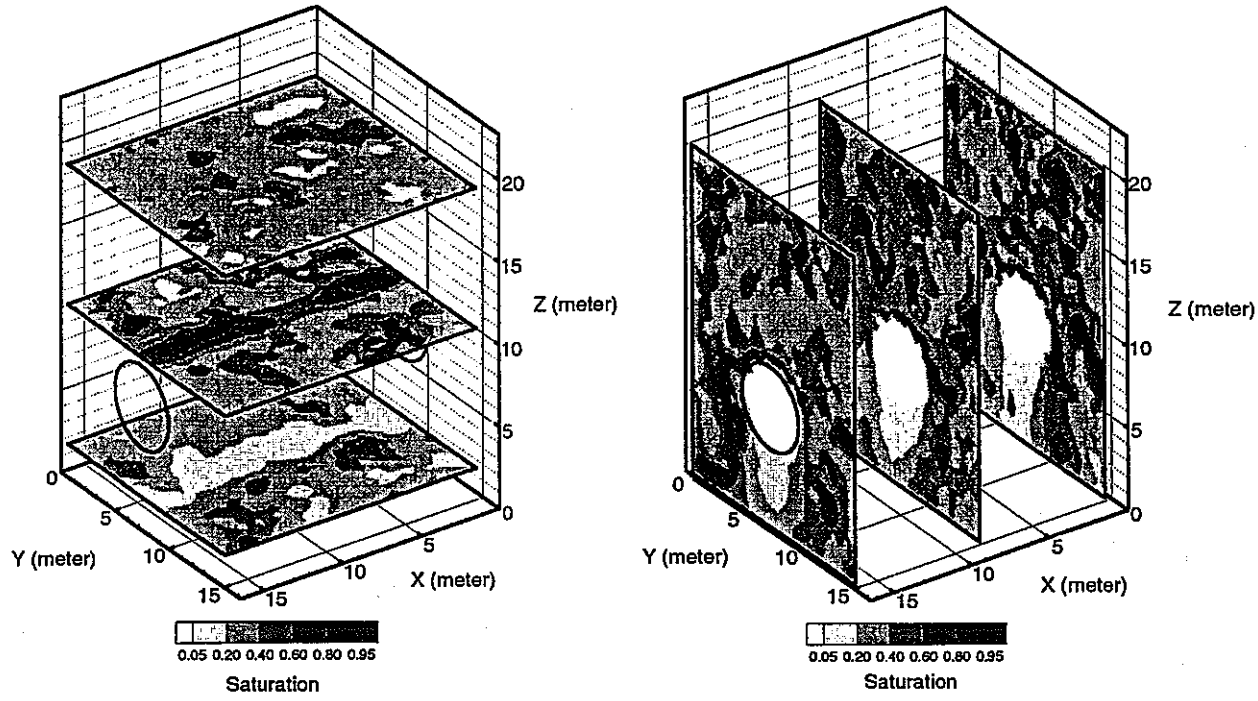

Figure 9. Saturation profiles in a 3D heterogeneous block with a drift, under percolation flux of 1000 mm/yr on the top boundary.

A shorter version to be published
Water Resource Research
Accepted, November, 2000

A Particle-Tracking Method for Advective Transport in Fractures with Diffusion into Finite Matrix Blocks with Application to Tracer Injection-Withdrawal Testing

Y.W. Tsang and C.F. Tsang

Earth Sciences Division,
Ernest Orlando Lawrence Berkeley National Laboratory,
One Cyclotron Road, Berkeley, California 94720, USA

The work was supported jointly by Sandia National Laboratories, Waste Isolation Pilot Plant (WIPP) Project Office, through their contract with the U.S. Department of Energy (DOE). No. DE-AC04-94AL85000; and by the Japan Nuclear Cycle Research Institute (JNC) under a binational agreement between JNC and DOE. Office of Environmental Management, Office of Science and Technology, under Berkeley Lab Contract, DE-AC03-76SF00098.

ABSTRACT

A particle-tracking method has been developed to calculate tracer transport in fractures with diffusion into finite rock matrix blocks. The method is an extension of the work of Yamashita and Kimura (1990), which is only applicable to diffusion into an infinite matrix. The new method has been verified against a number of analytic or semi-analytic solutions for transport in a homogeneous fracture medium with matrix diffusion. The method is applied to the calculation of tracer breakthrough curves for a hypothetical tracer injection-withdrawal experiment in a heterogeneous fracture zone, with variable hydraulic properties and finite matrix blocks.

INTRODUCTION

The importance of matrix diffusion and sorption for the transport of tracers in fractured porous rocks is well recognized [*Neretnieks*, 1980]. A number of methods have been developed for the calculation of these processes [e.g., *Tang et al.*, 1981; *Rasmuson and Neretnieks*, 1981; *Barker*, 1982, 1985; *Sudicky and Frind*, 1982; *Maloszewski and Zuber*, 1990, 1993; *Quinodoz and Valocchi*, 1993, *Moench*, 1995; and *Cvetkovic et al.*, 1999]. This paper presents a particle-tracking technique to calculate the effects of matrix diffusion and sorption on tracer transport and breakthrough curves. The technique is based on a procedure proposed by *Yamashita and Kimura* [1990] for calculation of diffusion into an infinite matrix medium. However, an infinite matrix is not realistic, as in practice one encounters diffusion into matrix blocks or layers of finite dimensions. In this paper, we have extended the particle tracking technique to the case of finite matrix blocks, and to the case involving heterogeneous systems, both of which cannot be easily handled by conventional methods. The proposed technique can be applied easily to a complex heterogeneous fracture system within the framework of a discrete fracture network or of a dual-porosity model, so long as a flow field is first calculated.

THEORY AND PROCEDURE

Let us assume that we have a steady-state flow field, which may have been calculated, for instance, by applying finite-difference or finite-element methods to a heterogeneous fracture continuum. The particle-tracking method involves the release at source locations of a large number of particles representing solutes, or tracers, and these are followed step by step as they move from grid cell to grid cell. Following chemical

engineering practice, the residence time t_w (without matrix diffusion) during which a particle resides within a grid cell without a source or sink is given by:

$$t_w = \frac{\phi_f \Delta x \Delta y \Delta z}{\frac{1}{2}\sum_j |Q_{ij}|} \quad (1)$$

where Δx, Δy, Δz are the dimensions of the grid cell i, ϕ_f is the fracture porosity of the medium, and Q_{ij} is the flow rate in volume per time between the cell of interest, i, and its neighbors j. After this residence time, outgoing tracer particles are distributed to the neighboring grid cells according to stream tubes, given that Q_{ij} (for all j) is known [*Moreno et al.*, 1990].

The effect of diffusion and linear sorption is represented by an increase in the particle residence time from t_w to a new time interval, t. In order to calculate the increased residence time, we use a solution for the tracer concentration attenuation over time, assuming the flow to be in contact with the matrix block into which diffusion occurs. The ratio of the concentration C exiting the grid cell over the initial concentration C_o entering the grid cell may be written as:

$$C/C_o = f(t, t_w, m_1, m_2, \ldots) \quad (2)$$

The left hand side varies from 0 to 1, and is dependent on t_w, the tracer residence time in the absence of matrix diffusion, and the other parameters m_1, m_2,... which specify properties of the rock matrix, such as porosity, matrix diffusion and sorption coefficients. To incorporate the effects of matrix diffusion into particle tracking, we follow the procedure of *Yamashita and Kimura* [1990], who proposed the use of a number R drawn randomly from the uniform distribution U[0,1] and equated with C/C_o. Then, the

residence time t for each particle in a discretized element, incorporating the effect of diffusion, is inversely calculated from the equation:

$$R=f\,(t,\ t_W,\ m_1,\ m_2,\ldots), \tag{3}$$

where all variables other than t (i.e., t_W, m_1, m_2,...) are known.

At this point, the particle residence time for the grid cell t_W is replaced by t, the increased residence time as a result of the diffusion of the particle into the matrix. As a large number of particles traverse the field in this manner, they are collected at observation points, such as a pumping well, as a function of their cumulative travel times since release at the source. The result is a tracer breakthrough curve. Assuming all the particles were released at the same time, the breakthrough curve will correspond to a tracer pulse injection. Generally if we define appropriately the particle release times at the source, we can calculate the breakthrough curves for any given tracer injection with variable concentration. For the remainder of the paper we shall consider only the case of tracer injection with a single concentration pulse at time 0.

To study the effect of diffusion into finite matrix blocks, we select from the literature, somewhat arbitrarily, the solution of *Rasmusson and Neretnieks* [1981] for the function f (t, t_W, m, m_2,...) in Equation (3). In their model, the tracer flows in orthogonal sets of fractures forming a regular network in 3-D, and the matrix volume between fractures are represented by spherical matrix blocks of radius r_m. Thus, the fracture-to-fracture spacing is $\lambda=2r_m$. The solution is given in terms of an infinite integral. A special case for a non-sorbing tracer with negligible longitudinal dispersion (i.e., Peclet number $Pe \longrightarrow \infty$) is used for our calculations. The solution in this case can be written as:

$$\frac{C}{C_o} = \frac{1}{2} + \frac{2}{\pi}\int_0^{\infty} \exp(-\delta_o H_1)\sin(y\ \omega^2 - \delta_o H_2)\frac{d\omega}{\omega} \qquad (4)$$

where

$$y = 2\frac{D_e}{\phi_m r_m^2}(t - t_w)$$

$$\delta_o = 3\frac{D_e}{r_m^2}\frac{(1-\phi_f)}{\phi_f}t_w$$

$$H_1(\omega) = \omega\left(\frac{\sinh 2\omega + \sin 2\omega}{\cosh 2\omega - \cos 2\omega}\right) - 1$$

$$H_2(\omega) = \omega\left(\frac{\sinh 2\omega - \sin 2\omega}{\cosh 2\omega - \cos 2\omega}\right)$$

and ϕ_m, matrix porosity; ϕ_f, fracture porosity; D_e, effective diffusion coefficient in the matrix pores (L^2/T), which is equal to $D.\tau.\phi_m$; τ, tortuosity (< 1); D, free water diffusion coefficient (L^2/T); and ω, the integration variable.

The fracture porosity ϕ_f is related to the fracture aperture b by:

$$m\,(b / \lambda) = \phi_f \qquad (5)$$

where λ is the fracture spacing, and m = 1 corresponds to the case where the fractures are parallel and non-intersecting, and m = 3 corresponds to the case where the fractures form three orthogonal and intersecting sets. The fracture spacing λ can also be thought of as the matrix block length.

Our definition of D_e differs from that of *Tang et al.* [1981] by the factor of ϕ_m (Tang's effective diffusion coefficient is the product of only D and τ). The parameter groups denoted by y and δ_o have, respectively, the physical meaning of a dimensionless increased residence time produced by diffusion into finite matrix blocks, and the ratio of

the advective time t_w to the diffusion time into the matrix blocks. Thus, Equation (4) describes the concentration of the particles which, moving in a fracture continuum with a given fracture porosity ϕ_f, are allowed also to diffuse into finite matrix blocks with radius r_m, porosity ϕ_m, and tortuosity τ.

So, given a generated random value R for C/C_0, y in Equation (4), and ultimately t, can be evaluated for a range of δ_0 values. This is done by interpolation from a table of calculated sets of (δ_0, C/C_0, y) values. The interpolation works well if the set of three numbers are densely and evenly spaced in the parameter space of C/C_0 and δ_0. After some experimentation, we found that this can be facilitated by evaluating C/C_0 versus y/δ_0 for $\delta_0 > 1$, and C/C_0 versus y/δ_0^2 for $\delta_0 < 1$.

The interpolation method can be described by reference to Figure 1. Given the parameter values for the flow system and t_w, δ_0 can be calculated. Then, the appropriate curve for the specific δ_0 value is chosen and the corresponding value on the horizontal axis for a particular $R=C/C_0$ value is found. This value is equal to y/δ_0 if $\delta_0 > 1$ or y/δ_0^2 if $\delta_0 < 1$. The diffusion-increased residence time t is then readily computed from this value.

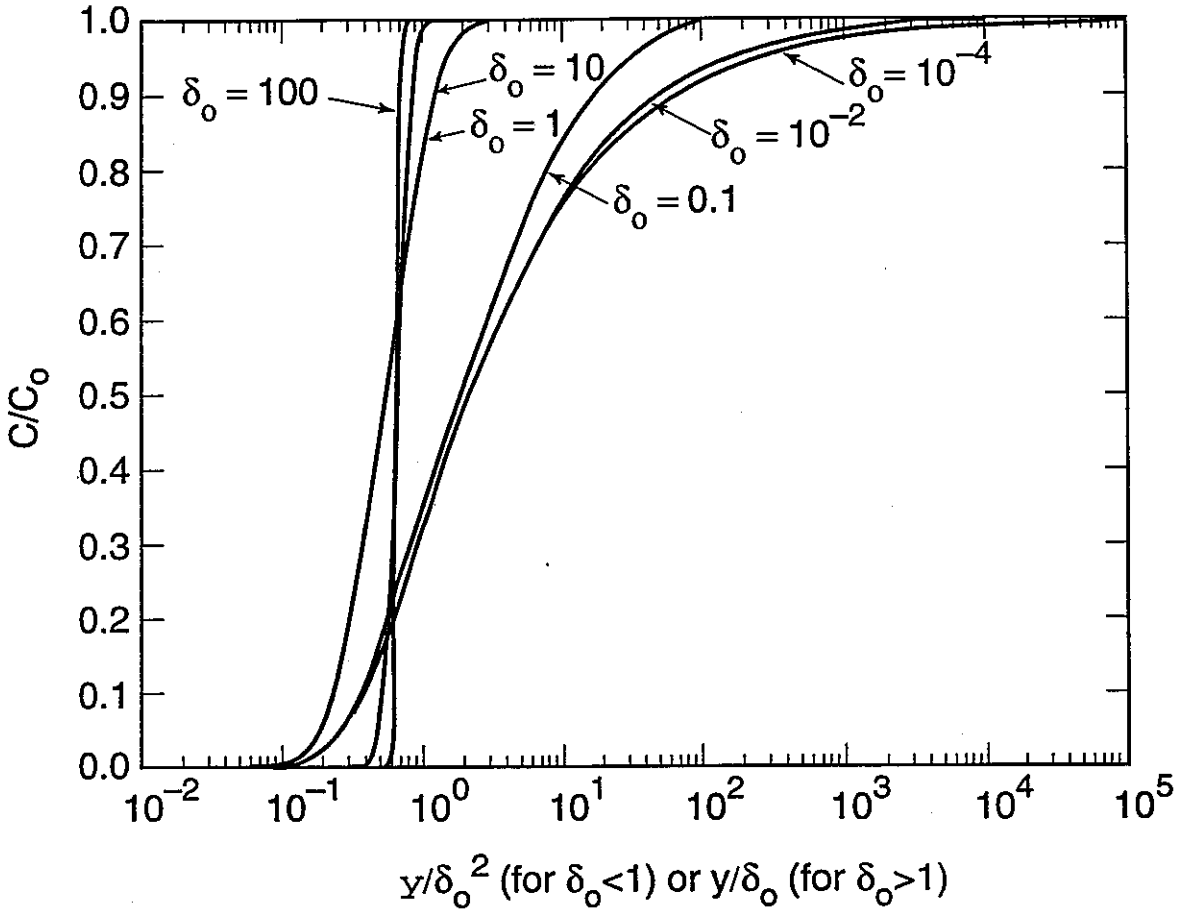

Figure 1. Relationship between C/C_o, δ_o, and y. The x-axis is plotted as y/δ_o^2 and y/δ_o depending on whether δ_o is smaller or larger than 1, respectively.

Equation (4) describes diffusion into finite rock matrix blocks. For diffusion into an infinite matrix, a simpler solution is available. Consider a parallel-plate fracture of constant aperture (b), and width (w), imbedded in an infinite matrix medium. For one-dimensional steady-state flow rate Q, the advective residence time for plug flow without matrix diffusion over a distance of L in the fracture is $t_w = Lwb/Q$. Assuming diffusion into an infinite matrix medium in the direction normal to the advective flow direction, an analytical solution [*Neretnieks*, 1980] is available:

$$\frac{C}{C_o} = \text{erfc}\left(\frac{(k_d \rho_p D_e)^{1/2}}{(t - t_w)^{1/2}} \frac{t_w}{b}\right) \qquad (6)$$

where D_e is the effective diffusion coefficient in the matrix pores (L^2/T); k_d is the linear sorption coefficient (L^3/M) and ρ_p is the rock matrix density (M/L^3). For a non-sorbing tracer, $k_d\rho_p$ is simply the matrix porosity ϕ_m.

Equation (6) is shown in Figure 2 for different values of the parameter group,

$$(K_d \rho_p D_e)^{1/2}/b$$

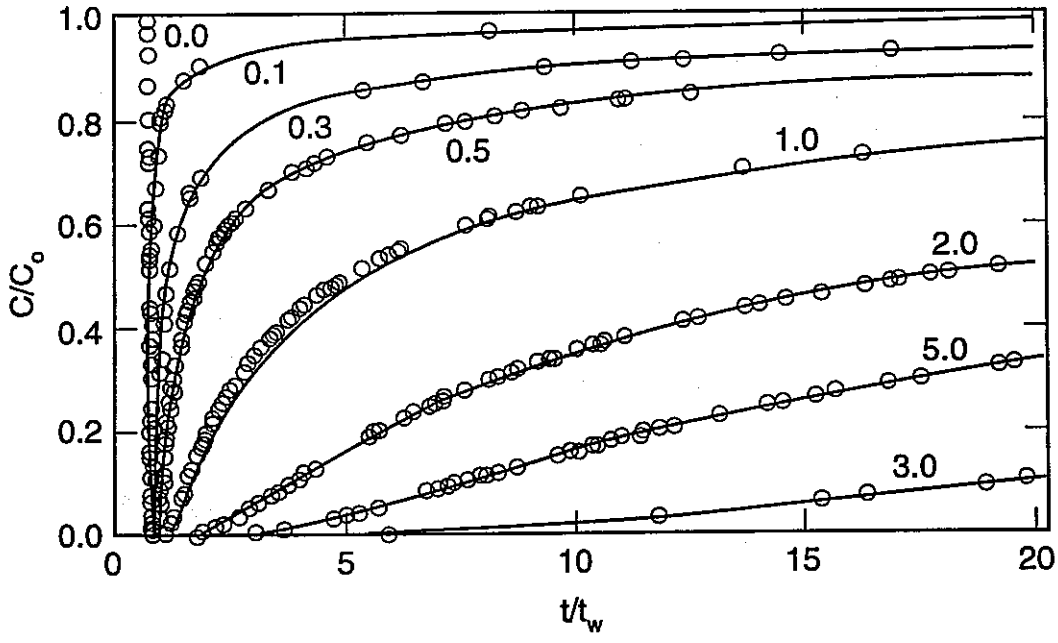

Figure 2. Forward and inverse calculations (lines and circles respectively) of the particle residence times based on Equation (5), with different values of the parameter group $(K_{d-p}D_e)^{1/2}/b$, which label the curves.

In terms of our particle tracking method, the implementation of Equation (6) is much simpler than that for Equation (4). Here, once the system parameters are specified, Equation (6) can be used directly to compute t/t_W from $R = C/C_o$, corresponding to one particular curve in Figure 2. This is unlike Equation (4) where interpolation using a set of

curves is required (Figure 1), since calculation of t/t_W depends not only on system parameters but also on t_W. Computationally, particle tracking based on Equation (6) is a factor of three to four more efficient than that based on Equation (4).

Particle tracking calculations based on Equations (4) and (6) should give the same results when the penetration of the tracer into the matrix is negligible compared with the matrix block size. Therefore a criterion for the use of the simpler and computationally more efficient Equation (6) may be developed as follows. The concentration in the matrix as a function of penetration depth from the fracture-matrix interface can be written as *(Carslaw and Jaeger*, 1959: p.60, Eq. 10):

$$\frac{C}{C_o} = \mathrm{erfc}\frac{z}{2(D_e t)^{1/2}} \tag{7}$$

Let us assume that the impact of finite block size is negligible if the concentration at the center of the matrix block is small, specifically if $C/C_o < 0.01$. Setting the right side of Equation (7) to be less than 0.01, we calculate that the argument for the complementary error function should be greater than 1.82, or 2 by rounding-off to integer. By setting $z = r_m$, the early time criterion for Equation (6) to be valid becomes $t < r_m^2/16D_e$.

A code named THEMM (Transport in Heterogeneous Medium with Matrix Diffusion) was developed to calculate flow in a general heterogeneous permeability field, with the finite difference technique and transport with the particle tracking method described above. This code allows the user to choose either Equation (4) or Equation (6) for the diffusion calculation.

VERIFICATION OF THE TECHNIQUE

The proposed particle-tracking method was verified against three analytical or semi-analytical solutions for transport in homogeneous media [Tang et al. (1981), Chen (1986) and Moench (1995)]. Unfortunately no such solutions are available for heterogeneous fields, for which the particle-tracking method has been designed.

Verification Problem 1: Linear Flow

Tang et al. [1981] provides an analytical solution for tracer concentration as a function of distance and transport time for 1-D linear flow in a single fracture, with matrix diffusion into the infinite rock matrix.

$$\frac{C}{C_o} = erfc\left[\frac{z\phi_m\sqrt{D\tau}}{v^{1/2}(vt-z)^{1/2}\delta}\right] \tag{8}$$

The symbols are explained in Table 1, together with the numerical values used in the verification exercise.

Note that Equation (8) is essentially the same as Equation (6). It assumes infinite matrix blocks, which is valid for a time period satisfying the early time criterion. If we assume that r_m = 1.5 m, a choice of time t= 10^5 s will certainly satisfy the condition. For verification purpose, the THEMM code is used with both finite and infinite block solutions - Equations (4) and (5). Figure 3 shows the comparison. The agreement is very good between the analytic solutions and our particle-tracking method. As to be expected, the particle tracking results from Equations (4) and (6) are essentially the same.

Table 1. Parameters and Values used in the Three Verification Examples.

Verification Problem 1: Linear Flow		
v	velocity	10^{-4} m/s
b	fracture aperature	10^{-3} m
D	free water diffusion	7.4×10^{-10} m^2/s
τ	tortuosity	0.11
ϕ_m	matrix porosity	0.16
Verification Problem 2: Radial Divergent Flow		
Q	injection rate	1.157×10^{-7} m^3/s
r_w	wellbore radius	0.11 m
b	fracture aperture	10^{-4} m
α	longitudinal dispersivity	0.5 m
D	free water diffusion coefficient	1.6×10^{-9} m^2/s
τ	tortuosity	0.1
ϕ_f	fracture porosity	10^{-4}
ϕ_m	matrix porosity	0.01
Verification Problem 3: Radial Convergent Flow; Finite Matrix Block		
Q	pumping rate	1.0×10^{-3} m^3/s
h	aquifer thickness	7.0 m
r_w	pumped well radius	0.4 m
r_L	distance of injection to pumped well	20 m
D	free water diffusion coefficient	7.2×10^{-10} m^2/s
τ	tortuosity	0.1
ϕ_f	fracture porosity	0.0015
ϕ_m	matrix porosity	0.15
$2r_m$	fracture spacing ($\gamma = 10^{-5}$, 10^{-3}, 10^{-1}, 10 respectively)	6.158m, 0.6158m, 0.06158m, 0.006158m)

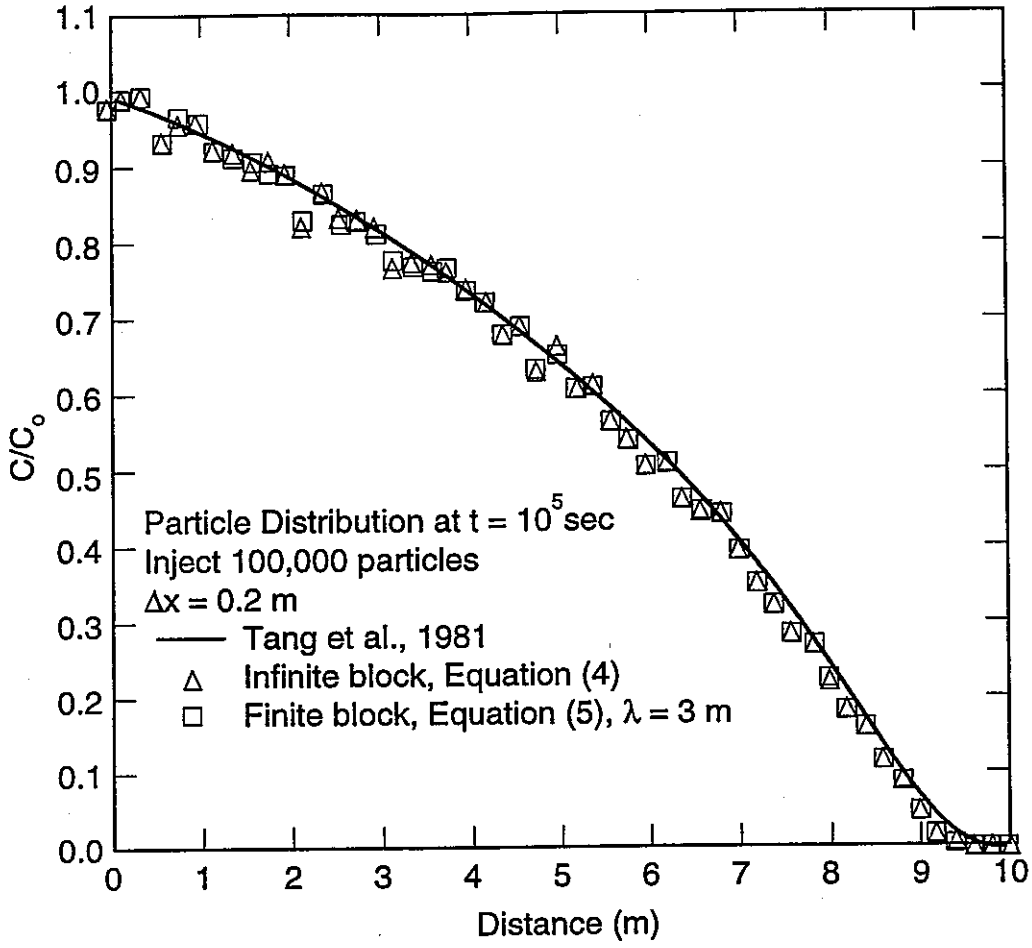

Figure 3. Comparison of THEMM results with the analytical solution of Tang et al. (1981). Tracer concentration is shown as a function of linear distance from the injection well.

Verification Problem 2: Radial Divergent Flow

An analytic solution for radially divergent, steady flow and transport in a fracture with diffusion into infinite matrix is given by Chen [1986]. He considered two models: Model I, which includes radial advection and longitudinal dispersion in the fracture plane, and Model II, which includes radial advection only. He also considered two boundary conditions at the tracer source, namely, constant concentration condition or a decaying-concentration condition. The solution of Model I is given in the Laplace

domain in terms of Airy functions and is evaluated by numerical inversion of the Laplace transforms. Small-time and long-time approximate solutions (which will not be reproduced here) are also derived by Chen [1986].

The solution for Model II is given by Chen [1986] in terms of complementary error function. For verification of our particle-tracking method, we use zero longitudinal dispersion and constant tracer concentration at the well with radius r_w, where the tracer is injected at a constant rate Q. Under these conditions, Chen's solution [Equation 59 of Chen (1986)] reduces simply to:

$$\frac{C}{C_o} = erfc\left(\frac{\phi_m \sqrt{D\tau}.\pi\left(r^2 - r_w{}^2\right)/Q}{\left(t - \pi\left[r^2 - r_w{}^2\right]b/Q\right)} \right) \qquad (9)$$

$$\text{for} \qquad t < \pi\left(r^2 - r_w{}^2\right)\, b/Q$$

$$\frac{C}{C_o} = 0 \qquad \text{for} \qquad t > \pi\left(r^2 - r_w{}^2\right)\, b/Q$$

The symbols in Equation (9) and their numerical values in the verification exercise are given in Table 1.

Note that Chen [1986] defines the fracture aperture to be 2b, but we define it as b, so that there is a factor-of-2 difference in the two b values. With this correction, the set of parameters indicated above is exactly the same as those of Chen [1986] in generating Figure 6b of his paper. In the list of parameters, we have included the longitudinal dispersion of 0.5 m. This parameter is not needed for Model II; however, in the results

below we also present, for comparison, Chen's results for Model I, where longitudinal dispersion is included.

Calculations were made for C/C_0 versus r at times 0.01 year, 0.1 year, and 1 year, with increasing radial transport distances. For the particle-tracking calculations using the THEMM code, we have chosen the radial grid lengths of 0.2, 0.5 and 2 m, to calculate results at 0.01, 0.1 and 1 year respectively, so that the accuracies of calculations are approximately the same. For each case, over 100,000 particles are used in the computation. In Figure 4, results of the THEMM code are compared with the results of Chen [1986], taken from Figure 6b of his paper. Excellent agreement can be seen between THEMM and Model II. The Model I results are shown only for comparison purposes to indicate the effects of longitudinal dispersion. Note that for later times, Model II results approach those of Model I, showing that the effect of longitudinal dispersion in the fracture decreases in importance for late-time results.

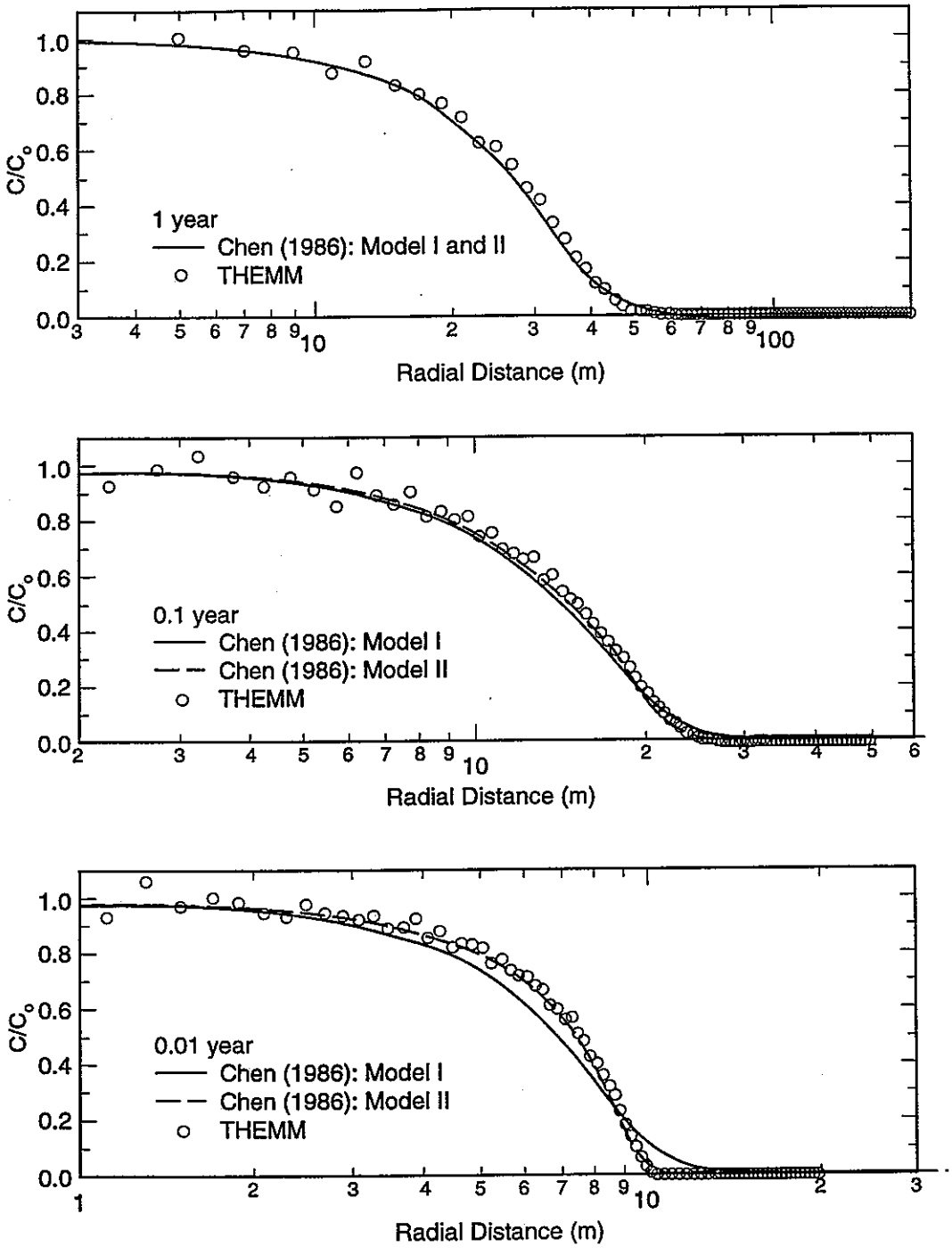

Figure 4. Comparison of THEMM results with the semi-analytic results of Chen (1986). Distribution of tracer concentration is shown as a function of radial distance from the injection well at three injection times as indicated.

Verification Problem 3: Radial Convergent Flow, Finite Matrix Blocks in a Double-Porosity Model

An exact Laplace transform solution was obtained by *Moench* [1995] for the problem of dispersion, advection, and adsorption of a tracer injected into a steady, horizontal, radially convergent flow field in a densely fractured porous formation. The medium is represented by a double-porosity medium with finite matrix blocks. Assuming that the tracer is released at distance r_L from a pumping well, no chemical retardation in the fracture or rock matrix, and no fracture skin effects, the three parameters used by *Moench*

$$Pe = r_L / \alpha_L$$

$$\sigma = \phi_m \left(\frac{1-\phi_f}{\phi_f} \right)$$

$$\gamma = \frac{D_e}{r_m^2} \frac{\left(r_L^2 - r_w^2 \right) \pi h \phi_f}{Q} \left(\frac{1-\phi_f}{\phi_f} \right)$$

[1995] may be defined using our notation as:

where, in addition to the symbols previously defined, α_L is the longitudinal dispersivity in the fracture, and h is the thickness of the fractured aquifer. Thus, (10) erse measure of the dispersion in the fracture, and σ may be considered as a measure of the double porosity character of the aquifer, so that σ=0 implies a single-porosity medium with zero matrix diffusion, and σ=100 implies a double-porosity medium with $\phi_m/\phi_f \sim$ 100. The parameter γ is proportional to D_e/r_m^2 and is a measure of diffusion into finite matrix blocks.

Moench's dual-porosity conceptual model corresponds with our formulation of Equation (4) where the 3-D network of fractures are separated by spherical matrix blocks of radius r_m. Tracer breakthrough curves are calculated using our particle-tracking code THEMM for the case of a pumping well with a constant-concentration tracer source at a distance r_L. Parameter values are taken from *Moench* [1995] and are listed in Table 1. Note that we assume $D_e=D.\tau.\phi_m$ for this comparison. Given the values of ϕ_f and ϕ_m, $\sigma=100$, corresponding to the set of curves in Figure 3a of *Moench* [1995].

The γ values used in the verification exercise extend over six orders of magnitude, thus covering scenarios ranging from very little diffusion into the matrix to such a large amount of diffusion that the matrix blocks are saturated with tracers and no further diffusion is possible. Figure 5 shows that the breakthrough curves display a piston shape for both small and large values of γ. The difference in time between the various cases is a reflection of the impact of diffusion on the tracer transport.

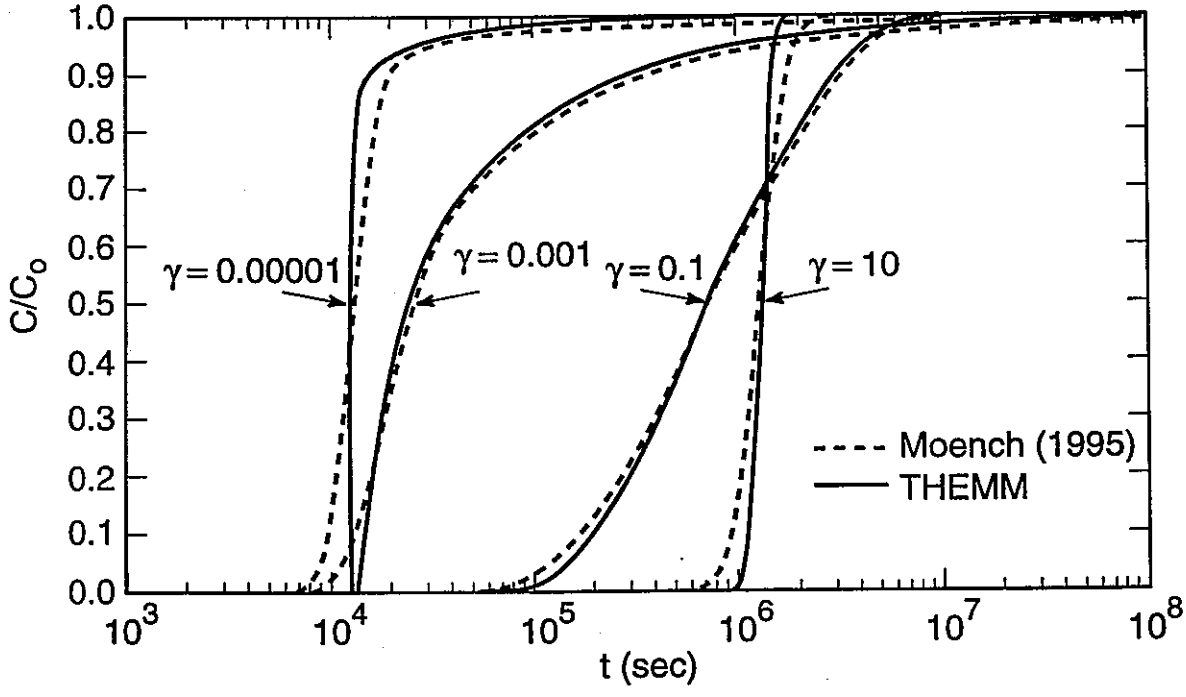

Figure 5. Comparison of THEMM results with the semi-analytical solution of Moench (1995). Tracer concentration at the pumping well is shown as a function of time for different γ values.

The comparison between our particle tracking approach and the solution of Moench is shown in Figure 5. The particle tracking method does not include longitudinal dispersion, whereas Figure 3a of *Moench* [1995] assumes Pe = 50, which translates to a dispersivity of 0.4 m. Thus, some difference between the Moench model and the THEMM code is to be expected. Taking this into account, we consider the agreement to be very good.

APPLICATION TO A HYPOTHETICAL INJECTION-WITHDRAWAL EXPERIMENT IN A HETEROGENEOUS MEDIUM

As a non-trivial example demonstrating the capability of the particle tracking technique, let us consider a hypothetical tracer injection-withdrawal test in a single well in a heterogeneous fracture zone (i.e. with spatially varying fracture permeablity). This is also sometimes called a "huff-puff" or a "push-pull" test. A tracer is injected for a certain time period and then withdrawn from the same well for an extended time period until almost all the tracer is recovered. One advantage of the injection-withdrawal test is that flow channeling effects produced by permeability heterogeneity [*Moreno and Tsang*, 1994] are cancelled in the injection and withdrawal sequence, since the fast outgoing paths during injection are also the fast incoming paths during withdrawal. Therefore, the diffusive-dispersive phenomenon can be isolated and clearly evaluated. To solve this problem for a heterogeneous fracture permeability field with finite matrix regions between adjacent fractures is a major challenge for conventional approaches. The particle tracking method described in this paper can address it quite efficiently as shown below.

We consider two hypothetical 2-D fractured aquifers: a homogeneous one and one with heterogeneous permeability field generated with the turning bands method [*Tompson* et al., 1989]. The heterogeneous field is generated using a standard deviation in natural log permeability (m^2) arbitrarily set to 1.73. In our hypothetical problem, the tracer is first injected at a constant rate for 24 hours. At the end of the first 100 minutes, the front of tracer plumes in the two cases are shown in Figure 6. These tracer fronts are actually the calculated positions of a larger number of particles 100 minutes after they are released at the injection well. Here, one sees that the tracer front is circular for the homogeneous case (as one would expect) and star-shaped for the heterogeneous case.

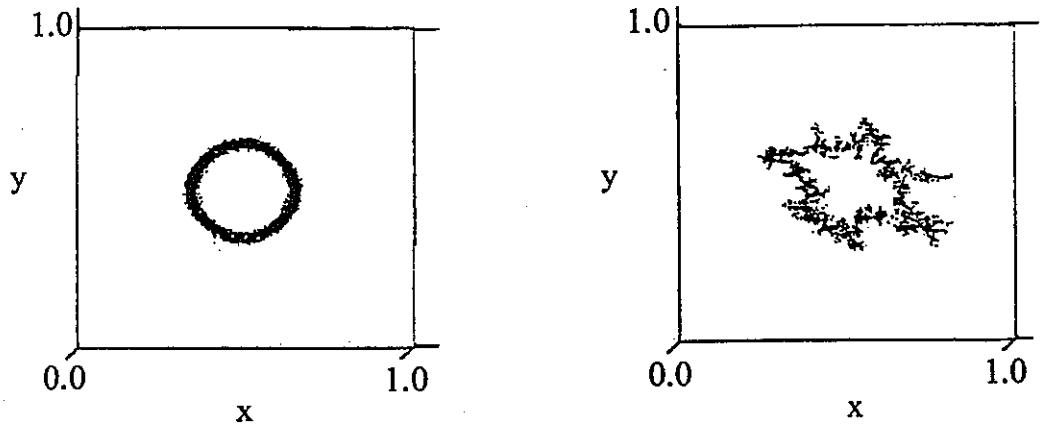

Figure 6. The front of tracer plumes after 100 minutes of injection. The injection well is at (0.5, 0.5). The case for the homogeneous fracture medium is shown on the left and that for the heterogeneous medium is shown on the right.

After 24 hours of tracer injection, the well is switched immediately over to pumping. The tracer production after this switch is calculated with our particle-tracking code THEMM and plotted as cumulative mass recovered over the total injected mass as a function of time. Both the finite matrix case (Equation 4) and the infinite matrix case

(Equation 6) are calculated. For the finite block case, the radius of the matrix blocks is assumed to be 5 cm.

The simulation results are shown in Figure 7. The homogeneous and heterogeneous results are almost identical, confirming the hypothesis that test results are not sensitive to the flow channeling produced by heterogeneity. At early times, the finite and infinite block results are similar, but they diverge at later times. For the finite block case, tracer concentration buildup in the matrix during the injection period is much faster, resulting in a strong diffusion back into the fracture during the withdrawal period. In this case, full recovery is found after about 8 months (2×10^7 seconds) of pumping. For the infinite matrix case, the recovery is below 90% even after 10 years (3.2×10^8 seconds).

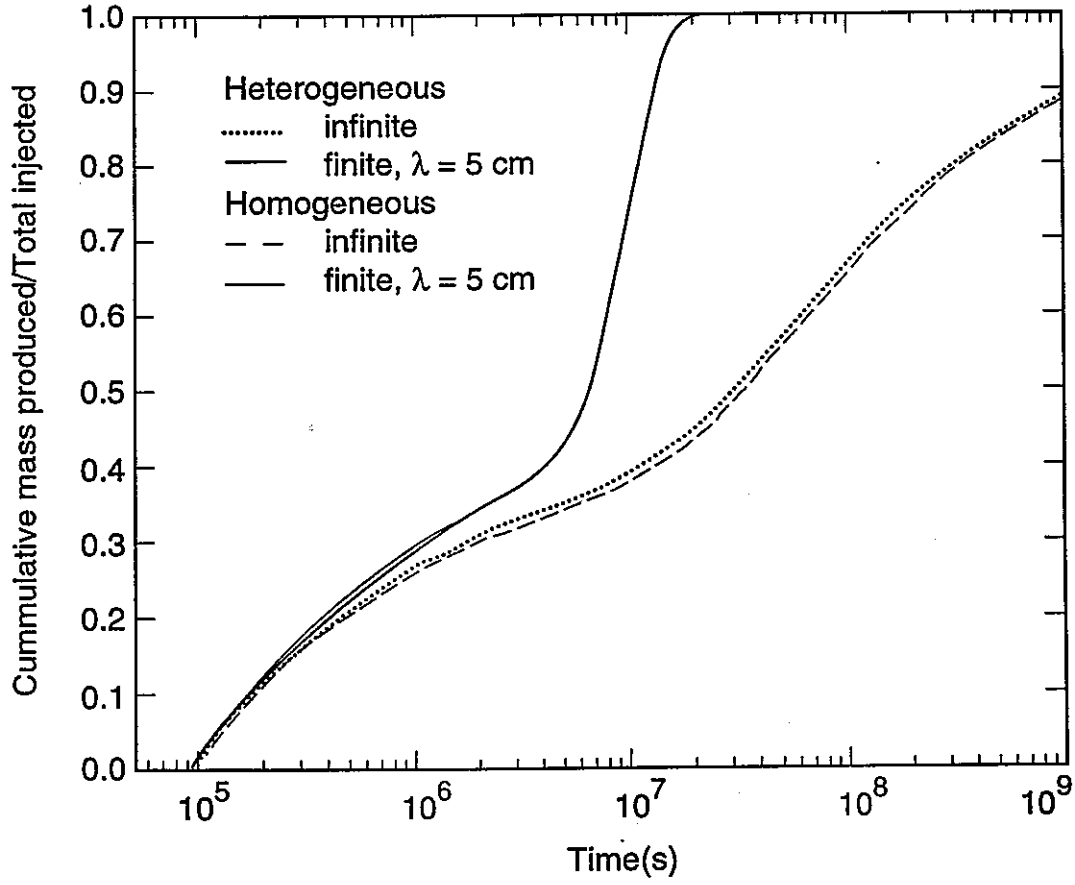

Figure 7. Tracer concentration as cumulative mass recovered divided by the total injected mass as a function of time during the withdrawal period in an injection-withdrawal test.

It is also interesting to note that all the curves in Figure 7 display a two-plateau structure. The first plateau is at y ~ 0.4 and the second is at y = 1.0. The first plateau represents the tracer mass in the fracture at the time of the switch from injection to withdrawal. The late-time part of the tracer withdrawal curve is controlled by the slower process of tracer diffusion from the matrix into the fracture. The time to recover the tracer from the matrix is several orders of magnitude smaller for the finite-block case than for the infinite-block case, as would be expected.

These numerical simulations may be used to analyze actual *in situ* injection-withdrawal tracer tests and to evaluate the parameters controlling matrix diffusion. This example illustrates the power of our particle tracking method to account for diffusion into finite rock matrix blocks, even in the case of heterogeneous fracture flow fields.

SUMMARY

This paper presents a new particle-tracking technique to calculate diffusion into finite matrix blocks for transport in a heterogeneous fracture system. It can be applied to either a fracture-network model or a dual-porosity model. Results are in good agreement with existing analytic or semi-analytic solutions. An example application of the method to calculate tracer breakthrough curves from a hypothetical tracer injection-withdrawal experiment in a heterogeneous fracture zone with finite matrix blocks demonstrates the utility of this new approach.

ACKNOWLEDGMENT

We thank Frank Hale of Ernest Orlando Lawrence Berkeley National Laboratory (Berkeley Lab) for his cooperation and for coding and running of the THEMM code. We appreciate discussions with Susan Altman, Lucy Meigs, and Paul Reeves of the Sandia National Laboratories, and their careful review of the manuscript. The work was supported jointly by Sandia National Laboratories, Waste Isolation Pilot Plant (WIPP) Project Office, through their contract with the U.S. Department of Energy (DOE), No. DE-AC04-94AL85000; and by the Japan Nuclear Cycle Research Institute (JNC) under a binational agreement between JNC and DOE, Office of Environmental Management, Office of Science and Technology, under Berkeley Lab Contract, DE-AC03-76SF00098.

REFERENCES

Barker, J. A.., Laplace transform solutions for solute transport in fissured aquifers, *Adv. Water Resour.* (5), 98-104, 1982.

Barker, J. A., Modeling the effects of matrix diffusion on transport on densely fissured media, *Mem. Int. Assoc. Hydrogeol.*, 18, 250-269, 1985.

Carslaw, H. S. and J. C. Jaeger, *Conduction of heat in solids*, 2nd Edition, Oxford University Press, 1959.

Chen C.S., Solution for radionuclide transport from an injection well into a single fracture in a porous formation. *Water Resour. Res.*, 22(4), 508-518, 1986.

Cvetkovic, V., J. O. Selroos and H. Cheng, Transport of reactive tracers in rock fractures, *Journal of Fluid Mechanics*, 378(10), 335-356, 1999.

Maloszewski, P., and A. Zuber, Mathematical modeling of tracer behavior in short-term experiments in fissured rocks, *Water Resour. Res.*, 26(7), 1517-1528, 1990.

Maloszewski, P., and A. Zuber., Tracer experiments in fractured rocks: Matrix diffusion and the validity of models, *Water Resour. Res.*, 29(8), 2723-2725, 1993.

Moench, A.F., Convergent radial dispersion in a double-porosity aquifer with fracture skin: Analytical solution and application to a field experiment in fractured chalk, *Water Resour. Res.*, 31(8), 1823-1835, 1995.

Moreno L., Y.W. Tsang, C.F. Tsang, and I. Neretnieks, Some anomalous features of flow and solute transport arising from fracture variability, *Water Resour. Res.*, 26(10), 2377-2391, 1990.

Moreno, L. and C.F. Tsang, Flow channeling in strongly heterogeneous porous media: A numerical study, *Water Resour. Res.*, 30(5), 1421-1430, 1994.

Neretnieks, I., Diffusion in the rock matrix: An important factor in radionuclide retardation? *J. Geophys. Res.*, 85 (B8), 4379-4397, 1980.

Quinodoz, H.A.M., and A.J. Valocchi, Stochastic analysis of the transport of kinetically sorbing solutes in aquifers with randomly heterogeneous hydraulic conductivity, *Water Resour. Res.*, 29(9), 3227-3240, 1993.

Rasmuson, A., and I. Neretnieks, Migration of radionuclides in fissured rock: the influence of micropore diffusion and longitudinal dispersion, *J. Geoph. Res.*, 86(B5), 3749-3758, 1981.

Sudicky, E. A., and E. O. Frind, Contaminant transport in fractured porous media: Analytical solution for a system of parallel fractures, *Water Resour. Res.*, 18(6), 1634-1642, 1982.

Tang, D.H., E.O. Frind and E.A. Sudicky, Contaminant transport in fracture porous media; Analytical solution for a single fracture, *Water Resour. Res.*, 17(3), 555-564, 1981.

Tompson, A.F.B., R., Ababou, and L.W. Gelhar, Implementation of the three-dimensional turning bands random field generator, *Water Resour. Res.*, 25(10), 2227-2243, 1989.

Yamashita, R., and H. Kimura, Particle -tracking technique for nuclide decay chain transport in fractured porous media, *Journal of Nuclear Science and Technology*, 27, 1041-1049, 1990.

LIST OF FIGURES

Figure 1. Relationship between C/C_o, δ_o, and y. The x-axis is plotted as y/δ_o^2 and y/δ_o depending on whether δ_o is smaller or larger than 1, respectively.

Figure 2. Forward and inverse calculations (lines and circles respectively) of the particle residence times based on Equation (5), with different values of the parameter group $(K_{d\_p}D_e)^{1/2}/b$, which label the curves.

Figure 3. Comparison of THEMM results with the analytical solution of Tang et al. (1981). Tracer concentration is shown as a function of linear distance from the injection well.

Figure 4. Comparison of THEMM results with the semi-analytic results of Chen (1986). Distribution of tracer concentration is shown as a function of radial distance from the injection well at three injection times as indicated.

Figure 5. Comparison of THEMM results with the semi-analytical solution of Moench (1995). Tracer concentration at the pumping well is shown as a function of time for different γ values.

Figure 6. The front of tracer plumes after 100 minutes of injection. The injection well is at (0.5, 0.5). The case for the homogeneous fracture medium is shown on the left and that for the heterogeneous medium is shown on the right.

Figure 7. Tracer concentration as cumulative mass recovered divided by the total injected mass as a function of time during the withdrawal period in an injection-withdrawal test.

Tracer Mixing at Fracture Intersections

Guomin Li

Earth Sciences Division
Lawrence Berkeley National Laboratory
One Cyclotron Road, Berkeley, California

ABSTRACT

Discrete network models are one of the approaches used to simulate a dissolved contaminant, which is usually represented as a tracer in modeling studies, in fractured rocks. The discrete models include large numbers of individual fractures within the network structure, with flow and transport described on the scale of an individual fracture. Numerical simulations for the mixing characteristics and transfer probabilities of a tracer through a fracture intersection are performed for this study. A random-walk, particle-tracking model is applied to simulate tracer transport in fracture intersections by moving particles through space using individual advective and diffusive steps. The simulation results are compared with existing numerical and analytical solutions for a continuous intersection over a wide range of Peclet numbers. This study attempts to characterize the relative concentration at the outflow branches for a continuous intersection with different flow fields. The simulation results demonstrate that the mixing characteristics at the fracture intersections are a function not only of the Peclet number but also of the flow field pattern.

1. INTRODUCTION

Fractures represent preferential pathways along which a dissolved contaminant, which is usually represented as a tracer in modeling studies, can migrate rapidly in geologic formations. Discrete network models are one of the approaches used to simulate tracer transport in fractured rocks. The discrete models include large numbers of individual fractures within a network structure, with flow and transport described on the scale of an individual fracture and from fractures to fractures. What is not sufficient clear for tracer transport in discrete fracture networks is how various tracer transfer processes, which act on a number of different scales, interact to determine transport patterns and tracer concentrations, and how we can develop quantitative methods to describe transport in a rock mass where fractures provide the dominant pathways for transport migration (Smith and Schwartz, 1993). Our particular issue is what is the flow and transport pattern at fracture intersections.

There are basically two types of fracture intersections (or junctions) formed when one fracture crosses a second fracture: continuous intersections and discontinuous intersections. A continuous intersection occurs when each inflow branch is connected by a corresponding outflow branch. At a discontinuous intersection, the sequence of inflow branches is interrupted by one or more outflow branches (an example is a T-intersection) (Berkowitz et al., 1994).

Wilson and Witherspoon (1976) describe experimental studies of flow through a continuous intersection; they proposed a streamline routing theory, in which the mass

flux is determined only by the discharge patterns in related fractures. Hull and Koslow (1986) report laboratory experiments for both continuous and discontinuous intersections, and explore streamline routing to explain the mass transport through the intersections. Robinson and Gale (1990) provide examples that illustrate the differences in mass distribution that develop with two different approximations: streamline routing and complete mixing in the fracture intersection. In the fracture network models, there can be significantly greater transverse spreading of tracer under the assumption of complete mixing, while streamline routing tends to minimize transverse spreading. Philip (1988) has solved the boundary-value problem that describes the micro-scale flow pattern at an intersection of two equal-aperture orthogonal fractures. Philip (1988) characterizes the mixing process at a fracture intersection in terms of a local Peclet number, representing the interplay between advective and diffusive tracer transfer. Park and Lee (1999) provide simple analytical solutions for the mixing characteristics at the continuous fracture intersections. As the Peclet number increases, the analytical solutions also indicate the transition from complete mixing to streamline routing at a fracture intersection (Park and Lee, 1999).

The particle-tracking technique has been widely used to study the solute dispersion in a heterogeneous porous medium. It was also used by Schwartz et al. (1983) to address the dispersion in an idealized fractured medium consisting of two sets of orthogonal fractures. Berkowitz et al. (1994) applied a random-walk particle-tracking method to study mixing behavior at an idealized fracture junction. In their studies, mixing ratios are expressed in terms of a local Peclet number. They indicate that as a general observation,

the concept of complete mixing within a fracture intersection does not properly represent the mass transfer process at any value of the Peclet number. Li (1995) applied a numerical lattice-gas automata (LGA) model to study the relationship between mixing behavior and the local Peclet number. The LGA simulations of the mixing behavior at fracture intersections predict that for Peclet numbers smaller than 1, diffusion dominates the process of tracer transport, and complete mixing occurs. For Peclet numbers larger than 1, both diffusion and advection play important roles in the mixing process. Stockman et al. (1997) applied LGA and lattice Boltzmann (LB) methods to simulate the mixing ratio versus the Peclet number, and compared their results with other experiments and numerical simulations. They investigated the significant effect of the boundary conditions and size of the computational domain on the result observed. Results from the LGA and LB simulations and the simulations of Berkowitz et al. (1994) shows significant differences from each other (Stockman et al., 1997).

The objective of our current study is to conduct numerical simulations using the random-walk particle-tracking method and to investigate the mixing behavior of tracer transport at fracture intersections, and to compare the results with those for earlier studies presented above. An equal flow rate model, in which the flow rate is the same in all fracture branches, is used as our base model for simulating the mixing behavior for four scenarios representing hydrodynamic dispersion: pure molecular diffusion, mechanical dispersion and two combinations of molecular diffusion and mechanical dispersion. The pure molecular model is also used to investigate the effect of initial tracer concentration. Two non-equal flow rate models are used to investigate the effect of changing flow fields

on the mixing behavior at fracture intersections. Finally, comparisons with existing numerical and analytical solutions are discussed.

2. METHODOLGY

A two-dimensional inviscid and irrotational steady flow is assumed in this study (Figure 1). The pressure H in the domain is described by the differential equation

$$\nabla^2 H = 0 \qquad (1)$$

subject to boundary conditions.

The fluid velocity can be defined for a chosen volumetric flow through the fracture intersection under chosen boundary conditions, for different permeability values of the inflow and out-flow branches. Then, the advective transfer of tracer spreading (resulting from streamlines taking a two-dimensional configuration with differing path lengths controlled under the distribution of velocities) can be estimated.

To compare different numerical results, we introduced the Peclet number P_e to represent the flow conditions. The local Peclet number can be defined as

$$P_e = 1.414\ bv/D \qquad (2)$$

where v is the average velocity within the intersecting area (Figure 1), b is the width of the fractures (where two intersecting fractures are assumed to have the same width), and D is the coefficient of local hydrodynamic dispersion. The coefficient of local hydrodynamic dispersion is defined as the sum of the coefficients of mechanical dispersion and molecular diffusion. The local Peclet number can be approximated by

$$P_e = 1.414\, bv/(\alpha_L v + D') \tag{3}$$

where α_L is the coefficient of longitudinal dispersion, and D' is the coefficient of molecular diffusion. The Peclet number expresses the relative importance between advection and diffusion within the intersection area. As the fluid velocity increases, the Peclet number increases, and the influence of diffusion decreases. On the other hand, as the fluid velocity decreases, the Peclet number decreases, and diffusion tends to play a relatively more important role in the transport process.

Diffusive processes within the individual fracture will depend upon boundary conditions, permeability distributions, residence time of mass in the system, and the magnitude of the fluid diffusion coefficient. Clearly, if the residence time in the fracture is sufficiently long, diffusion spreads mass across streamlines and results in a transverse concentration profile.

The general nonreactive mass-transport problem for a dissolved, neutrally buoyant species involves the solution of the mass balance equation

$$\partial c/\partial t + \nabla(c \bullet v) - \nabla(D \bullet \nabla c) = 0 \qquad (4)$$

for the concentration c over a period of time, subject to a set of initial and boundary conditions for c. D represents the dispersion coefficient.

In the calculations that follow, a random-walk, particle-tracking model is applied to simulate tracer transport in fracture intersections by moving particles through space using individual advective and diffusive steps. This method is based upon analogies between mass transport equations and certain stochastic differential equations. A particle is displaced according to the following simple relationship (Thomson and Gelhar 1990):

$$X^n = X^{n-1} + A(X^{n-1})\,\Delta t + B(X^{n-1}) \bullet Z \sqrt{\Delta t} \qquad (5)$$

where X^n is its position at time level $n\Delta t$, A is a deterministic forcing vector, B is a deterministic scaling matrix, and Z is a vector of random numbers with a mean of zero and variance of one. The motion of one particle will thus be statistically independent from that of another. If a large number of identical particles associated with a particular component are moved simultaneously, then their number density f (x, t) will approximately satisfy the Ito-Fokker-Planck equation (Kinzelbach 1988):

$$\partial f/\partial t + \nabla(A \bullet f) - \nabla\nabla : (1/2 B \bullet B^T \bullet f) = 0. \qquad (6)$$

Equation (4) represents the mass balance for a conservative aqueous constituent. The particle-tracking method succeeds if the particle number density f in Equation (6) is proportional to c in Equation (4), subject to A and B by

$$A \equiv v + \nabla \bullet D \tag{7}$$

and

$$B \bullet B^{T} \equiv 2D \tag{8}$$

Thompson and Gelhar (1990) discussed some of the issues concerning the computational approximations required in applying a random-walk particle-tracking model (Equation 5).

3. MODEL STRUCTURE AND BOUNDARY CONDITIONS

Figure 1 shows the fracture intersection model and its boundary conditions. The groundwater flow through this domain is also calculated for constant piezometric head boundaries: the left-hand and bottom boundaries are assumed to be at 1 μm head, and the right-hand and top boundaries are assumed to be at 0 μm head. The flow rates into left and bottom branches are assumed to be equal. .

The 2-D finite element method is used to discretize the flow domain (70 × 70 elements; each with a dimension of 1 × 1 μm). The domain is divided into two intersecting fractures, each 10 μm wide, and with a permeability of 1.0 μm^2, surrounded by a very low-permeability background of 1.0×10^{-30} μm^2, representing an impermeable rock matrix (Figure 1). The permeability is uniform over the flow field; i.e, the flow-rate in the

left fracture equals that in the lower fracture (flow ratio 50/50). Fractures (the higher permeability domain) represent preferential pathways along which a solute can migrate rapidly; however, tracer diffusion from the fractures to the matrix (the lower-permeability domain) can significantly reduce migration rates along the fractures.

For our study, particles are introduced at the left-hand high-head boundary. The random-walk method is based on particle transport under the influence of both rock spatial fluid velocities and diffusion. It is possible for some particles to travel backward across the left-hand inflow boundary or to jump into the impermeable rock matrix from one time step to the next. We assume that the particle will disappear if it goes out the left-hand boundary, or will be bounced back (perfect reflection) into the modeling domain if it goes out of the fracture domain into the low-permeability background region. This confines the tracer transport, represented by a number of particles, to the fractures and the fracture intersection.

4. SIMULATION RESULTS

From the flow model, the velocities can be calculated at any position in the domain. All particles are introduced at a distance of 5 μm from the left-hand high-piezometric head boundary and are collected at the right-hand and top low-piezometric head boundaries. A plot of the number of particles collected at the right-hand boundary and top boundary at different arrival times constitutes the breakthrough curves. In these calculations, 20 particles were used to show the solute flow lines and 5,000 particles to plot the breakthrough curves.

The mixing rule at fracture intersections is applied in numerical simulations of mass transport in modeling studies of discrete fracture networks. Three mixing rules have been proposed to simulate the partitioning of mass among the fractures carrying water away from an intersection: streamline routing, streamline routing with diffusion within fracture intersections, and complete mixing (Smith and Schwartz, 1993). Streamline routing and complete mixing rules may be appropriate for very high and very low Peclet numbers, respectively. However, these situations rarely happen in the real world. Therefore, streamline routing with diffusion within fracture intersections may be realistic to simulate tracer transport in discrete fracture networks. In this study, numerical simulations are performed for a wide range of Peclet numbers, between 5×10^{-3} and 6×10^{4}.

As previously stated, the Peclet number (Equation 3) is a function of longitudinal dispersion and molecular diffusion. Bear (1979) and Fried (1971) have plotted the results of many experiments that show the relationship between molecular diffusion and hydrodynamic dispersion. Experimental results with low Peclet numbers indicate five ranges: 1) $P_e \leq 0.4$, in which molecular diffusion predominates, as the average flow velocity is very small; 2) $0.4 < P_e \leq 5$, in which the effects of mechanical dispersion and molecular diffusion are of the same order of magnitude; 3) $5 < P_e \leq 300$, in which the spreading is mainly by mechanical dispersion; 4) $300 < P_e \leq 30{,}000$, in which mechanical dispersion dominates and the effect of molecular diffusion is negligible; and 5) $P_e \geq 30{,}000$, in which pure mechanical dispersion occurs, but beyond the range of Darcy's law.

Based on the above discussion, four models are used in our simulations to represent the relationship between molecular diffusion and longitudinal dispersion: pure molecular diffusion, mechanical dispersion and two combinations.

In the pure molecular diffusion and pure mechanical dispersion models, Equation (3) is simplified as $P_e = 1.414bv/D'$ and $P_e = 1.414b/\alpha_L$, respectively. In the pure molecular model, we consider only molecular diffusion, without advection by mechanical dispersion, even for high flow velocities (high Peclet numbers). The mixing may be accelerated and overestimated by the diffusion due to the difference between the concentrations of the streamlines. In the pure mechanical model, we consider only advection by longitudinal dispersion even for low velocities (low Peclet numbers). Therefore the mixing may be decreased and underestimated. These two models may provide the range of the mixing ratio in fracture intersections over a wide range of Peclet numbers.

4.1 Mixing Process

Figure 2 shows the 20 particle traces with different Peclet numbers for the base model. The pure molecular model is used to simulate the particle movement in the fractures and their intersection.

Figure 2a shows that all the particles move from the left-hand boundary to the top boundary at a very high Peclet number of 1.18×10^4. This indicates that the diffusion

term is too small to affect particle movement in the flow field, so those particles follow the streamlines. This is an example of streamline routing. In Figure 2b, under the conditions of a Peclet number of 118, some of the particles jump into nearby streamlines; some then move out of the right-hand boundary.

We need to know what percentage of particles can go through the right-hand boundary, and whether complete mixing can happen. It is clear that the smaller the Peclet number, the higher the number of particles that will go through the right-hand boundary.

Figure 3 shows the relative concentration of particle distribution in the outflow branches for a range of Peclet numbers between 5×10^{-3} and 6×10^{4}. It is clear in Figure 3 that solutions using the pure mechanical dispersion model underestimate the mixing ratio when compared with the results of the pure molecular diffusion model. As the Peclet number decreases, both results show more mass mixing at the intersection, and the mixing ratio increases toward an asymptotic value of 0.5, indicating that complete mixing may be occurring. Both models show a declining mixing ratio at the intersection as the Peclet number increases toward zero. The results of the two combinations of molecular diffusion and longitudinal dispersion fall between the results from the pure molecular diffusion and the pure mechanical models. The significantly lower results from the pure mechanical model indicate that the mixing ratio at the fracture intersection should be higher in the pure molecular diffusion model than in the pure mechanical model for the same Peclet number. Therefore, mixing accelerated by diffusion due to the difference in concentrations of the streamlines must be included to be more realistic. The results of the

pure mechanical model and the pure molecular model provide a wide range of mixing ratios for a range of Peclet numbers.

4.2 Effect of Initial Tracer Concentration

To investigate the relationship between the initial position of the particles relative to the left-hand boundary and the resulting characteristics of tracer transport, the particles are introduced 25, 10 and 5 μm from the intersection in the left-hand high-piezometric head branch. In these calculations, 5,000 particles are used in the pure molecular diffusion model to track the tracer transport and to plot the breakthrough curves. The flow rate in the left-hand fracture branch is assumed to be same as that in the lower fracture branch (flow ratio 50/50).

As seen in Figure 4, when $P_e < 1$ and $P_e > 10$, for the model with particles introduced 5 μm from the fracture intersection, relative concentrations from the right fracture branch are slightly higher than those from the other two models. However, for the 10 μm model (particles introduced 10 μm from the fracture intersection; i.e., the width of the fracture), no significant difference is found even at the lower Peclet number when compared to the 25 μm model. This indicates that errors due to the initial tracer concentration in the left fracture branch can be ignored when the particles are placed 10 μm or more from the fracture intersection.

4.3 Effect of Flow-Rate Ratio

In the above models, permeability, and therefore flow rate, are the same in all fracture branches. The flow field is expressed in terms of the ratio of the inflow in the left branch to that in the lower fracture branch (flow ratio 50/50).

If we adjust the permeability distribution, we will obtain different ratios of the flow rate in the right-hand fracture branch and the upper fracture branch. Two models, Model A and Model B, are chosen to study the tracer mixing in the fracture intersection. In Model A, we assume that the permeability in the upper and lower fracture branches is two times that in the left and right fracture branches. The permeability in the intersection area is the same as those in both left and right fracture branches. The ratio of the flow rate in the right fracture (Q_e) to that in the lower fracture (Q_n) is about 35/65 (Q_e/Q_n). In Model B, it is assumed that the permeability in the left and right fracture branches is 10 times that of the other two fracture branches, including the intersection area. The ratio of the flow rate in the left-hand fracture branch to that in the lower fracture branch is around 83/17 (Q_e/Q_n).

In Models A and B, all particles are introduced 25 μm from the fracture intersection in the left-hand high-piezometric fracture branch, and are collected at the right-hand low head boundary. In these calculations, 20 particles are used to show the solute flow lines and 5,000 particles to plot the breakthrough curves. Pure molecular diffusion is applied to simulate the mixing behavior at fracture intersections.

As shown in Figure 5a, for Model A, all particles move from the left-hand boundary to the top boundary at a very high Peclet number of 1.18×10^4. The mass distribution is controlled by the function of streamlines. Figures 5b shows that some of the incoming particles occupy the whole upper fracture and the rest of the particles from the left-hand fracture branch flow into the right-hand branch.

Figure 6 shows the relative concentration of particle distribution in the outflow branches versus the Peclet number in Model A, Model B and the equal-flow-rate pure molecular model (Q_e/Q_n = 35/65, 83/17 and 50/50, respectively). It is clear in Figure 6 that the relative concentration is not only affected by the mixing processes but also controlled by the flow fields.

In the right fracture branch, the mixing relative concentration of the models is near 0.5; i.e., complete mixing, at low Peclet numbers (Figure 6a). Streamline routing might occur at somewhere above a Peclet number of 500. Due to the relatively low flow rate through the right-hand branch in Model A, the particles easily go through the top fracture branch. Therefore, the result from Model A is an underestimation when compared with the base model. On the other hand, Model B has a relatively high flow rate through the right-hand fracture branch. Therefore, the relatively high-concentration number associated with the configuration of the flow field (Q_e/Q_n = 83/17) remains constant as the Peclet number increases toward a higher value than 1 (Figure 6a).

Mixing characteristics in terms of the resulting percentage of the relative concentration from the left fracture branch travelling into the top fracture branch at fracture intersections in Model A and Model B are compared with the base model (Q_e/Q_n = 50/50; Figure 6b). At $P_e < 10^{-2}$, the particles completely mix at the intersection and then dilute into the top fracture branch. For Models A and B, the transition zones have a range of about 3 orders of magnitude (10^{-2} to 10). We expect that as Peclet numbers increase above 10, tracer transport is dominated by streamline routing, and the relative concentration in the top fracture branch is controlled by the flow fields configurations.

5. DISCUSSION AND SUMMARY

The purpose of this study was to apply random-walk methods to simulate the mixing behavior of tracer transport at an idealized fracture intersection.

We have compared our results with the numerical solutions of Berkowitz et al. (1994) and Li (1995), and the analytical results of Park and Lee (1999). For the comparison, the tracer (relative concentration of 1) is introduced only into the left inflow branch (Figure 1). Results for an equal flow rate case are plotted in Figure 7, which shows that the results of the pure molecular diffusion model in this study match well the results of Li (1995) and Stockman et al. (1997). Both the results of Berkowitz et al. (1994) and Park and Lee (1999) underestimate the mixing ratio as compared with our results and those of Li (1995) and Stockman et al. (1997).

Berkowitz et al. (1994) applied a random-walk particle-tracking method to study mixing characteristics at fracture intersection. They never observed diffusion-controlled complete mixing in a simulation, even at an intersection Peclet number as low as 3×10^{-3}. They explained this less-complete mixing by noting that particles entering the intersection on a streamline close to the left side of the wall of the left-hand fracture have a higher probability of moving across the diving streamline into the left flow region than of remaining inside the original flow domain. Our results indicate that the errors due to the initial tracer concentration in the left fracture branch can be ignored when the particles are introduced 10 μm or more from the fracture intersection.

Park and Lee (1999) applied simple analytical solutions for the mixing characteristics and transfer probabilities of mass at the fracture intersection. They indicated that possible underestimation of both their solution and that of Berkowitz et al. (1994) compared with Stockman et al. (1997) might be explained by the assumptions on the boundary conditions and the occurrence of longitudinal diffusion. They concluded that the boundary conditions at fracture walls might not be responsible for the underestimation of the mixing ratio, and also that the mixing ratio may be underestimated unless longitudinal diffusion is considered, especially at a low Peclet number.

Li (1995) and Stockman et al. (1997) applied lattice gas automata (LGA) numerical simulations to investigate the mixing behavior at the fracture intersection. Their results shown that as the Peclet number decreases, the mixing ratio at the intersection increases toward an asymptotic value of 0.5. When the Peclet number is smaller than 0.68, there is

complete mixing. They expect that at a Peclet number somewhere above 3×10^2, the mixing ratio will approach zero.

Our results show that the Peclet number is the key parameter controlling tracer mixing at a fracture intersection. Due to difficulty in applying the unknown nonlinear relationship between mechanical dispersion and molecular diffusion, a pure mechanical dispersion (longitudinal dispersion) model, a pure molecular diffusion model and two linear combinations of mechanical dispersion and molecular diffusion were proposed to simulate the mixing behavior versus the Peclet number. These results provide the mixing characteristics over a range of Peclet numbers between 5×10^{-3} and 6×10^4.

Complete mixing may happen as the Peclet number becomes less than 1. The range of our results of the pure molecular diffusion model includes the results of Li (1995) and Stockman et al. (1997; Figure 7). From these results we expect that a nonlinear combination of molecular diffusion and mechanical dispersion, i.e., a relatively high molecular diffusion coefficient at low Peclet numbers, and vice versa, may fit well with a real-world mixing process.

For an equal flow rate model with a very small Peclet number, the streamlines are no longer important for particle migration calculations. Complete mixing might occur, so that the relative concentration of tracer moving across the right-hand boundary is near 0.5, as would be expected. As the Peclet number increases somewhere above 10^2, the mixing ratio approaches zero, the tracer transport is dominated by the streamline routing,

and the relative concentration in the right-hand branch approaches 0. These results indicate a transition zone of about 3 orders of magnitude in Peclet numbers (10^{-1} to 10^{2}).

Two non-equal flow rate models, Model A (Q_e/Q_n = 35/65) and Model B (Q_e/Q_n = 83/17), were used to investigate the effect of flow fields on the mixing behavior at fracture intersections. Under a low Peclet number of 10^{-2}, the particles completely mix at the intersection and then dilute into outflow fracture branches. We expect that as Peclet numbers increase above some value over 10, tracer transport is dominated by streamline routing. In the equal flow rate model, the transition zones exist. However, the transition zones have different ranges when compared with the equal flow rate model. For a non-equal flow rate model, our results indicate that the flow fields as well as the Peclet numbers control tracer transport.

ACKNOWLEDGEMENTS

The authors thank Chin-Fu Tsang and Mary Pratt of Lawrence Berkeley National Laboratory for their helpful comments and careful review of the manuscript. This work was supported by the Power Reaction and Nuclear Fuel Development Corporation (PNC) of Japan under a binational agreement between PNC and the U.S. Department of Energy, Office of Science, Office of Environmental Management, under Contract No. DE-AC03-76SF00098.

REFERENCES

Bear, J., *Hydraulics of Groundwater*, McGraw-Hill, New York, 569pp., 1979.

Berkowitz, B., C. Naumann, L. Smith, Mass transfer at fracture intersections: An evaluation of mixing models, Water Resour. Res., 30, 1765-1773, 1994.

Fried, J. J., *Groundwater Pollution*, Elsevier, Amsterdam, 930 pp., 1975.

Hull, L. C., K. Koslow, Streamline routing through fracture junctions, Water Resour. Res., 22, 1390-1400, 1984.

Kinzelbach, W., The random walk method in pollutant transport simulation, in Groundwater Flow and Quality Modeling, edited by E. Custodio, A. Gurgui, and J. P. Lobo Ferreira, pp. 227-245, D. Reidel, Norwell, Mass., 1988.

Li, C.H., Low Peclet number mixing behavior at fracture junctions, Ph.D. Thesis, New Mexico Institute of Mining and Technology, 1995.

Park, Y. J., K. K. Lee, Analytical solutions for solute transfer characteristics at continuous fracture junctions, Water Resour. Res., 35, 1531-1537, 1999.

Philip, J., The fluid mechanics of fracture and other junctions. Water Resour. Res., 24, 239-246, 1988.

Robinson, J.W., J.E. Gale, A laboratory and numerical investigation of solute transport in discontinuous fracture systems, Ground Water, 28(1), 25-36, 1990.

Schwartz, F. W., L. Smith, A. S. Crowe, A stochastic analysis of macroscopic dispersion in fracture media, Water Resour. Res., 19(5), 1253-1265, 1983.

Smith, L, F. W. Schwartz, Solute transport through fracture networks, *in Flow and Contaminant Transport in Fractured Rock*, edited by Bear, J., C. F. Tsang and G. Marsily, pp.129-167, Academic Press, San Diego, California, 1993.

Stockman, H. W., C. Li, J. L. Wilson, A lattice-gas and lattice Boltzmann study of mixing at continuous fracture junctions: Importance of boundary conditions, Geophys. Res. Lett., 24(12), 1515-1518, 1997.

Tompson, A. F. B., L. W. Gelhar, Numerical simulation of solute transport in three-dimensional, randomly heterogeneous parous media, Water Resour. Res., 26, 2541-2562, 1990

Tsang, Y.W., C.F. Tsang, Flow channeling in a singer fracture as a two-dimensional strongly heterogeneous porous medium, Water Resour. Res., 25, 2076-2080, 1989.

Wilson, C. R., P. A. Witherspoon, Flow interference effects at fracture intersections, Water Resour., Res., 12, 102-104, 1976.

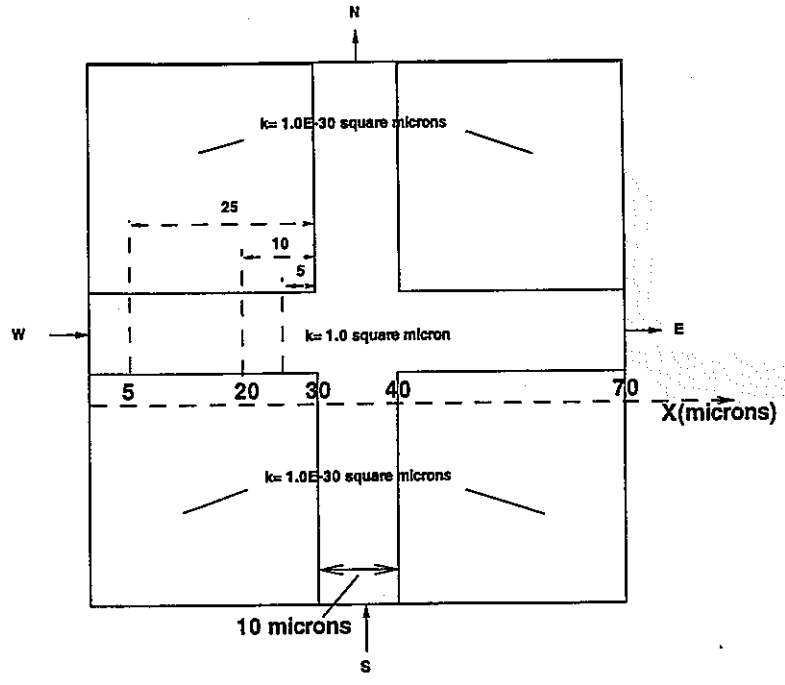

Figure 1. Fracture intersection model and boundary conditions. Pressure gradient from left to right and from down to up is 1.43×10^{-4}.

a

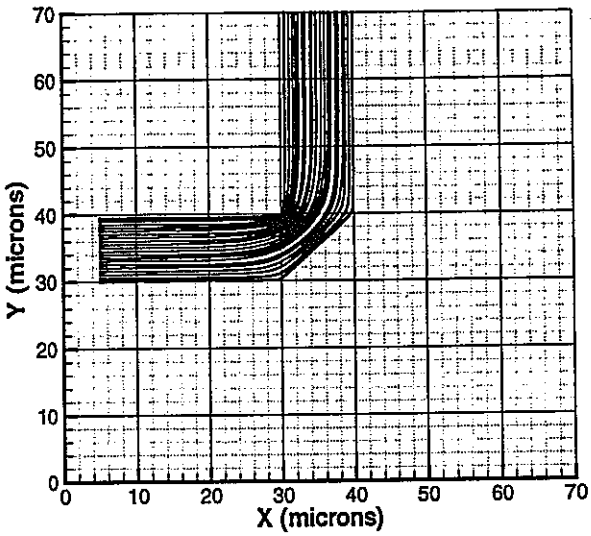

b

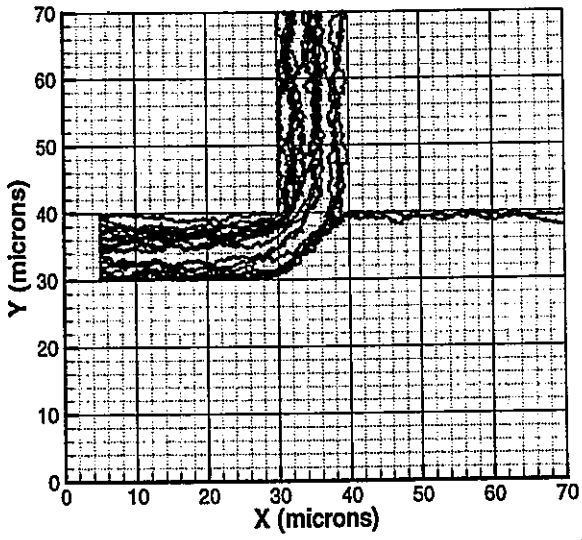

Figure 2. Spatial particle trace in the base model with flow rate ratio Q_e/Q_n = 50/50 for (a) Peclet number 1.18×10^5 and (b) Peclet number 1.18×10^2.

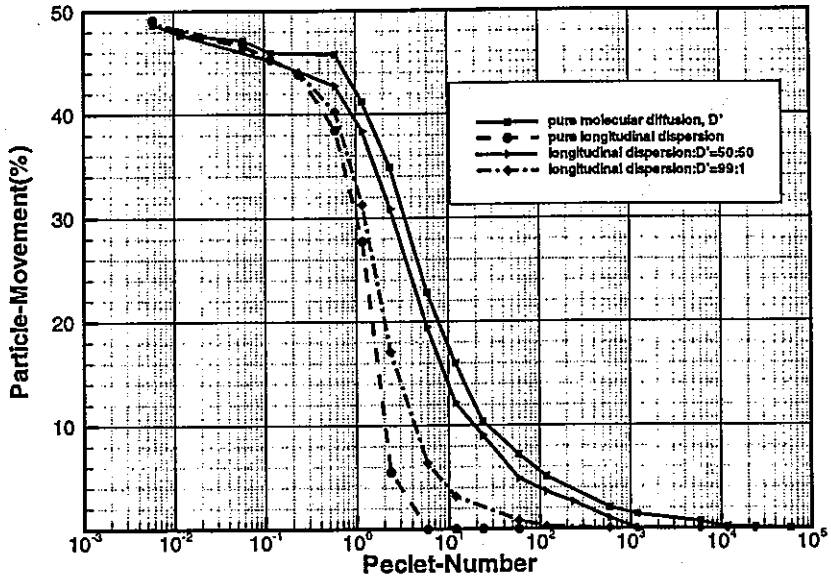

Figure 3. The relative concentration percentage of the particles passing through the boundaries over the total particles is a function of the Peclet number. The low curve is the percentage of the relative concentration passing through the right-hand boundary. Particles are placed in the left-hand fracture at 5 μm from the left boundary.

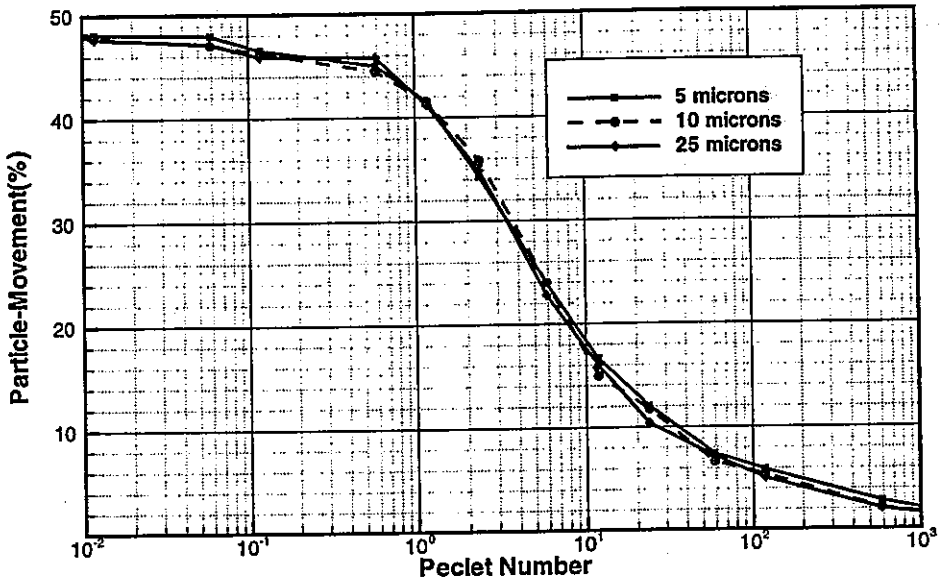

Figure 4. Comparisons of mixing characteristics at fracture intersections in terms of the resulting percentage of the relative concentration from the left fracture branch travelling into the right fracture branch. The different curves are for the different distances at which the particles were placed relative to the intersection in the left fracture branch (see Figure 1).

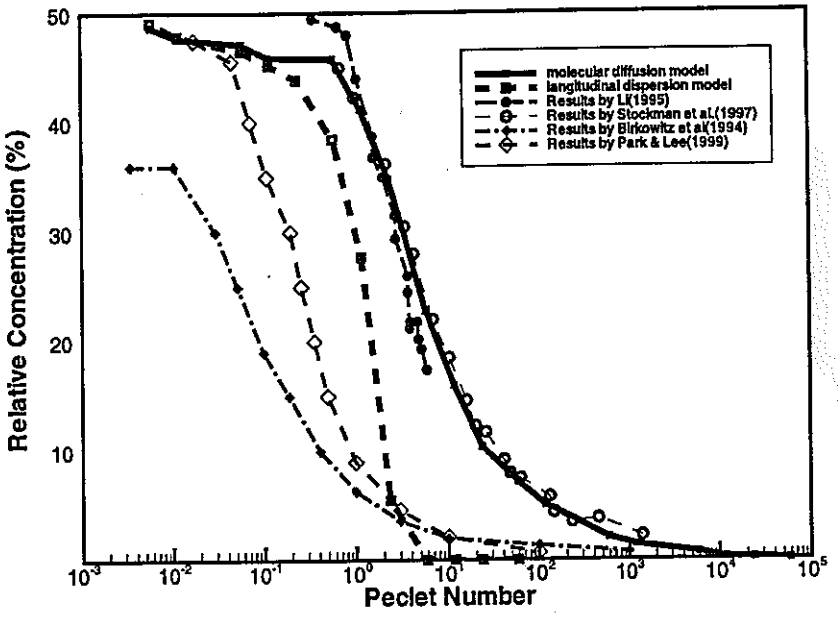

Figure 7. Comparisons of mixing characteristics (the percentage of the particles throughout the right-hand fracture branch) at the fracture intersection with an analytical result and two numerical results.

a

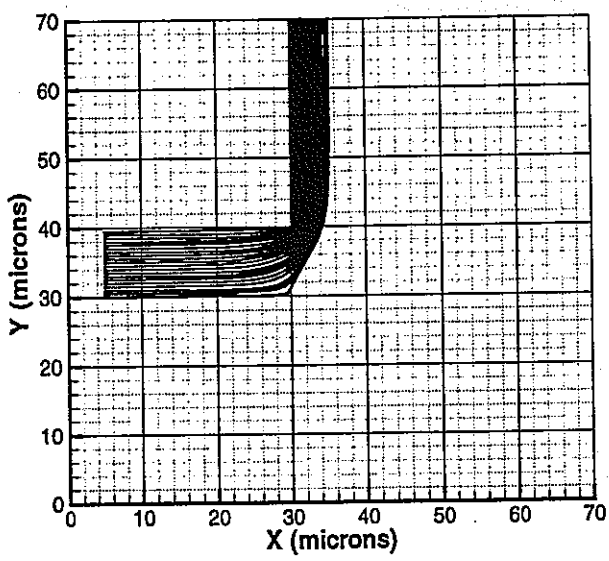

b

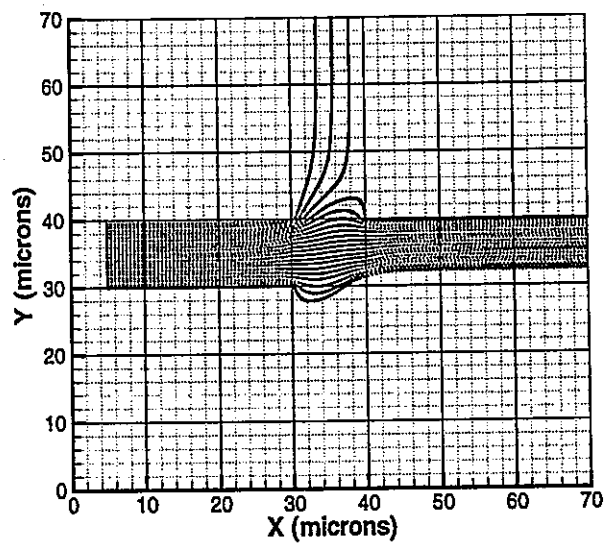

Figure 5. Spatial particle trace with Peclet number 1.18×10^5 . (a) Model A: plug flow W35/S65 and (b) Model B: plug flow W83/S17.

a

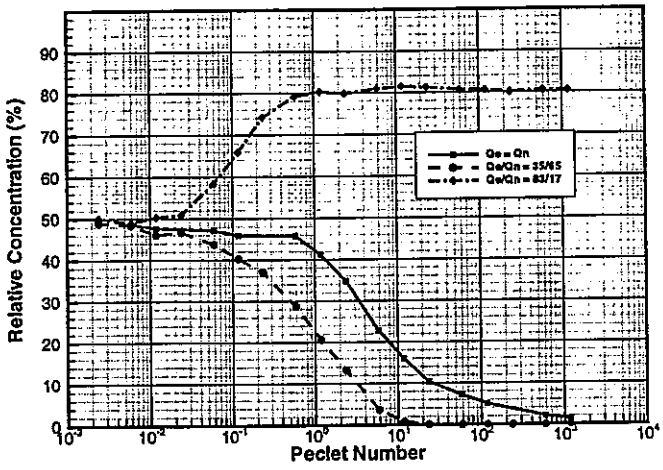

b

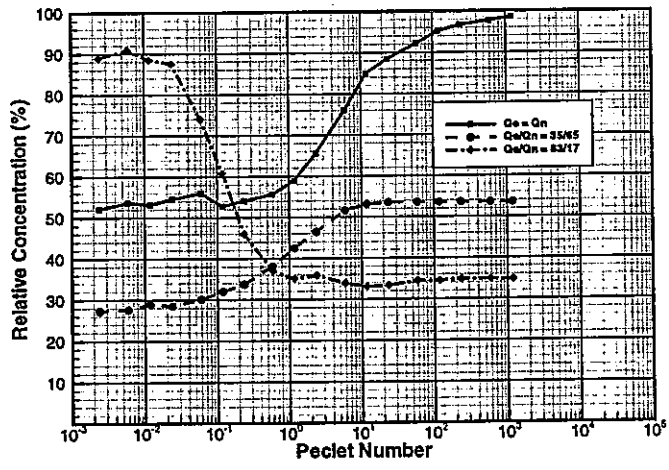

Figure 6. Comparisons of mixing characteristics at fracture intersections in Model A and Model B with the base model. (a) The relative concentration from the left fracture branch travelling into the right fracture branch. (b) The relative concentration from the left fracture branch travelling into the top fracture branch.

PA Methodologies from a Combined Review of NIREX95, SITE-94 and TILA-99

Chin-Fu Tsang
Earth Sciences Division
Ernest Orlando Lawrence Berkeley National Laboratory
Berkeley, California 94720

1. Introduction

The current reviews and comments are based on earlier reviews made on NIREX95[1], SITE-94[2] and TILA-99[3], details of which may be found in Annual Reports 1997–1998, 1998–1999 and1999–2000, respectively. The goal of the current combined review is to extract the best methodologies for conducting performance assessment (PA) of a potential nuclear waste repository. These, we hope, would be applicable and valuable to other nuclear waste management programs. The focus will be on identification of state-of-the-art approaches and techniques, and on lessons learned. Thus no specific sites, such as Sellafield or Äspö, will be particularly emphasized.

---

[1] Postclosure Performance Assessment: NIREX95 - A Preliminary Analysis of the Groundwater Pathway for a Deep Repository at Sellafield. Volume I: Development of the Hydrogeological Conceptual Model. Volume II: Derivation of Effective Hydrogeological Parameters for Regional Modeling. Volume III: Calculations of Risk. United Kingdom NIREX Limited, Science Report 5/95/012.1995.

[2] SKI SITE-94 - Deep Repository Performance Assessment Project, Volumes 1 and 2. Swedish Nuclear Power Inspectorate (SKI) Report 96:36, December 1996.

[3] TILA-99, Safety Assessment of Spent Fuel Disposal in Hästholmen, Kivetty, Olkiluoto and Romuvaara, by Timo Vieno and Henrik Norman, Report POSIVA 99-07, POSIVA OY, Helsinki, Findland: March 1999.

In conducting such a review and extraction, subjective judgments have to be made, which are probably biased by the experiences and views of the author.

The report will begin with some general initial comments, followed by key points on site selection, construction of a conceptual model, establishment of possible scenarios, and the use of the so-called features, events and processes (FEP) approach. The following sections will discuss the different types of uncertainties that need to be addressed and evaluated. Then three approaches to flow and transport modeling will be presented. Following this, sensitivity studies and "what if" analysis will be described. Finally, the report will conclude with several remarks and a few comments and suggestions on the approach and methodologies used in the JNC's H-12 report.[4]

2. Initial Comments

It is interesting to note that, while there are significant similarities in the approaches and methodologies used in NIREX95, SITE-94, and TILA-99 documents, they have three different emphases. Thus, TILA-99 emphasizes a simplified analysis to establish the basis for the safety of a geologic nuclear waste repository. SITE-94, on the other hand, emphasizes an evaluation of results from alternative model analyses. Finally, NIREX95 puts its emphasis on a detailed model study in which parameter ranges are explicitly addressed using not only site-specific data (where available), but also a structured expert-elicitation procedure. These will be discussed further below.

All three documents recognize that PA is complex, involves many judgment stages, and needs consistency and uncertainty evaluation. They also see the need for a comprehensive sensitivity and "what if" analysis for a suite of possibilities, to add confidence to the PA results.

[4] Japan Nuclear Cycle Development Institute, Second Progress Report on Research and Development for the Geological Disposal of HLW in Japan. H12: Project to Establish the Scientific and Technical Basis for HLW Disposal in Japan, April 2000.

The aim is that the PA exercise should be "robust, transparent, traceable, and reproducible."

3. Example Schedule and Timeline

Selecting a site for establishing a nuclear waste repository and investigating its suitability are not a simple, short-term enterprises. Rather, they are multiple-year programs requiring careful work every step of the way. The list below gives the steps and time needed, mainly based on the TILA-99 report, but other countries' nuclear waste programs follow a similar schedule.

- Site Identification Surveys — 2 years
- Preliminary Site Investigation (a few boreholes) — 6 years
- Detailed Site Investigations for 2-4 sites – a number of boreholes, still surface-based studies — 7 years
- Choice of one (or more than one) site for an underground rock characterization facility and confirmatory investigations. — 10 years
- Construction of repository for emplacement of waste — 10 years

4. Identification of Fractures and Fracture Zones

It has been well recognized that in almost any deep geologic formations, a site can be found for safe storage of nuclear waste if the formations were homogenous, having no fractures or fault zones. Thus, the identification and characterization of fractures and fracture zones are of critical importance in the evaluation of the isolation potential of a site. These are the main objectives of a site-investigation program.

Until the stage of subsurface studies in an underground characterization facility, site investigation will be conducted mainly by surface geological, geophysical and hydrological surveys, as well as downhole studies

through deep wells. Typically, these wells number around 10–30 and are 200–500 m in depth. Methods used in borehole studies include:

- Double packer tests (with testing interval of 2 m or larger, and in some cases smaller intervals were also used).
- Flow meter and injection tests (to measure flow-rate variation along the length of a borehole and hence the permeability variation).
- Long-term, multiple-well pressure tests (to study connectivity between intervals in different wells and regional permeability variations).

It has been noted that high-permeability intervals in a borehole normally correspond to presence of open fractures, but there are significant exceptional cases where this correspondence is absent. Care should be taken to account for that possibility.

There are alternative ways of classifying different type of fractures or fracture zones. For example, TILA-99 classifies observed fracture zones in three ways. The first is "fracture zone classes," defined according to the confidence level in the identification of these features. The classes are "directly observed," "probable," or "possible." The second way is according to fracture-zone types, based on the degree of fracturing. The types are "crushed zone," "major fracture zones," "fracture zones," and "open or more abundant fracturing." The third way of grouping is according to the dip angle of the fracture zones, defined as "steep (with dip angles greater than 60°)," "between 30° and 60°, and smaller than 30°."

NIREX95, on the other hand, emphasizes the single-fracture end of the range by classifying fractures and fracture zones into four types, 0, I, II, and III. Type 0 is a medium without fractures; in other words, just rock matrix. In some cases, this type includes also a few independent fractures. Type I is a rock block with hydrogeologically significant fractures. Type II includes cases in which there is an organized structure of fractures with scales of hundreds of meters, and finally, Type III are those with an organized structure of fractures associated with major fault zones having lengths of kilometers.

Other ways of classifying fractures are also possible, including one in which fractures are grouped as "clean" single fractures, single fractures with splay fractures on either side of them, or double fractures connected by cross fractures like a ladder. The particular choice of fracture classification scheme depends on its use. For example, TILA-99's approach is useful for site screening and selection early on in the PA effort, while NIREX95's scheme was used to derive properties of strategraphic layers that enter into their PA model calculations. The lesson is the same form of fracture grouping needed to be developed as part of the site-characterization and PA process.

5. Locating a Potential Repository within a Site

To conduct a PA of a repository for a given site, we would need to specify the location of the repository in that site, since this defines the distribution of potential sources for radionuclide leakage and migration. A few general but useful points for locating a repository are:

- Avoiding major hydraulic fracture zones (note that hydraulic fracture zones are not necessarily identical to the geological fracture zones).
- Choosing optimal location in the groundwater flow regimes. Thus, for instance, a repository should not be located near a groundwater discharge region.
- Accounting for hydrochemical environment. For example, depths and areas of high-salinity groundwater should be avoided because the salinity would require more expensive non-corrosive materials for some construction elements, and it would also adversely affect the performance of engineering barriers around nuclear waste packages
- Accounting for constructability, which depends on lithology, bedrock fracturing and bedrock geotechemical properties, and magnitude and orientation of *in situ* stresses. It turns out potentially unsafe construction conditions have ruled out the selection of certain sites.

- *In situ*, at-the-time adjustments to avoid layer hydraulic fractures in tunnels and waste package emplacement holes. It is possible that even after careful site evaluation and selection, and during repository construction, hydraulic features are found that will necessitate an adjustment of repository layout to avoid them. Thus, a repository may be constructed in two or more separated parts to avoid significant hydraulic fault zones.

6. Development of a Conceptual Model and Scenarios

An approach to constructing a conceptual model that will define the geological system containing a repository has been well accepted among the nuclear waste disposal scientific community internationally. It is a formal process that can be documented and thus defensible. It may involve three methodologies:

a) FEP – to define present system
b) Process Influence Diagrams (PID) – to study process relationships
c) External FEP (EFEP) – to study external influences and boundary conditions.

The conceptual basis for system identification is that the geologic repository can be described as a system of interconnected FEPs, which directly or indirectly influence the release and transport of radionuclides from the repository through the geosphere to the biosphere. Extensive lists of FEPs (approximately 1,000) were developed previously in a number of national and international nuclear waste programs, such as IAEA, NEA, AECL, Nagra, UK Nirex, and SKI/SKB. Screening criteria have developed to select from these lists those FEPs relevant to a particular site. The relevant FEPs were classified as groups related to scenarios, models, and primary data, respectively. They are evaluated, and then many can be excluded because of their low probability of occurrence or negligible impact.

A reference case is defined as one where there are no changes in the EFEPs, and a "central scenario" like one in which the climatic evolution due to glaciation (with a cycle of about 100,000 years) is included. In addition to these two cases, a number of variant scenarios are also considered. Attention is paid not only to individual EFEPs, but also to their combinations and to the identification of initiating events, such as volcano eruption that initiates a particular group of EFEPs.

For both system and scenario identification, opinions are solicited from a widely diverse group of experts. This needs to be conducted according to a careful, systematic procedure with full documentation. This would allow subsequent reviews, revisions, or updates that are defensible.

7. Uncertainties in System and Scenario Identification

Evaluation of uncertainties is an important element in the PA of a geologic repository. The SITE-94 report provides extensive discussions of uncertainties involved in system and scenario identification. The discussions serve to identify, clarify, and perhaps reduce these uncertainties. They are also useful in putting the identified system and scenarios in proper perspective.

First, there is the system uncertainty. Since the geologic repository system is not fully known, certain FEPs may be missing in the PID, other FEPs may be improperly linked to each other, or the influence levels of the links may be misjudged. Assessment of system uncertainty is subjective and can be treated only by open documentation and systematic expert review.

The second is scenario uncertainty. This is the uncertainty related to the EFEPs, concerning the completeness of the included EFEPs and their quantitative measures, such as their impact and occurrence probabilities. The scenario also depends on the definition of the boundaries of the repository system. Some boundary definitions, such as those along a known fault that has been extensively investigated, may involve less uncertainty than others. Also, a farther boundary enclosing a larger region

may reduce scenario uncertainty, but at the price of increasing system uncertainty. Here, as in the case of system uncertainty, the assessment is subjective and has to be treated again by open documentation and systematic expert review.

Conceptual model uncertainty is the third type. This refers to whether the set of FEPs adequately represent the real system and can be used for developing predictions of its evolution. Such uncertainty is treated by model validation exercises, in which model results are compared with field tests and observations. Model validation is an iterative process, progressively testing against newer field experiments and defining its applicability range, and is thus always provisional. There are often cases where alternative conceptual models are all consistent with field observations and data, and yet there are different and yield different predictions. In these cases, either the more "conservative" model should be used or all the models should be used for PA with their uncertainty ranges of predictions combined.

Finally, there is the parameter uncertainty, which is associated with parameter values. The definitions of parameters are usually model dependent, and thus conceptual model uncertainty will also result in additional parameter uncertainty. The parameter uncertainty is often handled by representing each parameter by a distribution function and calculating the consequences for the performance of the repository system using a range of values sampled from the distribution. Parameter uncertainty is not parameter variability. The former refers to the fact that the value of the parameter (which may be constant) is not definitely known, while the latter refers to the fact that the parameter varies in value over space and time. Thus variability is not uncertainty, but a property of the repository system. However, variability does increase parameter uncertainty.

To handle the interaction and propagation of uncertainties through the PID, SITE-94 uses what is called the Assessment Model Flowchart (AMF). This chart shows explicitly the flow of information and uncertainties between available tools, techniques, or experts. Thus, it has three main

components: models (which process information mathematically), clearing houses (which are less quantitative than models and may possibly involve expert judgment) and information sources (which includes experiments, previous observations and scientific literature).

Overall, the development of system and scenario definitions using methodologies of the FEP, PID, EPEP, and AMF is a very interesting one. It may be the best approach available today. The discussion of uncertainties presented in SITE-94 is also very comprehensive and needs to be considered when applying the approach to a real site.

8. Uncertainties in Field Measurements and Development of Site Structural Models

The first and most common potential uncertainty concerning field data is data clustering and sampling bias in the measurement design. Often measurements tend to focus on major hydrologic features, such as a fracture zone and an area near the proposed underground research laboratory (URL) location. The acquired data would be used in the design of the URL and to correlate surface manifestation of discrete features with measurements of the same features underground. However, in locating a repository, the major hydrologic features are to be avoided, and a significant separation will be maintained between it and these features. Then the main concern would be the relatively better rock next to the repository, whose properties should be carefully characterized. Further, for PA, we need to know the properties along potential flow paths from the repository all the way to the biosphere. Thus, measurements at regularly spaced points over the whole area are more useful, and (in general) a geostatistical sampling method can be used to design the measurement strategy. This is probably different from conventional designs, which focus on points where there will be "action." A carefully considered measurement strategy specifically for the purpose of PA is needed to avoid this kind of bias.

As part of the measurement design, special care should be taken to obtain characterization data on the boundaries of the geologic repository system

under study. The boundary conditions have a major impact on the system evolution, but are often slighted in conventional measurement schemes.

It has been noted that surface-based boreholes are mostly subvertical and their data tend to be biased toward measurement of horizontal hydrologic conductivity. This bias should be recognized in data analysis when obtaining input for PA and should be accounted for in uncertainty evaluation. Special effort also needs to be taken to obtain data on the base of the repository system model. This is not easy, but these data are an important input to PA because they define the lower-boundary condition of the model. The lower-boundary condition can be studied by using a number of subvertical wells.

Another uncertainty in site characterization concerns the analysis methods that are applied to extract parameter values from field data. So far, nearly all the data-analysis methods assume a homogeneous and constant-property system. However, the real system is heterogeneous, with parameter values varying over space. Thus, a conventional "homogeneous" data-analysis method introduces additional uncertainties, whose impact depends on uses of the results.

Another lesson learned is that data should be documented together with a specification of the tool and analysis method by which they are obtained. Then the accuracy of the data and their confidence level can be known, and these may be of significant use in the PA process.

Several comments can be made concerning uncertainties in the development of structural models:

(a) The identification and tracing of fractures and fracture zones require subjective judgment.
(b) Confidence level varies strongly over area; there are some areas without information (the "black holes").
(c) A regular pattern of boreholes is recommended to provide needed data for a well-constructed structural model.

(d) It is important to map features not only inside the region of interest, but also some distance outside it. Information from the periphery of the region is important to identify and characterize the features within.
(e) The structures do not fully correlate to flow zones. Thus it is important to develop effective techniques to detect major hydraulic features over a large area corresponding to the local scale model.
(f) Model construction and site characterization activities are iterative, and we should be ready to modify the model as new data come in. Thus, an efficient and well-documented procedure needs to be in place to make potential modifications.
(g) It has often been found that certain geological structures do not correspond to observed hydrogeology features. This is a major problem.

9. Approaches to Flow and Transport Modeling

It is interesting to note that the performance-assessment methods used in NIREX95, SITE-94 and TILA-99 have different emphases, each with its own strengths.

The TILA-99 emphasizes simplified models in which conservative conditions and data are used for different parts of the model, such as leaching rate of the canister, hydraulic gradient near the emplacement hole, etc. It also allows the selection of repository design so that some of the problems can be designed away. SITE-94, on the other hand, emphasizes the evaluation of alternative conceptual and calculational models, including the use of different modeling teams to address the same system. A careful evaluation of uncertainties was conducted. Finally, NIREX95 performed a rather detailed analysis of a "complete" model with layers and structures in different regions. For each region or layer, the fracture or fault types were identified and upscaled effective parameters are used. Details are given in the following subsections.

9.1 Simplified Analysis (TILA-99)

The analysis involves three parts: the near field flow, site-to-canister model, and the far field flow. In the near field, three escape routes are identified: (a) from bentonite around the canister to a rock fissure intersecting the emplacement hole Q_F; (b) from backfill at the top of the hole to the disturbed zone below the tunnel floor Q_{OZ}; and (3) from the tunnel to the rock medium or the near-field excavation disturbed zone Q_{TDZL}. The rock permeability around a 6 m emplacement borehole is built up from field data obtained in packer tests in boreholes with packer interval of 2 m. The flow rates around the emplacement hole are estimated by assuming maximum local hydraulic gradients. It is argued that the maximum transport resistance is the boundary-layer resistance between stagnant water in the bentonite and water flowing in rock fissures during the diffusion process.

In the site-to-canister model, calculations from a larger scale model are used to provide the boundary conditions and driving forces for this model. Flow through intact rock, excavation-disturbed zones, and fracture zones is evaluated using several conceptual models, ranging from infinite fractures, resistor network, to stochastic fracture network models. The key quantity controlling transport is found to be WL/Q where W is the width of flow path, L is its length and Q is the flow rate along it.

In modeling the far field flow, evaluation is made along identified migration pathways. The main process accounted for is matrix diffusion with sorption, in addition to the WL/Q factor. A number of effects, such as dispersion along the pathways, effects of fracture filling and stagnant pools, are ignored for conservatism.

9.2 Multiple-Model Analysis (SITE-94)

SITE-94 emphasizes on use of multiple models and evaluation of conceptual and calculational model uncertainties. In the very near field with length scale of less than 50 m, a 3D stochastic discrete fracture network model is used. This is supplemented by a 3D stochastic variable aperture fracture network model. For the site scale, which is defined as length scale less than 5 km, several conceptual hydrological models are used: namely, a 3D discrete feature model, a 3D stochastic continuum model and a 2D simple flow path model based on Darcy's law. Further, a lithofacies model was also applied in a feasibility study. It is at this and smaller near-field scales that distribution of hydrogeologic flow and transport parameters for radionuclide release and transport are calculated. At an even larger scale of 10 km, up to 1500 km, 2D vertical and 2D horizontal continuum models are used to analyze regional flow patterns and to provide boundary conditions for site-scale models.

Each of the different models at the site scale presents PA predictions (such as flow velocity near a repository as a range to account for uncertainties in parameter values used), and for stochastic models the range also corresponds to predictions for multiple realizations. Further, within each model, certain fracture set parameters are changed, generating additional prediction ranges. All the results are compared with each other and evaluated. Generally, predictions of the simple model overlaps with those of the complex model; however, the simple model has wider uncertainties (because its parameters have larger uncertain ranges to represent realistic situations) than complex models whose prediction ranges are much less. Thus, in one case (for instance), predictions of near-field Darcy velocity from a stochastic continuum model ranges from 2×10^{-6} to 7×10^{-3} m/yr., whereas the range from the simple flow path model is from 4×10^{-6} to 10^{1} m/yr.

9.3 Detailed Model Analysis

The focus of NIREX95's approach is on a complex model composed of 2D heterogeneous, layered continuum model to cover 10–15 Km scale with a detailed 3D stochastic fracture network model to cover about 3 km around the repository. The near-field fracture network is generated numerically for alternative realizations. In the far field, each layer or region is evaluated as to its fracture characteristics, from which an upscaling prescription is used to estimate its hydraulic properties. Often specific data is not available. Then a formal expert elicitaton procedure is used to estimate possible parameter ranges. All these are brought together for large scale flow calculations, whose results are used in a particle tracking computation to predict radionuclide transport from the repository to the biosphere.

9.4 Comment on NIREX95, SITE-94 AND TILA-99 Approaches

All three approaches are of interest and of significant usefulness to PA. It will be good to take all three simultaneously, considering that the cost of the PA will be mostly surface and subsurface site preparation and field measurements, the additional model activities would be a smaller part of the cost. These alternative approaches are valuable and add confidence to the overall PA effort and results.

10. Sensitivity and "What If" Analyses

In PA, there is a need for a careful consideration and clear presentation of sensitivity and "what if" analyses in order to provide a "robust" safety evaluation. For example, under sensitivity analysis, the following cases can be considered:

- Alternative canister failure times (canister disappearing at 0, 10^3, 10^5, and 10^6 years)

- Alternative source term models
- Case of very high solubilities in reducing conditions
- Case of oxidizing conditions in the near field
- Case of transport along 10 tunnel sections, each with a leaking canister
- Alternative penetration depths of matrix diffusion (1 and 4 cm)
- Alternative dispersion (Pe number = 2) along flow paths in the far field
- Alternative dose conversion factor (increased by a factor of 10)
- Use of realistic retardation data in the near field and far field respectively

The "what if" scenarios can include:

- Case of combination of very high groundwater flow and high saline groundwater chemistry
- Case of very poor performance of the bentonite buffer
- Case of gas production in a canister with its displacement of contaminant water out of the canister
- Effect of glacial melt water involving very high flow and oxidizing conditions in the geosphere, buffer, and backfill
- Effect of post-glacial faulting at 30,000 years, breaking canister, displacing bentonite, enhancing flow and transport and bringing about oxidizing conditions in the whole near field and geosphere.

As can be seen, some of these sensitivity and "what if" scenarios represent rather drastic conditions. For each, the impact and probability of occurrence are evaluated. The conclusion may indicate a consistent picture of performance for the modeled transport system – the system is robust and can tolerate even much more conservative assumptions without drastic impact on potential releases to the biosphere. Hopefully, except for certain very unlikely events, such as postglacial faulting (which cuts through several barriers at the same time), the results are still orders of magnitude below the regulatory limits.

11. Concluding Remarks and Comments on JNC's H-12 Report

SITE-94, TILA-99 and NIREX95 all have their strengths and useful methodologies. Identification and application of appropriate techniques from these three efforts will be very useful to the Japanese nuclear waste repository program. For example, if one were to pick one strong point from each of these three PA efforts, we may have the following:

- TILA-99: good sensitivity and "what if" analysis; effort towards robust, transparent, traceable, and reproducible analyses for building confidence on results.
- SITE-94: consistency evaluation among different data types and among different structural and hydrological models, and use of multiple groups for alternative model analysis.
- NIREX95: careful classification of fracture types and use of formalized expert elicitation procedure to build up a complex model for detailed analysis.

In view of the combined review of these three PA efforts, we may list below a number of general suggestions and comments to the JNC's H-12 report:

- It is good that the H-12 report has employed the FEP methodology, carried out analyses on "reference case," "base case," and alternatives cases; and conducted a series of "what if" studies.
- It may also be useful for the Japanese program to apply the methodologies of PID (Process Influence Diagram) and AMF (Assessment Model Flowchart) to guide its PA effort.
- The multiple independent-channel model used in the H-12 report may need to be advanced by using other models, such as the Channel Network Model, Fracture Network Model and Stochastic Continuum Model.
- The use of large values of "dispersion" along 1D channels is questionable. The dispersivity along each channel could well be less than 1 m. It is the combination of flows along many such 1D channels that may yield an apparent large dispersivity value.
- "Conservative" or "moderately conservative" are often not well-defined and thus may introduce uncertainties that need to be kept track of.

- It is useful for JNC's program to emphasize more the "iterative" approach, in which site measurements, modeling, and result evaluations are not a single-directional process, but iterative.
- There is a need for a careful evaluation of data uncertainties and uncertainties of the structural and conceptual model.
- The use of a structured expert-elicitation procedure may be helpful to the JNC's PA effort, but it should be carefully documented so that the results are defensible and traceable.
- It will be good if JNC can employ, in its PA effort, alternative models and efforts by different teams, to study model uncertainties and to increase the confidence and robustness of its conclusions.